

# Dissertation

*submitted to the*

Combined Faculties of the Natural Sciences and Mathematics  
of the Ruperto-Carola University of Heidelberg, Germany

*for the degree of*

Doctor of Natural Sciences

*Put forward by*

**Laura Classen**

Born in Geldern, Germany  
Oral examination: 4.11.2016



# Competing Orders in Strongly Correlated Systems

Dirac Materials and Iron-Based Superconductors

Referees: PD Dr. Michael M. Scherer  
Prof. Dr. Manfred Salmhofer



## **Competing Orders in Dirac Materials and Iron-Based Superconductors**

In this work we address the collective phenomena appearing in interacting fermion systems due to the competition of distinct orders at the example of Dirac materials and iron-based superconductors. On the one hand we determine leading ordering tendencies in an unbiased way, when Fermi liquid instabilities are expected simultaneously in the particle-particle and particle-hole channel. In this context we analyze the impact of electron-phonon interactions on the many-body instabilities of electrons on the honeycomb lattice. Furthermore we investigate the interplay between superconductivity, magnetism and orbital order in five-pocket iron-based superconductors including the full orbital composition of low-energy excitations. On the other hand we study how the close proximity of different phases affects the structure of the phase diagram and the nature of transitions, as well as the corresponding quantum multicritical behavior. To this end we consider the semimetal-insulator transitions to an antiferromagnetic and a staggered-density state of low-energy Dirac fermions. To account for the decisive role of interactions and the various degrees of freedom in these models, modern renormalization group techniques are applied.

## **Konkurrierende Ordnungen in Dirac Materialien und eisenbasierten Supraleitern**

Diese Arbeit befasst sich mit den kollektiven Phänomenen, die in wechselwirkenden Fermionensystemen aufgrund des Wettstreits zwischen verschiedenen Ordnungen auftreten, am Beispiel von Dirac Materialien und eisenbasierten Supraleitern. Einerseits werden die führenden Ordnungstendenzen vorurteilsfrei bestimmt, wenn Instabilitäten der Fermiflüssigkeit gleichzeitig im Teilchen-Teilchen und Teilchen-Loch Kanal erwartet werden. In diesem Zusammenhang wird der Einfluss von Elektron-Phonon Wechselwirkungen auf die Vielteilchen-Instabilitäten der Elektronen des Honigwabengitters analysiert. Außerdem wird das Wechselspiel zwischen Supraleitung, Magnetismus und orbitaler Ordnung in eisenbasierten Supraleitern mit fünf Pockets unter Berücksichtigung der vollen orbitalen Zusammensetzung der Anregungen bei niedriger Energie untersucht. Andererseits wird erforscht, wie die Nähe verschiedener Phasen sowohl die Struktur des Phasendiagramms und die Natur der Übergänge, als auch das entsprechende quanten-multikritische Verhalten beeinflusst. Dafür werden die Übergänge zwischen Halbmetall und Isolator zu einem antiferromagnetischem und einem Ladungsdichtezustand von niedrigerenergetischen Diracfermionen betrachtet. Um die entscheidende Rolle von Wechselwirkungen und der verschiedenartigen Freiheitsgrade in diesen Modellen zu berücksichtigen, werden moderne Renormierungsgruppentechniken angewandt.



---

## Contents

---

<b>1. Introduction</b>	<b>11</b>
1.1. Competing Orders . . . . .	11
1.2. Investigated Materials . . . . .	12
1.2.1. 2D Dirac Materials . . . . .	12
1.2.2. Iron-Based Superconductors . . . . .	14
1.3. Outline of the Thesis . . . . .	15
<b>2. Phase Transitions – Signals, Investigation Methods and Characteristics</b>	<b>19</b>
2.1. Interaction-Induced Fermi Liquid Instabilities . . . . .	19
2.1.1. Divergent Channels and Spontaneous Order . . . . .	19
2.1.2. Ginzburg-Landau-Wilson Action . . . . .	22
2.1.3. What is missing in this picture? . . . . .	23
2.2. Renormalization Group Methods . . . . .	24
2.2.1. Wilsonian Renormalization Group . . . . .	24
2.2.2. Functional Renormalization Group . . . . .	26
2.2.3. Example: The Ground State Phase Diagram of the Half-Filled Bilayer Hubbard Model . . . . .	32
2.3. Critical Phenomena . . . . .	36
2.3.1. Scaling from RG $\beta$ Functions and Fixed Points . . . . .	36
2.3.2. Multicritical Behavior . . . . .	38
<b>3. Interplay of Phonon and Electron Interactions in Graphene</b>	<b>41</b>
3.1. Electronic Correlations on the Dynamically Distorted Honeycomb Lattice . . . . .	41
3.2. The Honeycomb Lattice . . . . .	42
3.2.1. Extended Hubbard Model on the Honeycomb Lattice . . . . .	42
3.2.2. Inclusion of Phonon Modes . . . . .	43
3.2.3. Patching Scheme on the Honeycomb Lattice . . . . .	44
3.3. Instabilities and Phase Diagram . . . . .	45
3.3.1. Purely Phonon-Mediated Interaction . . . . .	45
3.3.2. Inclusion of Density-Density Interactions . . . . .	49
3.4. Conclusions . . . . .	50

<b>4. Competition of Density Waves and Quantum Multicritical Behavior in Dirac Materials</b>	<b>53</b>
4.1. The Multicritical Point Between Charge and Spin Density Waves in Dirac Materials	53
4.2. Effective Dirac Description	56
4.3. Classification of Fixed Points	58
4.4. Multicritical Behavior from the $\epsilon$ -Expansion	59
4.4.1. Flow Equations and Fixed Points	59
4.4.2. Phase Diagram	62
4.4.3. Conclusion on $\epsilon$ -Expansion	63
4.5. FRG-Improved Calculation	64
4.5.1. Truncation and Flow Equations	64
4.5.2. Chiral Ising and Chiral Heisenberg Universality Class for $N_f = 2$	68
4.5.3. From $4-\epsilon$ to 3 Space-Time Dimensions	70
4.5.4. Fixed Points as Function of Fermion Flavor Number	71
4.5.5. FRG Phase Diagram	73
4.6. Conclusion	76
<b>5. Interplay between Magnetism, Superconductivity and Orbital Order in 5-Pocket Iron-Based Superconductors</b>	<b>79</b>
5.1. The Multiorbital Nature of Low-Energy Excitations	79
5.2. 3-Orbital, 5-Band Model	80
5.2.1. Kinetic Part of the Hamiltonian	80
5.2.2. The Toy Model	82
5.2.3. Interactions	82
5.3. Analytic Parquet RG for the 5-Pocket Model	85
5.3.1. PRG for the Toy Model	85
5.3.2. PRG For the Full Model	92
5.4. Conclusion	94
<b>6. Concluding Remarks</b>	<b>95</b>
<b>Appendix</b>	<b>96</b>
<b>A. Competition of Density Waves and Quantum Multicritical Behavior in Dirac Materials – Flow Equations and Convergence</b>	<b>97</b>
A.1. Explicit FRG Flow Equations	97
A.1.1. Flow Equations for the Yukawa Couplings	97
A.1.2. Anomalous Dimensions	98
A.1.3. Projection Prescriptions for Anomalous Dimensions	99
A.2. Threshold Functions	99
A.2.1. General Expressions	100
A.2.2. Linear Cutoff	101
A.2.3. Sharp Cutoff	104
A.3. Check of Convergence	105



---

<b>B. Interplay between Magnetism, Superconductivity and Orbital Order in Iron-Based Superconductors – Orbital Makeup and PRG Equations</b>	<b>107</b>
B.1. Orbital Makeup . . . . .	107
B.2. PRG for the Toy Model . . . . .	108
B.2.1. PRG Equations for the 21 Couplings . . . . .	108
B.2.2. Weakly Unstable Fixed Trajectory of the Toy Model . . . . .	109
B.3. Pomerachuk Channel . . . . .	110
B.4. PRG for the Full 5-Pocket Model . . . . .	110
B.4.1. PRG Equations for the 40 Couplings . . . . .	110
B.4.2. Fixed Trajectories . . . . .	112
B.4.3. Susceptibilities . . . . .	114
<b>Danksagung</b>	<b>117</b>
<b>Bibliography</b>	<b>119</b>



# CHAPTER 1

---

## Introduction

---

### 1.1. Competing Orders

In quantum many-body systems fascinating collective phenomena appear, which cannot be explained by considering simply the sum of single-particle properties. Especially in the context of symmetry-breaking phase transitions in interacting condensed matter systems novel phases of matter are frequently discovered. They include e. g. very different kinds of magnetic order, BCS-type and unconventional superconductivity, or diverse topological phases. Hence the question arises, which mechanisms and circumstances lead to the large variety of intriguing states. The competition between various types of order is inherently related to this question. The possibility to induce superconductivity due to magnetic correlations in copper- or iron-based superconductors is a prevailing example [1–4]. However, the close proximity of several distinct phases appears in the phase diagram of many materials, and promises an equally rich behavior for the interplay of orders. Given the large variety of possible ordering patterns, it is generally challenging to identify the leading ordering tendencies in strongly correlated systems. Additionally, novel states of matter can arise in coexistence phases, where different ordering types occur simultaneously. One of many interesting examples for this is given by the possible existence of a supersolid between the solid and superfluid phase in  $^4\text{He}$  [5–7].

In the study of (competing) ordering tendencies interactions often play a decisive role and besides external tuning parameters, such as temperature or pressure, it depends on their structure and properties which states prevail. Related to this are quantum phase transitions, which clearly reveal the impact of microscopic parameters on macroscopic states. Thereby physical systems close to continuous transitions show the surprising phenomenon of universality, i. e. the critical behavior in the vicinity of the transition is the same for classes of models that can be very different in their microscopic details. On the contrary, only the system's symmetry and dimensionality determine its universal behavior. Furthermore fluctuations on all scales play a crucial role, particularly in low dimensions. They can drastically change the critical behavior as compared to mean-field expectations. In this context it is interesting how the presence of two or more types of order affects the critical behavior. A second order parameter field influences the symmetry considerations and provides a further source of fluctuations so that we cannot expect to rediscover the critical behavior of the separate phase transitions in this case (see e. g. [8–12] for a related discussion in  $O(N) \oplus O(M)$  models).

In summary the following key questions arise and serve as motivation to study the competition of orders

1. What are the leading correlations in the system under consideration and how can we approach their determination in an unbiased way?
2. If distinct phases meet, what is the resulting phase structure? Do mixed phases occur?
3. What is the nature of the phase transitions? What is the impact on the (multi-)critical behavior regarding continuous transitions?

In this thesis we consider two different model systems and reveal different aspects of the phenomena described above. With regard to Dirac materials, we determine the leading ordering tendencies of electrons on the honeycomb lattice in interplay with phonon degrees of freedom. Furthermore, we examine more closely the competition of different density waves and the corresponding multicritical point in the phase diagram of Dirac materials. In iron-based superconductors we investigate the interplay between distinct types of superconductivity, magnetism and orbital order for the material class with five Fermi pockets.

For our study we will employ different approaches of the renormalization group (RG) method [13–17]. The RG is particularly suited for the study of phase transitions and competing orders. The reason is twofold and demonstrates the versatility of the RG framework. On the one hand the renormalization group incorporates the idea of scale dependence. Consequently, it allows to monitor the evolution of a system to low energies and the build-up of the leading correlations. This, in turn, provides the possibility to detect scale-free points, related to continuous phase transitions, and determine the corresponding critical behavior. On the other hand the renormalization group formalism is not restricted to special channels or setups and can deal with many coupled degrees of freedom without favoring one and quenching another. This unbiased structure is especially advantageous in the context of competing orders.

## 1.2. Investigated Materials

### 1.2.1. 2D Dirac Materials

A growing number of related materials display low-energy Dirac-like excitations (cf. Fig. 1.1), which lead to universal properties in seemingly different samples [19]. In transport properties, for example, impurity scattering or screening effects exhibit common features [20] as a consequence of the Dirac spectrum. Interestingly these materials also relate high-energy and condensed matter systems. A prominent example for such a Dirac material is graphene [21–23], with a number of new relatives, such as silicene [24–27] and germanene [28–30]. Layered heterostructures [31–36], bosonic Dirac materials [37–39] and artificial graphenes [40–42], as well as 3D Dirac and Weyl semimetals [43–46] would also fall into the same class. The large number of examples demonstrates the great current interest in this novel type of materials, which has motivated a lot of studies of their fascinating properties, and led to the ambition to design and control their features in potential applications.

Several unconventional electronic properties of these materials can to a large extent be captured by means of a description in terms of free Dirac fermions [23, 47]. The experimental findings in graphene, such as, for example, the half-integer quantum Hall effect [48] or the Klein paradox [49], suggest that this single-particle picture provides a very good starting point for the theoretical description of the material. Electron-electron interactions therefore

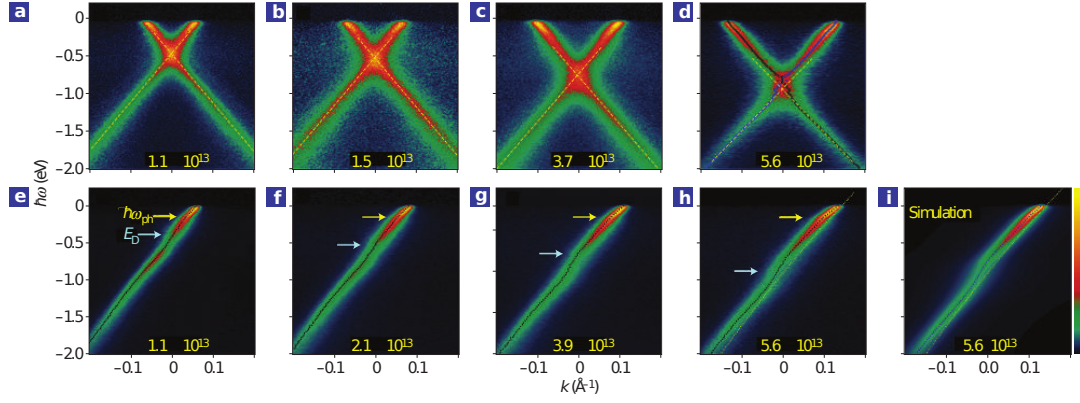


Figure 1.1.: The band structure of graphene near the Fermi level measured by ARPES. The Dirac cone is clearly visible. Figs. (a-d) and (e-h) show the experimental energy bands for different directions through the Dirac cone, respectively. The doping is increased from left to right. In Figs. (e-h) one of the bands is suppressed. (i) The simulated spectral function with data from (h) [18]

are often expected to play only a quantitative and not a qualitative role. In fact, due to the linear Dirac dispersion, in 2D the density of states vanishes linearly at charge neutrality for energies close to the Fermi level, and an interaction-induced transition toward an ordered – possibly Mott insulating – state appears only when a minimal critical value of the interaction strength is exceeded [50–55]. Depending on the interaction profile, such as the precise ratios of onsite, nearest-neighbor, and further interaction parameters, a great variety of different spontaneously broken symmetries has been proposed [56–63]. The symmetry breaking patterns, most prominently, include chiral symmetry breaking phases, such as the antiferromagnetic spin density wave (SDW) or a charge density wave (CDW) [58,64–66]. Furthermore, modulated and incommensurate charge density waves have been suggested, and more exotic states of matter such as the quantum spin Hall phase [59–61, 67–69], or the existence of a quantum spin liquid have been discussed [70, 71]. Additionally at finite doping, unconventional superconducting states can occur [57, 63, 72, 73]. In this regard, the investigation of interaction-induced phase transitions may yield an important contribution to an improved understanding and the possible manipulation of different states of matter in this class of materials. Thereby the coexistence of orders resulting in novel states has explicitly been considered in Ref. [74–76].

Current experimental data, however, suggest that e. g. free-standing graphene is in the semimetallic (SM) phase [77, 78]. From the theoretical side, calculations based on the constrained Random Phase Approximation (cRPA) and beyond provide values for the interaction parameters of the Coulomb repulsion for graphene and its few-layer relatives [79, 80]. Quantum Monte Carlo (QMC) studies for these parameters confirm the semimetallic behavior of physical graphene in agreement with the experimental findings [81, 82]. At the same time, these results suggest that the material may be not too far from a possible transition into an ordered state. Other QMC calculations also find sizable charge-density and spin-current correlations, although they do not become long-ranged within the accessible parameter region [83]. Furthermore, a uniform and isotropic strain of about 15% can be expected to induce an interaction-driven metal-insulator transition in graphene [84]. It is therefore not inconceivable that physical graphene could possibly be tuned through a symmetry-breaking quantum phase transition [51, 55, 85, 86]. Similar conclusions may be expected to hold for other Dirac materials [19, 24–30] and should also be relevant for “artificial graphene” [40–42]. Breaking the chiral symmetry through a

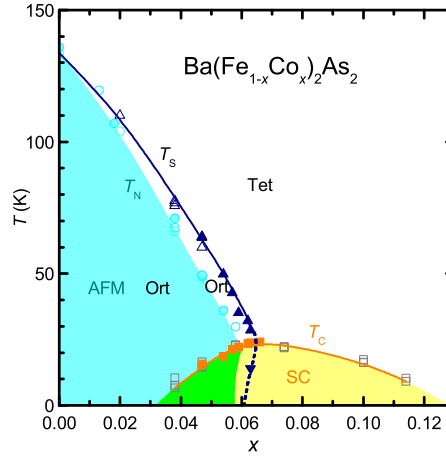


Figure 1.2.: The phase diagram for  $\text{Ba}(\text{Fe}_{1-x}\text{Co}_x)_2\text{As}_2$  as function of temperature  $T$  and doping  $x$  [87]. The paramagnetic tetragonal phase (Tet) for  $T > T_S$  or  $T > T_C$  either undergoes a superconducting (SC) or a structural, orthorhombic transition (Ort). For  $T < T_N$  long-range antiferromagnetic order (AFM) appears.

substrate can likewise induce a gap and enable to control the phase transition by varying the crystallographic alignment in layered heterostructures [31–36]. The multitude of suggestions and the vicinity of ordered states motivates our following studies of interaction-induced phase transitions and the interplay of different ordering tendencies in Dirac materials.

### 1.2.2. Iron-Based Superconductors

Superconductivity belongs to the most fascinating phenomena in interacting quantum systems and naturally attracts much interest. It occurs with many different faces regarding the mechanisms to induce an attractive pairing interaction, as well as the form and symmetry of the Cooper pairs. The corresponding exciting question, how the generally repulsive electronic interaction is turned into an attractive coupling, strongly depends on material properties and is often related to the interplay between different electronic correlations.

This is also the case in iron-based superconductors (FeSC) (e. g. [88–92]). These materials belong to a large family of different chemical compounds that possess a common iron-pnictogen or iron-chalcogen plane, which is responsible for the superconducting properties. In this plane the iron atoms are arranged on a simple square lattice, yet, due to the electronic configuration of the iron atoms one has to account for additional orbital degrees of freedom. This multi-orbital nature in turn leads to multiple Fermi surfaces and is responsible for characteristic properties of FeSCs [93]. In the phase diagram of most FeSCs, the superconducting state is located in the vicinity of a magnetic and a nematic phase. At the example of  $\text{BaFe}_2\text{As}_2$ , this can be seen in Fig. 1.2. The magnetic phase is often of stripe type, where neighboring spins are ferromagnetically aligned in one and antiferromagnetically aligned in the other direction. However, also more complex spin configurations due to multiple nesting vectors have been discussed [94–99]. In the nematic phase the fourfold lattice rotation symmetry is broken down to a twofold one. While its origin remains controversial, it is often related to spontaneous orbital order or to a concomitant of the magnetic phase called Ising-nematic spin order [100–111]. Fluctuations of both, magnetic and orbital type, have been suggested as driving force for the pairing instability in FeSCs and, depending on the mechanism, result in different pairing

symmetries [112, 113].

The interplay between superconductivity, magnetism, and spontaneous orbital order in FeSCs remains at the forefront of the analysis in this field [111, 114]. It has been argued by several groups [115–123] that the most unbiased way to analyze the competing orders is not to focus on a particular channel but rather follow the evolution of the interactions in all channels as temperature is lowered. This analysis can be rigorously justified in FeSCs because there are other channels, besides the superconducting (SC) one, in which interactions evolve logarithmically upon the lowering of temperature/energy: (i) the interaction in the particle-hole channel at momenta  $Q$ , separating hole and electron pockets, evolves logarithmically due to opposite sign of fermionic dispersions [95, 124] and leads to the magnetic instability in the phase diagram. (ii) The composite effect of two scatterings by  $Q$  in the particle-hole channel gives rise to logarithmic variation of the interaction in the Pomeranchuk channel, relevant to orbital ordering [122]. It is therefore desirable to study the complex interplay of orders in FeSCs including the full orbital content in an unbiased way.

### 1.3. Outline of the Thesis

In this work we present the results on the interplay of orders in two different material families, two-dimensional Dirac materials with an eye on graphene and 5-pocket iron-based superconductors. We start with a collection of the basic concepts appearing during the study of phase transitions and competing orders in Chap. 2. First, we recall the instabilities of Fermi liquids as revealed by specific ladder summations in Sec. 2.1 and briefly connect them to possible ordering patterns, which they hint at. Ginzburg-Landau-Wilson theory is presented as an alternative description in these cases. In Sec. 2.2 we explain the different RG techniques that we employ in this thesis to study the aforementioned Fermi liquid instabilities. These include perturbative one-loop approaches in the spirit of the “original” Wilson RG and functional RG (fRG) methods based on exact, but necessarily truncated equations. We thereby compare their advantages and disadvantages and give an example fRG calculation for the Hubbard model on the bilayer square lattice. As a last step in Sec. 2.3, we relate the RG framework to the universal critical behavior occurring in the vicinity of second order phase transitions and discuss the stability properties of multicritical points.

In the following chapters, we report three analyses about the interplay of ordering tendencies in different setups. In Chap. 3, we discuss the impact of electron-phonon interactions on the many-body instabilities of electrons on the honeycomb lattice and their interplay with repulsive local and non-local Coulomb interactions at charge neutrality. After a short motivation of the subject in Sec. 3.1, we introduce the tight-binding description of the honeycomb lattice and its distortions by in-plane optical phonon modes in Sec. 3.2. In Sec. 3.3 we calculate the instabilities due to the effective phonon-mediated electron-electron interaction, as well as its influence on electronically-driven instabilities due to further ranged density-density interactions. We also present the resulting phase diagram, which shows an extension of the spin-density wave regime and a suppression of competing orders.

In Chap. 4 we study the competition of spin- and charge-density waves and their quantum multicritical behavior for the semimetal-insulator transitions of low-dimensional Dirac fermions. We start with an introduction to the considered problem and an overview of the results (Sec. 4.1). We then motivate the effective Dirac description by deriving it from the honeycomb lattice of graphene in Sec. 4.2 and present the effective Gross-Neveu-Yukawa theory with two order parameters that allows us to study the multicritical point at which the semimetallic and the spin-

and charge-density-wave phases meet. In the subsequent sections we perform a fixed-point analysis in terms of two different methods, the one-loop RG approach in combination with an expansion close to the upper critical dimension of the model (Sec. 4.4) and the functional RG techniques (Sec. 4.5). We calculate the critical exponents and determine the structure of the phase diagram, including the nature of transition lines, in the vicinity of the intersection between the semimetal, antiferromagnetic and staggered density phases. Depending on the number of fermion flavors, we find qualitatively the same behavior with both methods. However, the clear picture drawn by the analytical considerations within the expanded one-loop analysis obtains crucial quantitative corrections from the fRG calculation.

We turn to the second class of investigated materials in Chap. 5, where we investigate the interplay of superconductivity, magnetism and orbital order for FeSCs with five Fermi pockets. We motivate the description that accounts for the orbital content of excitations close to the Fermi energies in Sec. 5.1 and explain the resulting, effective model containing five pockets made out of three orbitals in Sec. 5.2. Due to the complexity of the full model, we additionally consider a toy model, which captures already a large extent of the complete description. In Sec. 5.3 we determine the parquet RG flow of all the symmetry-allowed interactions, which we use as an input to calculate susceptibilities for the different orders. We find that the 5-pocket model effectively reduces either to a 3-pocket or a 4-pocket one and discuss consequences for the ordering tendencies.

We finally summarize and draw conclusion in Chap. 6. The appendix contains technical details regarding the RG flow. App. A supplements the calculations for the study of the multicritical point between density waves in Dirac materials. In App. B we list additional specifications for the analysis of the 3-pocket, 5-band model of FeSCs.



The compilation of this thesis is solely to the author. The results and presentations are largely based on work with my collaborators. The related publications are [125–128]:

- *Instabilities on graphene’s honeycomb lattice with electron-phonon interactions*  
Laura Classen, Michael M. Scherer, Carsten Honerkamp  
Physical Review B **90**, 035122 (2014)
- *Ground state phase diagram of the half-filled bilayer Hubbard model*  
Michael Golor, Timo Reckling, Laura Classen, Michael M. Scherer, Stefan Wessel  
Physical Review B **90**, 195131 (2014)
- *Mott multicriticality of Dirac electrons in graphene*  
Laura Classen, Igor F. Herbut, Lukas Janssen, Michael M. Scherer  
Physical Review B **92**, 035429 (2015)
- *Competition of density waves and quantum multicritical behavior in Dirac materials from functional renormalization*  
Laura Classen, Igor F. Herbut, Lukas Janssen, Michael M. Scherer  
Physical Review B **93**, 125119 (2016)
- *Interplay between magnetism, superconductivity, and orbital order in 5-pocket model for iron-based superconductors – a parquet renormalization group study*  
Laura Classen, Ruiqi Xing, Maxim Khodas, Andrey V. Chubukov  
Submitted to Physical Review Letters (Aug. 2016)

The foundations for [125] have already been established during my Master’s thesis and have then been extended during my doctoral research<sup>1</sup>.

---

<sup>1</sup>Electrons on the honeycomb lattice couple primarily to optical phonons with wavevectors close to  $\Gamma$  and  $K, K'$  points in the Brillouin zone. The couplings to  $\Gamma$  phonons has been studied in my Master’s thesis. The more dominant  $K, K'$  phonons have been included during my doctoral research.



## CHAPTER 2

---

### Phase Transitions – Signals, Investigation Methods and Characteristics

---

#### 2.1. Interaction-Induced Fermi Liquid Instabilities

Fermi liquid theory has been very successful to describe the behavior of metallic systems at low temperatures. It claims that an interacting fermion system is adiabatically connected to the state without interaction so that basic properties show qualitatively the same behavior as the non-interacting Fermi gas. Nevertheless many materials exist whose ground state qualitatively changes when the temperature is lowered. In other words the interactions between the fermions lead to an instability of the Fermi liquid in these cases. The criteria for the development of such an instability and its consequences will be discussed in the following.

##### 2.1.1. Divergent Channels and Spontaneous Order

Let us consider an interacting system of many fermions  $\psi^\dagger, \psi$  with spin  $\sigma$  that exhibits translation invariance and can be described by the Hamiltonian

$$H = \sum_{k,\sigma} \epsilon_k \psi_{k,\sigma}^\dagger \psi_{k,\sigma} + V. \quad (2.1)$$

The free part is determined by the dispersion  $\epsilon(k)$  and the interaction is further specified by

$$V = \frac{1}{N} \sum_{\substack{k_1, k_2, k_3, \\ \sigma, \sigma'}} V(k_1, k_2, k_3) \psi_{k_3, \sigma}^\dagger \psi_{k_1 + k_2 - k_3, \sigma'}^\dagger \psi_{k_2, \sigma'} \psi_{k_1, \sigma}. \quad (2.2)$$

Such a bare interaction also gives rise to an effective interaction due to multiple scattering events. Within perturbation theory, we can obtain a first estimate for the effect of several scattering processes by calculating the 1-loop correction to the bare interaction. For the general spin-rotation invariant interaction above, it is given by the three contributions

$$\tau_{pp} = \int_q V(k_1, k_2, q) G(q) G(k_1 + k_2 - q) V(q, k_1 + k_2 - q, k_3) \quad (2.3)$$

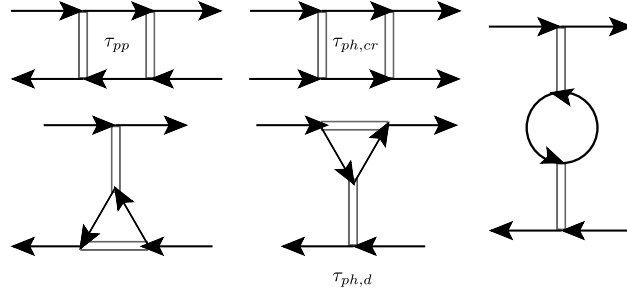


Figure 2.1.: The 1-loop contributions coming from the particle-particle channel  $\tau_{pp}$ , the crossed particle-hole channel  $\tau_{ph,cr}$  and the direct particle-hole channel  $\tau_{ph,d}$ .

$$\tau_{ph,cr} = \int_q V(k_1, k_2 + q - k_3, q) G(q) G(k_2 + q - k_3) V(q, k_2, k_3) \quad (2.4)$$

$$\tau_{ph,d} = \int_q -2V(k_1, q, k_3) G(q) G(k_1 + q - k_3) V(k_1 + q - k_3, k_2, q) \quad (2.5)$$

$$+ \int_q V(k_1, q, k_1 + q - k_3) G(q) G(k_1 + q - k_3) V(k_1 + q - k_3, k_2, q) \quad (2.6)$$

$$+ \int_q V(k_1, q, k_3) G(q) G(k_1 + q - k_3) V(k_2, k_1 + q - k_3, q) \quad (2.7)$$

$$(2.8)$$

according to the particle-particle, crossed particle-hole and direct particle-hole diagrams in Fig. 2.1. Here  $q = (q_0, \mathbf{q})$  collects the Matsubara frequencies and spatial momenta, and  $\int_q = (2\pi)^{-d} \int d^d q$  involves both of them, i. e. for simplicity we consider zero temperature. The three contributions differ by the combination of momenta in the interaction  $V$  and especially in the free propagator  $G(k) = (i\omega - \epsilon_k)^{-1}$ . In many physical systems specific momentum combinations exist that lead to divergences of the effective interaction at low energies. To see this, we choose a simple Hubbard-type interaction as example

$$V = \frac{U}{N} \sum_{\substack{k_1, k_2, k_3, \\ \sigma, \sigma'}} \psi_{k_3, \sigma}^\dagger \psi_{k_1 + k_2 - k_3, \sigma'}^\dagger \psi_{k_2, \sigma'} \psi_{k_1, \sigma}. \quad (2.9)$$

In this case the three diagrams of the direct particle-hole channel cancel and only the particle-particle and crossed particle-hole contributions remain. After performing the integration over Matsubara frequencies at zero temperature and relabeling  $k_2 = -k_1 + Q$  in the particle-particle and  $k_2 - k_3 = Q$  in the particle-hole channel, we obtain

$$\tau_{pp} = U^2 L_{pp}(q), \quad L_{pp}(q) = \int_q G(q) G(-q + Q) = \int_q \frac{1}{-iQ_0 + \epsilon_q + \epsilon_{-q+Q}} \quad (2.10)$$

$$\tau_{ph,cr} = U^2 L_{ph}(q), \quad L_{ph}(Q) = \int_q G(q) G(q + Q) = \int_q \frac{1}{iQ_0 + \epsilon_q - \epsilon_{q+Q}}. \quad (2.11)$$

In these expressions, we directly see that for zero external frequency  $Q_0 = 0$ , the particle-particle diagram develops a logarithmic divergence if  $\epsilon_q = \epsilon_{-q+Q}$ , which is often the case for

zero external momentum  $Q = 0$ . In turn the particle-hole contribution diverges logarithmically if the nesting condition  $\epsilon_{q+Q} = -\epsilon_q$  is satisfied. Then the integrals can be approximated as

$$\tau_{pp} \approx -\tau_{ph,cr} \approx U^2 \rho_0 \ln \frac{W}{\Lambda_{IR}}, \quad (2.12)$$

where we have introduced the density of states at the Fermi surface  $\rho_0$ , the bandwidth  $W$  and the infrared cutoff  $\Lambda_{IR}$ . If we now sum separately the particle-particle and particle-hole ladder we obtain

$$U_{pp/ph\text{-ladder}} = U - UL_{pp/ph}(Q)U_{pp/ph\text{-ladder}} \quad (2.13)$$

$$U_{pp/ph\text{-ladder}} = \frac{U}{1 + UL_{pp/ph}(Q)} \rightarrow \frac{U}{1 \pm U\rho_0 \ln \frac{W}{\Lambda_{IR}}}. \quad (2.14)$$

Already within this simple approximation, we can make several fundamental observations. First of all, we find that potential instabilities arise in our description because the effective interaction may diverge when  $1 \pm U\rho_0 \ln \frac{W}{\Lambda_{IR}} = 0$ . This can be interpreted as the formation of bound states or the emergence of new degrees of freedom such as the Cooper pairs in a superconductor. In other words these instabilities signal the possibility of spontaneous symmetry breaking. On its own, the particle-particle channel can only develop such an instability if the bare interaction is attractive. For the particle-hole channel to diverge a nesting condition must be satisfied. Furthermore the corrections contain the density of states, which means the number of available particles can promote or suppress interaction effects.

## Superconductivity

We have seen that an instability in the particle-particle channel can arise for an attractive bare interaction. The corresponding characteristic momentum structure of the singular part of the effective interaction with opposite momentum of incoming particles ( $k_2 = -k_1$ ) suggest the well-known Cooper pair, which is related to the superconducting gap, as order parameter

$$\Delta_{k,\sigma\sigma'} = \langle \psi_{k\sigma}^\dagger \psi_{-k,\sigma'}^\dagger \rangle. \quad (2.15)$$

Its symmetry properties depend on the pairing mechanism, which has to circumvent the usually repulsive, direct electronic coupling, and the symmetry of the considered material. Within BCS theory, it is shown that phonons can mediate an attractive interaction between the electrons, which then leads to a pairing instability in the spin singlet s-wave channel. The effect of phonon-mediated interactions on ordering tendencies in graphene will be studied in Chap. 3. However for example in strongly correlated materials the electron-phonon coupling can be too small to overcome the Coulomb repulsion, but superconductivity still occurs. To explain this we must consider the coupling between particle-particle and particle-hole channels. Then the Kohn-Luttinger mechanism can give rise to a pairing instability when singular particle-hole corrections are included in the interaction used to sum the particle-particle channel. Typically this will alter the momentum and/or spin dependence of the Cooper pair so that the pairing will develop in another channel than the conventional s-wave. Lots of examples exist for this unconventional superconductivity [129], e. g. d-wave pairing in the cuprates (e. g. [130–132]), spin-triplet p-wave pairing in  $^3\text{He}$  (e. g. [133, 134]) and  $\text{Sr}_2\text{RuO}_4$  (e. g. [135]), or chiral  $d \pm id$  in doped graphene [72, 73]. The interplay between instabilities in the particle-particle and particle-hole channels in iron-based superconductors will be subject of Chap. 5. Finally, let us mention that superconductivity can also occur with a finite pairing momentum [136–139].

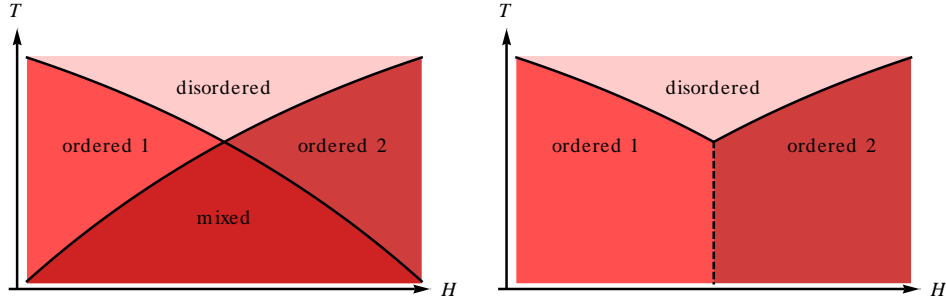


Figure 2.2.: A general phasediagram with two competing orders can have a phase of coexistence with a tetracritical point (left) or a direct transition between both orders with a bicritical point (right). Solid (dashed) lines denote (dis-)continuous phase transitions.

### Spontaneous Order from Particle-Hole Instabilities

An instability in the particle-hole channel can generally involve charge or spin degrees of freedom with the order parameters

$$m_q = \sum_{k,s,s'} \langle c_{k+q,s}^\dagger \sigma_{s,s'} c_{k,s'} \rangle \quad \text{or} \quad n_{k,q} = \sum_{k,s} \langle c_{k+q,s}^\dagger c_{k,s} \rangle, \quad (2.16)$$

because we can always decompose even a  $SU(2)$  spin-symmetric interaction into a charge and spin part in terms of the completeness relation  $\sum_i \sigma_{ss'}^i \sigma_{tt'}^i = 2\delta_{st'}\delta_{s't} - \delta_{ss'}\delta_{tt'}$ . Since the instability in the effective interaction occurs for those transfer momenta that fulfill the nesting condition  $q = Q_{nest}$ , the configuration  $m_{q=Q_{nest}}$  or  $n_{q=Q_{nest}}$  is singled out, respectively. This will lead to a periodic structure in real space

$$m_i/n_i \propto \exp(iQ_{nest}r_i) \quad (2.17)$$

corresponding to a charge or spin density wave. It can also be energetically favorable to form the particle-hole pair with a slightly different transfer momentum, leading to incommensurate density waves [69, 140]. Furthermore more exotic types of order might develop in the particle-hole channel. For example on the honeycomb lattice the topological quantum anomalous Hall and quantum spin Hall states have been suggested to be induced by a next-to-nearest neighbor repulsion [59, 60].

#### 2.1.2. Ginzburg-Landau-Wilson Action

In the case that the description in terms of Fermi liquid theory breaks down, alternative approaches to study the related phenomena are required. Ginzburg-Landau-Wilson theory has been established as a model to describe systems in the vicinity of a phase transition with an action of the form

$$S_{GLW}[\phi] = \int_x \left( \frac{1}{2} (\partial_\mu \phi)^2 + \mu \phi^2 + \lambda (\phi^2)^2 \right). \quad (2.18)$$

The field  $\phi$  plays the role of the order parameter and the parameters are functions of external quantities, such as temperature, pressure or magnetic field. In particular,  $\mu$  changes sign at the transition temperature  $\mu \sim (T - T_c)$ . The form of the action is obtained from symmetry consideration and has first been introduced as a phenomenological model. But the parameters

of the action can be derived microscopically within quantum field theory with the help of a Hubbard-Stratonovich transformation and integrating out the fermion degrees of freedom. Depending on the physical problem, the exact expressions for the parameters will differ, yet the general form of the action does not change demonstrating universality close to phase transitions. Since we will be concerned mainly with the competition of orders in the following, we generalize the Ginzburg-Landau-Wilson action so that it contains two order parameter fields

$$S_{GLW}^{(2)}[\phi, \chi] = \int_x \left( \frac{1}{2} (\partial_\mu \phi)^2 + \frac{1}{2} (\partial_\mu \chi)^2 + \mu_\phi \phi^2 + \mu_\chi \chi^2 + \lambda_\phi (\phi^2)^2 + \lambda_\chi (\chi^2)^2 + \lambda_{\phi\chi} \phi^2 \chi^2 \right). \quad (2.19)$$

There are four configurations  $(\phi_0, \chi_0)$  that potentially minimize the corresponding free energy  $F = k_B TS[\phi_0, \chi_0]$  and determine the state of the system. For  $\mu_\phi, \mu_\chi > 0$ , the symmetric phase is stable and  $\phi_0 = \chi_0 = 0$ . Further only one of the symmetries can be broken with  $\phi_0 = 0$  and  $\chi_0 \neq 0$  when  $\mu_\phi > 0$  and  $\mu_\chi < 0$  (or vice versa). But the most interesting situation arises if both sectors become critical  $\mu_\phi, \mu_\chi \leq 0$ . In this case there are two general, very different phase diagrams as sketched in Fig. 2.2. Their form is determined by the sign of  $4\lambda_\phi \lambda_\chi - \lambda_{\phi\chi}$ , which has been used as a criterion in a variety of studies that investigate the competition between different order parameters [11, 141–143]. For positive  $4\lambda_\phi \lambda_\chi - \lambda_{\phi\chi} > 0$  there is a phase of coexistence with  $\phi_0 \neq 0, \chi_0 \neq 0$ . In this case the multicritical point, where all phases meet, is governed by a tetracritical point. For the opposite sign both orders exclude each other leading to a bicritical structure.

### 2.1.3. What is missing in this picture?

So far we have ignored three important factors. First, when we investigate potential instabilities of the Fermi liquid, instead of summing single channels separately, we would like to include the mutual feedback of different channels into the consideration. This interplay is especially important when we study competing orders, where more than one channel develops an instability. For instance in iron-based superconductors, magnetic correlations in the particle-hole channel are crucial to induce an attractive pairing interaction and the resulting instability in the superconducting channel. A possibility to account for these relations is, amongst others, given by the so called parquet RG or the patching FRG scheme, which both will be introduced in Sec. 2.2.

Furthermore fluctuations of the order parameter around its expectation value play an important role when we consider possible phase transitions. They tend to reduce the ordering attempts of a system or even prevent the appearance of order at all, as e.g. when the Mermin-Wagner theorem applies. Furthermore fluctuations influence the universal critical behavior at a continuous phase transition or can induce a first order transition. Consequently in order to properly characterize a system at a phase transition, fluctuations have to be included. This means we have to include effects beyond the consideration of the minima of the Ginzburg-Landau-Wilson action and determine arising corrections of the parameters. A suitable method to do so is again provided by the RG framework. The universal critical behavior at continuous phase transitions and the scaling of correlations and susceptibilities will be explained in Sec. 2.3.

Eventually, we will discuss systems, where both of the above descriptions turn out to be insufficient. In these models the order parameter related to the phase transition couples to other massless modes so that the integrals that determine microscopically the Ginzburg-Landau-Wilson action do not exist. In other words the construction of the aforementioned purely

bosonic action is not possible and we need an extended description to study the properties of the phase transition [144]. In this work this will be the case for the (multi-)critical behavior in Dirac materials, where we consider the coupling of theories that separately lie in the chiral Ising and chiral Heisenberg universality class [145]. The corresponding models, which are assumed to correctly capture the critical behavior, incorporates massless Dirac fermions and bosonic order parameter fields at the same time.

## 2.2. Renormalization Group Methods

The introduction of renormalization group techniques has led to very successful developments in theoretical physics, thereby establishing the concept of understanding a physical system to be dependent on the energy scale where it is probed. In this way the RG provides insights about the validity of fundamental theories in high-energy as well as condensed matter physics and explains relations between different physical systems exhibiting universal behavior close to phase transitions [13–17]. Here we will first focus on the idea introduced by K. G. Wilson [146, 147] and subsequently explain the different formulations we employ in later chapters.

### 2.2.1. Wilsonian Renormalization Group

Typically we are interested in low energy, long-wavelength properties of interacting many-body systems. In the functional integral formalism, they are encoded in the partition function

$$Z = \int \mathcal{D}\varphi \exp(-S[\varphi]) , \quad (2.20)$$

where  $\varphi$  can contain several different fields. In the previous section we have seen that we encounter the problem of infrared singularities, when we approach the calculation of the full partition function. The Wilsonian idea is now to integrate out the degrees of freedom in Eq. (2.20) successively, because only the low-energy modes are responsible for the divergence. Thus we perform the integral merely over a suitable subset of fields, determine the corresponding change of the effective action and reiterate this procedure. Thereby we not only avoid the singularities, but typically the relevant processes in the coupled set of diagrams will also become clear. To implement this strategy, we divide the fields into slow and fast degrees of freedom

$$\varphi = \varphi^< + \varphi^> \quad (2.21)$$

corresponding to the high- and low-energy modes. For instance if energy is directly related to the absolute value of the momentum as in a quadratic dispersion relation, we can integrate out the modes within a momentum shell  $\Lambda_{UV}/b < p < \Lambda_{UV}$ , where  $\Lambda_{UV}$  is the ultraviolet cutoff of our theory and  $b$  defines the flow parameter characterizing the change in energy. Then  $\varphi^<$  includes all the Fourier components with  $p < \Lambda_{UV}/b$  and  $\varphi^>$  with  $p > \Lambda_{UV}/b$ . After the integration over  $\varphi^>$

$$Z = \int \mathcal{D}\varphi^< \mathcal{D}\varphi^> \exp(-S[\varphi^< + \varphi^>]) \quad (2.22)$$

$$= \int \mathcal{D}\varphi^< \exp(-S_{eff}[\varphi^<]) , \quad (2.23)$$



the action  $S_{eff}$  can again be written in the same form as the bare action by rescaling the momenta and fields, which, in turn, leads to a rescaling of the parameters. Unfortunately we cannot perform the integration exactly due to the presence of interactions, so the strategy will be to do perturbation theory. We will then recover the conventional diagrams from a loop expansion with the difference that internal integrations only involve fast modes, i. e. they are cut in the infrared. Furthermore it turns out that only one-particle irreducible diagrams contribute due to the constraint that internal lines have to carry high-energy modes, while external legs correspond to low-energy modes. The goal of the RG is now to study the evolution or the flow of the parameters in the action, when we iterate this process of eliminating fast modes and rescaling. Thereby it is convenient to formulate the change in a differential form resulting in flow equations for the parameters of our theory. In practice there are many different formulations how to perform the RG mechanism, in particular how to introduce the running energy scale and how to separate slow and fast modes. In the following we will introduce three approaches based on the Wilsonian idea: the momentum-shell RG combined with an expansion around the upper critical dimension of a theory, the parquet RG based on the simultaneous development of logarithmic instabilities at lower scales and the functional RG, which in principle does not rely on a perturbative treatment.

As there are commonly used notations for the different formulations of the RG, we will adapt these notations depending on the RG setting we employ. For clarity we summarize them in the following table.

Table 2.1.: Notation of flow parameters in different RG formulations. The UV cutoff  $\Lambda_{UV}$  labels the range of validity of the considered model and is of the order of the bandwidth  $\Lambda_{UV} \lesssim W$ .

	Flow parameter	Meaning
$\epsilon$ -expansion	$b$	Momentum shell $\Lambda_{UV}/b < p < \Lambda_{UV}$
pRG	$l = \ln(\Lambda_{UV}/E)$	Logarithmic polarization bubble with infrared cutoff $E$
fRG “Wetterich formulation”	$k$ and $t = \ln(k/\Lambda_{UV})$	Infrared cutoff $k$ and renormalization “time” $t$
fRG patching scheme	$\Lambda$	Infrared cutoff

### $\epsilon$ -Expansion

The  $\epsilon$ -expansion provides a useful tool when we study critical phenomena close to phase transitions (see e. g. [16]). Typically in this case, we implement the separation between low- and high-energy modes in terms of the already mentioned momentum-shell RG, where we constrain integrations to momenta that lie within  $\Lambda_{UV}/b < p < \Lambda_{UV}$  with the ultraviolet cutoff  $\Lambda_{UV}$  and the flow parameter  $b$ . The name  $\epsilon$ -expansion comes from the following consideration. In the study of critical physics, the upper critical dimension  $d_u$  is an important quantity. It separates the regimes, where mean-field theory correctly describes the critical behavior from where non-trivial corrections to scaling occur. We are interested in these non-trivial modifications and it turns out that below the upper critical dimension, the small parameter that controls the size of corrections to the mean-field behavior is the dimensionality difference  $\epsilon = d_u - d$ . Thus for a controlled approach to critical behavior within in the RG, we should expand the loop integrals of the perturbation series in  $\epsilon$ . Unfortunately we are often interested in systems, where  $\epsilon$  is not

small and the  $\epsilon$ -expansion is an asymptotic series, i. e. Borel summation techniques are needed to extract accurate results from the  $\epsilon$ -expansion under these circumstances. Nevertheless a first-order  $\epsilon$ -expansion can still be fruitful, because it reveals the qualitative structure of the flow and classifies the relevancy of couplings.

### Parquet Renormalization Group

The parquet RG (pRG) is a controlled weak coupling approach away from criticality with the goal to monitor the buildup of fluctuations, which are small at high energies comparable to the bandwidth  $W$  of the considered material, and increase when lowering the energy. In particular the pRG allows to study correlations that simultaneously develop in the particle-particle and particle-hole channel, thereby treating the competition of orders on equal footing. It is therefore convenient to take the identical logarithm of the particle-particle and particle-hole bubble as flow parameter  $L = \ln(\Lambda_{UV}/E)$ , where  $E$  is the flowing energy scale and the UV-cutoff is of the order of the bandwidth  $\Lambda_{UV} \sim W$ . An instability in a particular ordering channel is then signaled by the divergence of specific couplings at a scale  $L_{cr}$ . An educational description of the procedure to derive the pRG equations is given e.g. in Ref. [148] and the appendix of Ref. [122]. The pRG analysis works when  $E$  is larger than the Fermi energy, i.e., when  $L < L_F = \log \Lambda/E_F$  (see, e.g., Ref. [149]). If  $L_{cr} < L_F$ , the pRG analysis is valid all the way to the leading instability. If  $L_{cr} > L_F$ , pRG analysis allows one to determine the largest susceptibility at  $L = L_F$ . It is likely (although not guaranteed) that this susceptibility will diverge first at a lower energy.

A second energy scale that cuts the pRG flow is associated to deviations from perfect nesting. In principle non-perfect nesting, which is probably more realistic to assume, destroys the equality between particle-particle and particle-hole singularities. Small imperfections are still treatable though, in the sense that both bubbles are approximately the same over a large energy range before the logarithmic singularity in the particle-hole channel is cut. The effect of deviations from perfect nesting then depends again on the hierarchy of scales. If the leading instability occurs at a larger energy scale than the discrepancy between particle-particle and particle-hole channel, non-perfect nesting is an irrelevant perturbation. Otherwise only the pairing instability will continue growing, while the particle-hole instability does not develop.

#### 2.2.2. Functional Renormalization Group

In a sense the functional RG formalizes the Wilsonian idea and at the same time leads to a generalization that opens further application possibilities. The advantage of this formulation is that its starting point relies on a universal, exact flow equation for the effective action, i. e. in principle we are not restricted to perturbation theory. The draw-back may be that some control is sacrificed, because a small expansion parameter can be lost. The FRG method provides a unified framework to access universal as well as nonuniversal properties of physical systems. It may be employed to describe the critical behavior in the vicinity of continuous classical or quantum phase transitions and is also applicable to systems away from criticality. By means of suitable expansion schemes it has also been used to study first-order phase transitions. The FRG can be applied in arbitrary (fractional) dimension, and even low-order truncations already appear to give reasonably accurate results in both purely bosonic as well as coupled boson-fermion systems. For reviews related to condensed matter physics see e. g. [14, 15, 17, 117, 150]. We will explain two approaches in terms of the Wetterich equation here, which we eventually employ to study (multi-)critical phenomena in Dirac materials and the interplay of phonon and electron interactions on the honeycomb lattice, respectively.

### The Effective Action

The central object of the fRG is the scale-dependent effective action, which is the generating functional of one-particle irreducible (1PI) correlation functions. Therefore let us briefly remind of the formalities regarding correlation functions and their generating functionals. We can conveniently extract all information about a physical system from the Schwinger functional with a source term  $J\varphi$

$$W[J] = \ln Z[J] = \ln \int \mathcal{D}\varphi \exp \left( -S[\varphi] + \int J\varphi \right), \quad (2.24)$$

which is defined in terms of the partition function  $Z[J]$ . Then the correlation functions can simply be obtained by differentiation

$$\langle \varphi(p_1) \dots \varphi(p_n) \rangle = \frac{\delta^n}{\delta J(p_1) \dots \delta J(p_n)} W[J] \Big|_{J=0}. \quad (2.25)$$

But the Schwinger functional contains redundant information in the form of reducible correlation functions and as we have seen above only the 1PI diagrams contribute to the RG equations. These can be obtained via the Legendre transform of  $W[J]$ , which is the effective action

$$\Gamma[\phi] = \sup_J \left( \int J\phi - W[J] \right). \quad (2.26)$$

The scale- $k$ -dependent or flowing action  $\Gamma_k$  is then defined in such a way that it interpolates between the microscopic action at the UV cutoff  $\Lambda_{UV}$ , where no fluctuations have been included, and the full quantum effective action in the infrared, which accounts for fluctuations on all scales, i. e.

$$\Gamma_{k \rightarrow \Lambda_{UV}} = S \quad \text{and} \quad \Gamma_{k \rightarrow 0} = \Gamma. \quad (2.27)$$

The exact incorporation of the scale dependence of  $\Gamma_k$  slightly differs between both formulations of the fRG and will be presented below.

### Wetterich Equation

For the following formulation see the aforementioned reviews [14, 17, 150]. To implement Wilson's idea of successively performing the integration over degrees of freedom in the fRG formalism, a so-called regulator  $R_k$  is introduced that modifies the microscopic action by replacing

$$S \rightarrow S + \Delta S_k \quad \text{with} \quad \Delta S_k[\varphi] = \int_{(q,p)} \frac{1}{2} \varphi(-q) R_k(q,p) \varphi(p). \quad (2.28)$$

The flowing action is then defined as the Legendre transform of the regularized Schwinger functional  $W_k[J] = \ln \int \mathcal{D}\varphi \exp(-S[\varphi] - \Delta S_k[\varphi] + \int J\varphi)$

$$\Gamma_k[\phi] = \sup_J \left( \int J\phi - W_k[J] \right) - \Delta S_k[\phi]. \quad (2.29)$$

On the one hand the regulator function  $R_k$  induces the iterative integration procedure and ensures that only modes with high momentum  $|q| \gtrsim k$  give a contribution to the integral in

$\Gamma_k$ , i. e.  $R_k(q) = 0$  for  $|q| > k$  and  $R_k(q) \geq k^2$  for  $|q| < k$ . Thereby infrared singularities are avoided. On the other hand it ensures the interpolation between the microscopic and the full quantum action. Therefore it has to satisfy the requirements  $R_k(q) \rightarrow \infty$  for  $k \rightarrow \Lambda_{UV} \rightarrow \infty$  and  $R_k(q) \rightarrow 0$  for  $k/|q| \rightarrow 0$ . Calculating the scale-derivative of the regulated effective action then yields the exact functional differential equation [151]

$$\partial_t \Gamma_k = \frac{1}{2} \text{STr} \left[ (\Gamma_k^{(2)} + R_k)^{-1} \partial_t R_k \right], \quad (2.30)$$

which is also called Wetterich equation. We have abbreviated  $\partial_t = k \partial_k$ , using the renormalization group time  $t = \ln(k/\Lambda_{UV})$ . The Hessian  $\Gamma_k^{(2)}$  is given by

$$(\Gamma_k^{(2)})_{i,j}(p,q) = \frac{\overrightarrow{\delta}}{\delta \phi(-p)^T} \Gamma_k \frac{\overleftarrow{\delta}}{\delta \phi(q)}. \quad (2.31)$$

Let us again note that  $\phi$  can represent a collective field variable for all fermionic and bosonic degrees of freedom of our model. In this case in the Wetterich equation, the regulators for this model are combined to

$$R_k = \begin{pmatrix} R_k^{(B)} & 0 & 0 \\ 0 & 0 & R_k^{(F)} \\ 0 & -R_k^{(F)T} & 0 \end{pmatrix}, \quad (2.32)$$

if we separate the boson regulator  $R_k^{(B)}$  and the fermion regulator  $R_k^{(F)}$ . The notation  $\text{STr}$  sums over all degrees of freedom including a minus sign in the fermionic sector as well as a loop integration over momenta. Graphically the flow equation for the effective action can therefore be depicted as a 1-loop diagram (see Fig. 2.3) with a regulator insertion  $\partial_t R_k$ . However the propagator and vertices have to be understood as fully dressed n-point functions. Of course we still cannot solve this equation exactly and have to rely on suitable approximations as will be discussed in the next sections. The advantage is though that the flow equation allows to obtain improved results on a one-loop level compared to pure perturbation theory.

### Conventional RG from Functional RG

The relation between the conventional Wilson RG and the fRG becomes intuitively very clear when we sketch a typical regulator and its derivative as in Fig. 2.3. We can see that  $\partial_t R_k(q)$ , which appears on the right side of the flow equation, is peaked around  $|q| \approx k$  and we can directly connect this to the momentum shell of the Wilsonian picture. However we have a freedom in choosing an appropriate ansatz for the effective action together with a regulator individually tailored to the problem we address. For example to recover perturbation theory, we can adopt the loop expansion  $\Gamma_k = S + \hbar \Gamma_k^{1l} + \mathcal{O}(\hbar^2)$ , which leads to the free propagator on the right hand side of the flow equation  $\Gamma_k^{(2)} = S^{(2)}$ . This also means that only the microscopic bare values of the parameters appear on the right hand side. The flow equation for the one-loop action can then be integrated to the standard one-loop effective action

$$\Gamma^{1l} = S + \frac{1}{2} \text{STr} \ln (S^{(2)} + R_k) + \text{const.} \quad (2.33)$$

The standard renormalization-group improved, one-loop flow equations can be obtained from the Wetterich equation Eq. (2.30) by replacing all propagators and vertices on the right side

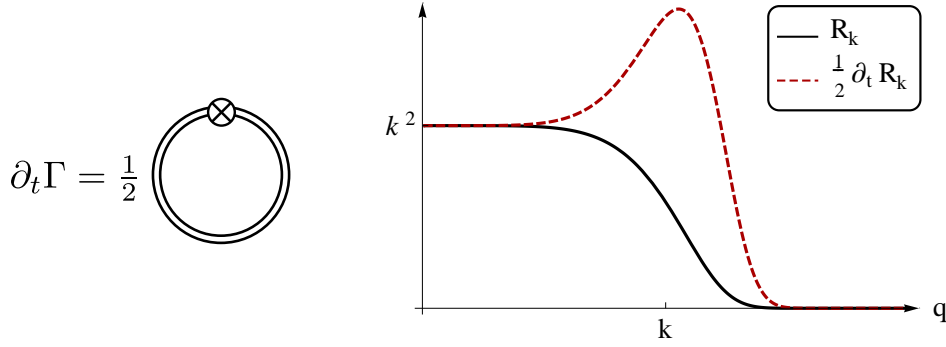


Figure 2.3.: (Left) Diagrammatic representation of the flow equation for the effective action Eq. (2.30). Despite of the one-loop structure the equation is exact due to the presence of the full propagator  $(\Gamma_k^{(2)} + R_k)^{-1}$ , which is represented by the double line. The crossed circle denotes the regulator insertion  $\partial_t R_k$ .

(Right) A regulator of the form  $R_k = \frac{q^2(q^2/k^2)^{n-1}}{e^{(q^2/k^2)^n} - 1}$  and its scale derivative ( $n = 3$  in the plot). The additive regulator in the propagator  $(\Gamma_k^{(2)} + R_k)^{-1}$  suppresses slow modes because  $R_k(q) \geq k^2$  for  $|q| < k$  so that infrared regularity is ensured. The derivative  $\partial_t R_k$  appearing in the numerator of the flow equation is responsible for the shell-wise integration.

through the bare ones, but with running couplings. Additionally we have to impose a regulator that corresponds to the sharp momentum-shell, which is therefore also called sharp regulator<sup>1</sup>. If we deal with critical phenomena, we further have to expand the resulting flow equations for the parameters in the difference to the upper critical dimension  $\epsilon = d_u - d$  to obtain the perturbative expression.

## Truncations

Besides the approximation that reproduces the conventional RG equations, we will employ the following two truncation schemes.

One possibility is to expand the effective action in powers of the fields resulting in a vertex expansion

$$\Gamma_k[\phi] = \sum_n \frac{1}{n!} \int_{p_1} \dots \int_{p_n} \delta(p_1 + \dots + p_n) \Gamma_{a\dots n,k}^{(n)}(p_1 \dots p_n) \phi_a(p_1) \dots \phi_n(p_n). \quad (2.34)$$

Inserting this ansatz into the Wetterich equation yields a coupled set of differential equations for the vertex functions  $\Gamma_k^{(n)}$ , which we have to truncate after a specific  $n$ . The solution for the remaining vertex functions then interpolates between the bare and effective vertices and allows to follow their individual development with energy scale. We also note that this formulation accounts for the mutual feedback of different channels since we did not make any assumption about the form of  $\Gamma_k^{(n)}$ .

An alternative expansion scheme is the derivative expansion, where we classify the terms by the number of derivatives

$$\Gamma_k[\phi] = \int_x \left( \frac{1}{2} Z_k(\rho) (\partial_\mu \phi)^2 + U_k(\rho) + \frac{1}{4} Y_k(\rho) (\partial_\mu \rho)^2 + \mathcal{O}(\partial^4) \right) \quad (2.35)$$

<sup>1</sup>When we use another regulator, we have to ensure that we include only 1-loop contributions on the right side in the coupling constants

with the symmetry invariant  $\rho = \frac{1}{2}\phi^2$ . We usually truncate this expansion to only include the effective potential  $U(\rho)$  and a running wave function renormalization  $Z_k$  that is independent of  $\rho$ . This scheme is often called “improved local potential approximation” (LPA). The effective potential itself can again be expanded in a Taylor series in  $\rho$  around its minimum, which is related to the expectation value of the field. It then may be that we have to include couplings that would be irrelevant in the standard RG sense. The reason being that although they eventually flow to zero, the intermediate evolution is non-universal and can be influenced by these couplings. An interesting option to overcome the limitations of local expansions in field space, for e.g.  $U(\rho)$ , is to use a grid. This has recently been put forward with the help of pseudo-spectral methods to access fixed points and critical exponents, see Ref. [152]. We will, however, employ the Taylor expansion of the effective potential below.

In every truncation scheme that we use, we are supposed check the results for consistency, because we lack a small parameter that controls our expansion. This can be approached by varying the ansatz and determining the effect on the results, which should converge at some level of truncation extensions. Furthermore we have to be careful when choosing a regulator. In principle different choices of regulators only represent different paths in theory space from the bare to the full effective action, i. e. they all give the same result in the infrared. But in practice we cannot integrate out all modes completely so that the results will depend on our choice and we will typically utilize optimized regulators [153–158].

### Patching Scheme

The patching scheme is designed to determine the low-energy instabilities of a (semi-)metal based on its band structure. It has been proven to be a suitable tool for the study of a large range of two-dimensional solid state systems with strongly-correlated phases, e.g. high- $T_c$  superconductors, such as cuprates, pnictides and investigations on the honeycomb lattice, see Refs. [15, 117] for recent reviews of this approach. We consider the fermion action

$$S[\psi, \bar{\psi}] = - \int_q \bar{\psi} G_0^{-1} \psi + V[\psi, \bar{\psi}]. \quad (2.36)$$

In this specific fRG scheme, the bare propagator  $G_0$  in the effective action is modified by a multiplicative regulator  $C^\Lambda$

$$G_0(p, n) \rightarrow G_0^\Lambda(p, n) = \frac{C^\Lambda(\xi_{n,p})}{ip_0 - \xi_{n,p}}. \quad (2.37)$$

with the single-particle energy  $\xi_{n,p} = \epsilon_{n,p} - \mu$  in band  $n$  and the chemical potential  $\mu$ . The regulator is chosen as a momentum cutoff, which suppresses the modes with energy less than  $\Lambda$  and reads  $C^\Lambda(\xi_{n,p}) = \Theta(|\xi_{n,p}| - \Lambda)$ . For numerical stability, we slightly soften the step function in the actual implementation. The flow equation for the scale-dependent effective action  $\Gamma_\Lambda$  then obtains the form

$$\frac{d}{d\Lambda} \Gamma_\Lambda = - \int \bar{\psi} \dot{Q}_0^\Lambda \psi - \frac{1}{2} \text{Tr} \left[ \dot{\mathbf{Q}}_0^\Lambda \left( \mathbf{\Gamma}_\Lambda^{(2)} \right)^{-1} \right], \quad (2.38)$$

where  $Q_0^\Lambda = (G_0^\Lambda)^{-1}$  and  $\mathbf{Q}_0(p, q) = \text{diag} (Q_0^\Lambda(p, q), -Q_0^\Lambda(q, p))$  and  $\mathbf{\Gamma}_\Lambda^{(2)}$  is the matrix of second derivatives. We recognize an equivalent structure as in Eq. (2.30) with the additional, trivial term  $\int \bar{\psi} \dot{Q}_0^\Lambda \psi$  due to the multiplicative regulator implementation. As an ansatz for the effective

action, we employ the aforementioned expansion in powers of the fields to obtain flow equations for the momentum dependent vertices.

In the calculations performed in this study, several approximations are employed to numerically integrate the resulting RG flow equations for the 1PI vertices efficiently: We truncate after the two-particle interaction vertex  $V^\Lambda$ , which means that the results are of second order in the interaction. The flow of  $V^\Lambda$  provides the essential information about the leading instabilities and we further neglect the effect of self-energy corrections as they couple to the flow of the interaction vertex only at third order, see e.g. Ref. [159]. In addition, we do not account for the frequency dependence of the vertex  $V^\Lambda$  and set the external frequencies to zero to single out the most singular contribution of the flow for the determination of the ground state properties of the system. This strategy has proven to provide reliable results in a large number of different two-dimensional fermionic solid state systems, cf. Refs. [15, 117]. Despite these approximations, one obtains an infinite-order summation of second order diagrams, which, importantly, accounts for the competition between different channels. The flow equation for a  $SU(2)$ -spin-symmetric coupling function  $V^\Lambda(p_1, p_2, p_3, n_4)$ <sup>2</sup>, then reads

$$\frac{d}{d\Lambda} V^\Lambda(p_1, p_2, p_3, n_4) = \tau_{pp}^\Lambda + \tau_{ph,d}^\Lambda + \tau_{ph,cr}^\Lambda \quad (2.39)$$

with  $p_i = (p_{0,i}, \mathbf{p}_i, n_i)$  labeling not only the Matsubara frequencies and wave vectors, but also the bands. We again find the three contributions from particle-particle, direct and crossed particle-hole diagrams as in Fig. 2.1, but here one of the internal lines denotes the scale-derivative of the propagator rather than the propagator itself. The particle-particle channel is given as

$$\tau_{pp}^\Lambda = \int_p V^\Lambda(p_1, p_2, p, n') L^\Lambda(p, p_{pp}) V^\Lambda(p, p_{pp}, p_3, n_4),$$

and  $\int_q = A_{BZ}^{-1} T \sum_{p_0} \int d^2p \sum_{n,n'}$ . The direct and the crossed particle-hole channels are given by

$$\begin{aligned} \tau_{ph,d}^\Lambda = \int_p & \left[ -2V^\Lambda(p_1, p, p_3, n') L^\Lambda(p, q_d) V^\Lambda(p_d, p_2, p, n_4) \right. \\ & + V^\Lambda(p, p_1, p_3, n') L^\Lambda(p, p_d) V^\Lambda(p_d, p_2, p, n_4) \\ & \left. + V^\Lambda(p_1, p, p_3, n') L^\Lambda(p, p_d) V^\Lambda(p_2, p_d, p, n_4) \right], \end{aligned}$$

and

$$\tau_{ph,cr}^\Lambda = \int_p V^\Lambda(p, p_2, p_3, n') L^\Lambda(p, p_{cr}) V^\Lambda(p_1, p_{cr}, p, n_4),$$

respectively, and we define the wave vectors  $p_{pp} = -p + p_1 + p_2$ ,  $p_d = p + p_1 - p_3$  and  $p_{cr} = p + p_2 - p_3$ .  $A_{BZ}$  denotes the area of the first Brillouin zone. The loop kernel reads

$$L^\Lambda(p, p') = \frac{d}{d\Lambda} [G_0^\Lambda(p) G_0^\Lambda(p')], \quad (2.40)$$

with the free propagator  $G_0^\Lambda$  due to the neglect of the self-energy.

<sup>2</sup>see e. g. [67, 160] for spin-resolved discussions



To solve the flow equations numerically, the wave vector dependence of the interaction vertex is discretized with a patching scheme that divides the Brillouin zone into  $N$  patches, in which the vertex is approximated to be constant. The representative momentum for each patch is placed close to the Fermi level, see Figs. 2.4 and 3.1 for examples on the bilayer square and the honeycomb lattice. This procedure has been established in Ref. [159] and successfully applied in a large number of works, cf. Ref. [15]. We also note at this point that in the meantime the patching scheme has been extended to achieve a better radial resolution, i. e. within one angular patch several ring patches in some distance from the Fermi surface have been included. It has been shown that this improvement is crucial on the honeycomb lattice to correctly identify the leading ordering tendency induced by a next-to-nearest-neighbor interaction.

During the lowering of the energy scale, some components of the effective two-particle interaction  $V^\Lambda$  typically grow large and diverge at a critical scale  $\Lambda_c > 0$  indicating an instability towards an ordered state. The pronounced momentum structure of the critical interaction vertex then allows to extract an effective Hamiltonian for the low-energy degrees of freedom and determines the leading order parameter. In this way the approach is unbiased because the structure of the effective low energy theory is not anticipated. In the actual numerical evaluation of a diverging interaction vertex, we stop the flow at a scale  $\Lambda_{\text{IR}}$  where the largest component of  $V_\Lambda$  is of the order of several times the bandwidth and use this  $\Lambda_{\text{IR}}$  as an estimate for the critical scale  $\Lambda_c$ . The critical scale  $\Lambda_c$  can be interpreted as an estimate for the temperature below which ordering occurs or correlations of the order parameter become important. The procedure described here is well-controlled for small interactions and can be expected to be reliable also in the regime of intermediate interaction strengths [15, 117, 161].

### 2.2.3. Example: The Ground State Phase Diagram of the Half-Filled Bilayer Hubbard Model

As an example for the appearance of an instability we present a study of the bilayer Hubbard model at half-filling in terms of the patching fRG scheme. It demonstrates the application of this scheme and also establishes a connection to the role of nesting and the density of states, which we have seen in Sec. 2.1.1. While the Hubbard model in general provides a fundamental description of correlation effects in many-body condensed matter systems, the bilayer Hubbard model additionally serves as a simple model with multiple Fermi surfaces and electron and hole pockets, cf. e. g. Ref. [162]. Such a Fermi surface composition with pockets of different nature is in particular important in the study of iron-based superconductors as we will see in Chap. 5. A related phenomenon in the bilayer Hubbard model is the transition between different pairing symmetries by tuning the interlayer hopping, cf. e.g. Ref. [163]. But in this section we would like to concentrate on the effect of the onsite interaction, which is expected to induce an antiferromagnetic instability due to the perfect-nesting property of the model at half filling [126]<sup>3</sup>.

#### The Model

The Hubbard model on the square lattice bilayer with intra-layer nearest-neighbor hopping  $t$ , inter-layer hopping  $t_\perp$  and a local Coulomb repulsion  $U$ , is described by the Hamiltonian

$$H = -t \sum_{\langle ij \rangle s \lambda} (c_{i\lambda s}^\dagger c_{j\lambda s} + \text{h.c.}) - t_\perp \sum_{is} (c_{i1s}^\dagger c_{i2s} + \text{h.c.}) + U \sum_{i\lambda} n_{i\lambda\uparrow} n_{i\lambda\downarrow}, \quad (2.41)$$

<sup>3</sup>See however [164, 165] for the prediction of an extended paramagnetic metallic phase at small onsite interactions



where the  $c_{i\lambda s}^{(\dagger)}$  denote annihilation (creation) operators for electrons of spin  $s \in \{\uparrow, \downarrow\}$  on site  $i$  in layer  $\lambda \in \{1, 2\}$ , and the  $n_{i\lambda s}$  denote local occupation number operators. For  $U = 0$ , Eq. (2.41) reduces to a tight-binding model, which can be solved by exact diagonalization and exhibits the single-particle dispersion

$$\epsilon_0^\pm(k, t_\perp) = -2t (\cos(k_x) + \cos(k_y)) \pm t_\perp. \quad (2.42)$$

This corresponds to two copies of the square lattice single-layer dispersion ( $t_\perp = 0$ ), shifted with respect to each other linearly in  $t_\perp$ . Since for the single-layer lattice the energies lie within the range  $-4t \leq \epsilon \leq 4t$ , a band gap opens for  $t_\perp > 4t$  and the system becomes band-insulating at half filling. Both bands remain perfectly nested for all values  $t_\perp/t$ , with a nesting vector  $Q = (\pi, \pi)$ , i.e.

$$\epsilon_0^+(k + Q, t_\perp) = -\epsilon_0^-(k, t_\perp). \quad (2.43)$$

The Fermi surface for  $t_\perp/t = 2$  and the nesting vector are shown in Fig. 2.4. As a consequence of Eq. (2.42), the density of states (DOS) of the bilayer lattice,  $\rho(\epsilon, t_\perp)$ , is the sum of two displaced single-layer DOS contributions, see Fig. 2.4. This causes the logarithmic van Hove singularity of the single-layer square lattice to be shifted away from the Fermi level to energies  $\pm t_\perp$ . Therefore one expects a suppression of interaction effects in the bilayer system. However, for  $t_\perp < 4t$ , the DOS stays finite at the Fermi surface. This, combined with the nesting property, leads to a divergence of the zero-temperature static spin-spin susceptibility given by the particle-hole bubble, as we have seen in Sec. 2.1. From the particle-hole ladder  $U_{ph-ladder} \approx \frac{U}{1 - U\rho_0 \ln \frac{W}{\Lambda}}$ , we can then extract an estimate for the scale where the instability occurs by setting the denominator to zero. Thereby we have to account for the different behavior of the DOS. For the bilayer with finite DOS  $\rho_0 \sim t$ , this yields

$$\Lambda_c \propto e^{-t/U}, \quad (2.44)$$

whereas the van Hove singularity of the single layer  $\rho_0 \sim t \ln(W/\Lambda)$  leads to

$$\Lambda_c \propto e^{-\sqrt{t/U}}. \quad (2.45)$$

### Effect of Onsite Interaction from FRG

In the following, we employ the fRG approach with the patching scheme that shows in an unbiased way how the antiferromagnetic instability indeed emerges in the weak-interaction regime from the noninteracting metallic state. As described in Sec. 2.2.2 the vertex  $V_\Lambda$  is discretized by dividing the Brillouin zone into  $N_p$  patches with a constant wavevector dependence within each patch, as shown in Fig. 3.1. Representative momenta for these patches are chosen to reside at the Fermi level. In the following, we employ a wavevector resolution with a patch number of  $N_p = 32$  and  $N_p = 48$ . We have also checked our results to be stable towards higher resolutions with up to  $N_p = 96$  patches. In summary, we obtain a vertex function  $V_\Lambda$  with  $N_p^3 \cdot N_b^4$  components, where  $N_b = 2$  is the number of energy bands, and a set of  $N_p^3 \cdot N_b^4$  coupled differential equations that has to be integrated.

As explained above we will observe a singularity in specific components of the effective interaction if ordering tendencies become relevant. In this case we can take the corresponding energy scale  $\Lambda_c$  as a reasonable estimate for the critical scale. In the fRG data at half filling and for arbitrary onsite repulsion, we observe as the prevailing divergence an antiferromagnetic spin density wave (AF-SDW) with momentum transfer  $Q = (\pi, \pi)$ , see Fig. 2.5 for a snapshot of

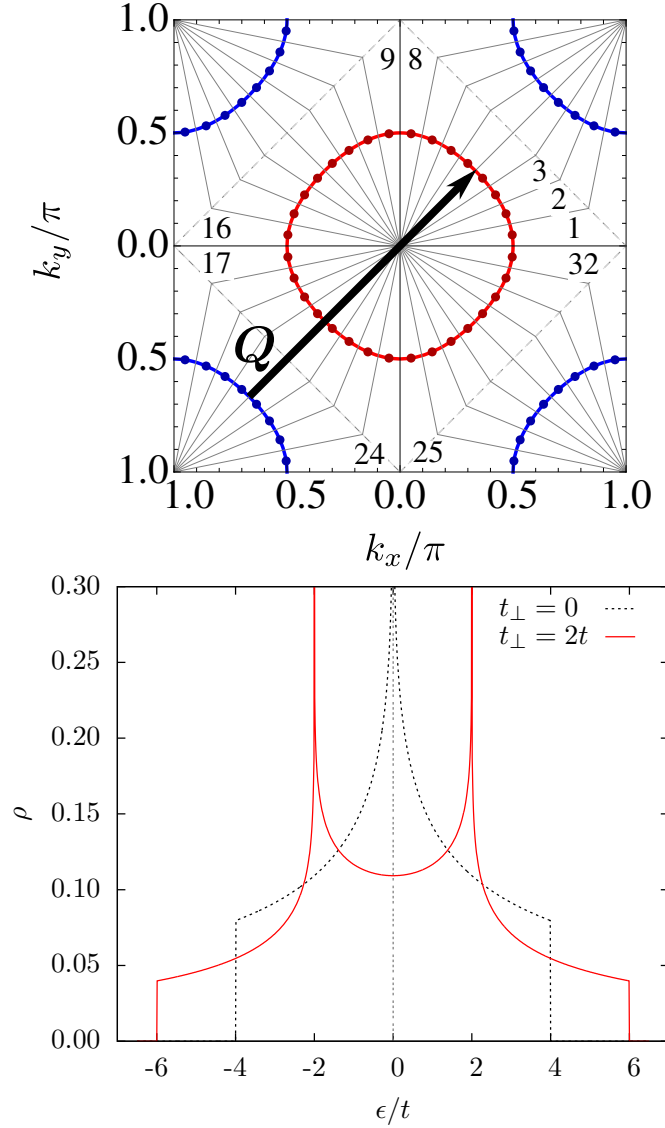


Figure 2.4.: (Top) The Fermi surface for  $t_{\perp} = 2t$  and the nesting vector  $Q$ . The upper band is colored in red, the lower in blue. We also show the patching scheme of the Brillouin zone for a total of  $N_p = 32$  patches. Depending on the energy band the coupling function is evaluated on a wave vector at the Fermi level indicated by the dots.

(Bottom) The  $U = 0$  bilayer density of states (DOS)  $\rho(\epsilon, t_{\perp})$  for  $t_{\perp} = 2t$  (solid red line) in comparison with the single-layer DOS (dashed black line). The dotted vertical line marks the position of the Fermi level.

the four-Fermi vertex close to the critical scale. This behavior clearly reflects the perfect nesting of the Fermi surface. If we insert the momentum structure extracted from Fig. 2.5 into the general form of the spin-symmetric interaction Eq. (2.2), the leading part close to the critical scale can be expressed in terms of an effective interaction Hamiltonian

$$H_{\text{SDW}} = -J \sum_{\lambda, i, j} e^{i\mathbf{Q} \cdot (\mathbf{r}_i - \mathbf{r}_j)} (\mathbf{S}_{i\lambda} \cdot \mathbf{S}_{j\lambda} - \mathbf{S}_{i\lambda} \cdot \mathbf{S}_{j\bar{\lambda}}), \quad (2.46)$$

where  $J > 0$ , and  $\bar{\lambda}$  denotes the layer opposite to  $\lambda$ . The spin operator  $\mathbf{S}_{i\lambda}$  is given by the

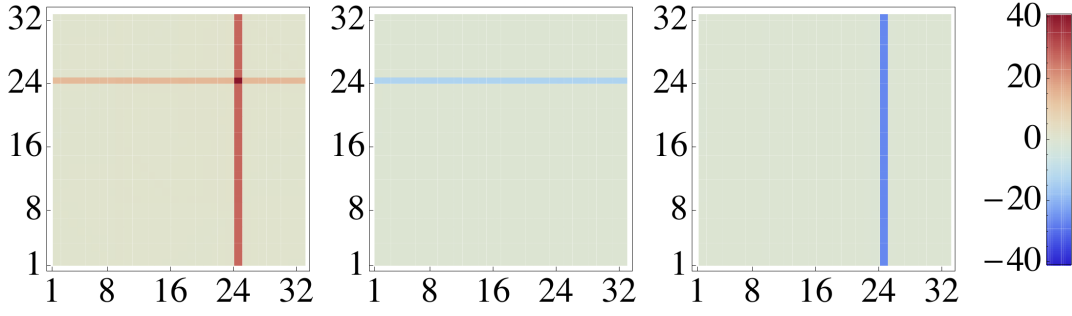


Figure 2.5.: Effective interaction vertex near the critical scale for the AF-SDW in units of  $t$ , exhibiting a sharply pronounced momentum structure. The axes are numbered according to the number of the patch, cf. Fig. 3.1, where wavevectors  $k_1$  are depicted vertically and  $k_2$  are depicted horizontally. We fix  $k_3$  to be on patch 1. Left Panel: Effective vertex or a combination of layer indices  $\lambda_i$  where  $\lambda_1 = \lambda_2 = \lambda_3 = \lambda_4$ . Middle Panel:  $\lambda_1 = \lambda_3, \lambda_2 = \lambda_4$ . Right panel:  $\lambda_1 = \lambda_4, \lambda_2 = \lambda_3$ .

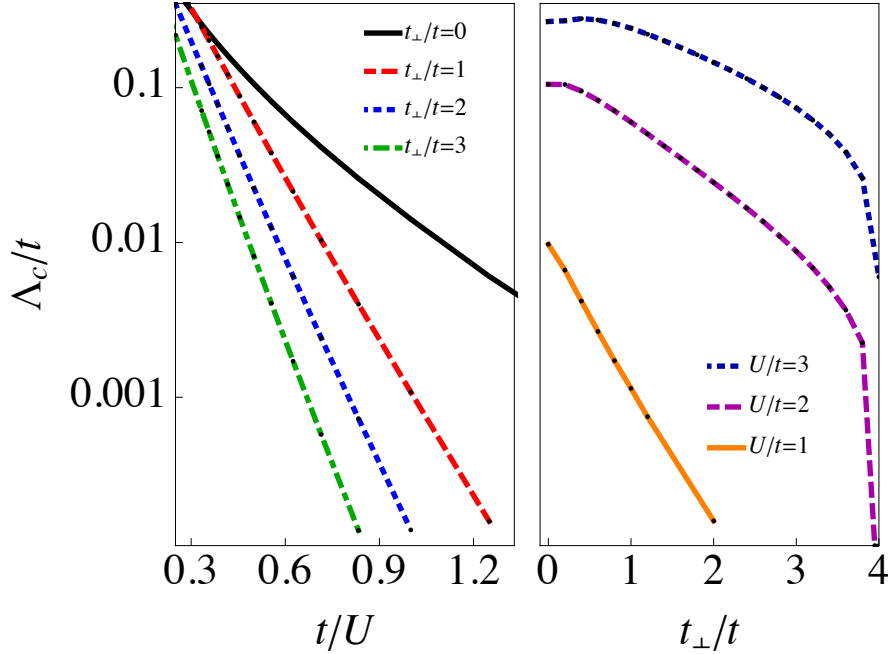


Figure 2.6.: (Left) fRG critical scale  $\Lambda_c$  as a function of  $t/U$  for the single-layer case (solid line) and the bilayer case with  $t_\perp = 1t, 2t, 3t$  (from top to bottom) using  $N_p = 48$  patches, exhibiting exponential decrease of  $\Lambda_c \sim e^{-\text{const.} \cdot t/U}$ . This functional dependence suggests an instability for any value of  $U > 0$  in accord with mean-field theory.

(Right) The fRG critical scale  $\Lambda_c$  decreases by several orders of magnitude when  $t_\perp/t$  is increased from 0 to 4. We show this behavior for three choices of  $U/t = 3, U/t = 2$  and  $U/t = 1$  by the solid, dashed and dotted lines, respectively.

relation  $\mathbf{S}_{i\lambda} = 1/2 \sum_{s,s'} c_{i\lambda s}^\dagger \boldsymbol{\sigma}_{ss'} c_{i\lambda s'}$  in terms of the Pauli matrices. As a result of the sharpness in momentum space the interaction becomes long-ranged in position space. With this effective Hamiltonian, we can thus perform a controlled mean-field decoupling. For the resulting effective Hamiltonian, the spins are aligned antiferromagnetically within each layer and also between the layers.

In Fig. 2.6, we compare the critical scales for several cases, namely the situation with vanishing perpendicular hopping amplitude  $t_{\perp} = 0$  which is equivalent to the one-band Hubbard model as well as for perpendicular hoppings of  $t_{\perp}/t = 1, 2, 3$ . For the single-layer case, we observe that in agreement with the expectations from a ladder resummation Eq. (2.45), the functional dependence of the critical scale on the onsite interaction  $U/t$  is an exponential  $\sim e^{-\text{const.} \cdot \sqrt{t/U}}$ , cf. Fig. 2.6. In contrast, the critical scales for the bilayer case are considerably lower, which can be understood given the reduced density of states at the Fermi level. Furthermore, the functional dependence on  $U/t$  is different and rather follows a behavior  $\sim e^{-\text{const.} \cdot t/U}$ , which is in accordance with the mean-field expectation (cf. Eq. 2.44). Using the fRG approach, treating all the fluctuation channels on equal footing, we can also check whether competing instabilities are present for this choice of parameters. Here, we do not observe the appearance of any other strong correlation effects apart from the AF-SDW instability. In the right panel of Fig. 2.6 we compare the  $t_{\perp}$ -dependence of the critical scale  $\Lambda_c$  for different values of  $U/t \in \{1, 2, 3\}$ . We observe a continuous decrease of  $\Lambda_c$  as a function of increasing interlayer hopping, i. e. a growing interlayer hopping reduces the gap size or the critical temperature.

## 2.3. Critical Phenomena

### 2.3.1. Scaling from RG $\beta$ Functions and Fixed Points

Close to continuous transitions, thermodynamic properties behave in a universal way, characterized by power laws with specific critical exponents. This phenomenon can be described by a scaling ansatz for the free energy, which not only allows to derive the symptomatic power laws for quantities as specific heat and susceptibility, but also gives scaling relations connecting the critical exponents. However, the microscopic explanation for the scaling ansatz has only been provided by the renormalization group. In this section we will briefly explain the connection (cf. e. g. [16, 17]).

We have seen that renormalization group theory describes the scale dependence of a physical system by providing flow equations for the different couplings of a theory. These flow equations, also called  $\beta$  functions, are differential equations encoding the evolution of the system with respect to the energy (or momentum) scale  $k$ . Starting from a “microscopic” model for a system at some ultraviolet cutoff scale  $k = \Lambda_{UV}$ , one can then infer the low-energy, or infrared, characteristics in terms of the solution of the  $\beta$  functions. More explicitly, we introduce the generalized set of dimensionless couplings for the theory by  $\alpha_i$ ,  $i \in \{1, 2, \dots\}$ . The  $\beta$  functions can be written in the form  $\partial_t \alpha_i = \beta_i(\alpha_1, \alpha_2, \dots)$ , where the change in scale is written in terms of the renormalization group time  $t = \ln(k/\Lambda_{UV}) \leq 0$ . A fixed point  $\alpha^*$  of these equations is given by

$$\beta_i(\alpha_1^*, \alpha_2^*, \dots) = 0 \quad \forall i, \quad (2.47)$$

and can be viewed as a scale-invariant point. Scale-invariance in turn is associated to continuous phase transitions. The critical properties and scaling behavior near such a transition are encoded in the RG flow in the vicinity of the fixed point  $\alpha^*$ ,

$$\partial_t \alpha_i = B_{i,j}(\alpha_j - \alpha_j^*) + \mathcal{O}((\alpha_j^* - \alpha_j)^2), \quad (2.48)$$

where  $B_{i,j} = (\partial \beta_i / \partial \alpha_j)|_{\alpha=\alpha^*}$ . The eigenvalues  $\theta_i$  of the so-called stability matrix  $(-B_{i,j})$  (“critical exponents”) are universal quantities that characterize the scaling laws at the putative

continuous phase transition. All positive critical exponents  $\theta_i$  correspond to RG-relevant directions, i.e., the fixed point repels the flow in that direction. Negative  $\theta_i$  are RG irrelevant and correspond to attractive directions. Finally  $\theta_i = 0$  determines marginal directions, where corrections of quadratic order have to be taken into account to determine if the flow approaches to or departs from the fixed point.

From the RG critical exponents we now would like to recover the phenomenological scaling ansatz that has been used to describe the universal power laws of thermodynamic quantities close to a phase transition. But let us consider the generalization to quantum critical points at zero temperature, where the imaginary time leads to an extra dimension. Then not only fluctuations in space but also in (imaginary) time have to be taken into account. This is done in terms of the dynamical critical exponent  $z$ , which describes the rescaling of temporal quantities as Matsubara frequencies or temperature, i. e. while we rescale momenta like  $p' = p/k$ , frequencies are rescaled with  $\omega' = \omega/k^z$ . We need the extra critical exponent because time and space coordinates need not to be related by any symmetry, but after rescaling of momenta and frequencies, it must be possible to rescale the field and bring the action into the old form. Let us further consider that the fixed point corresponding to the quantum phase transition is characterized by two relevant couplings. We denote the corresponding deviations to the fixed point as  $g$  and  $h$  and assume that they diagonalize the linearized flow equations, i.e.

$$\partial_t g = -\theta_g g \quad \text{and} \quad \partial_t h = -\theta_h h. \quad (2.49)$$

The solution of these flow equations reads

$$g_k = \bar{g}_0 e^{-\theta_g t} = g_0 k^{-\theta_g} \quad \text{and} \quad h_k = \bar{h}_0 e^{-\theta_h t} = h_0 k^{-\theta_h} \quad (2.50)$$

with  $g_0 = \bar{g}_0 \Lambda_{UV}^{\theta_g}$ ,  $h_0 = \bar{h}_0 \Lambda_{UV}^{\theta_h}$ . The singular part of the free energy density then transforms under the RG as

$$f(g_0, h_0) = k^{d+z} f(g_k, h_k) = k^{d+z} f(g_0 k^{-\theta_g}, h_0 k^{-\theta_h}), \quad (2.51)$$

where we used that the volume (including the time dimension) changes according to  $V \rightarrow V k^{d+z}$ . This expression is exactly the conventional scaling hypothesis. Similarly we obtain the scaling form of the two-point correlation function

$$G(\omega, p, g_0, h_0) = Z^2 k^{d+z} G(\omega', p', g_k, h_k) = Z^2 k^{d+z} G(\omega/k^z, p/k, g_0 k^{-\theta_g}, h_0 k^{-\theta_h}), \quad (2.52)$$

where  $Z$  defines the wavefunction renormalization  $\varphi'(p') = Z^{-1} \varphi(p)$  and itself is a function of the flow parameter  $k$ . The prefactor in Eq. (2.52) comes from the requirement that the form of the action does not change,  $\int_p \varphi(p) G^{-1}(\omega, p, g_0, h_0) \varphi(p) = \int_{p'} \varphi'(p') G^{-1}(\omega', p', g_k, h_k) \varphi'(p') = \int_p k^{-d-z} Z^{-2} \varphi(p) G^{-1}(\omega/k^z, p/k, g_k, h_k) \varphi(p)$ . If we now choose for example  $k = g_0^{1/\theta_g}$  as scaling factor and consider a trajectory with  $h_0 = 0$ , the two point function becomes

$$G(\omega, p, g, 0) = Z^2 g^{(d+z)/\theta_g} \Phi\left(\frac{\omega}{g^{z/\theta_g}}, \frac{p}{g^{1/\theta_g}}\right) \quad (2.53)$$

with  $\Phi(x, y) = G(x, y, 1, 0)$  and  $g_0 \rightarrow g$  for notational simplicity. Away from the critical point  $g \neq 0$ , we expect the two-point function to decay like  $G(r) \propto \exp(r/\xi)$  with the correlation length  $\xi$ , which means that its Fourier transform is a function of  $p\xi$ . We can thus extract that the correlation length scales as

$$\xi \propto g^{-1/\theta_g} \Rightarrow \nu = 1/\theta_g \quad (2.54)$$

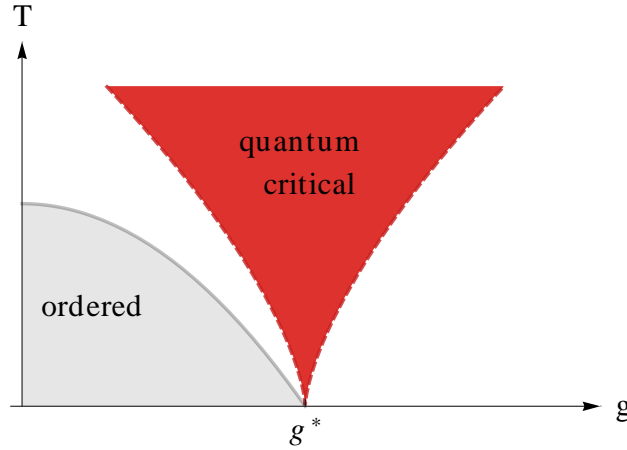


Figure 2.7.: A phase diagram in with a quantum critical point at  $(T, g) = (0, g^*)$  at the end of the ordered phase, which appears for small temperature  $T$  and coupling  $g$ . Above the quantum critical point a quantum critical region emerges with crossover lines at  $T = |g - g^*|^{\nu_z}$ .

so that the correlation length exponent  $\nu$  is the inverse from the critical exponent  $\theta_g$ . Additional to the correlation length exponent, we typically compute the anomalous dimension  $\eta$  from the flow of the wave function renormalization  $\eta = -\partial_t Z/Z$ . We can then determine the other conventional critical exponents (for the specific heat, the susceptibility, the magnetization or order parameter) due to various scaling relations that make only two of them independent.

We have discarded any irrelevant coupling in this example because they flow exactly to their fixed point values as the RG is iterated. However their bare values will determine the starting point of the flow and in general we cannot perform a calculation of the RG flow without approximation so that irrelevant couplings can play a role.

Furthermore analogous to the scaling for the correlation length, we obtain that the correlation time  $\tau_c$  behaves like  $\tau_c \propto g^{-\nu_z} \propto \xi^z$  and is thus related to the correlation length. The energy associated to the correlation time is  $E_c \sim 1/\tau_c$ , from which we can estimate the impact of the quantum critical point for non-zero, but still low temperature. It will play a role in the regime, where temperature can excite the quantum critical ground state  $T > 1/\tau_c = g^{\nu_z}$ . This defines the borders of a quantum critical region at nonzero temperature (see Fig. 2.7), which spreads from the quantum critical point [17, 166].

### 2.3.2. Multicritical Behavior

We speak of multicritical phenomena when the lines of continuous phase transitions meet at one point in the phase diagram [5, 8–12]. The structure of the phase diagram in the vicinity of such a point is a priori not clear, e. g. it can be bicritical or tetracritical (cf. Sec. 2.1.2). Furthermore, the multicritical behavior can differ from the one of the separate transitions. In the following we will be concerned with a (quantum) multicritical point of Dirac fermions, where a charge and spin density wave meet. To determine its nature regarding the previously mentioned issues, we will perform a fixed point analysis of a theory that incorporates the coupling between the two density waves. We then also have to account for the following stability considerations. Since deviations from the fixed point grow exponentially for relevant couplings, we have to fine-tune their bare values to reach the fixed point during the flow. In other words we cannot advance to a fixed point if there are more relevant couplings than parameters to fine-tune.

Therefore in our case, fixed points with no more than two relevant directions (corresponding to no more than two positive critical exponents,  $\theta_1$  and  $\theta_2$ ) can be accessed. This is related to the tuning of two microscopic parameters, e.g., onsite interaction  $U$  and nearest-neighbor interaction  $V$  for a microscopic theory (Chap. 4, Eq. (3.3)) or two masses  $m_\chi^2$  and  $m_\phi^2$  in an effective model (Chap. 4, Eq. (4.7)). We will call such fixed points “stable”. The third largest critical exponent  $\theta_3$  then decides over the stability of a fixed point. If it is negative the fixed point is stable and accessible through fine-tuning of two parameters, i. e. it will control the physics of our model. In contrast for positive  $\theta_3$ , the flow might come close to the corresponding fixed point but will eventually be repelled. The crossover exponent  $\phi = \theta_3/\theta_1$  quantifies this behavior [167]. It determines how fast or slow the crossover from one fixed point to the other, possibly stable fixed point occurs. If  $\phi$  is small the change will be very slow so that it could be hard to detect experimentally the critical behavior of other fixed points. That is although unstable, the considered fixed point can influence the observations. If a stable fixed point with only two relevant directions does not exist, the flow will eventually leave the vicinity to any unstable fixed point and flow away. We interpret this absence of scaling as indication for a discontinuous phase transition.





## CHAPTER 3

---

### Interplay of Phonon and Electron Interactions in Graphene

---

#### 3.1. Electronic Correlations on the Dynamically Distorted Honeycomb Lattice

As mentioned in the introduction, on the charge neutral honeycomb lattice, due to the vanishing density of states for energies close to the Fermi level, qualitative changes from interactions such as strongly correlated electronic phases can only appear beyond a critical interaction strength [50, 51, 55]. In this case, however, depending on the type of the interaction, different spontaneously broken symmetries, as e. g. charge and spin density waves, can occur [56–63, 68–71]. Doped graphene features a non-vanishing density of states at the Fermi level which enhances the role of electronic interactions as compared to the charge neutral situation and can give rise to, possibly unconventional superconductivity [57, 63]. A supercurrent in graphene has already been induced [168] by means of a contact of a graphene sample to superconducting electrodes. Furthermore the intercalation of bilayer graphene with Calcium has led to a superconducting transition at 4K [169, 170].

This raises the question under which circumstances graphene can give rise to intrinsic superconductivity. In this context, the role of electron-phonon interactions for different types of superconducting states has been investigated [171–174] with a focus on the effects of in-plane phonons that were identified in the Raman spectra of graphene [175]. Further ordering patterns as, e.g., a Kekulé order due to the electron-phonon coupling have been considered [176, 177]. However an unbiased approach that additionally accounts for competing effects from repulsive electronic interactions is missing.

In this chapter, we investigate the ordering tendencies of electrons on the honeycomb lattice when electron-phonon mediated electronic interactions from in-plane optical phonons as well as short-ranged Coulomb interactions are present. Therefore, we employ the functional renormalization group approach in the momentum-resolved patching scheme for the vertex function (cf. Sec. 2.2.2), allowing us to extract an effective Hamiltonian and determine the leading order parameters.

As a result of this investigation, we find that the leading correlations due to the phonon-mediated electronic interaction are not of superconducting type but rather form a bond order. The superconducting instability is only subleading. In addition, we observe a competition between two different kinds of bond orders depending on the relative strength of phonon

modes with different wavevectors coming from the center of the Brillouin zone (BZ),  $\Gamma$ , or from the corners of the BZ (the  $\pm K$ -points). The  $\Gamma$ -modes induce a nematic state whereas the  $\pm K$ -phonons support a Kekulé ordering pattern. By means of the fRG approach we resolve this competition.

By including short-ranged Coulomb interactions, we furthermore study the effects of phonons in a more realistic setup. In preceding RG investigations [55, 57, 59] antiferromagnetic spin density waves and charge density waves as well as topological quantum Hall states have been considered as relevant ground state candidates for the half-filled honeycomb lattice depending on the interactions. However it has been shown that the topological quantum Hall states are most likely suppressed by the appearance of density wave instabilities [67–69, 178–181]. In this chapter we show that the phonons affect the phase diagram in such a way that the antiferromagnetic regime benefits whereas the occurrence of the topological quantum Hall phase is reduced. This could also be relevant for bilayer graphene whose interaction parameters place it at the phase boundary between an antiferromagnetic spin density wave and a quantum spin Hall state [182, 183].

This chapter is organized as follows. In Sec. 3.2, we introduce our model in terms of a tight-binding Hamiltonian with nearest-neighbor hopping and density-density interactions. Phonon-modes are included upon expansion of the hopping amplitude in the displacements and integrated out to give a contribution to the electron-electron interaction. In Sec. 3.2.3, we briefly remind of the  $N$ -patch scheme of the functional renormalization group method, as well as the employed approximations. We present results on the ordering tendencies in Sec. 3.3, first by discussing exclusive in-plane optical phonons to analyze their isolated effect in Sec. 3.3.1. Then the interplay with short-ranged Coulomb interactions is studied and the impact of the electron-phonon coupling is discussed in Sec. 3.3.2. We draw conclusions in Sec. 3.4.

## 3.2. The Honeycomb Lattice

### 3.2.1. Extended Hubbard Model on the Honeycomb Lattice

#### Kinetic Hamiltonian

We consider a tight-binding model of electrons on the bipartite two-dimensional honeycomb lattice with nearest-neighbor hopping

$$H = -t \sum_{\langle i,j \rangle, s} \left( c_{A,i,s}^\dagger c_{B,j,s} + \text{h.c.} \right), \quad (3.1)$$

where  $c_{A,i,s}^{(\dagger)}$  annihilates (creates) an electron in unit cell  $i$  on sublattice  $A$  with spin  $s$  and analogous for sublattice  $B$ . The first sum includes all neighboring sites denoted by  $\langle i, j \rangle$ . They are connected by the nearest-neighbor hopping amplitude which in graphene has been estimated to be  $t \approx 2.8 \text{ eV}$ . After Fourier transformation with  $c_{o,i,s} = \sum_{\mathbf{k}} \exp(i\mathbf{k} \cdot \mathbf{r}_i) c_{o,\mathbf{k},s} / \sqrt{N}$  and  $o \in \{A, B\}$ , the tight-binding Hamiltonian reads

$$H = -t \sum_{\mathbf{k}, s} \left( \Delta_{\mathbf{k}} c_{A,\mathbf{k},s}^\dagger c_{B,\mathbf{k},s} + \text{h.c.} \right) \quad (3.2)$$

with  $\Delta_{\mathbf{k}} = \sum_i \exp(-i\mathbf{k} \cdot \mathbf{a}_i)$ , where  $\mathbf{a}_i$  labels the primitive lattice vectors together with zero, i.e.  $i \in \{1, 2, 3\}$ . Explicitly, the  $\mathbf{a}_i$  are given by  $\mathbf{a}_1 = \mathbf{0}$ ,  $\mathbf{a}_2 = \sqrt{3}a \mathbf{e}_x$  and  $\mathbf{a}_3 = \frac{\sqrt{3}a}{2} \mathbf{e}_x + \frac{3a}{2} \mathbf{e}_y$ , where  $a$  is the lattice constant. Diagonalization of  $H$  gives two bands  $\epsilon_{\mathbf{k}} = \pm t |\Delta_{\mathbf{k}}|$  with two

inequivalent, linear band crossing points at the Brillouin zone corners, the Dirac cones at  $K$  and  $-K$  as depicted in Fig. 3.1. This linear dispersion leads in two dimensions to the simple form of the density of states  $\rho(E) \propto E$  and its previously described vanishing at the Fermi level.

### Repulsive Electronic Interactions

Although the effect of interactions is reduced at half-filling due to the vanishing density of states, interactions on the honeycomb lattice induce instabilities beyond a critical strength. We here account for repulsive onsite, nearest and next-nearest neighbor interactions

$$H_I = U \sum_i n_{i,\uparrow} n_{i,\downarrow} + V_1 \sum_{\substack{\langle i,j \rangle \\ s,s'}} n_{i,s} n_{j,s'} + V_2 \sum_{\substack{\langle\langle i,j \rangle\rangle \\ s,s'}} n_{i,s} n_{j,s'}, \quad (3.3)$$

with the spin resolved density operator  $n_{i,s} = c_{o,i,s}^\dagger c_{o,i,s}$ . An estimate for the interaction parameters can be obtained from constrained random phase approximations [79]. Diagonalizing the single-particle Hamiltonian provides an orbital makeup for the interaction terms, i.e. we obtain a momentum-dependent vertex in the band representation  $V \rightarrow V(\mathbf{k}_1, n_1, \mathbf{k}_2, n_2, \mathbf{k}_3, n_3, n_4)$  determined by four band indices  $n_i$ , and three independent momenta  $\mathbf{k}_i$ .

#### 3.2.2. Inclusion of Phonon Modes

To determine the coupling of electrons and lattice displacements, we expand the hopping amplitude in the displacement fields  $\mathbf{u}$ , based on the assumption that it depends on the distance between neighboring sites, i.e.

$$t \rightarrow t - \alpha_{\parallel} (\mathbf{u}_i - \mathbf{u}_j) \cdot \hat{\delta}_{ij}. \quad (3.4)$$

The expansion depends on the bond direction  $\hat{\delta}_{ij}$  pointing along one of the three nearest neighbor vectors. The expansion parameter is determined by ab initio calculations to be  $|\alpha_{\parallel}| \approx 4.4 \text{ eV/\AA} - 5.3 \text{ eV/\AA}$  with  $\alpha_{\parallel} < 0$  [175, 184, 185]. We introduce the phonons by the usual quantization of the Fourier transformed displacement fields using the explicit expressions  $\mathbf{u}_i = \sum_{\mathbf{q}} \exp(i\mathbf{q} \cdot \mathbf{r}_i) \mathbf{u}_{\mathbf{q},A} / \sqrt{N}$  and  $\mathbf{u}_j = \sum_{\mathbf{q}} \exp(i\mathbf{q} \cdot (\mathbf{r}_i - \mathbf{a}_j)) \mathbf{u}_{\mathbf{q},B} / \sqrt{N}$  for site  $i$  in sublattice  $A$  and its nearest neighbor  $j$  in sublattice  $B$ . Further,

$$\mathbf{u}_{\mathbf{q},o} = \sum_{\lambda} u_{\mathbf{q}}^{\lambda} \mathbf{e}_{\mathbf{q},o}^{\lambda} = \sum_{\lambda} \frac{1}{\sqrt{2M\Omega_{\mathbf{q}}^{\lambda}}} (p_{\lambda,\mathbf{q}} + p_{\lambda,-\mathbf{q}}^{\dagger}) \mathbf{e}_{\mathbf{q},o}^{\lambda}. \quad (3.5)$$

The carbon mass is denoted by  $M$  and  $p_{\lambda,\mathbf{q}}^{(\dagger)}$  is the annihilation (creation) operator of a phonon in mode  $\lambda$  with momentum  $\mathbf{q}$ . Corresponding dispersions and polarizations are given by  $\Omega_{\mathbf{q}}^{\lambda}$  and  $\mathbf{e}_{\mathbf{q},o}^{\lambda}$ . This inclusion of lattice distortions in terms of the phonon operators leads to the following electron-phonon coupling in orbital momentum space

$$\delta H = \frac{\alpha_{\parallel}}{\sqrt{N}} \sum_{\substack{\mathbf{k}, \mathbf{q} \\ s, \lambda}} \frac{1}{\sqrt{2M\Omega_{\mathbf{q}}^{\lambda}}} \left[ g_{\mathbf{k}}^{\lambda}(\mathbf{q}) c_{A,\mathbf{k},s}^{\dagger} c_{B,\mathbf{k}-\mathbf{q},s} (p_{\lambda,\mathbf{q}} + p_{\lambda,-\mathbf{q}}^{\dagger}) + \text{h.c.} \right], \quad (3.6)$$

where  $g_{\mathbf{k}}^{\lambda}(\mathbf{q}) = \sum_i (e^{i\mathbf{q} \cdot \mathbf{a}_i} \mathbf{e}_{\mathbf{q},A}^{\lambda} - \mathbf{e}_{\mathbf{q},B}^{\lambda}) \cdot \hat{\delta}_i e^{-i\mathbf{k} \cdot \mathbf{a}_i}$ . Similar couplings were obtained for Carbon nanotubes [186] and by a fit to ab-initio values in graphene [175].

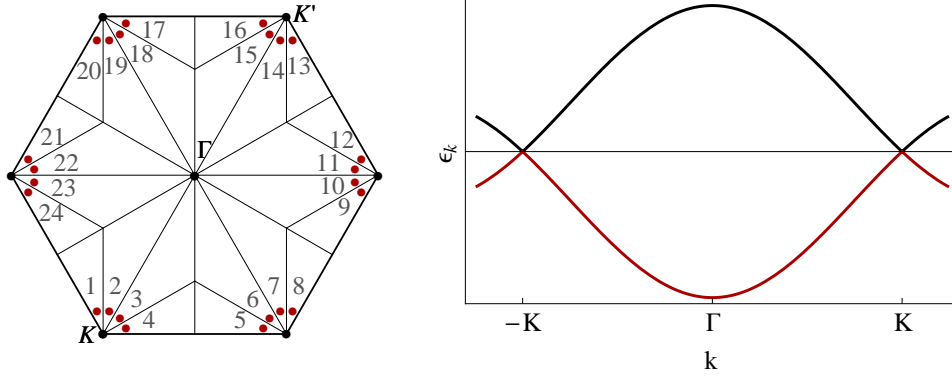


Figure 3.1.: (Left) Discretization of the momentum dependence (patching) in the Brillouin zone. Each patch is represented by a wave vector near the Fermi level as indicated by the dots. (Right) The energy bands  $\epsilon_{\mathbf{k}} = \pm |\Delta_{\mathbf{k}}|$  along the path  $K' - \Gamma - K$  in the Brillouin zone. They touch at  $K, K' = -K$ , where the dispersion can be approximated to be linear in momentum.

Integrating out the phonons in the functional integral representation gives an effective electronic interaction

$$H_{\text{ph-med}} = -\frac{\alpha_{\parallel}^2}{2MN} \sum_{q,\lambda} \sum_{\substack{k,s \\ k',s'}} \frac{1}{q_0^2 + \Omega_q^2} \left[ g_{\mathbf{k}}^{\lambda}(\mathbf{q}) g_{-\mathbf{k}'}^{\lambda}(\mathbf{q})^* c_{A,k,s}^{\dagger} c_{A,k',s'}^{\dagger} c_{B,k'+q,s'} c_{B,k-q,s} \right. \\ \left. + g_{\mathbf{k}}^{\lambda}(\mathbf{q}) g_{\mathbf{k}'}^{\lambda}(\mathbf{q})^* c_{A,k,s}^{\dagger} c_{B,k'-q,s'}^{\dagger} c_{A,k',s'} c_{B,k-q,s} + \text{c.c.} \right], \quad (3.7)$$

mediated by the phonons. As before the multiindex  $k = (k_0, \mathbf{k})$  collects the fermionic or bosonic Matsubara frequency and the wave vector.

In the following, we will need expressions for the phonon dispersion and polarization. In principle, a calculation of the phonon spectrum would give eigenvectors with  $x$ - and  $y$ -components of the displacements for a given lattice site that vary with the phonon-wavevector  $q$ . In this two dimensional, bipartite system, the eigenvectors correspond to four possible polarizations  $\lambda$  being orthogonal to each other. In DFT calculations it was shown that the optical modes with wavevector close to  $\Gamma$  and the highest-energy modes close to  $K, -K$  give the main contributions to the electron-phonon coupling strength [187]. This is why, we will concentrate on them and use only their energy and polarization in the phonon-mediated interaction, see Sec. 3.3. This approximation simplifies the study a lot, but should not affect the qualitative results, as the smaller variation of the phonon energy due to the dispersion of the optical modes in the denominator of Eq. (3.7) does not have a strong impact on the effective interaction.

### 3.2.3. Patching Scheme on the Honeycomb Lattice

We employ the patching scheme of the functional renormalization group approach described in Sec. 2.2.2. As a reminder we briefly list its advantages and the important approximations again. The patching scheme allows to monitor the evolution from the bare action to an effective action at low energy as a function of the energy scale in an unbiased way and accounts for effects beyond mean field and RPA as it also includes the interplay between different ordering tendencies. We only consider the two-particle interaction vertex  $V^{\Lambda}$ , i. e. the results are of

second order in the interaction, and we neglect the frequency dependence of the vertex  $V^\Lambda$ . This still leads to an infinite summation of coupled particle-particle and particle-hole diagrams. For the numerical treatment, the Brillouin zone is divided into  $N$  patches as shown in Fig. 3.1. Each patch is then represented by one momentum close to the Fermi level. Thereby the angular dependence of the interaction on the wavevectors is taken into account. We choose  $N = 24$  or  $N = 48$  patches to check that our findings do not depend on this choice.

### 3.3. Instabilities and Phase Diagram

In this section, we analyze the phases of the honeycomb lattice system at temperature  $T = 0$  as a function of the bare interaction parameters  $U$ ,  $V_1$  and  $V_2$  and the electron-phonon couplings  $\alpha_N$ ,  $\alpha_K$  that determine the impact of the phonons with wavevector close to  $\Gamma$  and  $K, -K$ , respectively.

#### 3.3.1. Purely Phonon-Mediated Interaction

We start with the study of the isolated effect of the phonon-mediated electron-electron coupling. As mentioned in the beginning, we focus on the phonons at  $\Gamma$  and  $K, -K$ . This means that we set  $\Omega_{\mathbf{q}}^\lambda = \Omega_\Gamma = \text{const}$  if  $\mathbf{q}$  is close to  $\Gamma$  and  $\lambda$  corresponds to the optical branches. For  $\mathbf{q}$  in the vicinity of the Dirac points and  $\lambda$  labeling the three highest-energy phonons  $\Omega_{\mathbf{q}}^\lambda = \Omega_K = \Omega_{-K} = \text{const}$ . The analogous approximation is used for the polarization vectors  $\mathbf{e}_{\mathbf{q},a}$ ,  $\mathbf{e}_{\mathbf{q},b}$  and all other modes are neglected. This ansatz accounts for the phonons that have been identified in the Raman spectrum of graphene and in DFT calculations to give the strongest electron-phonon coupling [175, 187]. They are often referred to as  $E_2$  and  $A'_1$  or  $A_1, B_1$  phonons, respectively. It has been shown in Refs. [176, 177] that the latter modes can give rise to an instability corresponding to Kekulé ordering. We also find this to be the dominating instability for equally strong coupling of both modes, whereas for an enhanced coupling of the  $E_2$  phonons, a nematic bond order is induced.

With these preliminaries and comments, we choose to parametrize the phonon-mediated contribution to the electron-electron interaction as

$$H_{\text{ph-med}} = -\frac{1}{N} \sum_{\substack{\mathbf{k}_1, \mathbf{k}_2, \mathbf{k}_3 \\ s, s'}} \left[ V_{\mathbf{k}_1, \mathbf{k}_2, \mathbf{k}_3}^{AABB} c_{A, \mathbf{k}_3, s}^\dagger c_{A, \mathbf{k}_4, s'}^\dagger c_{B, \mathbf{k}_2, s'} c_{B, \mathbf{k}_1, s} + V_{\mathbf{k}_1, \mathbf{k}_2, \mathbf{k}_3}^{ABAB} c_{A, \mathbf{k}_3, s}^\dagger c_{B, \mathbf{k}_4, s'}^\dagger c_{A, \mathbf{k}_2, s'} c_{B, \mathbf{k}_1, s} + \text{h.c.} \right] \quad (3.8)$$

$$V_{\mathbf{k}_1, \mathbf{k}_2, \mathbf{k}_3}^{AABB} = \begin{cases} \alpha_N \sum_{\lambda=1}^2 \frac{1}{\{\Omega_\Gamma^\lambda\}^2} g_{\mathbf{k}_3}^{\lambda, \Gamma}(\mathbf{k}_3 - \mathbf{k}_1) g_{-\mathbf{k}_4}^{\lambda, \Gamma}(\mathbf{k}_3 - \mathbf{k}_1)^* & : \quad \mathbf{k}_3 - \mathbf{k}_1 \text{ close to } \Gamma \\ \alpha_K \sum_{\lambda=1}^3 \frac{1}{\{\Omega_{\pm K}^\lambda\}^2} g_{\mathbf{k}_3}^{\lambda, \pm K}(\mathbf{k}_3 - \mathbf{k}_1) g_{-\mathbf{k}_4}^{\lambda, \pm K}(\mathbf{k}_3 - \mathbf{k}_1)^* & : \quad \mathbf{k}_3 - \mathbf{k}_1 \text{ close to } \pm K \end{cases} \quad (3.9)$$

$$V_{\mathbf{k}_1, \mathbf{k}_2, \mathbf{k}_3}^{ABAB} = \begin{cases} \alpha_N \sum_{\lambda=1}^2 \frac{1}{\{\Omega_\Gamma^\lambda\}^2} g_{\mathbf{k}_3}^{\lambda, \Gamma}(\mathbf{k}_3 - \mathbf{k}_1) g_{\mathbf{k}_2}^{\lambda, \Gamma}(\mathbf{k}_3 - \mathbf{k}_1)^* & : \quad \mathbf{k}_3 - \mathbf{k}_1 \text{ close to } \Gamma \\ \alpha_K \sum_{\lambda=1}^3 \frac{1}{\{\Omega_{\pm K}^\lambda\}^2} g_{\mathbf{k}_3}^{\lambda, \pm K}(\mathbf{k}_3 - \mathbf{k}_1) g_{\mathbf{k}_2}^{\lambda, \pm K}(\mathbf{k}_3 - \mathbf{k}_1)^* & : \quad \mathbf{k}_3 - \mathbf{k}_1 \text{ close to } \pm K \end{cases} \quad (3.10)$$

with  $\mathbf{k}_4 = \mathbf{k}_1 + \mathbf{k}_2 - \mathbf{k}_3$  due to momentum conservation and fixed polarization in  $g_{\mathbf{k}}^{\lambda, \mathbf{Q}}(\mathbf{q}) = \sum_i (e^{i\mathbf{q} \cdot \mathbf{a}_i} \mathbf{e}_{\mathbf{Q}, A}^\lambda - \mathbf{e}_{\mathbf{Q}, B}^\lambda) \cdot \hat{\mathbf{d}}_i e^{-i\mathbf{k} \cdot \mathbf{a}_i}$  as motivated before.  $\{\Omega_{\mathbf{Q}}^\lambda\}$  labels the value of the phonon energy,

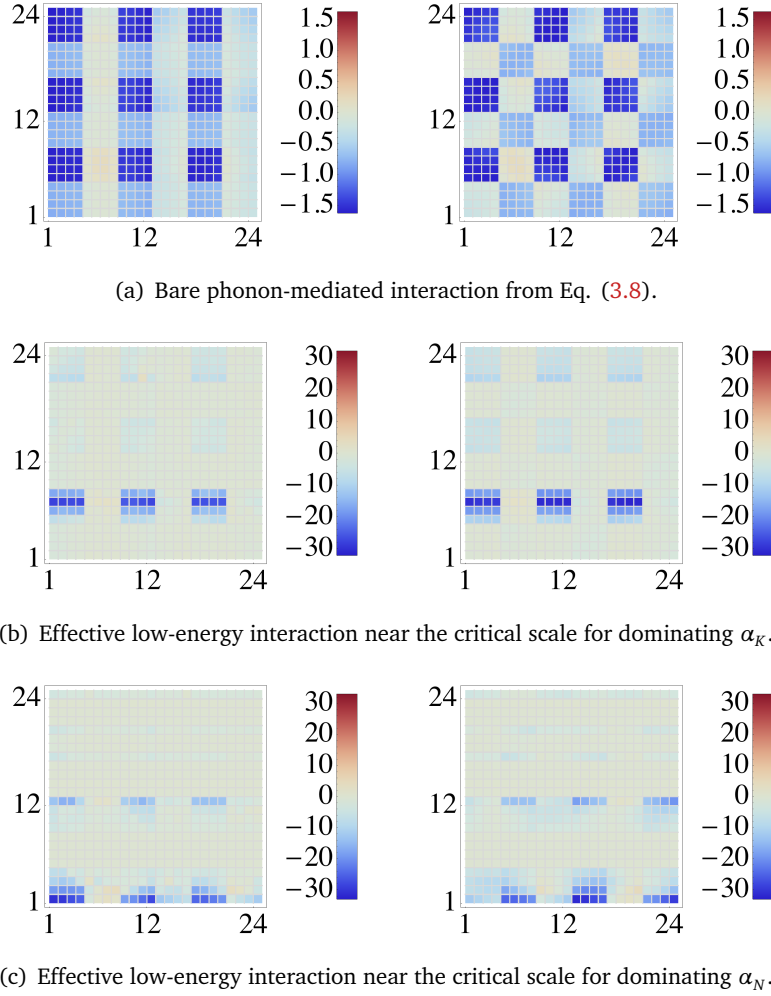


Figure 3.2.: Bare and effective phonon-mediated interaction in units of the hopping amplitude  $t$ . The numbers on the axes correspond to the patches of Fig. 3.1. The horizontal axes shows  $\mathbf{k}_2$ , the vertical  $\mathbf{k}_1$  and  $\mathbf{k}_3$  is fixed on the first patch. Orbital combinations are for all subfigures (a), (b) and (c),  $o_1 = o_4 \neq o_2 = o_3$  (left panel) and  $o_1 = o_2 \neq o_3 = o_4$  (right panel).

so that the interaction parameter  $\alpha_{N/K}$  has units of energy<sup>1</sup>. As is well known and also discussed in the context of RG e.g. in Ref. [188], the phonon-mediated interaction is suppressed for frequencies larger than the phonon frequency  $\Omega$ . Resolving this frequency dependence of the interactions in the RG flow with frequency-independent interactions requires some physical insights, at least if one wants to reduce the numerical effort<sup>2</sup>. Usually one tries to replace the frequency dependence with a dependence on the electronic excitation energy. One reasonable choice for studying the phonon-mediated interaction case separately would then be to only include interactions of electrons with excitation energies below  $\Omega$ . This would correspond to start the RG flow only at RG scale  $\Lambda_0 = \Omega$ . In this work, however, we chose to start the flow already at the bandwidth  $\Lambda_0 = 3t$ . This can be viewed as ignoring the retardation and

<sup>1</sup> $\alpha_N$  and  $\alpha_K$  should not be confused with  $\alpha_{\parallel}$  from the expansion of the hopping amplitude  $\alpha_{N/K} = \alpha_{\parallel}^2 / (2M[\Omega_{T/K}^{\lambda}]^2)$ . With the ab-initio values for  $\alpha_{\parallel}$  from above, the interaction parameter is of the order  $\alpha_{N/K} \approx 0.12t - 0.17t$ .

<sup>2</sup>Note that in some recent fRG works [189–191], the frequency dependence of the interactions have been taken into account.

artificially enhances the impact of electron-phonon interactions and makes its effects clearly visible.

We address several scenarios for the electron-phonon coupling by different choices for the interaction parameters  $\alpha_N$  and  $\alpha_K$ . We study the cases where only phonons from the vicinity of the  $\Gamma$  point ( $\alpha_K = 0$ ), or only phonons close to the Dirac points ( $\alpha_N = 0$ ), contribute. Moreover, we include their mutual influence on each other by tuning through different ratios of  $\alpha_N/\alpha_K$  with the most physical case around  $\alpha_N/\alpha_K \approx 1$ . The investigated parameter range spans from  $\alpha_{N/K} = 0$  to  $\alpha_{N/K} = t$ . In these flows, divergences develop only if the interaction parameter  $\alpha_{N/K}$  is large enough, otherwise the system is a stable semimetal. This phenomenon is clearly related to the vanishing density of states at the Fermi level and has been seen for many other types of interaction-driven instabilities for fermions with this spectrum before (e.g. Refs. [55, 57, 59]). First, we discuss the results for  $\alpha_N = \alpha_K$ . The discretized, bare interaction, which is the initial value of the flow equation, is shown in Fig. 3.2(a). Here, the critical parameter value for an instability to occur at half filling is  $\alpha_K^c \approx 0.28 t$ , cf. Fig. 3.3(a). The momentum structure of the effective interaction close to the critical scale is presented in Fig. 3.2(b). It has the same structure as the bare phonon-mediated interaction, however, only for momentum transfer with  $\mathbf{k}_3 - \mathbf{k}_1 = \mathbf{K}$  and  $\mathbf{k}_3 - \mathbf{k}_1 = -\mathbf{K}$ . Using this relation in the coupling function  $V(\mathbf{k}_1, \mathbf{k}_2, \mathbf{k}_3)$  gives the effective low-energy Hamiltonian

$$H_K = -\frac{V_{\text{eff}}}{N} \sum_{\lambda} \sum_{\mathbf{k}, s} \left( g_{\mathbf{k}}^{\lambda}(\mathbf{K}) c_{A, \mathbf{k}, s}^{\dagger} c_{B, \mathbf{k}-\mathbf{K}, s} + g_{\mathbf{k}}^{\lambda}(-\mathbf{K})^* c_{B, \mathbf{k}+\mathbf{K}, s}^{\dagger} c_{A, \mathbf{k}, s} \right) \times \sum_{\mathbf{k}', s'} \left( g_{\mathbf{k}'}^{\lambda}(-\mathbf{K}) c_{A, \mathbf{k}', s'}^{\dagger} c_{B, \mathbf{k}'+\mathbf{K}, s'} + g_{\mathbf{k}'}^{\lambda}(\mathbf{K})^* c_{B, \mathbf{k}'-\mathbf{K}, s'}^{\dagger} c_{A, \mathbf{k}', s'} \right) \quad (3.11)$$

with  $V_{\text{eff}} > 0$ . For this expression, we perform a mean-field decoupling with the molecular field

$$\Delta_{\text{ph}}^{\lambda}(\mathbf{Q}) = \frac{V_{\text{eff}}}{N} \sum_{\mathbf{k}, s} \left\langle g_{\mathbf{k}}^{\lambda}(\mathbf{K}) c_{A, \mathbf{k}, s}^{\dagger} c_{B, \mathbf{k}-\mathbf{K}, s} + g_{\mathbf{k}}^{\lambda}(-\mathbf{K})^* c_{B, \mathbf{k}+\mathbf{K}, s}^{\dagger} c_{A, \mathbf{k}, s} \right\rangle, \quad (3.12)$$

which also serves as order parameter field, e.g. in a mean-field approach. This yields

$$H_K \approx - \sum_{\mathbf{k}, s, \lambda} \left[ \Delta_{\text{ph}}^{\lambda}(-\mathbf{K}) \left( g_{\mathbf{k}}^{\lambda}(\mathbf{K}) c_{A, \mathbf{k}, s}^{\dagger} c_{B, \mathbf{k}-\mathbf{K}, s} + g_{\mathbf{k}}^{\lambda}(-\mathbf{K})^* c_{B, \mathbf{k}+\mathbf{K}, s}^{\dagger} c_{A, \mathbf{k}, s} \right) + \Delta_{\text{ph}}^{\lambda}(\mathbf{K}) \left( g_{\mathbf{k}}^{\lambda}(-\mathbf{K}) c_{A, \mathbf{k}, s}^{\dagger} c_{B, \mathbf{k}+\mathbf{K}, s} + g_{\mathbf{k}}^{\lambda}(\mathbf{K})^* c_{B, \mathbf{k}-\mathbf{K}, s}^{\dagger} c_{A, \mathbf{k}, s} \right) \right], \quad (3.13)$$

ignoring the constant term.

If we compare this expression to the coupling Hamiltonian, Eq. (3.6), we recover the contribution of the  $\pm\mathbf{K}$ -phonons from the beginning with the identification  $\Delta_{\text{ph}}^{\lambda}(\pm\mathbf{K}) = |\alpha_{\parallel}| u_{\pm\mathbf{K}}^{\lambda}$ . But in order to get a diverging phonon-mediated interaction parameter  $\alpha_K$ , the phonon frequency must tend to zero. Thus the observed instability results in a static lattice distortion formed by the modes from  $\pm\mathbf{K}$ , which modulates the hopping strength according to Eq. (3.4) by  $\delta t_{ij} = u \exp(i\mathbf{K}\mathbf{r}_i) \exp(-i\mathbf{K}\mathbf{a}_j) \Delta(\mathbf{r}_i) + \text{c.c.}$ , with amplitude  $u$  and  $\Delta(\mathbf{r}_i) = (\exp(i\mathbf{K}\mathbf{a}_j) \mathbf{e}_{\mathbf{K}, A}^{\lambda} - \mathbf{e}_{\mathbf{K}, B}^{\lambda}) \cdot \hat{\delta}_{ij}$ . Hence the hopping is non-uniform in the three bond directions resulting in a tripled unit cell. This distortion is also known as Kekulé order and is depicted in the inset of Fig. 3.3(b). Correspondingly, close to the Dirac points, the eigenenergies extracted from Eq. (3.13) coincide with previous investigations of the Kekulé phase [192, 193] and show the opening of a gap.

Now we tune the interaction to both extreme cases where one of the parameters is zero. For  $\alpha_N = 0$ , we again find the Kekulé distortion as leading instability. The only difference is that



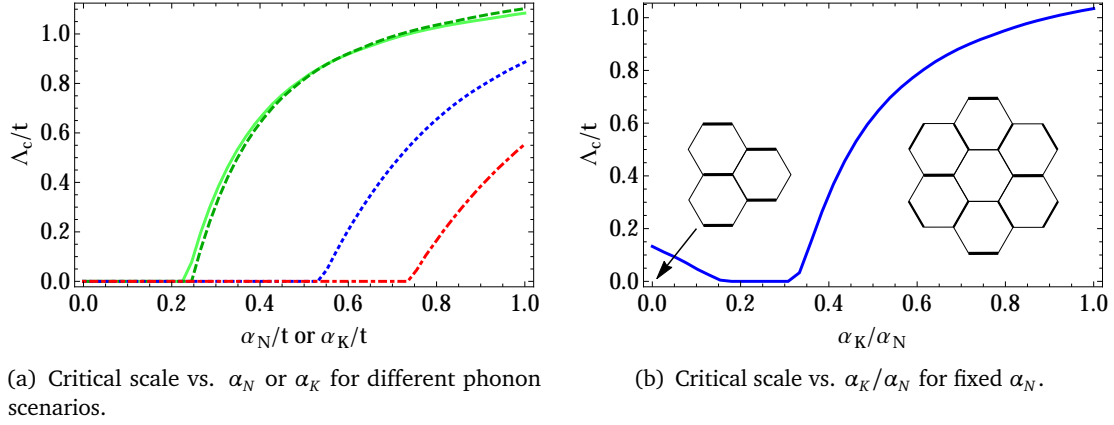


Figure 3.3.: (a) Critical scale as function of the phonon-mediated interaction parameter. For  $\alpha_N = \alpha_K$  (dashed) and  $\alpha_N = 0$  (solid) the Kekulé state is induced, whereas for  $\alpha_K = 0$  (dot-dashed) a nematic bond order develops. With particle-particle contributions only and  $\alpha_N = \alpha_K$  (dotted) a conventional superconducting ground state is favoured. (b) Critical scale as function of the ratio  $\alpha_K/\alpha_N$  at fixed  $\alpha_N = 0.8t$ . Insets show the nematic ( $\alpha_K/\alpha_N \leq 0.15$ ) and the Kekulé ( $\alpha_K/\alpha_N \geq 0.3$ ) state, respectively.

the critical  $\alpha_K$  needed to induce the ordering is slightly decreased to  $\alpha_K^c \approx 0.26t$ , as visible in Fig. 3.3(a). This already shows that the small-wavevector phonons controlled by  $\alpha_N$  have a destructive influence on the large-wavevector phonons controlled by  $\alpha_K$ , i.e. there is some degree of phonon-phonon interaction.

For  $\alpha_K = 0$ , the behavior is qualitatively different. As shown in Fig. 3.3(a), the instability does not occur until a threshold value  $\alpha_N^c \approx 0.78t$  is reached and cannot be due to  $\pm\mathbf{K}$ -phonons because they are not included in this case. Instead we find the momentum structure at low energies of Fig. 3.2(c), which mirrors the bare phonon-mediated interaction for zero momentum transfer  $\mathbf{k}_3 = \mathbf{k}_1$ . The extracted, low-energy Hamiltonian is

$$H_N = -\frac{\bar{V}_{\text{eff}}}{N} \sum_{\lambda} \sum_{\mathbf{k}, s} \left( g_{\mathbf{k}}^{\lambda} c_{A, \mathbf{k}, s}^{\dagger} c_{B, \mathbf{k}, s} + g_{\mathbf{k}}^{\lambda*} c_{B, \mathbf{k}, s}^{\dagger} c_{A, \mathbf{k}, s} \right) \sum_{\mathbf{k}', s'} \left( g_{\mathbf{k}'}^{\lambda} c_{A, \mathbf{k}', s'}^{\dagger} c_{B, \mathbf{k}', s'} + g_{\mathbf{k}'}^{\lambda*} c_{B, \mathbf{k}', s'}^{\dagger} c_{A, \mathbf{k}', s'} \right) \quad (3.14)$$

with  $\bar{V}_{\text{eff}} > 0$  and the abbreviation  $g_{\mathbf{k}}^{\lambda}(\mathbf{q} = 0) = g_{\mathbf{k}}^{\lambda}$ . The corresponding mean-field Hamiltonian results in

$$H_N \approx -2 \sum_{\mathbf{k}, s, \lambda} \Delta_{\text{ph}}^{\lambda} \left( g_{\mathbf{k}}^{\lambda} c_{A, \mathbf{k}, s}^{\dagger} c_{B, \mathbf{k}, s} + g_{\mathbf{k}}^{\lambda*} c_{B, \mathbf{k}, s}^{\dagger} c_{A, \mathbf{k}, s} \right), \quad (3.15)$$

where

$$\Delta_{\text{ph}}^{\lambda} = \frac{\bar{V}_{\text{eff}}}{N} \sum_{\mathbf{k}, s} \left\langle g_{\mathbf{k}}^{\lambda} c_{A, \mathbf{k}, s}^{\dagger} c_{B, \mathbf{k}, s} + g_{\mathbf{k}}^{\lambda*} c_{B, \mathbf{k}, s}^{\dagger} c_{A, \mathbf{k}, s} \right\rangle \quad (3.16)$$

is the order parameter. Comparison to the coupling Hamiltonian, Eq. (3.6) now gives the static lattice distortion due to the zone center  $E_2$  phonons with  $2\Delta_{\text{ph}}^{\lambda} = |\alpha_{\parallel}| u_0^{\lambda}$ . For  $\mathbf{q} = 0$ , the displacement of neighboring sites has different signs  $\mathbf{e}_{0,A}^{\lambda} = -\mathbf{e}_{0,B}^{\lambda}$ . This means that the two sub-lattices are moved in opposite directions in this state changing the hopping to  $\delta t_{ij} = \pm \mathbf{u} \cdot \hat{\mathbf{d}}_{ij}$  with constant displacement vector  $\mathbf{u}$  and sign modulation between sublattices. The sixfold symmetry of the original lattice is reduced to a twofold one, the translational symmetry of



the underlying Bravais lattice, however, is maintained, corresponding to a nematic ordering pattern. The best energy gain is a distortion along the bonds between two sites. As a result, we obtain the configuration shown in the inset of Fig. 3.3(b), where the hopping along one bond direction is enhanced and the Dirac points are shifted away from the Brillouin zone corners. Such a state was studied in Ref. [192].

In Fig. 3.3(b), we also show the evolution of the critical scale for fixed supercritical  $\alpha_N$  when  $\alpha_K$  is increased. We clearly see that the 'Kekulé phonons' with large wavevector transfer reduce the scale for the nematic instability and push it to zero already for  $\alpha_K \approx 0.2\alpha_N$ . This exhibits a clear 'anharmonic' interaction between phonon modes with different wavevectors that is revealed by the fRG treatment. When  $\alpha_K$  is increased further, one reaches the Kekulé-ordered phase again. Note that the rather high critical scales found here are not to be taken literally, due to the mentioned overestimation of the phonon effects when the retardation is ignored.

Usually, in more than one dimension, an important property of the electron-phonon interaction is to induce Cooper pairing, which seems to be suppressed here. We can indeed recover a conventional phonon-mediated superconducting state, but only if the RG flow equation for the interaction is reduced to the particle-particle term and all particle-hole terms are switched off. Through this the integration of the fRG equations is identical to a ladder summation in the particle-particle channel. However, the critical interaction strength needed to observe a flow to strong coupling for such an undisturbed Cooper instability is larger than in the bond-ordering case. Here, without the particle-hole term, we find  $\alpha^{SC} \approx 0.58t$  for  $\alpha_K = \alpha_N$ . This shows that phonon-mediated superconductivity arises in the particle-particle channel as one would expect, however only when the competing contributions from the particle-hole channels are completely neglected.

### 3.3.2. Inclusion of Density-Density Interactions

We now also include the Coulomb-induced repulsive density-density interactions  $U$ ,  $V_1$  and  $V_2$  as given in Eq. (3.3). First, we consider, in addition to the phonon-mediated interaction, each one of the three short-ranged interactions  $U$ ,  $V_1$  and  $V_2$  separately. This shows if the phonon-mediated interaction amplifies or weakens the effect of the respective electronic interaction. The results are compared to the case without the consideration of phonons.

Running the fRG flow with a fixed, supercritical on-site interaction for different phonon-mediated interaction strengths leads to an antiferromagnetic spin density wave as in the case without phonons. But with increasing phonon-mediated interactions, the critical scale of the flow is enhanced. This amplifying tendency is also observed if we determine the critical on-site interaction needed to induce an instability. It reduces from  $U^c = 2.6t$  to  $U^c = 1.3t$  if a phonon-mediated interaction of, e.g.  $\alpha = 0.2t$ , is turned on, cf. Fig. 3.4. For the nearest-neighbor interaction, we obtain qualitatively the same behavior. As without phonons, the nearest-neighbor interaction triggers a charge density wave whose critical scale is increased with increasing phonon mediated interaction. However, this effect is not as large as in the case of the on-site interaction. Nevertheless, the critical  $V_1$  changes from  $V_1^c = 0.4t$  for  $\alpha = 0$  to  $V_1^c = 0.25t$  for  $\alpha = 0.2t$ . The situation is different if we consider only a next-nearest-neighbor interaction, which induces in our truncation a quantum spin Hall state (QSH). Including an electron-phonon coupling suppresses the tendency for the formation of a QSH state as shown in the lower panel of Fig. 3.4.

These tendencies are confirmed when we run the fRG flow with all interactions, i.e. density-density repulsion up to the second nearest neighbor and the phonon-mediated interaction,

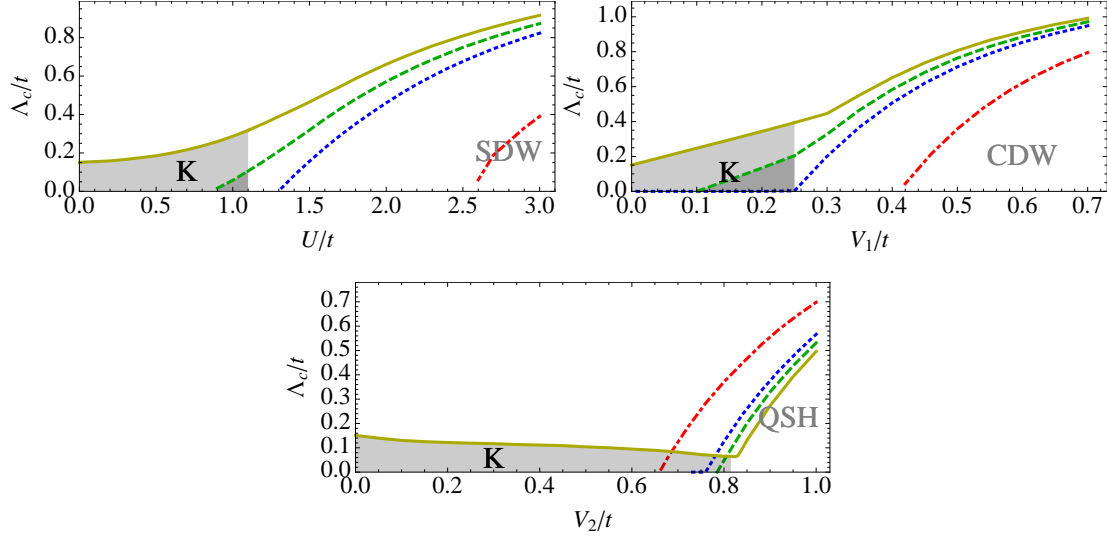


Figure 3.4.: Critical scale as function of the density-density interaction  $U, V_1$  and  $V_2$  (from top left to top right to bottom panel) for different values of the ph-med interaction  $\alpha \in \{0.28t, 0.24t, 0.20t, 0\}$  (solid, dashed, dotted, dot-dashed). For small density-density interactions the gray-shaded area shows the appearance of the Kekulé ordering tendency (K). For larger density-density interaction we recover SDW (onsite interaction, top panel), CDW (nearest-neighbor i.a., middle panel) and QSH (next-to-nearest neighbor i.a., bottom panel)

included. The parameter range which we account for extends from zero through the cRPA values from Ref. [79]. They are taken as upper bounds because the fRG tends to overestimate the critical scales. A summary of this investigation is given by Fig. 3.5.

### 3.4. Conclusions

In this chapter we have analyzed the impact of in-plane phonons on possible ground state orderings in a simple theoretical model for monolayer graphene. We focused on phonon eigenmodes arising from the modulation of nearest-neighbor bonds between the carbon  $\pi$ -orbitals on the honeycomb lattice with wave vectors near  $\Gamma$  and  $K/-K$ . These modes, classified as  $E_2$  for small wavevector and  $A'_1, A_1, B_1$  for large wavevector transfer, are known from DFT calculations to couple most strongly to the electrons.

The electron-phonon coupling and the phonon dynamics for these modes was transformed into an effective electron-electron interaction, with some idealizations. Studying the effects of the phonon-mediated interaction without including Coulomb interactions between the electrons we find the following results. Near charge neutrality (i.e. for the undoped system) the dominant instability is in the particle-hole channel, and not in the pairing channel as is usually the case in non-nested systems. While our study may not be fully quantitative, the picture we find is that the phonons with large momentum transfer dominate in the low-energy effective interactions and that the predominant instability is towards Kekulé bond order, where the unit cell is tripled by a pattern of strengthened and weakened bonds. This state opens a gap at the Dirac points, i.e. is an insulator. Various works have argued for the existence of this state due to Coulomb interactions [176, 177]. Previous RG studies of the same model [55, 57, 182, 183] did not find the Kekulé order for Coulomb interactions of density-density type in the effective model, but it

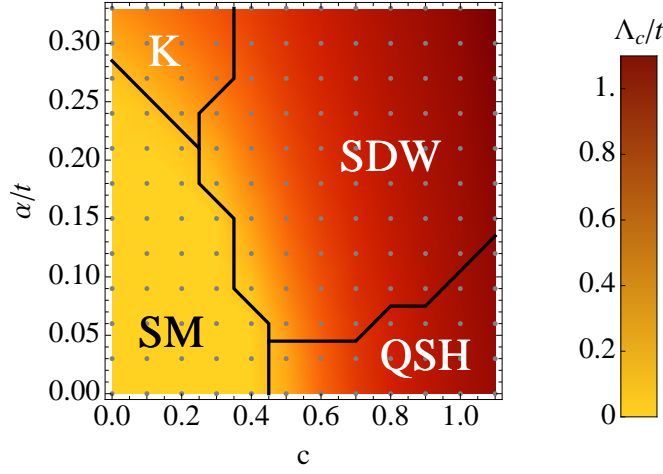


Figure 3.5.: Phase diagram for the rescaled ab initio density-density interaction profile in graphene from Ref. [79] with rescaling parameter  $c$  and the electron-phonon coupling strength  $\alpha = \alpha_N = \alpha_K$ . The density-density interactions are rescaled according to  $\{U/t, V_1/t, V_2/t\} \approx \{3.3, 2.0, 1.5\} \rightarrow c\{U/t, V_1/t, V_2/t\}$ . In case without electron-phonon coupling we find a Quantum Spin Hall state being favored for this interaction profile, cf. Ref. [182, 183]. In agreement with the previous observations the EPC supports the tendency towards the SDW phase.

now occurs due to the bond-bond interactions mediated by the phonons. We can also weaken the influence of the large-wavevector phonons in the effective electron-electron interaction, emphasizing the small- $q$  phonons. In this case, a nematic instability becomes dominant where one of the three bond directions is enhanced with respect to the other two directions. The resulting spectrum features shifted Dirac points. Considering the competition between the different phonon channels, we found that the large-wavevector Kekulé phonons considerably weaken the tendencies towards nematic order driven by the small-wavevector phonons. This means that there is a significant amount of non-RPA or anharmonic physics at low energy scales, where phonons with different wavevectors interact destructively.

More realistically, the phonon-mediated interaction should be considered together with the Coulomb interaction between the electrons. The Coulomb interactions alone have been studied with RG and many other methods on honeycomb lattices in a number of works (e.g. Refs. [55, 57, 59, 68, 69, 194]). In particular, quantum Monte Carlo calculations [50, 70, 71] have firmly established that the ground state for pure onsite repulsions becomes an antiferromagnetic spin-density-wave state when the Hubbard- $U$  exceeds a threshold value. For interactions that extend further in space, only less controlled techniques are applicable. RG and saddle-point calculations [59] found that charge-density wave states and interaction-induced quantum spin Hall states are relevant competitors, depending on the profile of the effective interaction and the employed truncation scheme [68, 69]. Adding phonons to this interplay of the electronic ordering tendencies shifts the balance toward the SDW, while the competing QSH channel gets weakened. Interestingly, the bond phonons considered in the work actually increase the SDW and also potential CDW ordering tendencies. This can be seen most clearly in the lowering of the threshold value for the Hubbard interaction  $U$  to change the semi-metal into the SDW state when the electron-phonon interaction is turned on. For the QSH state we found the reversed

trend, indicating a destructive interplay with the phonons. Furthermore recent fRG studies with improved momentum resolution showed that the QSH is also suppressed by the appearance of more complex charge density wave states [68,69]. These works imply that our results might not have been converged yet. In this context it would be interesting to reinvestigate the interplay of the newly appearing charge density waves with phonon degrees of freedom and see if the trend that density waves are supported is confirmed.

Hence, one important upshot of our study is the identification of the most relevant phonon-mediated effects on the ground state. Based on our study, we do not expect that the nature of potential ground state ordering or, more realistically according to the experimental state in single-layer graphene, the nature of the leading correlations if the overall interaction strength is insufficient to gap the semimetal, is determined by a phonon-mediated instability. However, we have shown that the phonon sector may actually shift the phase boundaries between different electronically-driven ordering tendencies. Hence, phonon effects may yet play an important role in deciding which of these channels wins. We can also try to extrapolate our results for the single-layer honeycomb lattice to multi-layer graphene, where experiments indeed show that the semimetal gives way to an ordered state at low temperatures which is gapped [195,196] or shows a non-gapped spectrum reconstruction [197]. Previous RG studies for electronic interactions in bilayer graphene in fact find a nematic state as leading instability [198–203]. From our theoretical experience with multi-layer honeycomb systems [182,183] we can state that the main ordering tendencies are still the ones of the single layer, while the stacking only modifies the available density of states at low scales. Then, we should expect that in the multi-layer system, the phonon degrees of freedom have a similar influence in modifying the interplay of the electronic ordering tendencies as we find here. This makes the SDW state a more robust candidate to explain the observed gaps. Notably, even though the SDW state does not feature spin-resolved edge states like the QSH state, it may still be useful resource for nano-spintronic devices when the multilayer system is slightly doped and gated [204].

## CHAPTER 4

---

### Competition of Density Waves and Quantum Multicritical Behavior in Dirac Materials

---

#### 4.1. The Multicritical Point Between Charge and Spin Density Waves in Dirac Materials

The honeycomb lattice of graphene, studied in the previous chapter, belongs to a larger class of related materials in which low-energy Dirac-like excitations are responsible for common properties. As in graphene by increasing repulsive onsite or nearest-neighbor density-density interactions, these systems are expected to exhibit a continuous quantum phase transition from the semimetallic phase into spin-density-wave and charge-density-wave phases, respectively [58, 64–66]. In the general introduction, we pointed out that the experimental findings together with the *ab initio* parameters suggest that graphene is close, but somewhat below the critical values for the formation of one of these ordered states, cf. Fig. 4.1. This motivates a consideration of circumstances under which Dirac materials in general could be driven through a quantum phase transition by tuning of external parameters.

Despite the great progress in the last years, our theoretical understanding of the role of interactions in Dirac materials is far from being complete. In fact, QMC simulations typically suffer from a sign problem when nonlocal interaction parameters grow large, inducing a strong bias toward the antiferromagnetic state [205]. Fermionic renormalization group approaches have provided important contributions to the understanding of interacting electrons in Dirac materials accounting for further-ranged interactions on equal footing [55–57, 67, 125]. These approaches are well-suited for the identification of the ordering tendencies and their classification by symmetries. However, the purely fermionic approach typically misses important order-parameter fluctuations and the description of symmetry-broken regimes in the phase diagram is intricate<sup>1</sup>. An inclusion of order-parameter fluctuations aiming at more quantitative studies of the phase transitions and their critical behavior in Dirac materials can be achieved within bosonized approaches [207, 208] that also allow to describe the symmetry-broken regime. In this spirit, the SDW and CDW transitions have been investigated, however, only as completely separate transitions [58, 66, 145, 209–213].

Here, we take the vicinity of graphene and related materials to both the SDW and the CDW

---

<sup>1</sup>See, however, [15, 206] for recent developments

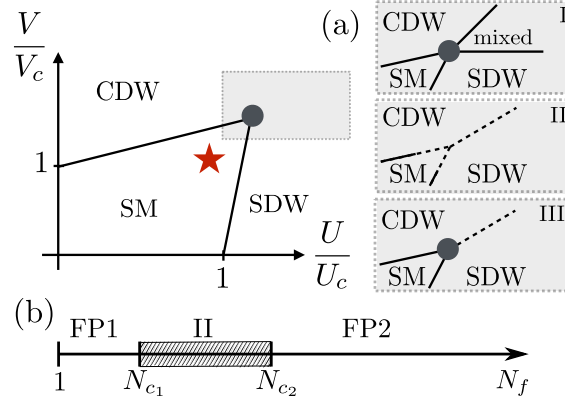


Figure 4.1.: (a) Schematic phase diagram of the extended Hubbard model on the honeycomb lattice with onsite interaction  $U$  and nearest-neighbor interaction  $V$ . Neutral suspended graphene is found to be in the semimetallic state indicated by the star. Solid lines denote second-order and dashed lines first-order transitions. The neighborhood of the multicritical point (gray shaded area) may be governed by either a (I) second-order tetracritical point or a (III) second-order bicritical point with first-order transition between the ordered states or by a (II) first-order triple point. (b) Sketch of stability ranges of fixed points for generalized fermion flavor number  $N_f$ . Two different fixed points FP1 and FP2 dominate for small and large  $N_f$ , respectively. Graphene lies in the hatched region, where no admissible fixed point exists. This leads to a first-order triple point in the phase diagram [situation (II)]. The critical flavor numbers  $N_{c_i}$  change considerably when including nonperturbative effects. In our approximation we find  $N_{c_1} = 1.6$  and  $N_{c_2} = 3.6$ .

ordered states as a motivation to study the nature of the quantum multicritical point connected to the intersection of the different phase transition lines. As we have seen in Sec. 2.1.2 and Sec. 2.3.2, the study of the multicritical point can be expected to reveal fascinating details of the phase diagram of Dirac materials, in particular, whether first-order or continuous phase transitions appear as a result of the competition of order parameters and whether there can be a coexistence of two ordered phases. In principle, we can distinguish three different possibilities for the multicritical point: we can have either (I) a second-order tetracritical point, allowing for the coexistence of the two ordered states, or (II) a triple point at which all transitions become first order, or (III) a second-order bicritical point with first-order transitions between the ordered states. A sketch of the phase diagram together with the three possible behaviors near the multicritical point is depicted in Fig. 4.1(a).

For graphene and related materials multicritical behavior has previously been studied in different contexts using the  $\epsilon$  expansion to first order, with  $\epsilon$  being the distance from the upper critical space-time dimension of four [75, 76]. Concerning the multicritical behavior and competition of CDW and SDW orders, we perform a corresponding study using an effective Gross-Neveu-Yukawa model with two coupled order parameters. We consider a generalized theory of this type with an arbitrary number of fermion flavors  $N_f$ . The  $SO(3)$  order parameter describes the antiferromagnetic transition and the  $\mathbb{Z}_2$  order parameter describes the transition to a staggered density state. Their coupling induces multicritical behavior which determines the structure of the phase diagram close to the multicritical point [8]. To first order in  $\epsilon$ , we find that a rather complex picture emerges as a function of the fermion “flavor” number  $N_f$ , i.e. the number of Dirac fermions. The graphene case,  $N_f = 2$ , appears to be dominated by a second-order tetracritical point [situation (I) in Fig. 4.1] with the universal behavior

being in the same universality class as the SM-SDW transition, i.e., the “chiral Heisenberg” universality class [145]. The first-order  $\epsilon$  expansion is a formidable tool to detect and discover the qualitative aspects of these systems. It may, however, be subject to considerable quantitative corrections when including higher orders [214, 215]. Furthermore, the convergence properties of the asymptotic series related to this type of expansion are *a priori* not clear, in particular when  $\epsilon$  becomes of order one.

Therefore we improve the precision of the qualitative investigation in terms of the  $\epsilon$ -expansion by employing the functional renormalization group. In the context of multicritical behavior of bosonic systems with  $O(N_1) \oplus O(N_2)$  symmetry, the significant quantitative improvement of the FRG approach as compared to the first-order  $\epsilon$  expansion has been explicitly demonstrated [11, 12].

Employing the FRG, we are able to confirm the qualitative picture from the  $\epsilon$ -expansion results. However, large quantitative modifications appear concerning the stability of the various fixed points as a function of  $N_f$ , with severe implications for the phase diagram in the graphene case,  $N_f = 2$ . Here the notion stability refers to the number of tuning parameters needed to access a fixed point. In the considered case of competing CDW and SDW order, two such tuning parameters are available: the strength of on-site and nearest-neighbor interaction. We find that:

- (1) For small number of fermion flavors,  $N_f < 1.6$ , the decoupled fixed point related to the antiferromagnetic transition (“chiral Heisenberg” universality class) is stable.
- (2) For intermediate fermion flavor numbers,  $1.6 < N_f < 3.6$ , including the graphene case  $N_f = 2$ , there is no admissible stable fixed point, suggesting a triple point and corresponding first-order transitions.
- (3) For large number of flavors,  $N_f > 3.6$ , we rediscover a novel stable fixed point with nontrivial interactions between the different sectors, found previously in the  $\epsilon$  expansion.

Our results concerning the ranges of stable fixed points are sketched in Fig. 4.1(b). In the case where stable fixed points exist, we furthermore study the critical behavior in detail by investigating critical exponents and anomalous dimensions.

The rest of the chapter is organized as follows: In the next section we introduce our effective model, which couples the fermionic and bosonic degrees of freedom that become dominant in the vicinity of the multicritical point. We start the investigation by analyzing the inherited fixed points that we expect from the separate transitions in Sec. 4.3. We then compute the fixed-point structure as a function of  $N_f$  within first-order  $\epsilon$  expansion in Sec. 4.4. We discuss the resulting phase diagram and briefly give concluding remarks. In Sec. 4.5 we present the FRG truncation that we use to subsequently determine the more precise fixed-point structure and the concomitant critical behavior as function of space-time dimension and fermion flavor number  $N_f$ . We also compare various limits to literature results. In the limit of large  $N_f$  we are able to present an analytic solution of the flow equations, including the full form of the fixed-point potential. The implications from the fRG calculation for the nature of the phase diagram are studied in Sec. 4.5.5 and we draw our conclusions in Sec. 4.6.



## 4.2. Effective Dirac Description

### Free Theory

From the lattice description above we can derive an effective description in terms of Dirac fermions. Retaining the Fourier modes near  $\mathbf{K}, \mathbf{K}'$  only, the low-energy model of the free electrons at temperature  $T = 0$  can be written as a relativistic Dirac field theory in the continuum [55]

$$S_F = \int d\tau dx^{D-1} [\bar{\Psi} (\mathbb{1}_2 \otimes \gamma_\mu) \partial_\mu \Psi], \quad (4.1)$$

with space-time index  $\mu = 0, \dots, D-1$  and the  $D$ -dimensional derivative  $\partial_\mu = (\partial_\tau, \nabla)$ . The  $(4 \times 4)$  gamma matrices obey the Euclidian Clifford algebra  $\{\gamma_\mu, \gamma_\nu\} = 2\delta_{\mu\nu}$ . In  $D = 2 + 1$  dimensions they are explicitly represented by  $\gamma_0 = \mathbb{1}_2 \otimes \sigma_z$ ,  $\gamma_1 = \sigma_z \otimes \sigma_y$ ,  $\gamma_2 = \mathbb{1}_2 \otimes \sigma_x$ . In this frame the spin- $\frac{1}{2}$  electrons and holes are described by an 8-component Dirac fermion  $\Psi = (\Psi_\uparrow, \Psi_\downarrow)^T$  and its conjugate  $\bar{\Psi} = \Psi^\dagger (\mathbb{1}_2 \otimes \gamma_0)$ . The Dirac field  $\Psi$  is related to the Grassmann fields  $c_{A/B,k,s} \equiv c_{A/B,s}(k)$  (cf. Eq. (3.2)) by

$$\Psi_s^\dagger(\mathbf{x}, \tau) = \int \frac{d\omega d^{D-1}\mathbf{q}}{(2\pi)^D} e^{i\omega\tau + i\mathbf{q}\cdot\mathbf{x}} [c_{A,s}^\dagger(\mathbf{K} + \mathbf{q}, \omega), c_{B,s}^\dagger(\mathbf{K} + \mathbf{q}, \omega), c_{A,s}^\dagger(-\mathbf{K} + \mathbf{q}, \omega), c_{B,s}^\dagger(-\mathbf{K} + \mathbf{q}, \omega)] \quad (4.2)$$

We can define two additional  $(4 \times 4)$  matrices that anticommute with all  $\gamma_\mu$ :  $\gamma_3 = \sigma_x \otimes \sigma_y$  and  $\gamma_5 = \sigma_y \otimes \sigma_y$ . Their product  $\gamma_{35} = -i\gamma_3\gamma_5$  commutes with all  $\gamma_\mu$ , while it anticommutes with  $\gamma_3$  and  $\gamma_5$ .

Although we started here from the graphene case, the low-energy Dirac description Eq. (4.1) is valid for a broader class of materials as it represents general Dirac excitations and is not reminiscent of its microscopic origin.

### Bosozined Interactions in Effective Dirac Description

To describe the multicritical point in the phase diagram we introduce bosonic degrees of freedom related to the SDW and CDW fluctuations. These can be written in terms of the order-parameter fields [47, 55]

$$\Phi = (\chi, \phi) = (\langle \bar{\Psi} \Psi \rangle, \langle \bar{\Psi} (\sigma \otimes \mathbb{1}_4) \Psi \rangle), \quad (4.3)$$

which can also be understood as order parameters for the various possible chiral symmetries [216].

Another very interesting set of order parameters, with possibly the *same* quantum critical behavior [58], is given by

$$\tilde{\Phi} = (\tilde{\chi}, \tilde{\phi}) = (\langle \bar{\Psi} \gamma_{35} \Psi \rangle, \langle \bar{\Psi} (\sigma \otimes \gamma_{35}) \Psi \rangle). \quad (4.4)$$

These can be related to the much-discussed Quantum Anomalous and Quantum Spin Hall states [217], and may also be relevant in the phase diagram of Dirac materials [59]. Note that  $\tilde{\Phi}$ 's zeroth component  $\tilde{\chi}$  breaks the time-reversal symmetry, defined by the time-reversal operator [56]

$$T = (\sigma_y \otimes i\gamma_1\gamma_5)K, \quad (4.5)$$



where  $K$  denotes complex conjugation, while its spatial part  $\tilde{\phi}$  breaks the  $SU(2)$  spin-rotational symmetry but respects time-reversal symmetry. In the following, we will focus on a condensation of the chiral order parameters  $\chi$  and  $\phi$  only, cf. Eq. (4.3), and assume that the fields  $\tilde{\chi}$  and  $\tilde{\phi}$  are sufficiently massive so that their fluctuations become subdominant.

The spin-singlet Ising field  $\chi \propto c_{A,s}^\dagger c_{A,s} - c_{B,s}^\dagger c_{B,s}$  characterizes the staggered density phase, i.e., the CDW state, whereas the Heisenberg triplet  $\phi \propto c_{A,s}^\dagger \sigma_{ss'} c_{A,s'} - c_{B,s}^\dagger \sigma_{ss'} c_{B,s'}$  corresponds to the antiferromagnetic SDW state. Near the putative transitions into the CDW and SDW states the fluctuations of the corresponding order parameters play a decisive role. We incorporate their dynamics in the bosonic action

$$S_B = \int d\tau dx^{D-1} \left[ \frac{1}{2} \chi (-\partial_\mu^2 + m_\chi^2) \chi + \frac{1}{2} \phi (-\partial_\mu^2 + m_\phi^2) \phi + \lambda_\chi \chi^4 + \lambda_\phi (\phi^2)^2 + \lambda_{\chi\phi} \chi^2 \phi^2 \right], \quad (4.6)$$

where we also allow for a coupling  $\lambda_{\chi\phi}$  between the two order parameters.<sup>2</sup> This semi-phenomenological ansatz is crucial to capture the critical behavior of the low-energy fermions interacting with self-generated charge- and spin-density-waves. The dynamical parts and the couplings  $\lambda_{i,j}$ , initially absent after a Hubbard-Stratonovich decoupling, will develop below some energy scale, indicating that the fluctuations in the corresponding particle-hole channel become relevant degrees of freedom. Finally, fermions and composite bosons are coupled in terms of the Yukawa interactions

$$S_Y = \int d\tau dx^{D-1} \left[ g_\chi \chi \bar{\Psi} (\mathbb{1}_2 \otimes \mathbb{1}_4) \Psi + g_\phi \phi \bar{\Psi} (\sigma \otimes \mathbb{1}_4) \Psi \right].$$

The complete action  $S$  is then given by

$$S = S_F + S_B + S_Y, \quad (4.7)$$

which respects Lorentz, spin-rotational, time-reversal and sublattice-exchange symmetry. The ordered phases are characterized by a finite expectation value of one or both bosonic fields, leading to the spontaneous breaking of the spin-rotational or sublattice-exchange symmetry.

### Generalized Fermion Flavors

In the following, it will prove useful to consider an arbitrary number  $N_f$  of Dirac points in the spectrum, implemented by the replacement

$$\bar{\Psi} (\sigma \otimes \mathbb{1}_4) \Psi \mapsto \bar{\Psi} (\sigma \otimes \mathbb{1}_{2N_f}) \Psi, \quad (4.8)$$

$$\bar{\Psi} (\mathbb{1}_2 \otimes \mathbb{1}_4) \Psi \mapsto \bar{\Psi} (\mathbb{1}_2 \otimes \mathbb{1}_{2N_f}) \Psi, \quad (4.9)$$

where  $\Psi$  and  $\bar{\Psi}$  now have  $2N_f$  components *for each spin projection*. We will refer to  $N_f$  as the fermion “flavor” number, with  $N_f = 2$  for graphene. Let us note that the explicit implementation of the flavor number is not important. To derive the results, only the Clifford algebra and the product  $d_\gamma N_f$  is needed, where  $d_\gamma$  denotes the dimension of the gamma matrices. We will also consider general space-time dimension  $2 < D < 4$ , with an eye on the physical  $D = 2 + 1$ .

<sup>2</sup>In Sec. 4.5.1 we will slightly change the notation for the truncation of the fRG calculation. The bosonic self-interaction terms will then be of the form  $S_B^{(4)} = \frac{1}{8} \lambda_{2,0} \chi^4 + \frac{1}{8} \lambda_{0,2} (\phi^2)^2 + \frac{1}{4} \lambda_{1,1} \chi^2 \phi^2$  (cf. Eq. (4.44))

### 4.3. Classification of Fixed Points

As pointed out above, we are interested in the stable fixed points of the system, governing the quantum multicritical behavior of its phase diagram. We call a fixed point stable if it has only two relevant directions, i.e. not more than two positive critical exponents (cf. Sec. 2.3.2). In this case, we can reach the fixed point by tuning two parameters corresponding to the interactions  $U$  and  $V$  in Eq. (3.3), or the masses  $m_\chi^2$  and  $m_\phi^2$  in the bosonized description, Eq. (4.7). In addition, unitarity requires real Yukawa couplings  $g_{\chi,*}, g_{\phi,*} \in \mathbb{R}$ , and the action has to be bounded from below, i.e.,  $\lambda_\chi^*, \lambda_\phi^* \geq 0$  and  $\lambda_{\chi\phi}^* > -2\sqrt{\lambda_\chi^* \lambda_\phi^*}$ . Here and below we denote the fixed point values with asterisks.

The model incorporates the separate SM-to-SDW and the SM-to-CDW transitions described by the chiral Ising and chiral Heisenberg universality classes, respectively, as well as a purely bosonic model with a  $O(1) \oplus O(3)$ . Just as in such bosonic models, we can deduce the existence of some of the appearing fixed points and critical properties from symmetry considerations and from the limiting cases of the separate models [11, 66]:

- (1) The bosonic system, when the fermions completely decouple, i.e.,  $g_{\chi,*}^2 = 0$  and  $g_{\phi,*}^2 = 0$ , which puts the fermionic sector at its Gaussian fixed point. For the remaining bosonic sector there are three possible fixed points of the  $O(1) \oplus O(3)$  model: the decoupled, the isotropic and the biconical one.
- (2) The chiral Ising sector with the Ising field  $\chi$  at its nontrivial fermionic fixed point  $g_{\chi,*}^2 \neq 0$ , and with the fermions decoupled from the Heisenberg field  $\phi$ ,  $g_{\phi,*}^2 = 0$ , which is then either at its bosonic Gaussian or Wilson-Fisher (Heisenberg) fixed point. The latter will be called “chiral Ising plus Heisenberg” (cI+H) fixed point in the following.
- (3) The chiral Heisenberg sector with the Heisenberg field  $\phi$  at its nontrivial fermionic fixed point  $g_{\phi,*}^2 \neq 0$ , and with the fermions decoupled from the Ising field  $\chi$ ,  $g_{\chi,*}^2 = 0$ , which is then either at its bosonic Gaussian or Wilson-Fisher (Ising) fixed point. The latter will be called “chiral Heisenberg plus Ising” (cH+I) fixed point.

Regarding the stability of these fixed points, we can infer the following: Every fixed point of the separate sectors will have one relevant direction related to its mass parameter. The chiral Heisenberg and the chiral Ising fixed point do not show further relevant directions in the individual, uncoupled systems [66]. In contrast, the Wilson-Fisher fixed point of the uncoupled sector  $i$  ( $i \in \{\chi, \phi\}$ ), specified by  $g_i^{2*} = 0$ , features one additional relevant direction corresponding to the Yukawa coupling. But upon coupling this sector to the second bosonic field, this direction may or may not become irrelevant. Thus, the cI+H and the cH+I are the most promising candidates for stable fixed points. Due to the Yukawa couplings being relevant below four space-time dimensions, the purely bosonic fixed points are unlikely to become stable by the coupling of both systems.

This general expectation will indeed be confirmed in the first-order  $\epsilon$ -expansion study of the coupled model, in which the cH+I fixed point will appear stable in the case of graphene ( $N_f = 2$ ). On the other hand, for large  $N_f$  a novel fixed point with both Yukawa interactions  $g_{\chi,*}^2 \neq 0$  and  $g_{\phi,*}^2 \neq 0$  will become stable. A third option, which we will also encounter, is that there is no stable fixed point at all. In this case the flow does not exhibit scale-invariant behavior and the phase diagram close to the intersection of the various phases (SM, SDW and CDW) is governed by a triple point with first-order transitions.

## 4.4. Multicritical Behavior from the $\epsilon$ -Expansion

### 4.4.1. Flow Equations and Fixed Points

For the above action  $S$  and at zero temperature we can calculate the renormalization group equations in the Wilsonian scheme explained in Sec. 2.2. We simultaneously integrate out the fermionic as well as the bosonic modes within the narrow momentum shell  $\Lambda/b < (\omega^2 + \vec{q}^2) < \Lambda$ . At one-loop order in  $D = 4 - \epsilon$  dimensions we find the following equations for the two Yukawa couplings

$$\frac{dg_\chi^2}{d \ln b} = \epsilon g_\chi^2 - (3 + 2N_f)g_\chi^4 - 9g_\chi^2 g_\phi^2, \quad (4.10)$$

$$\frac{dg_\phi^2}{d \ln b} = \epsilon g_\phi^2 - (1 + 2N_f)g_\phi^4 - 3g_\chi^2 g_\phi^2, \quad (4.11)$$

where we have rescaled  $g_i^2 \rightarrow g_i^2/(8\pi^2\Lambda^\epsilon)$ . Additionally, in the  $\epsilon$  expansion we obtain RG flow equations for the bosonic masses  $m_\chi^2, m_\phi^2$  and the bosonic couplings  $\lambda_\chi, \lambda_\phi, \lambda_{\chi\phi}$  that will be displayed below. The fixed points of this set of equations and their surrounding will determine the properties of the multicritical point.

The flow in the  $g_\phi^2$ - $g_\chi^2$  plane decouples from the bosonic flow equations, and analytical solutions of the zeros of the Yukawa-coupling beta functions  $\{\beta_{g_\chi^2}, \beta_{g_\phi^2}\}$  can be readily displayed. We find the values

$$\text{A: } g_\chi^{2,*} = 0, \quad g_\phi^{2,*} = 0, \quad (4.12)$$

$$\text{B: } g_\chi^{2,*} = 0, \quad g_\phi^{2,*} = \frac{\epsilon}{1 + 2N_f}, \quad (4.13)$$

$$\text{C: } g_\chi^{2,*} = \frac{\epsilon}{3 + 2N_f}, \quad g_\phi^{2,*} = 0, \quad (4.14)$$

$$\text{D: } g_\chi^{2,*} = \frac{\frac{1}{2}(N_f - 4)\epsilon}{N_f^2 + 2N_f - 6}, \quad g_\phi^{2,*} = \frac{\frac{1}{2}N_f\epsilon}{N_f^2 + 2N_f - 6}. \quad (4.15)$$

We illustrate the flow and fixed-point structure in the  $g_\phi^2$ - $g_\chi^2$  plane for different values of  $N_f$  in Fig. 4.2. Let us emphasize, however, that the zeros A, B, C, and D, in order to represent true fixed points of the full system, need to be supplemented with suitable (and physically admissible) fixed-point values in the bosonic sector. In terms of the rescaled bosonic couplings  $\{\lambda_\chi, \lambda_\phi, \lambda_{\chi\phi}\} \rightarrow \{\lambda_\chi/(8\pi^2\Lambda^\epsilon), \lambda_\phi/(8\pi^2\Lambda^\epsilon), \lambda_{\chi\phi}/(8\pi^2\Lambda^\epsilon)\}$  the  $\beta$  functions in the bosonic sector read

$$\frac{d\lambda_\chi}{d \ln b} = \epsilon \lambda_\chi - 36\lambda_\chi^2 - 3\lambda_{\phi\chi}^2 - 4N_f \lambda_\chi g_\chi^2 + N_f g_\chi^4, \quad (4.16)$$

$$\frac{d\lambda_\phi}{d \ln b} = \epsilon \lambda_\phi - 44\lambda_\phi^2 - \lambda_{\phi\chi}^2 - 4N_f \lambda_\phi g_\phi^2 + N_f g_\phi^4, \quad (4.17)$$

$$\frac{d\lambda_{\phi\chi}}{d \ln b} = \epsilon \lambda_{\phi\chi} - 8\lambda_{\phi\chi}^2 - 20\lambda_\phi \lambda_{\phi\chi} - 12\lambda_\chi \lambda_{\phi\chi} - 2N_f \lambda_{\phi\chi} g_\phi^2 - 2N_f \lambda_{\phi\chi} g_\chi^2 + 6N_f g_\chi^2 g_\phi^2, \quad (4.18)$$

and

$$\frac{dm_\chi^2}{d \ln b} = 2(1 - N_f g_\chi^2)m_\chi^2 + 12\lambda_\chi(1 - m_\chi^2) + 6\lambda_{\phi\chi}(1 - m_\phi^2) - 4N_f g_\chi^2, \quad (4.19)$$

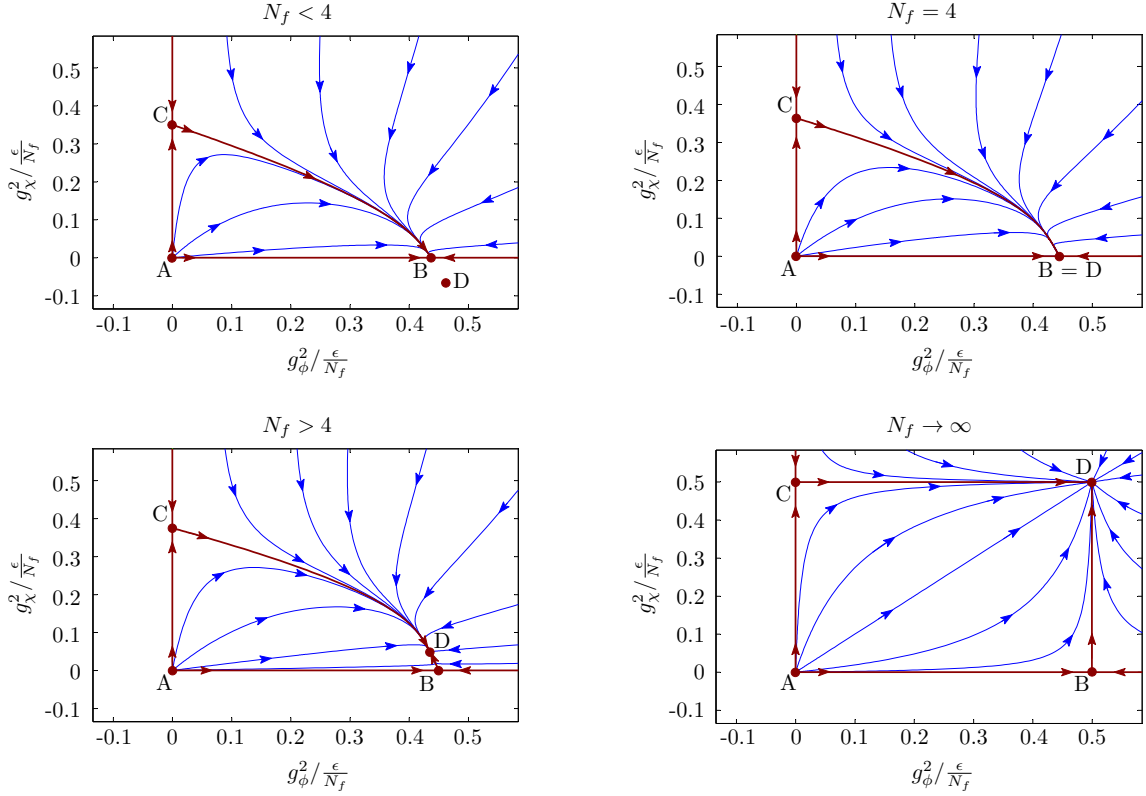


Figure 4.2.: RG flow and fixed-point structure in the Yukawa-coupling subsector for different values of  $N_f$  below, at, and above the critical value of  $N_f = 4$ . For  $N_f < 4$  fixed point B is stable within this subsector, while fixed point D is located in the unphysical domain  $g_\chi^2 < 0$  (top left). At  $N_f = 4$ , D becomes physical and collides with B (top right), and subsequently exchanges stability with the latter for  $N_f > 4$  (bottom left). For  $N_f \rightarrow \infty$  the stable fixed point D is located at  $g_\phi^{*2} = g_\chi^{*2}$  (bottom right). Note that A, B, C, and D may be true (and possibly stable) fixed points of the full system only if suitable corresponding zeros of the bosonic beta functions can be found, see text.

$$\frac{dm_\phi^2}{d \ln b} = 2(1 - N_f g_\phi^2) m_\phi^2 + 20 \lambda_\phi (1 - m_\phi^2) + 2 \lambda_{\phi\chi} (1 - m_\chi^2) - 4 N_f g_\phi^2. \quad (4.20)$$

For a fixed point A, B, C or D to be physically admissible it has to satisfy the conditions explained in Sec. 4.3. We hence classify the fixed points according to their number of relevant directions, i.e., their number of positive eigenvalues of the stability matrix. For the fully Gaussian fixed point A, we find that the Yukawa couplings already provide two additional relevant directions with eigenvalues  $\epsilon$  for any  $N_f$ . Thus in the following it will be discarded in our discussion.

Fixed point B leads to the least number of relevant directions in the full system when supplemented with the bosonic couplings

$$\lambda_\chi^* = \frac{\epsilon}{36}, \quad \lambda_{\phi\chi}^* = 0, \quad (4.21)$$

$$\lambda_\phi^* = \frac{1 - 2N_f + \sqrt{1 + 4N_f(43 + N_f)}}{88(2N_f + 1)} \epsilon, \quad (4.22)$$

which, in fact, means that the order parameters  $\phi$  and  $\chi$  decouple at B, with the Heisenberg field at its fermionic *chiral* fixed point, and the Ising field at the purely bosonic (standard) Ising fixed point. We thus denote fixed point B also as “chiral Heisenberg plus Ising” (cH+I) fixed point. Its critical exponents are

$$\theta_1 = 2 - \frac{\epsilon}{3}, \quad (4.23)$$

$$\theta_2 = 2 - \frac{5 + 34N_f + 5\sqrt{1 + 4N_f(43 + N_f)}}{22(2N_f + 1)}\epsilon, \quad (4.24)$$

$$\theta_3 = \frac{N_f - 4}{N_f + \frac{1}{2}}\epsilon. \quad (4.25)$$

For the physical situation with  $N_f = 2$  we obtain  $\{\theta_1, \theta_2, \theta_3\} = \{2 - \frac{\epsilon}{3}, 2 - \frac{84\epsilon}{55}, -\frac{4\epsilon}{5}\}$ , rendering the cH+I fixed point stable as  $\theta_3 < 0$ . The situation changes upon increasing the value of  $N_f$ , cf. Fig. 4.2. For  $N_f = 4$ , B collides with another fixed point D, with which it exchanges stability for  $N_f > 4$ . For  $N_f > 4$  the cH+I fixed point thus becomes unstable. The scenario is similar to the well-known situation in the purely bosonic  $O(N)$  models, in which the Wilson-Fisher fixed point approaches the Gaussian fixed point when the dimension is increased towards the upper critical dimension, and subsequently exchanges stability with the latter.

Fixed point C, when completed with the bosonic fixed-point values

$$\lambda_\chi^* = \frac{3 - 2N_f + \sqrt{9 + 4N_f(33 + N_f)}}{72(3 + 2N_f)}\epsilon, \quad (4.26)$$

$$\lambda_\phi^* = \frac{\epsilon}{44}, \quad \lambda_{\phi\chi}^* = 0, \quad (4.27)$$

could then, within our nomenclature, be termed “chiral Ising plus Heisenberg” (cI+H) fixed point. It has *three* relevant directions for all admissible choices of  $N_f$  and  $\epsilon$ ,

$$\theta_1 = 2 - \frac{5\epsilon}{11}, \quad (4.28)$$

$$\theta_2 = 2 - \frac{3 + 10N_f + \sqrt{9 + 4N_f(33 + N_f)}}{6(3 + 2N_f)}\epsilon, \quad (4.29)$$

$$\theta_3 = \frac{2N_f}{3 + 2N_f}\epsilon, \quad (4.30)$$

and is thus never stable. Its critical exponents and anomalous dimensions for the physical case  $N_f = 2$  are listed together with the those of fixed point B in Table 4.1.

For the mixed fixed point D the computation of the bosonic fixed-point values  $\lambda_i^*$  is slightly more involved, but can readily be done numerically. The bosonic fixed-point couplings lead to a quite intriguing behavior as a function of  $N_f$ , as displayed in Fig. 4.3. First, we observe that there are two ranges of  $N_f$  where no real fixed-point values in the bosonic sector can be found for the given values of  $g_\phi^{*2}$  and  $g_\chi^{*2}$  [Eq. (4.15)]. The first range covers small  $N_f \lesssim 3.8$  and the second range is  $N_f \in [4.7, 15.7]$ . These intervals are indicated in Fig. 4.3 by the gray-shaded areas. In the narrow range  $N_f \in [3.8, 4.7]$  the solution for fixed point D is physically admissible only for  $N_f \geq 4$ , since  $g_\chi^2 < 0$  for  $N_f < 4$ . For  $N_f = 4$  the fixed points B and D collide and exchange stability, so that for  $4.7 > N_f \geq 4$  the fixed point D is stable. For  $15.7 \lesssim N_f \lesssim 16.6$ , while corresponding real fixed-point values can now be found, the solution for fixed point

Table 4.1.: The largest three critical exponents and anomalous dimensions for fixed points B and C in first order  $\epsilon$  expansion for the physical choice  $N_f = 2$ . Here, fixed point B (“chiral Heisenberg plus Ising” fixed point) is stable and thus governs the multicritical behavior. In the decoupled bosonic sector the anomalous dimension vanishes as it is of  $\mathcal{O}(\epsilon^2)$ .

	$\theta_1$	$\theta_2$	$\theta_3$	$\eta_\phi$	$\eta_\chi$	$\eta_\psi$
B (cH+I)	$2 - \frac{1}{3}\epsilon$	$2 - \frac{84}{55}\epsilon$	$-\frac{4}{5}\epsilon$	$\frac{4}{5}\epsilon$	0	$\frac{3}{10}\epsilon$
C (cI+H)	$2 - \frac{5}{11}\epsilon$	$2 - \frac{20}{21}\epsilon$	$\frac{4}{7}\epsilon$	0	$\frac{4}{7}\epsilon$	$\frac{1}{14}\epsilon$

D remains unphysical, since  $\lambda_\chi < 0$  (see Fig. 4.3). Finally, for  $N_f \gtrsim 16.6$  the fixed point D constitutes a physically admissible solution with negative exponent  $\theta_3$ , i.e., it is the stable fixed point. We have checked that between  $N_f = 4$  and  $N_f = 16$  no other real and stable solution exists in our approximation scheme. In the limit of large  $N_f$ , we find

$$g_\chi^{2,*} = g_\phi^{2,*} = \frac{\epsilon}{2N_f}, \quad (4.31)$$

and we obtain a stable fixed point in agreement with the large- $N_f$  calculation [55]. It has the bosonic coupling coordinates

$$\lambda_\chi^* = \lambda_\phi^* = \frac{\epsilon}{4N_f}, \quad \lambda_{\phi\chi}^* = \frac{3\epsilon}{2N_f}. \quad (4.32)$$

#### 4.4.2. Phase Diagram

We have seen in Sec. 2.1.2 that an important quantity to classify the critical behavior of a multicritical point is the parameter  $\Delta$ ,

$$\Delta = 4\lambda_\chi\lambda_\phi - \lambda_{\phi\chi}^2, \quad (4.33)$$

with  $\lambda_\chi, \lambda_\phi$  and  $\lambda_{\phi\chi}$  being the boson couplings of the effective infrared theory. The sign of  $\Delta$  determines the nature of the multicritical point, i.e., whether it is bicritical or tetracritical. When  $\Delta \leq 0$  the transition line between the two ordered phases is expected to be of first order, whereas for  $\Delta > 0$  coexistence of the two orders is expected with second order transitions between the four different regimes. We expect that the presence of Dirac fermions does not affect this argument, since it relies only on the consideration of the boson effective potential. If we start the RG flow near the stable fixed point, it remains in its vicinity for a long RG “time”. In this way, the direct neighborhood of the multicritical point in the phase diagram should depend only on the properties of the effective potential *at the fixed point*. To determine the behavior near the multicritical point, it then suffices to compute the value for  $\Delta$  using the fixed-point values for the quartic couplings. Eventually, of course, the system will flow away from the critical surface and the argument breaks down far from the multicritical point.

We identify three different regimes if we classify the nature of the multicritical point in terms of  $\Delta$ , cf. Fig. 4.4. For small fermion flavor number  $N_f \lesssim 4.64$ , including the graphene case  $N_f = 2$ , we find a positive  $\Delta$  at the stable fixed point. Here, tetracritical behavior dominates the phase transitions and a mixed phase appears with a coexistence of SDW and CDW order. In a large range of this regime  $1 \leq N_f \leq 4$ , the cH+I fixed point B with vanishing  $g_\chi^2$  is stable indicating that the properties at the multicritical point are dominated by the chiral Heisenberg

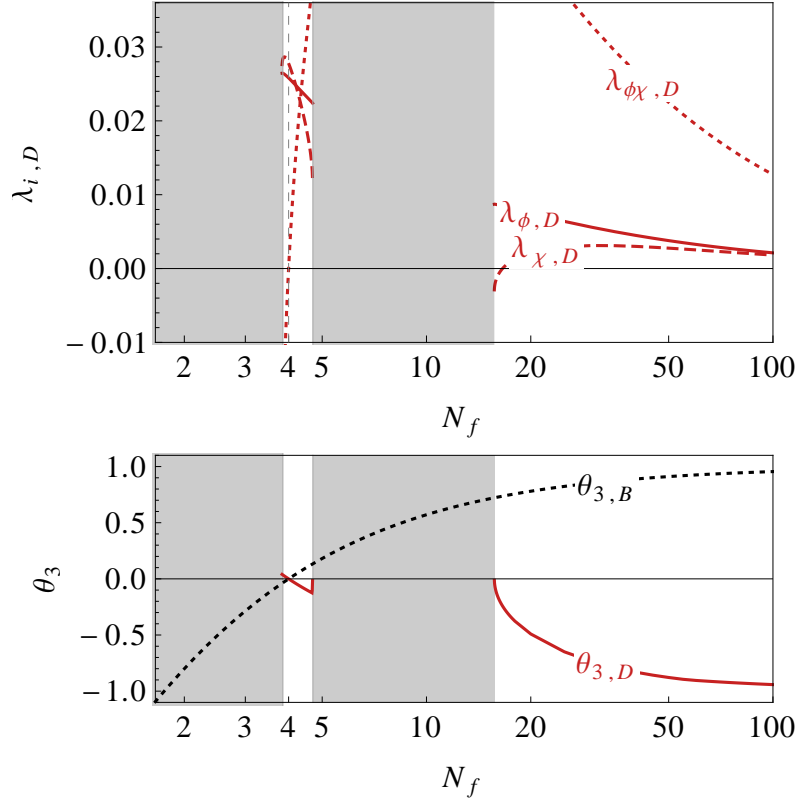


Figure 4.3.: (Top) Coordinates of the bosonic couplings at the fixed point D as a function of  $N_f$ . The gray areas indicate the ranges of  $N_f$  where fixed point D does not exist and no other stable fixed point exists. (Bottom) Third critical exponent as function of  $N_f$  for the two possible stable fixed points B and D.

universality class. This universality class also describes the transition from the semimetal to the antiferromagnetic state for increasing nearest-neighbor interaction. The stability suggests the continuation of this behavior up to the multicritical point. On the bosonic side of the transition the order parameters decouple, whereas they interact with each other if fixed point D becomes stable. The stability of fixed point D is accompanied by a negative  $\Delta$  for  $N_f \in (4.64, 4.7)$  and  $N_f > 16.6$ . In this regime the phase diagram exhibits bicritical behavior with continuous transitions between SM and SDW or CDW, respectively, and a first order line between SDW and CDW. The large- $N_f$  behavior is thus consistent with the previous  $1/N_f$  approaches [55]. The intermediate regime  $N_f \in (4.7, 16.6)$  is characterized by the absence of any stable fixed point. Here, the second order lines of the separate transitions from SM to SDW and CDW end in a discontinuous point and the transition from SDW to CDW is also of first order.

#### 4.4.3. Conclusion on $\epsilon$ -Expansion

In conclusion, we presented an effective description of the multicritical point between the semimetallic, the CDW and the SDW state on the honeycomb lattice that becomes exact near three spatial dimensions. A rather complex picture emerges as a function of the fermion flavor number, in which the graphene case appears dominated by the chiral Heisenberg universality class, at least to the present order of the  $\epsilon$  expansion. A tetracritical phase diagram with



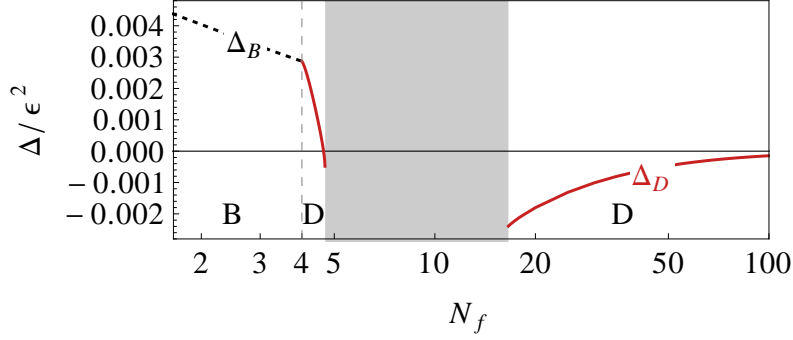


Figure 4.4.: Value of the parameter  $\Delta$  as a function of  $N_f$  for the stable fixed point, which governs the multicritical behavior in the phase diagram of Fig. 4.1(a). For  $N_f \leq 4$  the multicritical point is given by the chiral Heisenberg plus Ising fixed point (B) and it has positive  $\Delta > 0$ , corresponding to tetracritical behavior with a mixed CDW and SDW phase, as indicated in Fig. 4.1(b). For  $4 < N_f < 4.64$  the multicritical point is still tetracritical, but its long-range behavior defines a new universality class governed by fixed point D. For  $4.64 < N_f < 4.7$  the multicritical point is bicritical (see Fig. 4.1(c)). For  $4.7 < N_f < 16.6$  there is no physically admissible stable fixed point in the system and we expect the multicritical point to become discontinuous. For  $N_f > 16.6$  the multicritical behavior is again bicritical.

a coexistence phase of SDW and CDW is the consequence. In purely bosonic multicritical systems [8, 142], as well as in the separate Gross-Neveu-Yukawa models [66], the leading-order  $\epsilon$  expansion captures well the qualitative behavior of the systems. We expect this to hold for our model as well and, at the very least, our results should qualitatively correct describe the  $N_f$  dependence of the fixed-point structure in two spatial dimensions as appropriate for the description of graphene. However, the bare numbers of the critical  $N_f$  values at which the multicritical behavior of the system changes can possibly be reduced substantially if one went beyond the leading-order  $\epsilon$  expansion [214, 215] and more elaborate investigations may be needed to settle the true nature of the multicritical point in graphene's phase diagram. A promising complimentary approach to the critical  $N_f$  values is provided by a functional renormalization group study [11, 66] which allows to work directly in two spatial dimensions. This will be discussed in the next section.

## 4.5. FRG-Improved Calculation

### 4.5.1. Truncation and Flow Equations

We have seen in Sec. 2.2.2 that, while the Wetterich equation itself is an exact identity, it can usually not be solved exactly. In this section, we therefore use a scheme inspired by the derivative expansion, which we truncate after the leading order. Explicitly, we employ the following ansatz (the LPA' ansatz, cf. Sec. 2.2.2) for  $\Gamma_k$ ,

$$\begin{aligned} \Gamma_k = \int d^D x \Big( & Z_{\Psi,k} \bar{\Psi} (\mathbb{1}_2 \otimes \gamma_\mu) \partial_\mu \Psi - \frac{1}{2} Z_{\chi,k} \chi \partial_\mu^2 \chi - \frac{1}{2} Z_{\phi,k} \phi \partial_\mu^2 \phi + U_k(\bar{\rho}_\chi, \bar{\rho}_\phi) \\ & + \bar{g}_{\chi,k} \chi \bar{\Psi} (\mathbb{1}_2 \otimes \mathbb{1}_4) \Psi + \bar{g}_{\phi,k} \phi \bar{\Psi} (\sigma \otimes \mathbb{1}_4) \Psi \Big), \end{aligned} \quad (4.34)$$

which is a direct generalization of the quantitatively successful truncation used for the separate chiral Heisenberg and chiral Ising universality classes [66, 207, 208]. In the first line of Eq. (4.34),



we have introduced the kinetic part of the fermion fields, followed by the kinetic parts of the order-parameter fields. We assume scale-dependent, but field-independent wave-function renormalizations  $Z_{\Psi,k}$ ,  $Z_{\chi,k}$  and  $Z_{\phi,k}$ . In the second line, the Yukawa couplings also become scale-dependent quantities. The scale-dependent effective bosonic potential  $U_k$ , also appearing in the first line, only depends on the invariants  $\rho_\varphi = \frac{1}{2}\varphi^2$ ,  $\varphi \in \{\chi, \phi\}$ , as imposed by the symmetry of the original action, Eq. (4.7). For most purposes, we will in the following expand the effective potential about its scale-dependent minimum  $(\bar{\rho}_{\chi,\min}, \bar{\rho}_{\phi,\min})$ , the latter being either zero or positive, then describing a regime of spontaneously broken symmetry. In case a nonvanishing  $(\bar{\rho}_{i,\min})$  survives the integration towards the IR,  $k \rightarrow 0$ , it corresponds to a finite vacuum expectation value for the order-parameter fields  $\chi$  and/or  $\phi$ , i.e., an ordered phase.

## Flow Equations

**Effective Potential** In order to determine the scaling behavior of the effective action, we will consider dimensionless quantities in the following. Therefore, we define the dimensionless version of the effective potential

$$u(\rho_\chi, \rho_\phi) = k^{-d} U\left(\frac{k^{D-2}}{Z_{\chi,k}} \bar{\rho}_\chi, \frac{k^{D-2}}{Z_{\phi,k}} \bar{\rho}_\phi\right), \quad (4.35)$$

and the corresponding Yukawa couplings

$$g_{\chi/\phi}^2 = \frac{k^{D-4}}{Z_{\chi/\phi,k} Z_{\Psi,k}^2} \bar{g}_{\chi/\phi,k}^2. \quad (4.36)$$

We also define the anomalous dimensions

$$\eta_{\chi/\phi} = -\frac{\partial_t Z_{\chi/\phi,k}}{Z_{\chi/\phi,k}} \quad \text{and} \quad \eta_\Psi = -\frac{\partial_t Z_{\Psi,k}}{Z_{\Psi,k}}. \quad (4.37)$$

To obtain the flow equation for the dimensionless scale-dependent effective potential  $u$ , Eq. (2.30) is evaluated for constant bosonic fields  $\chi$ ,  $\phi$  and vanishing fermion fields  $\Psi$ . The resulting flow equation can be compactly written as

$$\begin{aligned} \partial_t u &= (D-2+\eta_\chi)\rho_\chi u^{(1,0)} + (D-2+\eta_\phi)\rho_\phi u^{(0,1)} - Du \\ &\quad + I_R(\omega_\chi, \omega_\phi, \omega_{\phi\chi}^2) + 2I_G(u^{(0,1)}) - 2N_f \left[ I_\psi(\omega_\psi^+) + I_\psi(\omega_\psi^-) \right], \end{aligned} \quad (4.38)$$

where we have defined the following quantities

$$u^{(i,j)} = \frac{\partial^{i+j}}{\partial \rho_\chi^i \partial \rho_\phi^j} u(\rho_\chi, \rho_\phi), \quad (4.39)$$

$$\omega_\chi = u^{(1,0)} + 2\rho_\chi u^{(2,0)}, \quad (4.40)$$

$$\omega_\phi = u^{(0,1)} + 2\rho_\phi u^{(0,2)}, \quad (4.41)$$

$$\omega_{\phi\chi}^2 = 4\rho_\phi \rho_\chi (u^{(1,1)})^2, \quad (4.42)$$

$$\omega_\psi^\pm = 2\rho_\chi g_\chi^2 + 2\rho_\phi g_\phi^2 \pm 4\sqrt{\rho_\chi \rho_\phi} g_\chi g_\phi. \quad (4.43)$$

The *threshold* functions  $I_R$ ,  $I_G$ , and  $I_\psi$  involve the loop integrations and the regulator dependence. For a suitable choice of the regulator functions for the bosons and fermions, these integrations can be performed analytically and the result can be given in a closed form, see Appendix A.2.

The effective dimensionless potential  $u$  is expanded about its scale-dependent dimensionless minimum at  $(\kappa_\chi, \kappa_\phi) = ((k^{D-2}/Z_\chi)\bar{\rho}_{\chi,\min}, (k^{D-2}/Z_\phi)\bar{\rho}_{\phi,\min})$ . Its IR limit corresponds to the vacuum expectation values of  $\chi$  and  $\phi$ ,  $\lim_{k \rightarrow 0} \kappa_\varphi = \langle \frac{1}{2} \varphi^2 \rangle$ ,  $\varphi \in \{\chi, \phi\}$ . We may distinguish four qualitatively different combinations for the location of the minimum of  $u$ :

- (i) Both sectors remain in the symmetric regime (SYM-SYM) with  $(\kappa_\chi, \kappa_\phi) = (0, 0)$ , or
- (ii) either of the symmetries is spontaneously broken  $\kappa_\chi \neq 0, \kappa_\phi = 0$  (SSB-SYM) or vice versa (SYM-SSB), or
- (iii) both order parameters attain a nonzero vacuum expectation value  $\kappa_{\chi,\phi} \neq 0$  (SSB-SBB).

The following parameterization of the effective potential in terms of a two-dimensional Taylor expansion accounts for all of these scenarios

$$u(\rho_\chi, \rho_\phi) = \sum_{m+n \geq 1}^{m+n=N} \frac{\lambda_{n,m}}{n!m!} (\rho_\chi - \kappa_\chi)^n (\rho_\phi - \kappa_\phi)^m, \quad (4.44)$$

with  $\lambda_{1,0} = m_\chi^2$  if  $\kappa_\chi = 0$  and  $\lambda_{1,0} = 0$  if  $\kappa_\chi \neq 0$ . Analogous definitions are used for  $\lambda_{0,1}, \kappa_\phi$  and  $m_\phi^2$ . The  $\beta$  functions for the expansion parameters in the different regimes are then obtained by the projections:

- (i) SYM-SYM regime:

$$\partial_t \lambda_{n,m} = (\partial_t u)^{(n,m)} \Big|_{\substack{\rho_\chi=0 \\ \rho_\phi=0}}. \quad (4.45)$$

- (ii) SSB-SYM regime:

$$\partial_t m_\phi^2 = (\partial_t u)^{(0,1)} + \lambda_{1,1} \partial_t \kappa_\chi \Big|_{\substack{\rho_\chi=\kappa_\chi \\ \rho_\phi=0}}, \quad (4.46)$$

$$\partial_t \kappa_\chi = - \frac{(\partial_t u)^{(1,0)}}{\lambda_{2,0}} \Big|_{\substack{\rho_\chi=\kappa_\chi \\ \rho_\phi=0}}, \quad (4.47)$$

$$\partial_t \lambda_{n,m} = (\partial_t u)^{(n,m)} + \lambda_{n+1,m} \partial_t \kappa_\chi \Big|_{\substack{\rho_\chi=\kappa_\chi \\ \rho_\phi=0}}. \quad (4.48)$$

The projections of the SYM-SSB regime can be obtained accordingly by exchanging  $\chi$  and  $\phi$  in Eq. (4.46) - (4.48).

- (iii) SSB-SBB regime:

$$\partial_t \kappa_\chi = \frac{\lambda_{1,1}(\partial_t u)^{(0,1)} - \lambda_{0,2}(\partial_t u)^{(1,0)}}{\lambda_{2,0}\lambda_{0,2} - \lambda_{1,1}^2} \Big|_{\substack{\rho_\chi=\kappa_\chi \\ \rho_\phi=\kappa_\phi}}, \quad (4.49)$$

$$\partial_t \kappa_\phi = \frac{\lambda_{1,1}(\partial_t u)^{(1,0)} - \lambda_{2,0}(\partial_t u)^{(0,1)}}{\lambda_{2,0}\lambda_{0,2} - \lambda_{1,1}^2} \Big|_{\substack{\rho_\chi=\kappa_\chi \\ \rho_\phi=\kappa_\phi}}, \quad (4.50)$$

$$\partial_t \lambda_{n,m} = \left[ (\partial_t u)^{(n,m)} + \lambda_{n+1,m} \partial_t \kappa_\chi + \lambda_{n,m+1} \partial_t \kappa_\phi \right] \Big|_{\substack{\rho_\chi=\kappa_\chi \\ \rho_\phi=\kappa_\phi}}. \quad (4.51)$$

For our numerical results we expand the effective potential up to order  $\chi^8, \phi^8$  (LPA' 8) and check the convergence of critical quantities with respect to the inclusion of higher orders in the fields up to order  $\chi^{12}, \phi^{12}$  (LPA' 12).

**Yukawa Couplings** For the projection of the flow of the Yukawa couplings we split the two-point function into its fluctuation dependent and independent parts  $\Gamma_{k,0}^{(2)} = \Gamma_k^{(2)} \Big|_{\chi=\phi=\psi=0}$ , and  $\Delta\Gamma_k^{(2)} = \Gamma_k^{(2)} - \Gamma_{k,0}^{(2)}$ . Then we expand the Wetterich equation in the following way

$$\begin{aligned} \partial_t \Gamma_k &= \frac{1}{2} \tilde{\partial}_t \text{STr} \left[ \ln(\Gamma_k^{(2)} + R_k) \right] \\ &= \frac{1}{2} \tilde{\partial}_t \text{STr} \left[ \ln(\Gamma_{k,0}^{(2)} + R_k) \right] + \frac{1}{2} \tilde{\partial}_t \text{STr} \sum_{n=1}^{\infty} \frac{(-1)^{n+1}}{n} \left[ (\Gamma_{k,0}^{(2)} + R_k)^{-1} \Delta\Gamma_k^{(2)} \right]^n. \end{aligned} \quad (4.52)$$

Here, the scale derivative  $\tilde{\partial}_t$  acts only on the  $t$ -dependence of the regulator. The fields are divided into their vacuum expectation value and a fluctuating part,  $\chi = \chi_0 + \Delta\chi$ ,  $\phi_3 = \phi_{3,0} + \Delta\phi_3$ , and  $\phi_{1,2} = \Delta\phi_{1,2}$ . This allows us to devise suitable projection rules to extract the flow of Yukawa couplings

$$\partial_t g_\chi = \frac{1}{6N_f d_\gamma} \text{Tr} \left[ \frac{\overrightarrow{\delta}}{\delta \Delta\chi(p')} \frac{\overrightarrow{\delta}}{\delta \bar{\Psi}(p)} \tilde{\partial}_t \text{STr} \left[ \left( \frac{\Delta\Gamma_k^{(2)}}{\Gamma_{k,0}^{(2)} + R_k} \right)^3 \right] \frac{\overleftarrow{\delta}}{\delta \Psi(q)} \right]_{\substack{p'=p=q=0 \\ \bar{\Psi}=\Psi=\Delta\chi=\Delta\phi=0}}, \quad (4.53)$$

$$\partial_t g_\phi = \frac{1}{6N_f d_\gamma} \text{Tr} \left[ (\sigma_1 \otimes \mathbb{1}_4) \frac{\overrightarrow{\delta}}{\delta \phi_1(p')} \frac{\overrightarrow{\delta}}{\delta \bar{\Psi}(p)} \tilde{\partial}_t \text{STr} \left[ \left( \frac{\Delta\Gamma_k^{(2)}}{\Gamma_{k,0}^{(2)} + R_k} \right)^3 \right] \frac{\overleftarrow{\delta}}{\delta \Psi(q)} \right]_{\substack{p'=p=q=0 \\ \bar{\Psi}=\Psi=\Delta\chi=\Delta\phi=0}}. \quad (4.54)$$

The resulting  $\beta$ -functions can again be calculated analytically and presented in a closed form. For these Yukawa couplings, the expressions, however, are rather lengthy and are therefore deferred to Appendix A.1.1.

**Anomalous Dimensions** We finally need a projection prescription for  $\partial_t Z_i$ ,  $i \in \{\chi, \phi, \psi\}$ . To this end, the expansion of the Wetterich equation, Eq. (4.52), is evaluated for momentum-dependent fields to calculate the anomalous dimensions according to Eq. (4.37). Here, we choose to project onto the Goldstone modes. Note that a projection onto the radial mode would provide admixtures of additional terms. Details on this choice are presented in Appendix A.1.3. For the anomalous dimension of the Heisenberg field we can arbitrarily select one of the two Goldstone modes in order to determine  $\partial_t Z_\phi$ . For the Ising field, however, there is no Goldstone. Here, we define  $\eta_\chi$  as the limiting case  $N \rightarrow 1$  of  $N$  copies of the Ising field, see Appendix A.1.3 for details. In summary, we use the following prescriptions:

$$\partial_t Z_\psi = \frac{i}{4DN_f d_\gamma} \text{Tr} \left[ (\mathbb{1}_2 \otimes \gamma_\mu) \frac{\partial}{\partial p_\mu} \int \frac{d^D q}{(2\pi)^D} \frac{\overrightarrow{\delta}}{\delta \bar{\Psi}(p)} \tilde{\partial}_t \text{STr} \left[ \left( \frac{\Delta\Gamma_k^{(2)}}{\Gamma_{k,0}^{(2)} + R_k} \right)^2 \right] \frac{\overleftarrow{\delta}}{\delta \bar{\Psi}(q)} \right]_{\substack{p=q=0 \\ \bar{\Psi}=\Psi=0 \\ \Delta\chi=\Delta\phi=0}}. \quad (4.55)$$

and

$$\partial_t Z_\chi = \lim_{N \rightarrow 1} \left( -\frac{1}{4} \frac{\partial}{\partial p^2} \int \frac{d^D q}{(2\pi)^D} \frac{\vec{\delta}}{\delta \Delta \chi_{G,1}(-p)} \tilde{\partial}_t \text{STr} \left[ \left( \frac{\Delta \Gamma_k^{(2)}}{\Gamma_{k,0}^{(2)} + R_k} \right)^2 \right] \frac{\overleftarrow{\delta}}{\delta \Delta \chi_{G,1}(q)} \Big|_{\substack{p=q=0 \\ \vec{\Psi}=\Psi=0 \\ \Delta \chi=\Delta \phi=0}} \right), \quad (4.56)$$

$$\partial_t Z_\phi = -\frac{1}{4} \frac{\partial}{\partial p^2} \int \frac{d^D q}{(2\pi)^D} \frac{\vec{\delta}}{\delta \Delta \phi_1(-p)} \tilde{\partial}_t \text{STr} \left[ \left( \frac{\Delta \Gamma_k^{(2)}}{\Gamma_{k,0}^{(2)} + R_k} \right)^2 \right] \frac{\overleftarrow{\delta}}{\delta \Delta \phi_1(q)} \Big|_{\substack{p=q=0 \\ \vec{\Psi}=\Psi=0 \\ \Delta \chi=\Delta \phi=0}}, \quad (4.57)$$

with  $\chi \rightarrow (\chi_R + \Delta \chi_{R,1}, \Delta \chi_{G,1}, \dots, \Delta \chi_{G,N-1})$ . The full analytical expressions for the anomalous dimensions in terms of threshold functions are given in Appendix A.1.2. Further, in Appendix A.2, the corresponding threshold functions are listed for general regulator, as well as explicit expressions for the linear and sharp regulators are given.

In this study, we use the optimized linear regulator [153–157, 218] to calculate critical exponents and the sharp regulator to determine the perturbative limit of the above flow equations. We use this as a crosscheck in the following way: The upper critical space-time dimension of the theory is four. Consequently, in  $D = 4 - \epsilon$  dimensions, perturbation theory becomes reliable. The one-loop flow equations obtained in a standard Wilsonian approach can be reproduced from the FRG approach as a limiting case (cf. Sec. 2.2.2). To this end, we consider the symmetric regime and neglect all perturbatively irrelevant operators in the ansatz for the effective action. Then, expanding the flow equations in  $\epsilon = 4 - D$  yields exactly the 1-loop results of the  $\epsilon$ -expansion in the previous section.

#### 4.5.2. Chiral Ising and Chiral Heisenberg Universality Class for $N_f = 2$

Using the FRG flow equations, we can now search for fixed points and study their evolution as a function of space-time dimension  $D$  and number of fermion flavors  $N_f$ . We start with benchmarking by comparing to the results on the separate chiral Ising and the chiral Heisenberg universality classes from Ref. [66, 127].<sup>3</sup>

In Tables 4.2 and 4.3, we give our best estimates for the critical exponents of the chiral Ising plus Heisenberg (cI+H) and the chiral Heisenberg plus Ising (cH+I) fixed points, respectively, for  $N_f = 2$  and  $D = 3$ . As an important result, we find that both of these fixed points exhibit three relevant directions and are therefore unstable. This finding is different from the leading-order  $\epsilon$ -expansion, in which the cH+I fixed point appeared stable, featuring only two relevant directions. Since these fixed points are composites from a chiral and a purely bosonic model, we can compare several quantities with previous fRG calculations and results from other methods. The exponent  $\theta_1$  is given by the correlation length exponent in a O(1) or a O(3) model for the cH+I and the cI+H fixed point, respectively. The second critical exponent  $\theta_2$  is inherited from the chiral Heisenberg (chiral Ising) model. Additionally, the values of the anomalous dimensions are inherited from the separate models, cf. Table 4.2. In the case of the cI+H fixed point, the anomalous dimensions  $\eta_\chi$  and  $\eta_\psi$  come from the chiral Ising model, and  $\eta_\phi$  from

<sup>3</sup>We have also checked the existence and properties of the purely bosonic fixed points, which can be compared with Ref. [11]—however, since these fixed points turn out to have more than three relevant directions when fermions are present (as expected), they will not play a role in the remainder of this study.

Table 4.2.: Anomalous dimensions and largest critical exponents from this work (first line) in comparison with different methods and models for the chiral Ising universality class,  $N_f = 2$  and  $D = 3$ . The boldface numbers show the values of the decisive third critical exponent, exhibiting that this multicritical fixed point is unstable.

model	method	$\theta_1$	$\theta_2$	$\theta_3$	$\eta_\chi$	$\eta_\phi$	$\eta_\psi$
cI+H	FRG	1.359	0.983	<b>0.719</b>	0.760	0.041	0.032
	$\epsilon^1$ exp [127]	1.545	1.048	<b>0.571</b>	0.571	0	0.071
cI	FRG [66]		0.982		0.760		0.032
	FRG [211]		0.996		0.789		0.031
	$\epsilon^2$ exp [145]		1.055		0.695		0.065
	MC [212]		1.00		0.754		
O(3)	$\epsilon^5$ exp [219]	1.419				0.037	
	MC [220]	1.406				0.038	

Table 4.3.: Anomalous dimensions and largest critical exponents from this work (first line) in comparison with different methods and models for the chiral Heisenberg universality class,  $N_f = 2$  and  $D = 3$ . The boldface numbers show the values of the decisive third critical exponent. Note the dramatic change in  $\theta_3$  for the cH+I when going from the  $\epsilon$  expansion to the FRG results, rendering the cH+I fixed point unstable.

model	method	$\theta_1$	$\theta_2$	$\theta_3$	$\eta_\chi$	$\eta_\phi$	$\eta_\psi$
cH+I	FRG	1.564	0.773	<b>0.241</b>	0.044	1.015	0.084
	$\epsilon^1$ exp [127]	1.667	0.473	<b>-0.8</b>	0	0.8	0.3
cH	FRG [66]		0.772			1.015	0.084
	$\epsilon^2$ exp [145]		0.834			0.959	0.242
	MC [213]		0.98			0.70	
O(1)	$\epsilon^5$ exp [219]	1.590			0.036		
	MC [221]	1.587			0.036		

the bosonic O(3) (Heisenberg) model. For the cH+I fixed point,  $\eta_\phi$  and  $\eta_\psi$  can be inferred from the chiral Heisenberg system, while  $\eta_\chi$  is adopted from the bosonic O(1) (Ising) model. Although the central question of this paper is concerned with the coupled model, i.e.  $\theta_3$  for these fixed points, we briefly discuss the inherited critical exponents  $\theta_1, \theta_2$  and  $\eta_\chi, \eta_\phi, \eta_\psi$  for a complete presentation. Our estimates for the well-known results of the bosonic Heisenberg (bosonic Ising) universality class show less than 5% deviation from fifth order  $\epsilon$ -expansion and Monte Carlo calculations when comparing the first critical exponent  $\theta_1$ . The anomalous dimension lies within a 10% (Heisenberg) and 18% (Ising) error range as expected from an FRG calculation in this truncation scheme. For the chiral Ising (chiral Heisenberg) universality class, the exponents [ $\theta_2$  and  $\eta_\chi$  ( $\eta_\phi$ )] are not precisely known. In any case, different FRG computations [66, 211] coincide within 1% with our estimate, and agree inside an 8% error with the second-order  $\epsilon$ -expansion results [145]. When comparing our estimates with the Monte-Carlo results, we find an agreement within 2% in the case of the chiral Ising universality class [212], whereas in the case of the chiral Heisenberg universality class we observe significant discrepancies to the newest Monte-Carlo estimates [71, 209, 213, 222], see Ref. [66, 213] for a discussion.

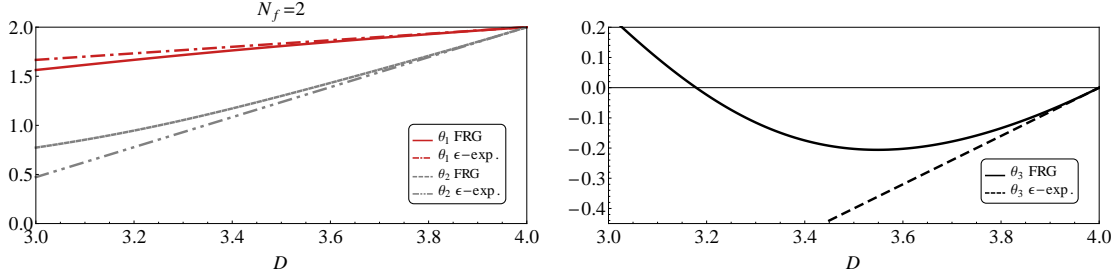


Figure 4.5.: Three largest critical exponents  $\theta_1$ ,  $\theta_2$  (left), and  $\theta_3$  (right) at the cH+I fixed point from FRG and  $\epsilon$  expansion [127] as function of the space-time dimensions, for  $N_f = 2$ . The cH+I fixed point is stable close to four dimensions. In the FRG approach, however, it bends to positive values below  $D = 3.17$  and renders the cH+I fixed point unstable in  $D = 3$ .

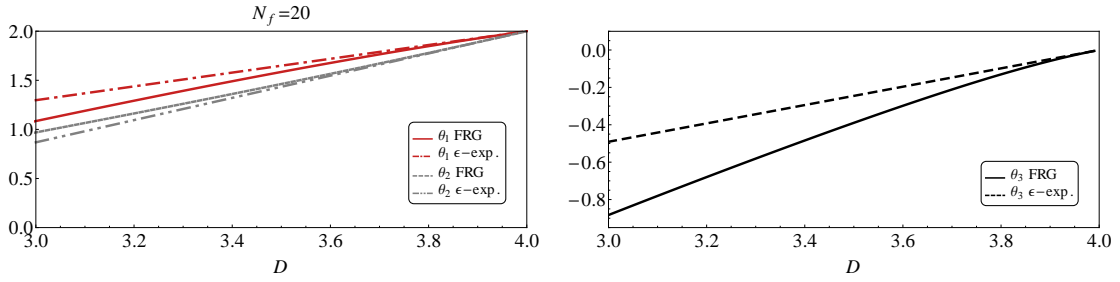


Figure 4.6.: Three largest critical exponents  $\theta_1$ ,  $\theta_2$  (left), and  $\theta_3$  (right) at large- $N_f$  fixed point from FRG and  $\epsilon$  expansion [127] as function of the space-time dimensions, for  $N_f = 20$ . Here, the large- $N_f$  fixed point is stable in both approaches for all  $3 \leq D < 4$ .

#### 4.5.3. From $4-\epsilon$ to 3 Space-Time Dimensions

Using the FRG equations, we can directly evaluate the fixed points in arbitrary space-time dimensions  $2 < D < 4$ . This allows us to systematically compare to the fixed-point solutions of the  $\epsilon$ -expansion and track deviations when approaching  $D = 3$ , i.e., for large values of  $\epsilon$ . As explained in Sec. 4.4.1, the study of the quantum multicritical point in first-order  $\epsilon$ -expansion has revealed two fixed points, which became stable at different ranges of the fermion flavor number  $N_f$ . For the graphene case,  $N_f = 2$ , the  $\epsilon$ -expansion renders the cH+I fixed point stable, whereas a novel interacting fixed point that couples both chiral sectors of the theory became stable at large  $N_f$ . We will refer to this fixed point as “large- $N_f$  fixed point” in the following. We can identify both fixed points within the FRG approach close to four space-time dimensions and then investigate their stability, as determined by the third-largest critical exponent  $\theta_3$ , as function of dimension  $D$ . The evolution of all three largest critical exponents upon varying the dimension is depicted in Fig. 4.5 for the cH+I fixed point and in Fig. 4.6 for the large- $N_f$  fixed point.

In contrast to the first two critical exponents, the decisive third exponent shows large deviations in comparison to the leading-order  $\epsilon$ -expansion results in three space-time dimensions. Regarding the cH+I fixed point, this effect can be traced back to the propagators in the loop contributions, which to first order in  $\epsilon$ , are accounted for only in the flow equations of the masses. However, for this fixed point  $\theta_3$  is predominantly determined by  $\beta_{g_\chi^2}$ . Dimensional analysis shows that  $g_\chi^2$  scales like  $(4 - D)$ , which is corrected by the loop contributions and the anomalous dimensions. These are much smaller in the FRG compared to the first order

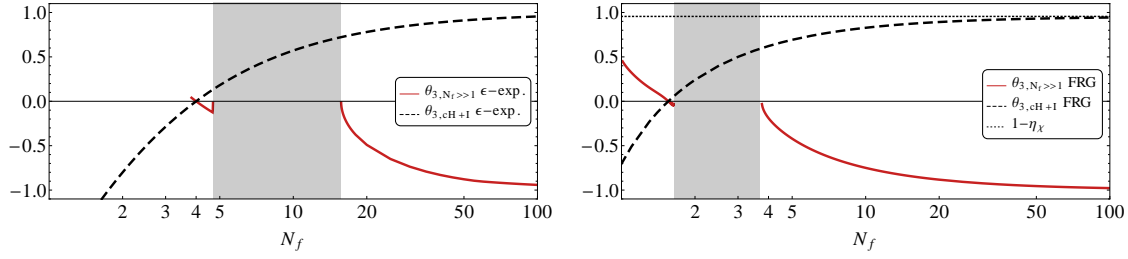


Figure 4.7.: Third largest critical exponent  $\theta_3$  as function of the fermion flavor number  $N_f$  of cH+I fixed point (dashed/black) and large- $N_f$  fixed point (solid/red), from  $\epsilon$  expansion [127] (left) in comparison to FRG (right). We also show  $1 - \eta_\chi$  for the cH+I fixed point in the FRG (bottom), note the offset from 1 for large  $N_f$ .

in  $\epsilon$  due to the threshold effects of the propagators. Thus, while to first order in  $\epsilon$  the loop contributions reduce  $\theta_3$  below zero, the reduction is not as large in the nonperturbative setting. In contrast, main contributions to  $\theta_1$  and  $\theta_2$  come from the mass flow equations so that the  $\epsilon$ -expansion captures their behavior already quite well to first order. For larger values of  $N_f$ , loop contributions become less important and the critical exponents are mainly fixed by the canonical scaling. Here, the first order  $\epsilon$ -expansion underestimates the anomalous dimensions, so that the exponents tend faster to the final values of  $\pm 1$  within the FRG approach. The effect is larger for  $\theta_3$  because the anomalous dimension enters it twice, both directly as well as through the derivative with respect to  $g_\chi^2$ . Such significant quantitative improvement of the FRG approach as compared to the first-order  $\epsilon$ -expansion is well-known from the corresponding multicritical bosonic systems with  $O(N_1) \oplus O(N_2)$  symmetry [11], for which the true regions of stability of the different fixed points are by now well established [16].

Eventually, the difference in  $\theta_3$  leads to an important change of the stability analysis in three space-time dimensions for  $N_f = 2$  because the cH+I fixed point loses its stability at about  $D = 3.17$ . At this point it collides with a new fixed point that couples both sectors. However, the new fixed point is unphysical for  $D < 3.17$  as it has a negative square of the Yukawa coupling  $g_\chi^2 < 0$ . Therefore, in  $D = 3$  no stable and physically admissible fixed point is found for the graphene case, i.e., all allowed fixed points have more than two relevant directions for  $N_f = 2$ .

#### 4.5.4. Fixed Points as Function of Fermion Flavor Number

##### Dependence on $N_f$ in $D = 3$

In this section, we study the fixed-point structure as function of the fermion flavor number  $N_f$  in three space-time dimensions. We find several regimes exhibiting the qualitative behavior known from first-order  $\epsilon$ -expansion: (1) For small  $N_f$  the cH+I fixed point is stable, followed by a regime of (2) intermediate  $N_f$  where no stable and physically admissible fixed point exists. (3) For large  $N_f$ , a novel fixed point with a coupling between the different sectors is stable.

On the other hand, the values of  $N_f$  marking the borders change considerably when going from the first order  $\epsilon$ -expansion to the FRG approach. We again investigate the sign of  $\theta_3$  to analyze the stability and determine the critical flavor numbers for the different regimes. The result is depicted in Fig. 4.7, where for comparison we also show the  $\epsilon$ -expansion results from the previous section. One can explicitly see that the qualitative behavior is the same within both approaches, but the different regimes are shifted and shrunk. Within the FRG, the first regime at small flavor numbers  $N_f < 1.6$  is characterized by the cH+I fixed point. At  $N_f = 1.6$



Table 4.4.: LPA' 8 results of the stable fixed point for  $N_f = 1$  and  $N_f = 20$  in  $D = 3$ .

$N_f$	stable FP	$\theta_1$	$\theta_2$	$\theta_3$	$\eta_\phi$	$\eta_\chi$	$\eta_\psi$
1	cH+I	1.564	0.558	-0.703	1.003	0.044	0.207
20	large- $N_f$	1.085	0.969	-0.883	0.980	0.913	0.010

it collides with another fixed point and loses stability. As pointed out before, the other fixed point is unphysical due to a negative  $g_\chi^2$  for  $N_f > 1.6$ . Hence, for  $N_f \in (1.6, 3.6)$  no stable and physically admissible fixed point is found. Finally, for  $N_f > 3.6$  the large- $N_f$  fixed point known from the  $\epsilon$  expansion becomes stable.

For numerical comparison, we give the three largest critical exponents and the anomalous dimensions for two examples of  $N_f$ , for which a stable fixed point is found, in Table 4.4.

### Large $N_f$ Behavior

To complete the stability analysis for the cH+I and the large- $N_f$  fixed points, we finally study the limit  $N_f \rightarrow \infty$ , for which we can calculate the exponents analytically. To this end, we rescale the potential and the bosonic wave function renormalization by suitable factors of  $N_f$ ,  $U \rightarrow U/N_f$ ,  $Z_{\chi/\phi} \rightarrow Z_{\chi/\phi}/N_f$ , ensuring that  $g_\chi$  and  $g_\phi$  remain positive. After this rescaling, the boson loops become of order  $\mathcal{O}(1/N_f)$  and the flow equations to leading order read

$$\partial_t u = -Du + (D-2+\eta_\chi)\rho_\chi u^{(1,0)} + (D-2+\eta_\phi)\rho_\phi u^{(0,1)} - 2[I_\psi(\omega_\psi^+) + I_\psi(\omega_\psi^-)] + \mathcal{O}\left(\frac{1}{N_f}\right), \quad (4.58)$$

and

$$\partial_t g_{\chi/\phi}^2 = (D-4+\eta_{\chi/\phi})g_{\chi/\phi}^2 + \mathcal{O}\left(\frac{1}{N_f}\right), \quad (4.59)$$

$$\eta_{\chi/\phi} = \frac{32v_D}{D}m_4^{(F)}(0)g_{\chi/\phi}^2 + \mathcal{O}\left(\frac{1}{N_f}\right), \quad (4.60)$$

$$\eta_\psi = \mathcal{O}\left(\frac{1}{N_f}\right), \quad (4.61)$$

with the threshold functions as given in Appendix A.2 and  $v_D = (\Gamma(D/2)2^{D+1}\pi^{d/2})^{-1}$ .

The problem becomes symmetric with respect to  $\chi$  and  $\phi$  and can be solved exactly. In the sector of the Yukawa couplings, the fixed-point solutions are

$$g_{\chi/\phi}^{*2} = 0 \quad \text{or} \quad g_{\chi/\phi}^{*2} = \frac{(4-D)D}{32v_D m_4^{(F)}(0)}. \quad (4.62)$$

Further, the partial differential equation for the effective potential is solved by

$$u(\rho_\chi, \rho_\phi) = \frac{8v_D}{D^2} \left[ \frac{{}_2F_1\left(\frac{D}{2}, \frac{D}{2}; \frac{D+2}{2}; \frac{\omega_-}{1+\omega_-}\right)}{(1+\omega_-)^{D/2}} + \frac{{}_2F_1\left(\frac{D}{2}, \frac{D}{2}; \frac{D+2}{2}; \frac{\omega_+}{1+\omega_+}\right)}{(1+\omega_+)^{D/2}} - 2 \right] + \rho_\chi^{D/2} c\left(\frac{\rho_\phi}{\rho_\chi}\right),$$



$$\text{with } \omega_{\pm} = \frac{4\nu_D}{D} \frac{(4-3D)}{(D^2-6d+8)} (\sqrt{\rho_{\phi}} \pm \sqrt{\rho_{\chi}})^{-2}, \quad (4.63)$$

and  ${}_2F_1(a, b; c; z)$  denotes the Gaussian hypergeometric function (see, e.g., [223]). For any smooth function  $c(\rho_{\phi}/\rho_{\chi})$  that depends only on the ratio of the invariants  $\rho_{\phi}/\rho_{\chi}$  the corresponding  $u(\rho_{\chi}, \rho_{\phi})$  solves the fixed-point equation (4.58). We can restrict  $c$  by the physical requirement that the effective potential should be bounded from below and finite for  $\rho_{\chi} \rightarrow 0$  and  $\rho_{\phi} \rightarrow 0$ . Alternatively, it can be determined so that  $u$  equals the large- $N_f$  limit of the Taylor-expanded effective potential.

Regarding the stability analysis, we find that in this limit the entries  $\partial \beta_{g_{\chi}^2} / \partial g_{\chi}^2$  and  $\partial \beta_{g_{\phi}^2} / \partial g_{\phi}^2$  in the stability matrix fix  $\theta_3 = \theta_4$ . As can be seen in Eq. (4.59),  $\theta_3$  is then determined by the canonical scaling only

$$\theta_3 = -\frac{\partial \beta_{g_{\chi}^2}}{\partial g_{\chi}^2} = -\left(D - 4 + \eta_{\chi} + g_{\chi}^2 \frac{\partial \eta_{\chi}}{\partial g_{\chi}^2} + \mathcal{O}\left(\frac{1}{N_f}\right)\right).$$

For the stable large- $N_f$  fixed point both Yukawa couplings are nonzero and uniquely determined by the requirements  $\eta_{\chi} = \eta_{\phi} = 4 - D$ . We furthermore have  $g_{\chi}^2 \partial \eta_{\chi} / \partial g_{\chi}^2 = \eta_{\chi}$  and  $g_{\phi}^2 \partial \eta_{\phi} / \partial g_{\phi}^2 = \eta_{\phi}$  [Eq. (4.60)]. This requires that the third (and fourth) largest critical exponent  $\theta_3$  must tend to minus one in  $D = 3$ ,

$$\text{large-}N_f \text{ fixed point: } \lim_{N_f \rightarrow \infty} \theta_3 = -1. \quad (4.64)$$

To investigate the cH+I fixed point in the limit of  $N_f \rightarrow \infty$ , we scale only the Heisenberg sector with the factor  $1/N_f$ , since the Ising sector completely decouples and becomes purely bosonic. Again the third critical exponent is determined by  $\beta_{g_{\chi}^2}$ . But now only loops including  $g_{\phi}^2$  are suppressed by  $1/N_f$ , such that  $\theta_3$  is given by

$$\theta_3 = -\frac{\partial \beta_{g_{\chi}^2}}{\partial g_{\chi}^2} = -\left(D - 4 + \eta_{\chi} + g_{\chi}^2 \frac{\partial \eta_{\chi}}{\partial g_{\chi}^2} + \frac{\partial}{\partial g_{\chi}^2} \mathcal{L}(g_{\chi}^4) + \mathcal{O}\left(\frac{1}{N_f}\right)\right), \quad (4.65)$$

where  $\mathcal{L}(g_{\chi}^4)$  denotes loops that are at least proportional to  $g_{\chi}^4$ . With  $g_{\chi}^2 = 0$  this reduces to

$$\text{cH+I: } \lim_{N_f \rightarrow \infty} \theta_3 = 1 - \eta_{\chi} \quad (4.66)$$

in  $D = 3$  space-time dimensions. We therefore see that the third critical exponent for the cH+I fixed point computed within the FRG does *not* coincide with the one from  $\epsilon$ -expansion. This is due to the contribution from the anomalous dimension in the Ising sector, which becomes nonvanishing only to second order in  $\epsilon$ . In our approximation we have  $\eta_{\chi} = 0.044$ , such that  $\eta_{\chi} \rightarrow 1$  for large  $N_f$ . The large- $N_f$  behavior of both fixed points is exhibited in Fig. 4.7.

#### 4.5.5. FRG Phase Diagram

##### Phase Diagram from Fixed Points

In the case that a stable, physical fixed point is found, the structure of the phase diagram near the multicritical point is again extracted from the sign of

$$\Delta_{fRG} = \lambda_{2,0} \lambda_{0,2} - \lambda_{1,1}^2, \quad (4.67)$$

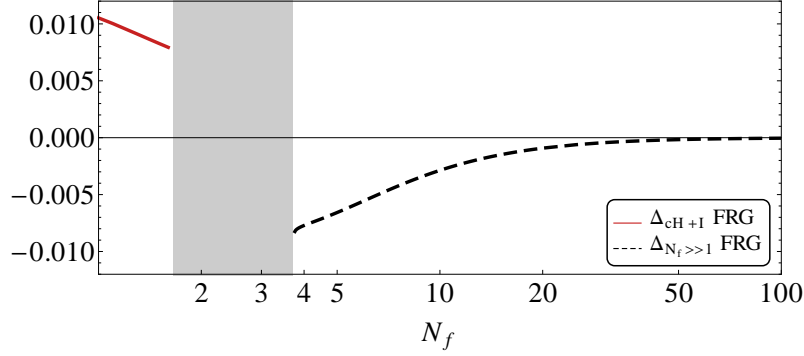


Figure 4.8.:  $\Delta = \lambda_{2,0}\lambda_{0,2} - \lambda_{1,1}^2$  at the stable fixed point for different fermion flavor numbers. Each  $\lambda$  is scaled with  $v_{D=3}$ . For small  $N_f < 1.6$ ,  $\Delta$  is positive at the stable (cH+I) fixed point, whereas for large  $N_f > 3.6$ ,  $\Delta$  is negative at the stable (large- $N_f$ ) fixed point. For intermediate  $N_f$  (gray shaded region), there is no stable and physically admissible fixed point.

where the infrared values of  $\lambda_{2,0}$ ,  $\lambda_{0,2}$  and  $\lambda_{1,1}$  are estimated through the expansion coefficients of the fixed point effective potential.<sup>4</sup> Fig. 4.8 shows the value for  $\Delta_{fRG}$  at the cH+I fixed point for  $N_f < 1.6$  and the large- $N_f$  fixed point for  $N_f > 3.6$ .  $\Delta_{fRG}$  is positive at the cH+I, so that the phase diagram exhibits tetracritical behavior and a coexistence phase [situation I in Fig. 4.1(a)] for small  $N_f$ . On the other hand,  $\Delta_{fRG}$  is negative at the large- $N_f$  fixed point, leading to bicritical behavior with a first-order transition between the ordered states for large  $N_f$ . The transition across the multicritical point, however, remains continuous [situation III in Fig. 4.1(a)]. This is in qualitative, however not quantitative, agreement with the previous result of the  $\epsilon$ -expansion.

When a stable and physically admissible fixed point does *not* exist, the phase diagram close to the intersection of SM, SDW, and CDW is governed by a triple point, with *all* transitions in its vicinity appearing first order [situation II in Fig. 4.1(a)]. As an important observation within the FRG approach, we in fact find the scenario with the triple point to be realized for the physical case of graphene,  $N_f = 2$  (gray shaded region in Fig. 4.8).

### Phase Diagram from Flow

Additionally to the fixed point analysis, we can extract the structure of the phase diagram close to the multicritical point from the flow of the parameters in the action Eq. (4.34). The form of the boson potential in the infrared then determines if one or both of the symmetries are spontaneously broken: an infrared value  $\lim_{k \rightarrow 0} \kappa_\chi \neq 0$  signals the CDW phase, and the SDW state is characterized by  $\lim_{k \rightarrow 0} \kappa_\phi \neq 0$ . In turn, if  $\lim_{k \rightarrow 0} \kappa_\chi \neq 0$  and  $\lim_{k \rightarrow 0} \kappa_\phi \neq 0$  at the end of the flow, there is a phase of coexistence. We calculate the flow in the LPA' 8 truncation in  $2 + 1$  space-time dimensions for different values of the fermion flavor number  $N_f$ . To examine the phase diagram we choose to scan either different bare values for the Yukawa couplings or for the boson masses, while setting the remaining parameters to the values of the stable fixed point, respectively.

For  $N_f = 20$  we therefore start the flow in the symmetric regime, i. e. at the UV cutoff we have  $\kappa_\chi = \kappa_\phi = 0$ . The resulting phase diagram is shown in Fig. 4.9. It confirms the expectation from the fixed point consideration; within the applied numerical precision we find

<sup>4</sup>Note that the other conventions regarding the factors in the action in Eq. (4.6) and Eq. (4.44) leads to a different factor in the definition of  $\Delta$ .

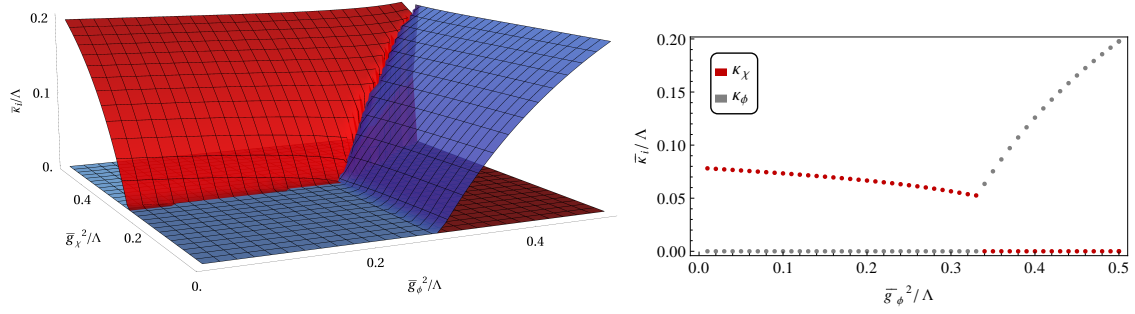


Figure 4.9.: (Left) The infrared limit of the scale dependent minimum of the boson potential  $\lim_{k \rightarrow 0} \bar{\kappa}_\chi$  (red) and  $\lim_{k \rightarrow 0} \bar{\kappa}_\phi$  (gray) as function of the bare, dimensionfull Yukawa couplings  $\bar{g}_\chi^2$  and  $\bar{g}_\phi^2$  at the UV scale  $\Lambda$  for  $N_f = 20$ . The infrared limits  $\lim_{k \rightarrow 0} \bar{\kappa}_\chi$  and  $\lim_{k \rightarrow 0} \bar{\kappa}_\phi$  correspond to the vacuum expectation values of the fields  $\chi$  and  $\phi$ , i. e. a finite value of  $\bar{\kappa}_\chi$  ( $\bar{\kappa}_\phi$ ) represents the CDW (SDW) phase. We fix the remaining bare parameters to the values of the stable fixed point (large- $N_f$  fixed point). (Right)  $\lim_{k \rightarrow 0} \bar{\kappa}_\chi$  and  $\lim_{k \rightarrow 0} \bar{\kappa}_\phi$  for fixed  $\bar{g}_\chi^2 = 0.31\Lambda$  and different bare  $\bar{g}_\phi^2$ . Within the numerical precision, the transition from CDW to SDW is discontinuous.

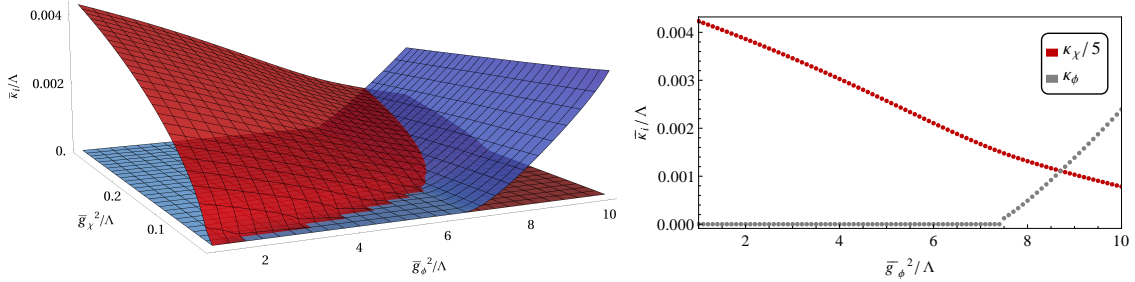


Figure 4.10.: (Left) The infrared limit of the scale dependent minimum of the boson potential  $\lim_{k \rightarrow 0} \bar{\kappa}_\chi/5$  (red) and  $\lim_{k \rightarrow 0} \bar{\kappa}_\phi$  (gray) as function of the bare, dimensionfull Yukawa couplings  $\bar{g}_\chi^2$  and  $\bar{g}_\phi^2$  at the UV scale  $\Lambda$  for  $N_f = 1$ . A finite value of  $\bar{\kappa}_\chi$  ( $\bar{\kappa}_\phi$ ) represents the CDW (SDW) phase. We fix the remaining bare parameters to the values of the stable fixed point (cH+I); in particular in this case  $\lim_{k \rightarrow \Lambda} \bar{\kappa}_\chi \neq 0$ . (Right)  $\lim_{k \rightarrow 0} \bar{\kappa}_\chi$  and  $\lim_{k \rightarrow 0} \bar{\kappa}_\phi$  for fixed  $\bar{g}_\chi^2 = 0.29\Lambda$  and different bare  $\bar{g}_\phi^2$ . There is a mixed phase with  $\lim_{k \rightarrow 0} \bar{\kappa}_\phi \neq 0$  and  $\lim_{k \rightarrow 0} \bar{\kappa}_\chi \neq 0$ .

a discontinuous transition between CDW and SDW phases. In the case  $N_f = 1$ , the stable fixed point is located in the regime where the CDW sector is spontaneously broken, i. e. we start the flow with finite  $\bar{\kappa}_\chi \neq 0$ . The corresponding phase diagram is presented in Fig. 4.10 and exhibits, as expected, a regime of coexistence between the different phases. When we start at the cH+I fixed point, but with  $N_f = 2$ , we obtain an analogous phase diagram as for  $N_f = 1$ , i. e. we cannot observe the appearance of a first-order multicritical point. We relate this to the small crossover exponent  $\theta_3/\theta_1 = 0.154$  and the proximity of the initial values to the fixed point.

We also begin the flow in the symmetric regime for  $N_f = 1$  and choose the bare values at the chiral Ising and chiral Heisenberg fixed points from the separate models (note that this is not a fixed point of the coupled theory). We obtain the phase diagram shown in Fig. 4.11 when we vary the bare masses. In this case there is no mixed phase because we did not fine-tune to

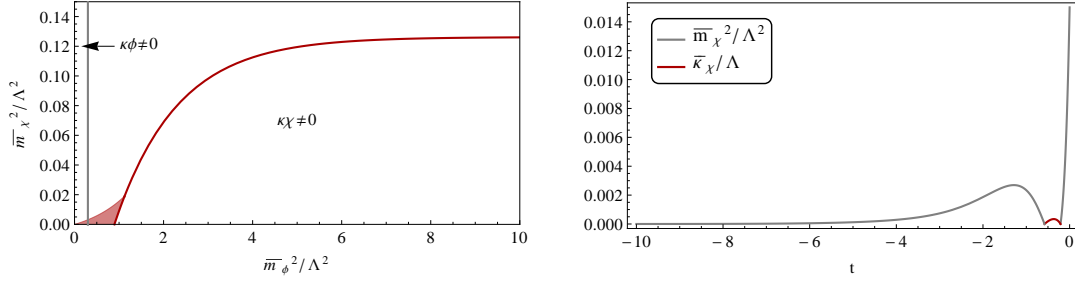


Figure 4.11.: (Left) The phase diagram for  $N_f = 1$  with regimes of finite  $\lim_{k \rightarrow 0} \kappa_\chi$  and  $\lim_{k \rightarrow 0} \kappa_\phi$  as function of the bare, dimensionfull boson masses  $\bar{m}_\chi^2$  and  $\bar{m}_\phi^2$  at the UV scale  $\Lambda$ . A finite value of  $\kappa_\chi$  ( $\kappa_\phi$ ) represents the CDW (SDW) phase. We fix the remaining bare parameters to the values of separate chiral Ising and chiral Heisenberg fixed points, which is not a fixed point of the coupled theory. Pre-condensation appears in the red shaded area (Right) Flow of  $\bar{m}_{\chi,k}^2$  and  $\bar{\kappa}_{\chi,k}$  for bare values in the pre-condensation regime ( $\bar{m}_\chi^2/\Lambda = 0.015$  and  $\bar{m}_\phi^2/\Lambda = 1$ ), the remaining bare couplings are the same as in the left figure. We see the appearance of a finite  $\bar{\kappa}_\chi$  for intermediate scales.

the multicritical point. Instead a regime of pre-condensation appears, where we observe the development of a non-zero minimum of the potential at intermediate scales, which vanishes again when further lowering the scale (Fig. 4.11). The phenomenon is known from fRG calculations at finite temperatures e. g. in ultra cold atoms [150] and QC<sub>2</sub>D [224]. However in our case the role of the temperature is played by the presence of the additional fluctuating field.

Finally for intermediate  $N_f$  the fixed point analysis revealed a first-order triple point. At the same time, the separate phase transitions from semimetal to CDW/SDW lie in the chiral Ising/Heisenberg universality class and are of second order. We note that, although we did not focus on this case here, the regime of the critical endpoint marking the change from first to second order transition can in principle be assessed within our approach. However, this may require a more suitable ansatz for the effective potential to detect the first order transitions (see e. g. [152, 225, 226]).

## 4.6. Conclusion

We have studied a multicritical point in the phase diagram of electrons on the honeycomb lattice using an effective field theory as low-energy theory of an extended Hubbard model with onsite and nearest-neighbor interaction. Our theory accounts for the universal behavior in the regime where the semimetallic phase, the charge density wave phase, and the spin density wave phase meet. Within a nonperturbative FRG approach we were able to investigate the dependence on space-time dimension  $2 < D < 4$  and flavor number  $N_f$  in Sec. 4.5, thereby extending the study close to four space-time dimensions of Sec. 4.4.

We have calculated the fixed-point structure and its stability ranges to describe the competition of the different phases. This enables us to determine the nature of the transition lines and the possibility of a CDW-SDW coexistence phase, as function of the number of fermion flavors. Besides, we provide a quantitative description of the critical behavior in the cases when the transitions are continuous. We have followed the two fixed points that are stable (at different ranges of  $N_f$ ) from the upper critical space-time dimension  $D = 4$  down to  $D = 3$ . While our results agree near  $D = 4$  both qualitatively and quantitatively with the  $\epsilon$ -expansion results, we

have found significant quantitative changes in the decisive third critical exponent and anomalous dimensions in  $D = 3$ . This leads to modified stability ranges, although the qualitative picture remains the same as in the  $\epsilon$ -expansion. The borders of the different stability regimes are determined by the collision of fixed points. They move in theory space as function of dimension and fermion flavor number and exchange stability when they meet.

Explicitly, we have found three different regimes for varying fermion flavor number. For small number of flavors the cH+I fixed point determines the physical properties at the multicritical point. In other words, the semimetal-to-antiferromagnet transition determines also the universal behavior at the multicritical point. Beyond this point, our results suggests a mixed phase in which both SDW and CDW orders coexist (tetracritical point). For large  $N_f$  a new fixed point of the coupled system emerges and becomes stable. The transition between both ordered states now is first order, whereas directly at the multicritical point the transition is continuous and defines a novel universality class (bicritical point), in agreement with the large- $N_f$  calculations within the fermionic description [55]. Within the fRG calculation, the graphene case is placed in a third regime that occurs for intermediate  $N_f$ . Here we do not find any stable fixed point, leading us to the prediction that a triple point appears with first-order transitions only. The investigation of the phase diagram in terms of the actual flow confirms the fixed point analysis in the regimes where stable fixed points are found. In addition it would be interesting to compute the global behavior of the fixed-point potential at intermediate  $N_f$ , in light of the first-order phase transitions we predict. This could be done, for instance, along the lines suggested in Ref. [152, 225, 226]. While in our description the number of fermion flavors has been introduced merely as a theoretical control parameter, a similar deformation of the honeycomb lattice system should be relevant for the novel systems with a large number of Dirac cones [227].

We have employed the FRG in terms of a local potential approximation within the derivative expansion including anomalous dimensions. As a crosscheck, we have compared our results with known limits from, on the one hand, the separate universality classes [66], and, on the other hand, the  $\epsilon$ -expansion results near the upper critical dimension [127]. In both limits we find perfect agreement, as it should be. We have also compared our predictions for  $D = 3$  with various literature results. As shown in [66], the FRG critical exponents in the Gross-Neveu-Yukawa model of the separate transitions also become exact close to the lower critical dimension of the corresponding, purely fermionic Gross-Neveu model, and the FRG interpolates continuously in between both exact limits. We expect this also to hold for the additional critical exponents arising from the coupling of both the chiral Ising and the chiral Heisenberg sectors. Concerning the convergence of our polynomial truncation we have verified the convergence of the critical exponents upon inclusion of higher polynomial orders within our potential expansion, see Appendix A.3. However, in order to resolve the discrepancy between FRG and Monte Carlo results [71, 209, 222] for the critical exponents of the chiral Heisenberg universality class it may be necessary to go beyond our approximation. This could be done, for instance, by accounting for field-dependent Yukawa couplings [211] and/or field-dependent wave function renormalizations.



---

## Interplay between Magnetism, Superconductivity and Orbital Order in 5-Pocket Iron-Based Superconductors

---

### 5.1. The Multiorbital Nature of Low-Energy Excitations

As we pointed out in the introduction, the interplay between superconducting, magnetic, and orbital order provides an active field in the research of Fe-based superconductors [111,114]. The problem of competing orders in many-fermion systems is inherently complex and is even more complicated in these materials due to the multi-orbital nature of their low-energy excitations. A controllable way to analyze the interplay between these different ordering tendencies in an unbiased way is to use the machinery of parquet renormalization group as explained in Sec. 2.2.1. The pRG has been applied to FeSCs before, but earlier works either neglected the orbital content of the Fermi pockets [119–121, 149] or analyzed simplified models with reduced number of pockets [122]. As a consequence it was not properly accounted for orbital order [100–110] and the orbital dependence of different symmetry-breaking patterns could not be resolved. It, however, can play a crucial role, as for example in the orbital-antiphase  $s^{+-}$  state suggested to explain the gap structure of LiFeAs [228]. In this chapter we perform the complete analytical pRG analysis of the most generic five-pocket model for FeSCs with full orbital content of low-energy excitations. The goal is to understand how the orbital composition of low-energy excitations affects the interplay between magnetism, orbital order, and superconductivity.

The five-pocket model contains three hole pockets, and two electron pockets (see Fig. 5.1). Two hole pockets are made out of  $d_{xz}$  and  $d_{yz}$  orbitals and symmetry requires that  $d_{xz}$  and  $d_{yz}$  contents interchange under the rotation by  $\pi/2$ . The third hole pocket consists merely of the  $d_{xy}$  orbital. The electron pockets contain  $d_{xz}(d_{yz})$  and  $d_{xy}$  orbitals (see e. g. Ref. [229, 230]). We argue that the number of symmetry allowed 4-fermion terms, which describe interactions between low-energy fermions, is 40 in the generic 5-band model in the absence of spin-orbit coupling (for a 4-band model this number equals 30 [231]). The bare values of these couplings are linear combinations of on-site inter-orbital and intra-orbital Hubbard interactions  $U$  and  $U'$ , and Hund interactions  $J$  and  $J'$ . But during the pRG procedure, all 40 couplings flow differently. Because the full analysis of the set of 40 pRG equations is quite involved, we first analyze a toy model in which we approximate the orbital composition of the two electron pockets as pure  $d_{xy}$ , and then extend the analysis to the full 5-pocket model.



For both models, we find the low-energy behavior amazingly simple. Namely, the renormalization group flow brings the system to one of the two regimes. In one regime, the system effectively becomes a 4-pocket model with two hole pockets and two electron pockets, in the other it becomes a 3-pocket model with two electron pockets and one hole pocket. In both cases, superconductivity eventually wins over magnetism, although magnetic correlations are larger at high energies. The superconductivity is of  $s^{+-}$  type, with sign change between the gaps on hole and electron pockets. The aforementioned orbital-antiphase gap structure only comes as subleading s-wave superconducting state. The distinction between the effective 3-pocket and 4-pocket model is in the magnitude of the gap on the  $M$  pocket compared to that on the  $\Gamma$ -centered hole pockets – their ratio is larger in the 3-pocket case. Furthermore a non-equal density on  $d_{xz}$  and  $d_{yz}$  orbitals, a nematic order likely occurring in FeSe [232–237], may first develop in the 4-pocket case. For the 3-pocket case with dominant  $d_{xy}$  interactions, orbital order does not develop as independent instability, but can be induced by a composite Ising-nematic spin order. SDW magnetism develops if the Fermi energy  $E_F$  cuts the pRG flow (cf. 2.2.1) and the type of SDW order is different for the effective 3-pocket and 4-pocket model. In the first case, SDW order is of stripe type, while for the second case it is a checkerboard [95, 238]. Interestingly, stripe order for the 3-pocket case correlates with the absence of spontaneous orbital order in the pRG formalism and points towards a magnetic origin of the nematic phase above stripe SDW magnetism [239]. This is consistent with the behavior observed in Fe-pnictides [240].

## 5.2. 3-Orbital, 5-Band Model

### 5.2.1. Kinetic Part of the Hamiltonian

We use as an input the fact that the low-energy excitations near all 5 Fermi surfaces are composed out of three orbitals –  $d_{xz}$ ,  $d_{yz}$ , and  $d_{xy}$ . We perform calculations in the 1-Fe unit cell and neglect the dispersion in the third direction and processes, which hybridize the pockets.

One way to obtain the dispersion of low-energy excitations is to use the tight-binding model in the orbital basis, restrict to  $d_{xz}$ ,  $d_{yz}$ , and  $d_{xy}$  orbitals, and expand around the high-symmetry points in the Brillouin zone, where different electron and hole pockets are located [93] (cf. Fig. 5.1). Another way to obtain low-energy dispersions is to identify the symmetry properties around the Fermi level and construct the invariants to leading order in the deviations from the symmetry points [231]. The two approaches are equivalent to quadratic order in the deviations near the centers of the pockets. Explicitly, two hole pockets are located at  $\Gamma = (0, 0)$  and one at  $M = (\pi, \pi)$ , the electron pockets are at  $X = (\pi, 0)$  and  $Y = (0, \pi)$ . The effective low-energy Hamiltonian reads

$$H_0 = \sum_{\mathbf{k}, \sigma} \left[ \psi_{\Gamma, \mathbf{k}, \sigma}^\dagger h_\Gamma(\mathbf{k}) \psi_{\Gamma, \mathbf{k}, \sigma} + \psi_{X, \mathbf{k}, \sigma}^\dagger h_X(\mathbf{k}) \psi_{X, \mathbf{k}, \sigma} + \psi_{Y, \mathbf{k}, \sigma}^\dagger h_Y(\mathbf{k}) \psi_{Y, \mathbf{k}, \sigma} + \psi_{M, \mathbf{k}, \sigma}^\dagger h_M(\mathbf{k}) \psi_{M, \mathbf{k}, \sigma} \right] \quad (5.1)$$

with

$$\begin{aligned} h_\Gamma(\mathbf{k}) &= \begin{pmatrix} \epsilon_\Gamma + \frac{k^2}{2m_\Gamma} + ak^2 \cos 2\theta_k & ck \sin 2\theta_k \\ ck \sin 2\theta_k & \epsilon_\Gamma + \frac{k^2}{2m_\Gamma} + ak^2 \cos 2\theta_k \end{pmatrix} \\ h_{X/Y}(\mathbf{k}) &= \begin{pmatrix} \epsilon_1 + \frac{k^2}{2m_1} \pm a_1 k^2 \cos 2\theta_k & -iv_{X/Y}(\mathbf{k}) \\ iv_{X/Y}(\mathbf{k}) & \epsilon_3 + \frac{k^2}{2m_3} \pm a_3 k^2 \cos 2\theta_k \end{pmatrix} \\ h_M(\mathbf{k}) &= \epsilon_M - \frac{k^2}{2m_M} \end{aligned} \quad (5.2)$$



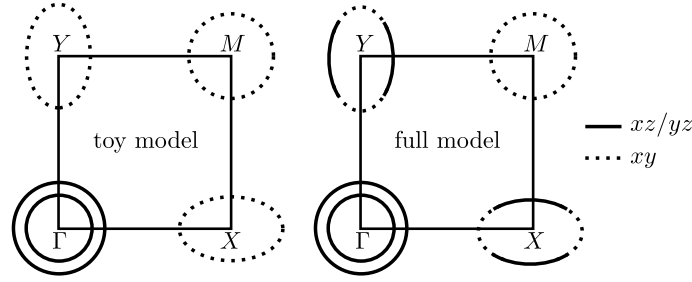


Figure 5.1.: The two 5-pocket models that we consider. The toy and the full model differ in the orbital content of electron pockets. For the full model, the electron pocket at  $X$  has contributions from  $d_{yz}$  and  $d_{xy}$  orbitals and the one at  $Y$  has contributions from  $d_{xz}$  and  $d_{xy}$  orbitals. For the toy model, we approximated these pockets as consisting exclusively from  $d_{xy}$  orbital.

where  $v_X(k) = 2vk \sin \theta_k$ ,  $v_Y(k) = 2vk \cos \theta_k$  and  $\theta_k = \arctan \frac{k_y}{k_x}$ . The spinors in Eq. (5.1) are defined as  $\psi_{\Gamma,k,\sigma} = (d_{yz,k,\sigma}, d_{xz,k,\sigma})^T$ ,  $\psi_{X,k,\sigma} = (d_{yz,X+k,\sigma}, d_{xy,X+k,\sigma})^T$ ,  $\psi_{Y,k,\sigma} = (d_{xz,Y+k,\sigma}, d_{xy,Y+k,\sigma})^T$  and  $\psi_{M,M+k,\sigma} = d_{xy,k,\sigma}$ . Below we shorten notations to  $d_{yz,k,\sigma} = d_{1,k,\sigma}$ ,  $d_{xz,k,\sigma} = d_{2,k,\sigma}$ ,  $d_{yz,X+k,\sigma} = f_{1,k,\sigma}$ ,  $d_{xz,Y+k,\sigma} = f_{2,k,\sigma}$ ,  $d_{xy,X+k,\sigma} = f_{31,k,\sigma}$ ,  $d_{xy,Y+k,\sigma} = f_{32,k,\sigma}$ , and  $d_{xy,k,\sigma} = d_{3,k,\sigma}$ . In these notations, the spinors are  $\psi_{\Gamma,k,\sigma} = (d_{1,k,\sigma}, d_{2,k,\sigma})^T$ ,  $\psi_{X/Y,k,\sigma} = (f_{1/2,k,\sigma}, f_{31/32,k,\sigma})^T$  and  $\psi_{M,M+k,\sigma} = d_{3,k,\sigma}$ .

To make the RG analysis more tractable, we make several simplifications in Eq. (5.2). For the  $\Gamma$ -centered hole pockets we set  $a = c$ . Then the transformation from orbital to band basis is a rotation around the angle  $\theta_k = \arctan \frac{k_y}{k_x}$  and the dispersions of band fermions  $c_{k,\sigma}$  and  $d_{k,\sigma}$  are isotropic in  $\mathbf{k}$ :

$$\epsilon_{c/d,k,\sigma} = -\frac{k^2}{2m_c/d} \quad (5.3)$$

where  $m_{c/d}^{-1} = m_{\Gamma}^{-1} \pm 2a$ . The two hole Fermi surfaces are obviously circular. A third hole pocket arises around the  $M$ -point in the Brillouin zone. Here the transformation from orbital to band basis is trivial, because the spectral weight comes entirely from the  $d_{xy}$  orbital. The dispersion is given in Eq. (5.2). The presence of this hole pocket is material dependent and relatively small changes in the system parameters may sink this pocket below the Fermi level (at least at  $k_z = 0$ , when the  $k_z$  dispersion is included). However, such a pocket is definitely present in, e.g., hole-doped  $K_x\text{Ba}_{1-x}\text{Fe}_2\text{As}_2$  and  $\text{LiFeAs}$ , which motivates to include it into our model.

Regarding the electron pockets, the diagonalization of  $h_X$  ( $h_Y$ ) gives two bands, of which only one crosses the Fermi level and forms the electron pocket around  $X$  ( $Y$ ). The electron pockets at  $X$  and  $Y$  are related by  $C_4$  symmetry, i.e. they map onto each other under a rotation by  $\pi/2$ . Due to the non-diagonal hybridization  $v_{X/Y}(k)$ , the transformation from orbital to band basis is not a simple rotation, see App. B.1 for details. The dispersion of these fermions is

$$\xi_{e1} = k_x^2/(2m_{ex}) + k_y^2/(2m_{ey}) - \mu_e \quad (5.4)$$

$$\xi_{e2} = k_x^2/(2m_{ey}) + k_y^2/(2m_{ex}) - \mu_e. \quad (5.5)$$

For simplicity we assume  $m_{ex} = m_{ey} = m_e$ , i.e., set  $\xi_{e1} = \xi_{e2} = \xi_e = k^2/(2m_e) - \mu_e$ . We checked that keeping  $m_{ex}$  and  $m_{ey}$  different will not change the pRG equations, once we properly rescale the couplings.

### 5.2.2. The Toy Model

In the toy model, which we analyze prior to the full one, we approximate the orbital content of the two electron pockets as pure  $d_{xy}$ . In this case, the electron dispersions are already diagonal in the orbital basis, i.e. orbital and band representations are identical. Our notation for the electron operators is in this approximation  $\psi_{X/Y,k,\sigma} = f_{1/2,k}$ , where 1/2 just labels the pockets. This toy model allows us to study the impact of the fifth pocket in a transparent way. Furthermore, we expect that the toy model already captures a substantial part of the physics of the full model, because adiabatically changing the tight-binding parameters of the underlying lattice model, one can move the spectral weight from  $d_{xz}(d_{yz})$  to  $d_{xy}$  orbital everywhere on the electron pockets [230]. There are, however, several features of the full model, which are not captured by the toy model. These are caused by the interactions which involve both  $xz/yz$  and  $xy$ -orbital states on the electron pockets.

### 5.2.3. Interactions

#### Toy Model

The toy model contains 14 couplings within the subset of the two electron and the two  $\Gamma$ -centered hole pockets [122], and 7 couplings involving fermions near the  $M$ -hole pocket, so the total number of couplings is 21. In terms of the spinor components defined above, the 14 interaction terms are

$$\begin{aligned}
 H_I^{4ps} = & U_1 \sum' [f_{1\sigma}^\dagger f_{1\sigma} d_{1\sigma'}^\dagger d_{1\sigma'} + f_{2\sigma}^\dagger f_{2\sigma} d_{2\sigma'}^\dagger d_{2\sigma'}] + \bar{U}_1 \sum' [f_{2\sigma}^\dagger f_{2\sigma} d_{1\sigma'}^\dagger d_{1\sigma'} + f_{1\sigma}^\dagger f_{1\sigma} d_{2\sigma'}^\dagger d_{2\sigma'}] \\
 & + U_2 \sum' [f_{1\sigma}^\dagger d_{1\sigma} d_{1\sigma'}^\dagger f_{1\sigma'} + f_{2\sigma}^\dagger d_{2\sigma} d_{2\sigma'}^\dagger f_{2\sigma'}] + \bar{U}_2 \sum' [f_{1\sigma}^\dagger d_{2\sigma} d_{2\sigma'}^\dagger f_{1\sigma'} + f_{2\sigma}^\dagger d_{1\sigma} d_{1\sigma'}^\dagger f_{2\sigma'}] \\
 & + \frac{U_3}{2} \sum' [f_{1\sigma}^\dagger d_{1\sigma} f_{1\sigma'}^\dagger d_{1\sigma'} + f_{2\sigma}^\dagger d_{2\sigma} f_{2\sigma'}^\dagger d_{2\sigma'} + h.c.] \\
 & + \frac{\bar{U}_3}{2} \sum' [f_{1\sigma}^\dagger d_{2\sigma} f_{1\sigma'}^\dagger d_{2\sigma'} + f_{2\sigma}^\dagger d_{1\sigma} f_{2\sigma'}^\dagger d_{1\sigma'} + h.c.] \\
 & + \frac{U_4}{2} \sum' [d_{1\sigma}^\dagger d_{1\sigma} d_{1\sigma'}^\dagger d_{1\sigma'} + d_{2\sigma}^\dagger d_{2\sigma} d_{2\sigma'}^\dagger d_{2\sigma'}] + \frac{\bar{U}_4}{2} \sum' [d_{1\sigma}^\dagger d_{2\sigma} d_{1\sigma'}^\dagger d_{2\sigma'} + d_{2\sigma}^\dagger d_{1\sigma} d_{2\sigma'}^\dagger d_{1\sigma'}] \\
 & + \tilde{U}_4 \sum' d_{1\sigma}^\dagger d_{1\sigma} d_{2\sigma'}^\dagger d_{2\sigma'} + \tilde{\bar{U}}_4 \sum' d_{1\sigma}^\dagger d_{2\sigma} d_{2\sigma'}^\dagger d_{1\sigma'} \\
 & + \frac{U_5}{2} \sum' [f_{1\sigma}^\dagger f_{1\sigma} f_{1\sigma'}^\dagger f_{1\sigma'} + f_{2\sigma}^\dagger f_{2\sigma} f_{2\sigma'}^\dagger f_{2\sigma'}] + \frac{\bar{U}_5}{2} \sum' [f_{1\sigma}^\dagger f_{2\sigma} f_{1\sigma'}^\dagger f_{2\sigma'} + f_{2\sigma}^\dagger f_{1\sigma} f_{2\sigma'}^\dagger f_{1\sigma'}] \\
 & + \tilde{U}_5 \sum' f_{1\sigma}^\dagger f_{1\sigma} f_{2\sigma'}^\dagger f_{2\sigma'} + \tilde{\bar{U}}_5 \sum' f_{1\sigma}^\dagger f_{2\sigma} f_{2\sigma'}^\dagger f_{1\sigma'}, \tag{5.6}
 \end{aligned}$$

where the sum  $\sum'$  denotes the summation over spin  $\sigma, \sigma'$ , momenta  $\mathbf{k}_1 + \mathbf{k}_2 - \mathbf{k}_3 - \mathbf{k}_4 = 0$  and includes the normalization factor  $1/N$ . The other 7 couplings are

$$\begin{aligned}
 H_I^{5p} = & U_{1n} \sum' [d_{3\sigma}^\dagger d_{3\sigma} f_{1\sigma'}^\dagger f_{1\sigma'} + d_{3\sigma}^\dagger d_{3\sigma} f_{2\sigma'}^\dagger f_{2\sigma'}] + U_{2n} \sum' [d_{3\sigma}^\dagger f_{1\sigma} f_{1\sigma'}^\dagger d_{3\sigma'} + d_{3\sigma}^\dagger f_{2\sigma} f_{2\sigma'}^\dagger d_{3\sigma'}] \\
 & + \frac{U_{3n}}{2} \sum' [d_{3\sigma}^\dagger f_{1\sigma} d_{3\sigma'}^\dagger f_{1\sigma'} + d_{3\sigma}^\dagger f_{2\sigma} d_{3\sigma'}^\dagger f_{2\sigma'} + h.c.] + \frac{U_{4n}}{2} \sum' d_{3\sigma}^\dagger d_{3\sigma} d_{3\sigma'}^\dagger d_{3\sigma'} \\
 & + U_a \sum' [d_{3\sigma}^\dagger d_{3\sigma} d_{1\sigma'}^\dagger d_{1\sigma'} + d_{3\sigma}^\dagger d_{3\sigma} d_{2\sigma'}^\dagger d_{2\sigma'}] + U_b \sum' [d_{3\sigma}^\dagger d_{1\sigma} d_{1\sigma'}^\dagger d_{3\sigma'} + d_{3\sigma}^\dagger d_{2\sigma} d_{2\sigma'}^\dagger d_{3\sigma'}] \\
 & + \frac{U_c}{2} \sum' [d_{3\sigma}^\dagger d_{1\sigma} d_{3\sigma'}^\dagger d_{1\sigma'} + d_{3\sigma}^\dagger d_{2\sigma} d_{3\sigma'}^\dagger d_{2\sigma'} + h.c.] \tag{5.7}
 \end{aligned}$$

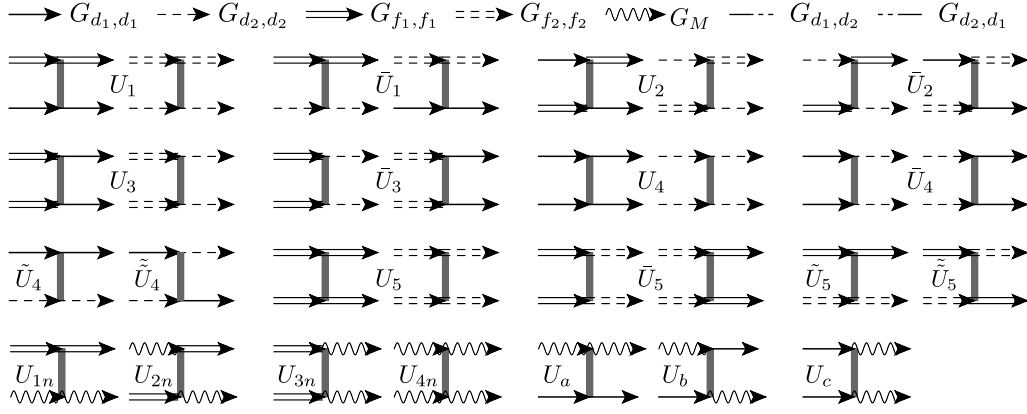


Figure 5.2.: Diagrammatic representation of the 21 interaction terms in the toy model. Each interaction term is invariant under  $C_4$  rotations. We also show the notation for the different propagators.

The interactions of the toy model are sketched in Fig. 5.2. Each single interaction term in Eq. (5.6) and Eq. (5.7) obeys the  $C_4$  symmetry separately, which is why they do not need to flow equally under the RG.

The bare values of the 21 couplings are expressed in terms of the parameters of the microscopic model for intra-orbital and inter-orbital interactions between fermions. The commonly used model approximates all interactions as local in real space:

$$\begin{aligned}
 H_I = & U \sum_{i, \mu} n_{i, \mu, \uparrow} n_{i, \mu, \downarrow} + \frac{U'}{2} \sum_{i, \mu \neq \mu'} n_{i, \mu} n_{i, \mu'} + \frac{J}{2} \sum_{i, \mu \neq \mu'} \sum_{\sigma, \sigma'} d_{i, \mu, \sigma}^\dagger d_{i, \mu', \sigma'}^\dagger d_{i, \mu', \sigma'} d_{i, \mu, \sigma} \\
 & + \frac{J'}{2} \sum_{i, \mu \neq \mu'} \sum_{\sigma, \sigma'} d_{i, \mu, \sigma}^\dagger d_{i, \mu, \sigma'}^\dagger d_{i, \mu', \sigma'} d_{i, \mu', \sigma}.
 \end{aligned} \tag{5.8}$$

Here the sums run over the sites  $i$ , the spin components  $\sigma$ , and the three orbitals  $\mu = xy, xz, yz$ . The density operator on site  $i$  in orbital  $\mu$  is labeled by  $n_{i, \mu} = \sum_{\sigma} n_{i, \mu, \sigma}$  and  $n_{i, \mu, \sigma} = d_{i, \mu, \sigma}^\dagger d_{i, \mu, \sigma}$ . The interactions in Eq. (5.8) involve the Hubbard interaction  $U$  between electrons on the same orbital, the onsite repulsion  $U'$  between electrons in different orbitals, the Hund's rule coupling  $J$  and the pair-hopping term  $J'$ . By comparing with Eq. (5.8), we obtain the bare values of the 21 couplings

$$\begin{aligned}
 U &= U_4 = U_5 = \bar{U}_5 = \tilde{U}_5 = \tilde{\bar{U}}_5 = U_{1n} = U_{2n} = U_{3n} = U_{4n} \\
 U' &= U_1 = \bar{U}_1 = \tilde{U}_4 = U_a \quad J = U_2 = \bar{U}_2 = \tilde{\bar{U}}_4 = U_b \quad J' = U_3 = \bar{U}_3 = \bar{U}_4 = U_c
 \end{aligned} \tag{5.9}$$

### Full Model

In the full model with  $d_{xz}/d_{xy}$  and  $d_{yz}/d_{xy}$  orbital content of fermions near the electron pockets, 19 more couplings are allowed by symmetry. This increases the total number of the  $C_4$ -symmetric interaction terms to 40. Of 19 new couplings, 13 are obtained by substituting  $f_1$  and  $f_2$  by  $f_{31}$  and  $f_{32}$  in Eqs. (5.6) and (5.7)

$$\begin{aligned}
 H_I^{(2)} = & V_1 \sum' [f_{31\sigma}^\dagger f_{31\sigma} d_{1\sigma'}^\dagger d_{1\sigma'} + f_{32\sigma}^\dagger f_{32\sigma} d_{2\sigma'}^\dagger d_{2\sigma'}] \\
 & + \bar{V}_1 \sum' [f_{32\sigma}^\dagger f_{32\sigma} d_{1\sigma'}^\dagger d_{1\sigma'} + f_{31\sigma}^\dagger f_{31\sigma} d_{2\sigma'}^\dagger d_{2\sigma'}]
 \end{aligned}$$

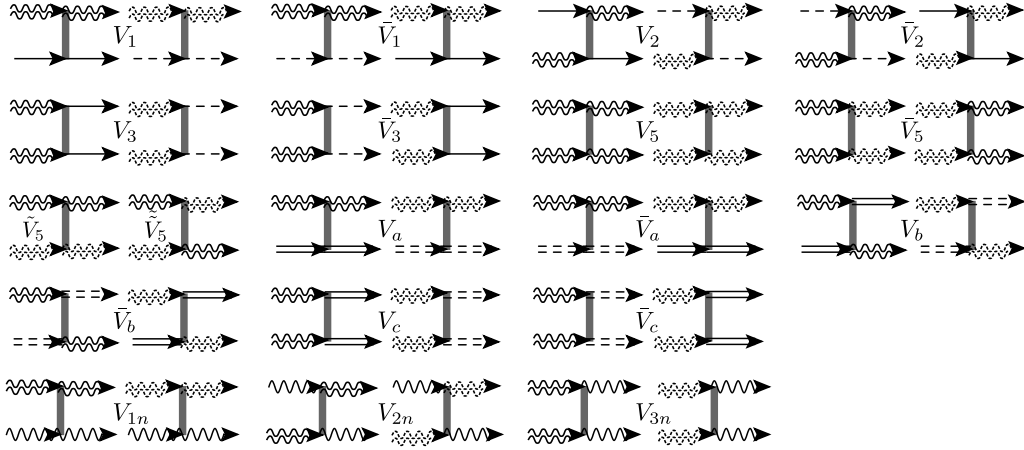


Figure 5.3.: Additional interactions allowed by  $C_4$  symmetry in the full model. The double (dashed) wavy line represents fermions with  $xy$  orbital index on the electron pocket at Y (X).

$$\begin{aligned}
& + V_2 \sum' [f_{31\sigma}^\dagger d_{1\sigma}^\dagger d_{1\sigma'}^\dagger f_{31\sigma'} + f_{32\sigma}^\dagger d_{2\sigma}^\dagger d_{2\sigma'}^\dagger f_{32\sigma'}] \\
& + \bar{V}_2 \sum' [f_{31\sigma}^\dagger d_{2\sigma}^\dagger d_{2\sigma'}^\dagger f_{31\sigma'} + f_{32\sigma}^\dagger d_{1\sigma}^\dagger d_{1\sigma'}^\dagger f_{32\sigma'}] \\
& + \frac{V_3}{2} \sum' [f_{31\sigma}^\dagger d_{1\sigma} f_{31\sigma'}^\dagger d_{1\sigma'} + f_{32\sigma}^\dagger d_{2\sigma} f_{32\sigma'}^\dagger d_{2\sigma'} + h.c.] \\
& + \frac{\bar{V}_3}{2} \sum' [f_{31\sigma}^\dagger d_{2\sigma} f_{31\sigma'}^\dagger d_{2\sigma'} + f_{32\sigma}^\dagger d_{1\sigma} f_{32\sigma'}^\dagger d_{1\sigma'} + h.c.] \\
& + \frac{V_5}{2} \sum' [f_{31\sigma}^\dagger f_{31\sigma} f_{31\sigma'}^\dagger f_{31\sigma'} + f_{32\sigma}^\dagger f_{32\sigma} f_{32\sigma'}^\dagger f_{32\sigma'}] \\
& + \frac{\bar{V}_5}{2} \sum' [f_{31\sigma}^\dagger f_{32\sigma} f_{31\sigma'}^\dagger f_{32\sigma'} + f_{32\sigma}^\dagger f_{31\sigma} f_{32\sigma'}^\dagger f_{31\sigma'}] \\
& + \tilde{V}_5 \sum' f_{31\sigma}^\dagger f_{31\sigma} f_{32\sigma'}^\dagger f_{32\sigma'} + \tilde{\bar{V}}_5 \sum' f_{31\sigma}^\dagger f_{32\sigma} f_{32\sigma'}^\dagger f_{31\sigma'} \\
& + V_{1n} \sum' [d_{3\sigma}^\dagger d_{3\sigma} f_{31\sigma'}^\dagger f_{31\sigma'} + d_{3\sigma}^\dagger d_{3\sigma} f_{32\sigma'}^\dagger f_{32\sigma'}] \\
& + V_{2n} \sum' [d_{3\sigma}^\dagger f_{31\sigma} f_{31\sigma'}^\dagger d_{3\sigma'} + d_{3\sigma}^\dagger f_{32\sigma} f_{32\sigma'}^\dagger d_{3\sigma'}] \\
& + \frac{V_{3n}}{2} \sum' [d_{3\sigma}^\dagger f_{31\sigma} d_{3\sigma'}^\dagger f_{31\sigma'} + d_{3\sigma}^\dagger f_{32\sigma} d_{3\sigma'}^\dagger f_{32\sigma'} + h.c.]. \tag{5.10}
\end{aligned}$$

The remaining six come from interactions involving  $xy$  and  $xz/yz$  orbital states on the electron pockets

$$\begin{aligned}
H_I^{(2)} = & V_a \sum' [f_{31\sigma}^\dagger f_{31\sigma} f_{1\sigma'}^\dagger f_{1\sigma'} + f_{32\sigma}^\dagger f_{32\sigma} f_{2\sigma'}^\dagger f_{2\sigma'}] \\
& + \bar{V}_a \sum' [f_{32\sigma}^\dagger f_{32\sigma} f_{1\sigma'}^\dagger f_{1\sigma'} + f_{31\sigma}^\dagger f_{31\sigma} f_{2\sigma'}^\dagger f_{2\sigma'}] \\
& + V_b \sum' [f_{31\sigma}^\dagger f_{1\sigma} f_{1\sigma'}^\dagger f_{31\sigma'} + f_{32\sigma}^\dagger f_{2\sigma} f_{2\sigma'}^\dagger f_{32\sigma'}] \\
& + \bar{V}_b \sum' [f_{31\sigma}^\dagger f_{2\sigma} f_{2\sigma'}^\dagger f_{31\sigma'} + f_{32\sigma}^\dagger f_{1\sigma} f_{1\sigma'}^\dagger f_{32\sigma'}] \\
& + \frac{V_c}{2} \sum' [f_{31\sigma}^\dagger f_{1\sigma} f_{31\sigma'}^\dagger f_{1\sigma'} + f_{32\sigma}^\dagger f_{2\sigma} f_{32\sigma'}^\dagger f_{2\sigma'} + h.c.] \\
& + \frac{\bar{V}_c}{2} \sum' [f_{31\sigma}^\dagger f_{2\sigma} f_{31\sigma'}^\dagger f_{2\sigma'} + f_{32\sigma}^\dagger f_{1\sigma} f_{32\sigma'}^\dagger f_{1\sigma'} + h.c.]. \tag{5.11}
\end{aligned}$$

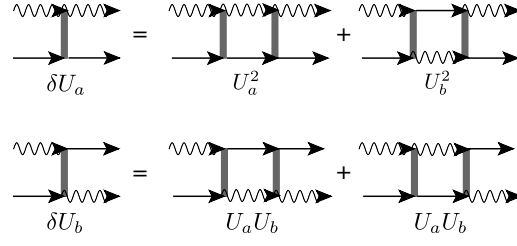


Figure 5.4.: Diagrammatic representation of the 1-loop renormalizations of the interactions  $U_a$  and  $U_b$ . They decouple from the remaining interactions and are representative for the subgroup of interactions flowing to zero.

We show these additional interactions graphically in Fig. 5.3. Note that, in contrast to the simplified model,  $f_{1/2}$  now labels fermions with  $yz/xz$  orbital content, whereas  $f_{31,32}$  labels fermions with  $xy$  orbital content. The bare values of the 40 couplings are again expressed in terms of  $U, U', J, J'$ , and are given by

$$\begin{aligned}
 U &= U_1 = U_2 = U_3 = U_4 = U_5 = \bar{U}_5 = U_{4n} = V_5 = \bar{V}_5 = \tilde{V}_5 = \tilde{\tilde{V}}_5 = V_{1n} = V_{2n} = V_{3n} \\
 U' &= \bar{U}_1 = \tilde{U}_4 = \tilde{U}_5 = U_{1n} = U_a = V_a = \bar{V}_a = V_1 = \bar{V}_1 \\
 J &= \bar{U}_2 = \tilde{U}_4 = \tilde{U}_5 = U_{2n} = U_b = V_b = \bar{V}_b = V_2 = \bar{V}_2 \\
 J' &= \bar{U}_3 = \bar{U}_4 = \bar{U}_5 = U_{3n} = U_c = V_c = \bar{V}_c = V_3 = \bar{V}_3.
 \end{aligned} \tag{5.12}$$

### 5.3. Analytic Parquet RG for the 5-Pocket Model

We employ the pRG approach introduced in Sec. 2.2.1 to study the hierarchy of the orders that the system develops at low energies. The pRG procedure allows us to see how the susceptibilities in different ordering channels evolve as the system flows to low energies, including their mutual feedback. As explained earlier, we describe the flow of interactions in terms of the RG scale  $L = \log \Lambda_{UV}/E$ , where  $\Lambda_{UV}$  is the UV-cutoff, generally of the order of the bandwidth. The logarithmic energy scale  $L$  appears due to the fact that the polarization bubbles in the particle-particle channel at zero total momentum *and* the particle-hole channel at momenta  $(\pi, 0)$  and  $(0, \pi)$  are logarithmic. As a result of the integration procedure, we obtain coupled differential equations -the flow equations- for all the interactions, describing their evolution with  $L$ . We solve for the running couplings  $U_i(L)$ , which typically flow to strong coupling. But thereby they approach so-called fixed trajectories (FTs) along which their ratios become constant. We use these solution for the couplings as inputs to calculate susceptibilities in different ordering channels (SDW, CDW, superconducting and Pomeranchuk channels). For an instability to occur the corresponding susceptibility must diverge. We recall that it depends on the hierarchy between the scale of divergence  $L_{cr}$  and the scale of the Fermi energy  $L_F$ , which instability actually develops. Below we show the pRG analysis for the toy model and the full model.

#### 5.3.1. PRG for the Toy Model

##### PRG Equations and Fixed Trajectories

We derive the pRG equations by collecting all possible one-loop diagrams that contribute to the logarithmic renormalization of each of the interactions. The procedure has been described in Ref. [122] for a simplified 4-pocket, 2-orbital model and in Ref. [149] for a 3-pocket, 1-orbital

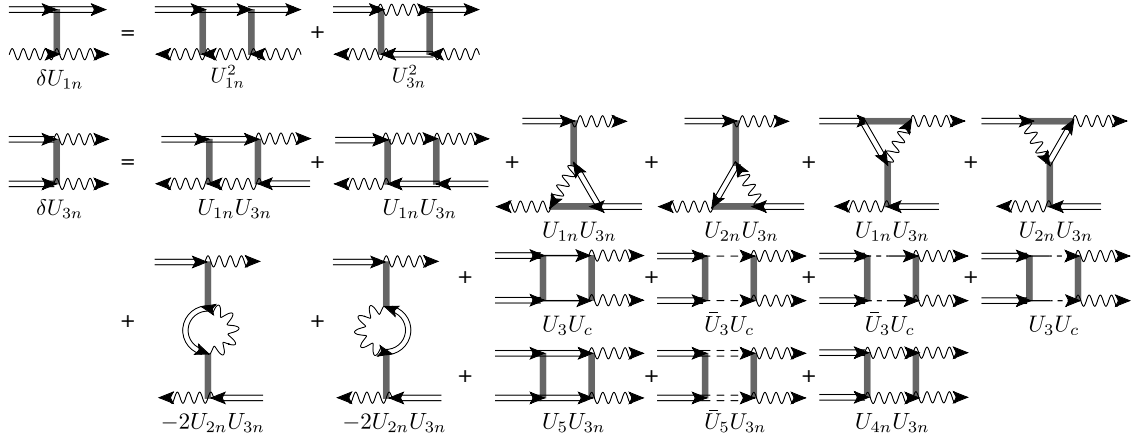


Figure 5.5.: Diagrammatic representation of the 1-loop renormalization of the interactions  $U_{1n}$  and  $U_{3n}$ .

model. We obtain the pRG equations for our 5-pocket model by combining and modifying the pRG equations from these two models. Similar to Ref. [122], we find that the pRG equations for six combinations of the couplings  $(\tilde{U}_4 \pm \tilde{U}_5)$ ,  $(\tilde{U}_5 \pm \tilde{U}_3)$  and  $(\tilde{U}_a \pm \tilde{U}_b)$  decouple from the other RG equations. These combinations all flow to zero if their bare values are positive, which is the case for  $U' \geq J$  (see App. B.2). We assume that this inequality holds. If it does not hold, the system may develop a superconducting instability in the spin-triplet  $A_{2g}$  channel [241]. We show examples for the one-loop diagrams that renormalize representative couplings for this set in Fig. 5.4.

Furthermore we find that the system always flows to  $U_i = \bar{U}_i$  so that we set them equal in the following. The pRG flow of the remaining ten couplings determines the FTs. Exemplary one-loop renormalizations are presented in Fig. 5.5. Upon rescaling to dimensionless couplings, the flow equations read

$$\begin{aligned}
 \dot{u}_1 &= u_1^2 + \frac{u_3^2}{a^2} & \dot{u}_{1n} &= u_{1n}^2 + \frac{u_{3n}^2}{a_n^2} \\
 \dot{u}_2 &= 2u_2(u_1 - u_2) & \dot{u}_{2n} &= 2u_{2n}(u_{1n} - u_{2n}) \\
 \dot{u}_3 &= 2u_3(2u_1 - u_2 - u_5) - 2bu_3u_4 - u_{3n}u_c & \dot{u}_{3n} &= 2u_{3n}(2u_{1n} - u_{2n} - u_5) - u_{3n}u_{4n} - 2bu_3u_c \\
 \dot{u}_4 &= -2bu_4^2 - 2u_3^2 - 2u_c^2 & \dot{u}_{4n} &= -u_{4n}^2 - 2u_{3n}^2 - 2bu_c^2 \\
 \dot{u}_5 &= -2u_5^2 - 2bu_3^2 - u_{3n}^2 & \dot{u}_c &= -2bu_4u_c - u_{4n}u_c - 2u_3u_{3n}
 \end{aligned} \tag{5.13}$$

The derivatives are with respect to  $L$  and  $a > 1$ ,  $a_n > 1$ , and  $b$  are parameters, which depend on the ratio of quasiparticle masses near each of the Fermi pockets. When the masses on the two  $\Gamma$ -centered hole pockets are equal, as we assume below for simplicity,  $b = 1$  (reasonable  $b \neq 1$  do not change the results). We give the full set of pRG equations and the definitions of the parameters in App. B.2. From an RG point of view, we will take the parameters as free quantities and study their influence on the flow.

### The Solution of PRG Equations

The solution of Eq. (5.13) reveals a flow to strong coupling and thus signals potential instabilities of the Fermi liquid (Fig. 5.6). These instabilities are represented by different fixed trajectories along which the couplings diverge and their ratios tend to fixed values. This can be seen in

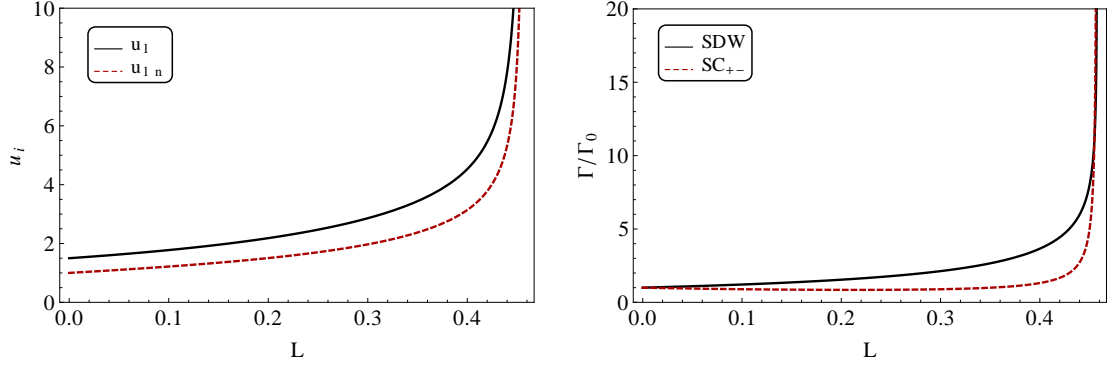


Figure 5.6.: (Left) Flow to the 4pFT for representative couplings  $u_1$  and  $u_{1n}$ . Bare values and parameters are  $U'/U = 1.5$ ,  $J = J'$  with  $J/U = 0.3$  and  $a = a_n = b = 1$ . (Right) Flow of the SDW and SC  $s^{+-}$  vertices for the same flow. Note the crossing at the end of the flow.

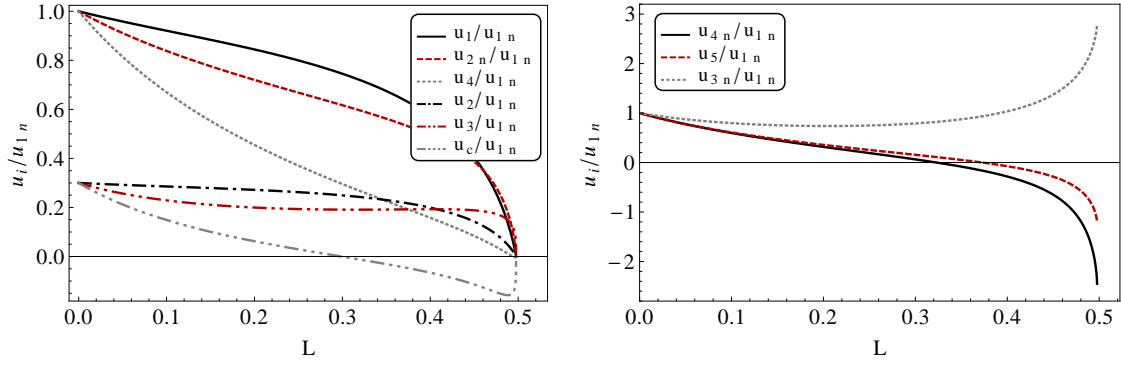


Figure 5.7.: Ratios of couplings for the flow to the 3-pocket fixed trajectory (3pFT) in the toy model for bare values  $U = U'$ ,  $J = J'$  and  $a = a_n = 1$ . All ratios tend to zero (left), except for those within the triad of electron pockets and the  $M$ -centered hole pocket (right).

Fig. 5.6 and Fig. 5.7. Accordingly, we single out one of the coupling, say  $u_0$ , and write all other couplings as

$$u_i = \gamma_i u_0, \quad (5.14)$$

where we choose  $u_0$  to be one of the leading divergent, positive couplings. Solving for the fixed trajectory of the set of coupled pRG equations, Eq. (5.13), then reduces to finding the fixed point solution of

$$\beta_i := \partial_L \gamma_i = \frac{1}{u_i} (\partial_L u_i - \gamma_i \partial_L u_0) = 0. \quad (5.15)$$

The fixed trajectory is stable if small perturbations around the fixed point do not grow, i.e. the stability matrix  $\partial \beta_i / \partial \gamma_j|_{\gamma^*}$ , which describes the linearized flow around the fixed point, should

have only negative eigenvalues. For the toy model we find two stable fixed trajectories

4pFT	3pFT
$u_i = \gamma_i u_1$	$u_i = \gamma_i u_{1n}$
$u_1 = \frac{1}{1 + \gamma_3^2/a^2} \frac{1}{L_0 - L}$	$u_{1n} = \frac{1}{1 + \gamma_{3n}^2/a_n^2} \frac{1}{L_0 - L}$
$\gamma_2 = \gamma_{1n} = \gamma_{2n} = \gamma_{3n} = \gamma_{4n} = \gamma_c = 0$	$\gamma_{2n} = \gamma_c = \gamma_1 = \gamma_2 = \gamma_3 = \gamma_4 = 0$
$\gamma_3 = \pm a \sqrt{8a^2 - 1 + 4\sqrt{1 - a^2 + 4a^4}}$	$\gamma_{3n} = \pm a_n \sqrt{4a_n^2 - 1 + 2\sqrt{4 - 2a_n^2 + 4a_n^4}}$
$\gamma_4 = \gamma_5 = 1 - 2a^2 - \sqrt{1 - a^2 + 4a^4}$	$\gamma_{4n} = 2\gamma_5 = 2 - 2a_n^2 - \sqrt{4 - 2a_n^2 + 4a_n^4}$

For the first stable FT (4pFT) all  $\gamma_{in}$  involving the  $M$  pocket vanish, so the 5-pocket model effectively reduces to the four-pocket model. This does not mean that the interactions  $u_{in}$  vanish, only the ratios  $u_{in}/u_i$  tend to zero. On a more careful look we find that the couplings  $u_{in}$  still grow, but with smaller exponents, i.e. as  $u_{in} \propto 1/(L_0 - L)^{a_i}$ ,  $a_i < 1$ . These subleading terms are not essential for the interplay between superconductivity and other orders, but they are important for the structure of the SC gap. For the second stable FT (3pFT) the situation is the opposite – interactions involving the two  $\Gamma$ -centered hole pockets grow more slowly than the interactions involving the other three pockets, i.e., along the FT the five-pocket model effectively reduces to the three-pocket model consisting of two electron pockets and the  $M$ -hole pocket. We checked the stability of the 4pFT and the 3pFT by expanding around them and verified that all eigenvalues are negative. Whether the system flows to one FT or the other is determined by the bare values  $U, U', J, J'$  and the parameters  $a$  and  $a_n$ . We show the phase diagram for different bare interactions in Fig. 5.8. The result of our study of the stability regimes of the 4pFT and the 3pFT at various  $a_n/a$  is presented in Fig. 5.9. We also find a symmetry-enhanced fixed trajectory in the sense that  $u_1 = u_{1n}, u_3/a = u_{3n}/a_n$ , etc (see App. B.2.2 for details). However, performing the linear stability analysis, we find one positive eigenvalue, implying that this FT is unstable. On the phase diagram in Fig. 5.8 the symmetric FT determines the separatrix between the basins of attraction of the two stable FTs.

### Susceptibilities

The next step in the pRG analysis is to use the couplings along the FTs as inputs and compute the susceptibilities in different channels,  $\chi_j$ , to decide which order wins and develops at low energies. We introduce vertices  $\Gamma_i$  that describe the coupling between fermions and order parameters. The vertices in turn determine the susceptibilities in the corresponding ordering channel, whose divergence would signal a phase transition. Here we focus on SDW, CDW, and SC channels. The analysis of the susceptibilities in the Pomeranchuk channel is discussed afterwards. The susceptibilities in SC, SDW and CDW channels are given by

$$\chi_i \propto \int_L dL' \Gamma_i^2(L'), \quad (5.16)$$

where the vertices renormalize according to the one-loop diagrams shown in Fig. 5.10. In analytic form, the pRG equations for the vertices in the SDW and CDW channels are

$$\begin{aligned} \partial_L \Gamma_{SDW}^\Gamma &= \left(u_1 + \frac{u_3}{a}\right) \Gamma_{SDW}^\Gamma & \partial_L \Gamma_{CDW}^\Gamma &= \left(u_1 - 2u_2 - \frac{u_3}{a}\right) \Gamma_{CDW}^\Gamma \\ \partial_L \Gamma_{SDW}^M &= \left(u_{1n} + \frac{u_{3n}}{a_n}\right) \Gamma_{SDW}^M & \partial_L \Gamma_{CDW}^M &= \left(u_{1n} - 2u_{2n} - \frac{u_{3n}}{a_n}\right) \Gamma_{CDW}^M. \end{aligned} \quad (5.17)$$



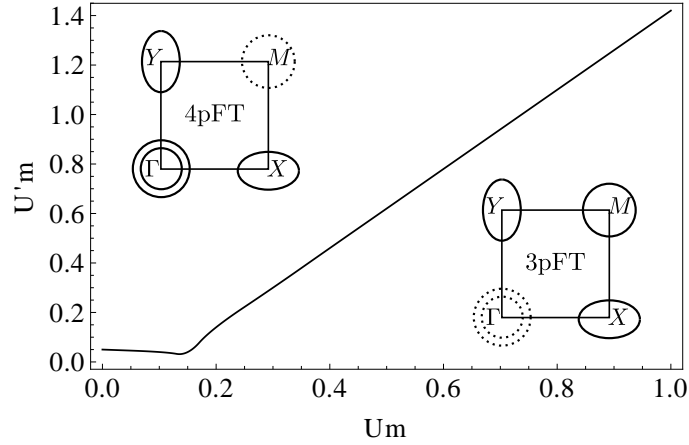


Figure 5.8.: Fixed trajectories of the pRG flow for different values of  $U, U'$  for fixed  $a = a_n = 1$  and  $J = J' = 0.3/m$ . The interactions are measured in terms of the quasiparticle mass  $m$ . Mass ratios are all set to one. 3pFT denotes the FT along which interactions involving fermions near the  $\Gamma$ -centered hole pockets become weaker compared to the interactions within the subset of the two electron pockets and the  $M = (\pi, \pi)$ -hole pocket, and 4pFT is the FT along which interactions involving fermions near the  $M$ -hole pocket get weaker.

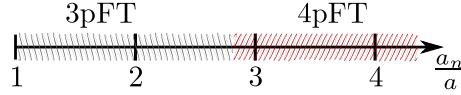


Figure 5.9.: Fixed trajectory at the end of the flow for different values of  $a_n/a$ . Bare values are  $U = U', J = J'$  and  $J/U = 0.3$ .

Here  $\Gamma_{SDW}^{\Gamma, M}$  are SDW vertices between fermions near one of the electron pockets and either the  $\Gamma$ -centered or the  $M$ -hole pocket (and analogously for  $\Gamma_{SDW}^{\Gamma, M}$ ). The pRG flow of the vertices in the particle-particle channel obeys

$$\partial_L \begin{pmatrix} \Gamma_{SC}^e \\ \Gamma_{SC}^\Gamma \\ \Gamma_{SC}^M \end{pmatrix} = \begin{pmatrix} -2u_5 & -2u_3 & -2u_{3n} \\ -2u_3 & -2u_4 & -2u_c \\ -u_{3n} & -u_c & -u_{4n} \end{pmatrix} \begin{pmatrix} \Gamma_{SC}^e \\ \Gamma_{SC}^\Gamma \\ \Gamma_{SC}^M \end{pmatrix}, \quad (5.18)$$

$\Gamma_{SC}^{e, \Gamma, M}$  are SC vertices for fermions near one of these sets of pockets. By inserting the values for  $u_i$  along the FTs and solving Eqs. (5.17) and (5.18), we obtain  $\Gamma_i \propto (L_0 - L)^{\beta_i}$  and  $\chi_i \propto (L_0 - L)^{2\beta_i - 1}$ . Thus in order to diverge the vertex exponent must satisfy  $\beta \geq 1/2$ . Along the 4pFT and 3pFT, the exponents of the density waves are

$$\begin{aligned} \beta_{SDW}^{(4p)} &= \frac{1 + \gamma_3/a}{1 + \gamma_3^2/a^2} & \beta_{CDW}^{(4p)} &= \frac{1 - \gamma_3/a}{1 + \gamma_3^2/a^2} \\ \beta_{SDW}^{(3p)} &= \frac{1 + \gamma_{3n}/a_n}{1 + \gamma_{3n}^2/a_n^2} & \beta_{CDW}^{(3p)} &= \frac{1 - \gamma_{3n}/a_n}{1 + \gamma_{3n}^2/a_n^2}. \end{aligned} \quad (5.19)$$

Note that  $\gamma_3, \gamma_{3n}$  also depend on  $a, a_n$  in these expressions. The exponents attain their maximal values at  $a = 1, a_n = 1$  with  $\beta_{SDW}^{(4p)} \approx 0.30$ ,  $\beta_{CDW}^{(4p)} \approx -0.18$  and  $\beta_{SDW}^{(3p)} \approx 0.43$ ,  $\beta_{CDW}^{(3p)} \approx -0.20$ . These values do not lead to a divergent susceptibility, i.e. the corresponding order does not develop if the normal state becomes unstable before the Fermi energy is reached. The

diagonalization of Eq. (5.18) yields for the 3pFT and the 4pFT

$$\begin{aligned}\beta_{SC,+/-++}^{(4p)} &= \frac{-\gamma_4 - \gamma_5 \pm \sqrt{(\gamma_4 - \gamma_5)^2 + 4\gamma_3^2/a^2}}{1 + \gamma_3^2/a^2} \\ \beta_{SC,+/-++}^{(3p)} &= \frac{-\gamma_{4n} - 2\gamma_5 \pm \sqrt{(\gamma_{4n} - 2\gamma_5)^2 + 8\gamma_{3n}^2/a_n^2}}{1 + \gamma_{3n}^2/a_n^2}.\end{aligned}\tag{5.20}$$

The largest eigenvalues correspond to the  $s^{+-}$  superconducting state, where the SC vertices have opposite sign on electron and hole pockets. The corresponding exponents satisfy  $\beta_{SC,+/-} > 1/2$ . For  $a = a_n = 1$  they are  $\beta_{SC,+/-}^{(4p)} = 0.86$ , and  $\beta_{SC,+/-}^{(3p)} = 0.72$ . For all  $a$  and  $a_n$ ,  $\beta_{SC} > 1/2$  while  $\beta_{SDW} < 1/2$ , i.e.  $\chi_{SC}$  diverges at  $L = L_0$ , while  $\chi_{SDW}$  remains finite, despite that it is the largest at the beginning of pRG flow. This implies that the system develops SC order but not SDW or CDW order. We show the flow of  $\Gamma_{SDW}^\Gamma$  and  $\Gamma_{SC}^{+-}$  along the 4pFT in Fig. 5.6.

To determine the sign of the superconducting gap on the remaining hole pocket(s), we must include the residual interactions (the once which diverge with smaller exponents). To do this and to verify our analytical reasoning, we solved the set of pRG equations for the couplings and the set of the vertices in the SC channel, Eq. (5.18), numerically. We find two positive (attractive) and one negative eigenvalue in the SC channel. The negative one corresponds to a repulsive interaction in the  $s^{++}$  channel. The positive eigenvalues correspond to  $s^{+-}$  gap structure. For the largest positive eigenvalue along the 3pFT or the 4pFT the gap(s) on the remaining hole pocket(s) align such that the sign of the gap on all three hole pockets is the same (and opposite to the gap sign on the two electron pockets). This is the "conventional"  $s^{+-}$  gap structure. The smaller positive eigenvalue along the 3pFT or the 4pFT actually starts negative at small  $L$  and then changes the sign in the process of the RG flow. For the 4pFT, the gap structure that corresponds to this eigenvalue has the same sign of the gap on the  $M$ -centered hole pocket as on the electron pockets, i.e., there is one sign of the gap on the two  $\Gamma$ -centered hole pockets and another sign on the other three pockets. For the 3pFT and for this eigenvalue, the sign of the gap on the  $\Gamma$ -centered hole pockets and on the electron pockets is the same, and opposite to that on the  $M$ -hole pocket. A gap structure of this kind was proposed in Ref. [228] and termed as "orbital anti-phase". Our RG analysis shows that along the fixed trajectory such a state is subleading to a conventional  $s^{+-}$ . Finally, we compute the gap structure along the weakly unstable FT (Eq. (B.7)) and find that it is also a conventional  $s^{+-}$ . The analysis of the magnitudes of the superconducting gaps on different pockets in the SC phase requires one to solve the non-linear gap equations and is beyond the scope of the pRG analysis. Still, the pRG flow points out that the gap on the  $M$  pocket should be larger for the 3pFT than for the 4pFT.

To analyze orbital ordering, we calculate the vertices and susceptibilities in the Pomeranchuk channel with the orbital densities  $n_\mu = d_\mu^\dagger d_\mu$  as order parameters. The analysis is somewhat different than before because the polarization bubbles that renormalize the Pomeranchuk vertices are not logarithmically divergent, as can be seen in Fig. 5.11. However, the scale-dependence of the interaction provides a logarithmic renormalization. Summing only logarithmic terms then leads to pRG equations in the Pomeranchuk channel of the form  $\partial_L \Gamma_\mu \propto \Gamma_\mu^0 \partial_L u$ , i.e.  $\Gamma_\mu \propto \Gamma_\mu^0 (1 + u)$  with initial  $\Gamma_\mu^0$  (see App. B.3 for details). Since the couplings flow as  $u \propto (L_0 - L)^{-1}$ , the Pomeranchuk vertex grows with exponent  $\beta_\mu = 1$  and overtakes the SC vertex at the end of the flow. Note, however, that the renormalization of the Pomeranchuk vertex develops when the couplings become of order one so that corrections to 1-loop RG may

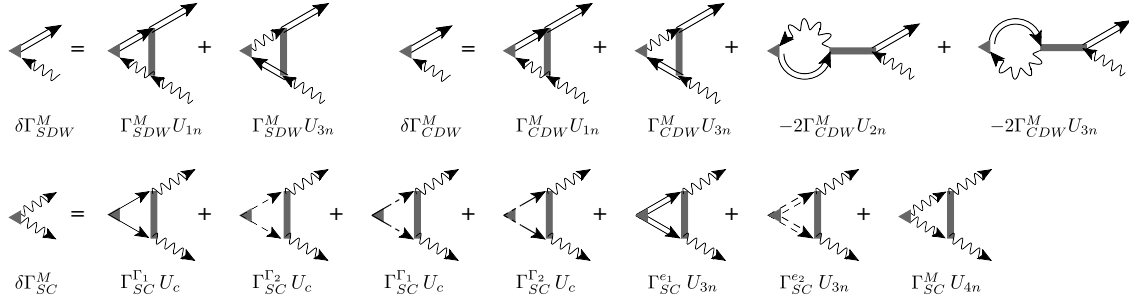


Figure 5.10.: Diagrammatic representation of the 1-loop renormalization of representative SDW, CDW, and SC vertices. In the RG equations of the superconducting vertices, only the combinations  $\Gamma_{SC}^\Gamma := \Gamma_{SC}^{\Gamma_1} + \Gamma_{SC}^{\Gamma_2}$ ,  $\Gamma_{SC}^e := \Gamma_{SC}^{e_1} + \Gamma_{SC}^{e_2}$  appear. Propagator lines are defined in Fig. 5.2.

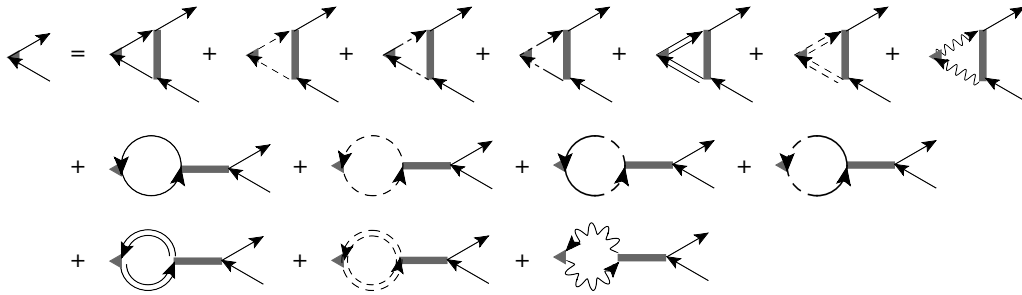


Figure 5.11.: Diagrammatic representation of the 1-loop renormalization of a representative Pomeranchuk vertex corresponding to the orbital density  $n_{xz}$ . The polarization bubbles are not logarithmic as they involve two identical propagators. Propagator lines are define in Fig. 5.2.

contribute. Explicitly the pRG equation of the Pomeranchuk channel for the toy model reads

$$\frac{d}{dL} \begin{pmatrix} \Gamma_{xz}^\Gamma \\ \Gamma_{yz}^\Gamma \\ \Gamma_{xy}^X \\ \Gamma_{xy}^Y \\ \Gamma_{xy}^M \end{pmatrix} = -2 \frac{d}{dL} \begin{pmatrix} u_4 & 0 & \frac{A_e}{A}(2u_1 - u_2) & \frac{A_e}{A}(2u_1 - u_2) & 0 \\ 0 & u_4 & \frac{A_e}{A}(2u_1 - u_2) & \frac{A_e}{A}(2u_1 - u_2) & 0 \\ \frac{A_h}{A}(2u_1 - u_2) & \frac{A_h}{A}(2u_1 - u_2) & u_5 & 0 & \frac{A_M}{A_n}(2u_{1n} - u_{2n}) \\ \frac{A_h}{A}(2u_1 - u_2) & \frac{A_h}{A}(2u_1 - u_2) & 0 & u_5 & \frac{A_M}{A_n}(2u_{1n} - u_{2n}) \\ 0 & 0 & \frac{A_e}{A_n}(2u_{1n} - u_{2n}) & \frac{A_e}{A_n}(2u_{1n} - u_{2n}) & u_{4n} \end{pmatrix} \begin{pmatrix} \Gamma_{xz}^\Gamma \\ \Gamma_{yz}^\Gamma \\ \Gamma_{xy}^X \\ \Gamma_{xy}^Y \\ \Gamma_{xy}^M \end{pmatrix} \quad (5.21)$$

where we have omitted the irrelevant couplings and set  $m_c = m_d$ . As has been already obtained in Ref. [122], the largest eigenvalue of Eq. (5.21) along the 4pFT corresponds to  $s^{+-}$  Pomeranchuk order, where electron and hole densities change in opposite directions. This does not break any symmetry, while it may indicate temperature dependent relative chemical potentials  $\mu_h - \mu_e$ . We obtain the analogous order also along the 3pFT. However the true instability has to occur in a different channel, which breaks a symmetry. Along the 4pFT we reproduce the result of Ref. [122] that this instability develops in the  $d$ -wave Pomeranchuk channel. An instability in this channel leads to a spontaneous orbital order [100–110, 122], i.e., to non-equal densities of fermions on  $d_{xz}$  and  $d_{yz}$  orbitals. We find that no orbital order develops along the 3pFT because the electron and the  $M$  pocket have  $d_{xy}$  character. However, the system still breaks  $C_4$  symmetry by developing an order with  $\langle d_{xy}^\dagger d_{xy} \rangle$  of opposite signs on the two electron pockets (cf. [242]).

Finally, we comment on the behavior in a situation when the system does not reach a

fixed trajectory before the RG scale  $L$  becomes comparable to  $L_F = \log \Lambda / E_F$ . Because the susceptibility in the SDW channel is the largest over a wide range of  $L$  (Fig. 5.6), it is most likely that in this situation the system develops an SDW order. We compare the behavior of the SDW vertices involving fermions from one of the electron pockets and either fermions from the  $\Gamma$ -centered hole pockets ( $\Gamma_{SDW}^\Gamma$ ) or from the  $M$ -pocket ( $\Gamma_{SDW}^M$ ). We find that  $\Gamma_{SDW}^M > \Gamma_{SDW}^\Gamma$  if the flow is towards the 3pFT, and  $\Gamma_{SDW}^\Gamma > \Gamma_{SDW}^M$  if the flow is towards the 4pFT. This implies that in the first case SDW order predominantly involves the triad of two electron pockets and the  $M$  hole pockets, while in the second case it involves two electron pockets and two  $\Gamma$ -centered hole pockets. For the 4-pocket model the SDW order is a checkerboard (Ref. [243]), while for the 3-pocket model SDW order is a stripe. [244–246]. In this respect, our pRG results imply that if the pRG flow is towards the 4pFT, the system may develop a spontaneous orbital order, but there is no spin Ising-nematic order, while if the flow is towards the 3pFT, the system develops an Ising-nematic spin order, but no spontaneous orbital order.

### 5.3.2. PRG For the Full Model

#### PRG Equations and Fixed Trajectories

The analysis of the full 5-pocket model with  $d_{xz}/d_{xy}$  and  $d_{yz}/d_{xy}$  orbital content of the electron pockets is more involved as one has to analyze the set of 40 equations for the coupling constants. We find that now 12 couplings decouple and flow to zero. Furthermore we make the same conjecture as for the toy model, i.e., assume that for stable and weakly unstable fixed trajectories  $U_i = \bar{U}_i$ . This reduces the number of couplings further by 10 and leads to 18 remaining couplings. We present the full set of pRG equations in App. B.4.1. We search for FTs by varying the initial values of the couplings and the ratios of masses of the dispersions. Interestingly, we find much the same behavior as in the toy model. Namely, the five-pocket model effectively becomes either a 4-pocket model (interactions involving the  $M$  pocket get weaker in the process of the pRG flow), or a 3-pocket model (interactions involving the two  $\Gamma$ -centered pockets get weaker). The new feature, not present in the toy model, is that each of these effective models now has two FTs (4pFT<sub>1,2</sub> and 3pFT<sub>1,2</sub>), along which interactions involving fermions from either  $d_{xz}$  ( $d_{yz}$ ) or  $d_{xy}$  regions on the electron pockets become dominant. We verified that the FTs 4pFT<sub>1,2</sub> and 3pFT<sub>1,2</sub> remain stable in the full five-pocket model. That is, at the end of the flow, the electron pockets can be approximated as pure  $d_{xz}$  ( $d_{yz}$ ) or pure  $d_{xy}$ , respectively. There are several “symmetric” FTs, along which a larger subset of couplings remains of the same order. These FTs are again unstable and act as separatrices between the basins of attractions of effective 4-pocket and 3-pocket models. These symmetry-enhanced fixed trajectories possess one or two unstable directions. One of them corresponds to the weakly unstable fixed trajectories that we found in the toy model and separates 4pFT<sub>1</sub> and 3pFT<sub>2</sub>. Further three FTs with only one unstable direction analogously divide the other stable FTs from each other. Additionally there is a high-symmetry FT with two unstable directions, along which all related couplings from the four stable FTs become the same. The explicit solution for the four stable and five weakly unstable fixed trajectories are given in App. B.4.2. We show the phase diagram for different bare interactions in Fig. 5.12.

#### Susceptibilities

As in the toy model, we introduce vertices that couple to different order parameter fields to determine which order develops first at low energies. In the SDW channel, we now have four

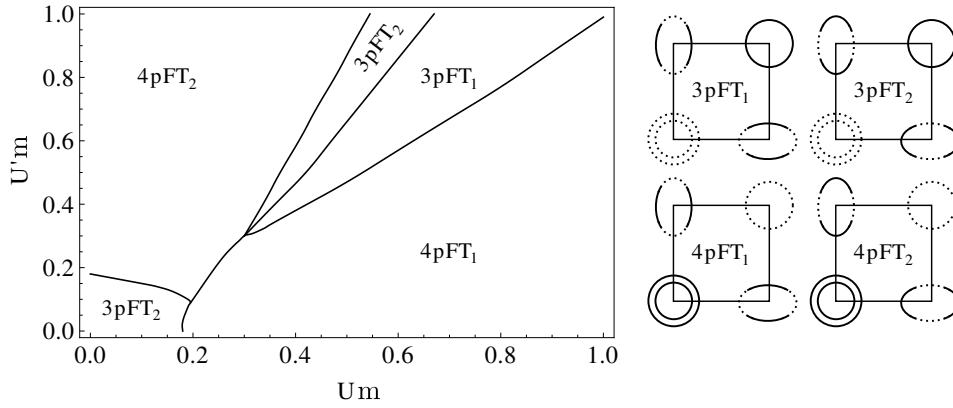


Figure 5.12.: Fixed trajectories of the pRG flow of the full model for different values of  $U, U'$  and fixed  $J = J' = 0.3m$ . The interactions are measured in terms of the quasiparticle mass  $m$ . Mass ratios are all set to one.  $3pFT_{1,2}$  denotes the FT along which interactions involving fermions near the  $\Gamma$ -centered hole pockets become weaker compared to the interactions within the subset of the two electron pockets and the  $M = (\pi, \pi)$ -hole pocket, and  $4pFT_{1,2}$  is the FT along which interactions involving fermions near the  $M$ -hole pocket get weaker. The index 1, 2 distinguishes if contributions of the  $d_{xz}/d_{yz}$  or  $d_{xy}$  character of the electron pockets are dominant.

vertices, where either fermions on electron pockets with  $d_{xz}$  and  $d_{yz}$  or  $d_{xy}$  orbital content, and fermions from either the hole pockets at  $\Gamma$  or  $M$  are involved. Similarly we have to account for four superconducting vertices in the full model. They can be grouped into pairing vertices involving fermions near the  $\Gamma$ -centered ( $\Gamma_{SC}^\Gamma$ ) or  $M$ -centered ( $\Gamma_{SC}^M$ ) hole pockets, and fermions in the vicinity of the electron pockets with either  $d_{xz}/d_{yz}$  ( $\Gamma_{SC}^{e,xz/yz}$ ) or  $d_{xy}$  ( $\Gamma_{SC}^{e,xy}$ ) orbital index. The interplay between SDW and SC susceptibilities is qualitatively the same for all four stable FTs – SDW susceptibility is larger at intermediate scales, but does not diverge, i. e. if  $E_F$  is small enough, the system develops  $s^{+-}$  SC order but no SDW order. The exponents  $\beta_i$  are the same as in the toy model for parameter settings equivalent to  $a = a_n$ . We show the detailed calculation in App. B.4.3.

To determine the SC gap structure on all pockets, we need to include the residual interactions besides the dominant ones from the stable fixed trajectories. We do this numerically. We find that, like in the toy model, the largest eigenvalue in the SC channel corresponds to a “conventional”  $s^{+-}$  gap structure, although the magnitude of the gap on the “secondary” pockets is small. Specifically, this means that for the  $4pFT_1$  the gap magnitude is relatively small on the  $M$ -centered hole pocket and the  $xy$ -part of the electron pockets, for the  $4pFT_2$  it is small on the  $M$ -centered hole pocket and the  $xz/yz$ -parts of the electron pockets. In the 3p case, the gap almost vanishes on both  $\Gamma$ -centered hole pockets, and the two 3pFTs differ in the gap magnitude on the  $xz/yz$  and  $xy$  portions of the electron pockets. For the second largest eigenvalue the gap structure for the FTs, where the dominant interactions are within the same orbitals (i.e.  $4pFT_1$  and  $3pFT_2$ ) is the orbital-antiphase  $s^{+-}$  state, Ref. [228] ( $\text{sign}(\Gamma_{SC}^{e,xz/yz}, \Gamma_{SC}^{e,xy}, \Gamma_{SC}^\Gamma, \Gamma_{SC}^M) = (+, -, -, +)$ ). For the FTs with dominant couplings between different orbitals ( $4pFT_2$  and  $3pFT_1$ ) the sign structure corresponds to an “orbital-antiphase  $s^{++}$ ” state ( $\text{sign}(\Gamma_{SC}^{e,xz/yz}, \Gamma_{SC}^{e,xy}, \Gamma_{SC}^\Gamma, \Gamma_{SC}^M) = (+, -, +, -)$ ). When the pRG flow is towards  $4pFT_{1,2}$ , the system may also develop a spontaneous orbital order prior to SC.

#### 5.4. Conclusion

In this chapter we analyzed the pRG flow of the couplings and susceptibilities in different channels in the full 5-pocket model for FeSCs. We included into consideration the orbital composition of hole and electron pockets in terms of  $d_{xz}$ ,  $d_{yz}$ , and  $d_{xy}$  orbitals. Therefore we could analyze how the orbital composition of low-energy fermions affects the interplay between magnetism, orbital order and superconductivity. The total number of symmetry-allowed couplings between low-energy fermions in the considered model is 40, but the behavior along stable FTs of the pRG flow is amazingly simple – depending on initial values of the interactions and quasiparticle masses the system flows to one of four stable FTs. For two of these FTs, the interactions involving the  $M$ -hole pocket become weaker than the rest, and the system flows to a 4-pocket model at low energies. For the other two FTs, the interactions involving the  $\Gamma$ -centered hole pockets become subleading, and the system behavior becomes the same as in a 3-pocket model consisting of two electron pockets and the  $M$  hole pocket. This behavior was already captured in a toy model with electron pockets only made out of  $d_{xy}$  orbitals, which we analyzed prior to the full model.

In the full model we found for both 4-pocket and 3-pocket models two stable FTs with larger interactions involving either  $d_{xz}$  ( $d_{yz}$ ) or  $d_{xy}$  states on the two electron pockets. In all four cases  $s^{+-}$  SC wins over SDW if  $E_F$  is small enough, and SDW wins if  $E_F$  is larger. We also analyzed the structure of the superconducting gap and, in particular, found that the orbital-aniphase gap structure, proposed in several recent semi-phenomenological studies, comes as subleading s-wave superconducting state. In the parameter range, where the pRG flow is towards a 4pFT, the system develops a spontaneous orbital order with unequal densities between fermions on  $d_{xz}$  and  $d_{yz}$  orbitals close to the Brillouin zone origin. When the pRG flow is towards a 3pFT, the system does not develop a spontaneous orbital order, but may develop a vestigial Ising-nematic order and unequal densities of  $d_{xy}$  orbitals on the two electron pockets.

## CHAPTER 6

---

### Concluding Remarks

---

We have presented a collection of RG studies with focus on different aspects of the interplay between several types of order so that, as a result, we obtain a comprehensive picture of the fascinating phenomena appearing when strong correlations from different ordering channels compete with each other.

We have demonstrated that it is crucial in this case to account for the mutual feedback between particle-hole and pairing channels. One reason is that destructive interactions may occur such as the suppression of phonon-mediated superconductivity by bond order in the analysis of the electron-phonon coupling in Sec. 3.3.1. At the same time, ordering tendencies can profit from the presence of further correlations, which we have seen at the example of the extended spin density wave regime for the dynamically distorted honeycomb lattice (Sec. 3.3.2), or the inducing of an attractive pairing interaction by magnetic fluctuations in the study of FeSCs (Chap. 5). In both investigations the parquet RG approach and the patching formalism of functional RG have proven beneficial for the unbiased consideration of the various ordering channels.

The next step after having established the leading ordering tendency is to resolve the structure of the phase diagram in more detail. Typically, order parameter fluctuations therefore have to be taken into account in addition to the fermion degrees of freedom. We have put forward one possibility to do so in Chap. 4 in the context of the meeting of the antiferromagnetic and the staggered density phase in Dirac materials. There we have set up a semi-phenomenological Gross-Neveu-Yukawa model with two coupled order parameters. The bosonized description is crucial to investigate symmetry-broken regimes of the phase diagram and hence necessary to determine whether orders can coexist. Depending on the number of fermion flavors, we indeed found different phase structures with and without a phase of coexistence (Sec. 4.4.2 and Sec. 4.5.5). Another way to account for the effect that fluctuations of the order parameter tend to reduce the formation of exactly the corresponding order has been presented in Chap. 5 with application to FeSCs. In this case we have introduced vertices for the different bilinears representing the order parameters and calculated their RG flow using the scale-dependent four-Fermi couplings as input (Sec. 5.3). This allowed us to study the susceptibilities of various orders, and even though the divergence of specific couplings pointed at an instability, the susceptibilities did not need to confirm the occurrence of an ordered phase. For instance, we

argued that the spin density wave state does not develop if Fermi energies are small.

When a transition to a symmetry-broken state occurs, we aimed at determining its properties. Again order parameter fluctuations play a crucial role in the analysis of this issue, in particular if two or more orders are present. In addition, multicritical behavior can occur at the intersection of different transition lines. In this context we have determined the nature of transition lines and the (multi-)critical exponents for the point in the phase diagram of Dirac materials where charge and spin density waves meet in Sec. 4.4.1 and Sec. 4.5.4.

Eventually we note that our results can only be as good as the ansatz that we use and several direct extensions of the presented discussions can be made. On the one hand it would be desirable to improve the precision of the fRG calculations. For the patching scheme this can for example be achieved in the spirit of [68, 69]. Regarding the Gross-Neveu-Yukawa model, improved truncation schemes could be useful to obtain more precise critical exponents [211] and to resolve the form of the effective potential in particular with respect to the predicted first order transitions [152, 225, 226]. On the other hand we can extend the models that we have used to describe the different physical situations. Regarding the competition of orders in Dirac materials, the variety of proposed symmetry-broken states suggest the incorporation of further composite order parameters. We have already mentioned the quantum anomalous and quantum spin Hall state (see Eq. (4.4)) with possibly the same quantum critical behavior as the combination of charge and spin density wave. Furthermore, the inclusion of a finite chemical potential together with superconducting phases promises interesting findings [247]. Regarding the 3-orbital, 5-band model for FeSCs, depending on the initial setup, the system can remain close to the weakly unstable trajectories. A more detailed study of their ordering properties can clarify their relevance for observations. For the 3-pocket, 4-orbital model this is under way [248]. Furthermore we have neglected the spin-orbit coupling, which, however, can be straightforwardly included [93, 242].



# APPENDIX A

---

## Competition of Density Waves and Quantum Multicritical Behavior in Dirac Materials – Flow Equations and Convergence

---

### A.1. Explicit FRG Flow Equations

#### A.1.1. Flow Equations for the Yukawa Couplings

Here, we explicitly display the full analytical expressions for the flow of the two Yukawa couplings in terms of threshold functions, which contain the loop integration and regulator dependence. The definitions for the threshold functions and explicit expressions for the case of particular regulator choices can be found in Appendix A.2. Note that the threshold functions are defined such that they also depend on the Yukawa couplings. Then they reduce to familiar expressions in the uncoupled limit ( $\omega_\phi = 0$ ). First, we display the flow equation of the Yukawa coupling to the Ising field  $\chi$ :

$$\begin{aligned}
 \partial_t g_\chi^2 = & (D - 4 + \eta_\chi + 2\eta_\psi)g_\chi^2 + 4\nu_D \sum_{\sigma=\pm 1} \left\{ g_\chi^3 l_{(11)R_\chi}^{(FB),\sigma}(g_\chi, g_\phi; \omega_\chi, \omega_\phi, \omega_{\phi\chi}, \omega_\psi^\sigma) \right. \\
 & + g_\chi^2 g_\phi \left[ l_{(11)R_\phi}^{(FB),\sigma}(g_\phi, g_\chi; \omega_\phi, \omega_\chi, \omega_{\phi\chi}, \omega_\psi^\sigma) + 2g_\phi l_{(11)G_\phi}^{(FB)}(u^{(0,1)}, \omega_\psi^\sigma) \right] \\
 & - 2(\sqrt{2\kappa_\chi} g_\chi + \sigma \sqrt{2\kappa_\phi} g_\phi)^2 \left[ g_\chi^3 l_{(21)R_\chi}^{(FB),\sigma}(g_\chi, g_\phi; \omega_\chi, \omega_\phi, \omega_{\phi\chi}, \omega_\psi^\sigma) \right. \\
 & + g_\chi^2 g_\phi \left( l_{(21)R_\phi}^{(FB),\sigma}(g_\phi, g_\chi; \omega_\phi, \omega_\chi, \omega_{\phi\chi}, \omega_\psi^\sigma) + 2g_\phi l_{(21)G_\phi}^{(FB)}(u^{(0,1)}, \omega_\psi^\sigma) \right) \Big] \\
 & - g_\chi (\sqrt{2\kappa_\chi} g_\chi + \sigma \sqrt{2\kappa_\phi} g_\phi) \left[ \omega_{\chi\chi\chi} l_{(12)R_\chi}^{(FB),\sigma}(g_\chi, g_\phi; \omega_\chi, \omega_\phi, \omega_{\phi\chi}, \omega_\psi^\sigma) \right. \\
 & + \omega_{\chi\phi\phi} l_{(12)R_\phi}^{(FB),\sigma}(g_\phi, g_\chi; \omega_\phi, \omega_\chi, \omega_{\phi\chi}, \omega_\psi^\sigma) + 2g_\phi^2 \sqrt{\kappa_\chi} u^{(1,1)} l_{(12)G_\phi}^{(FB)}(u^{(0,1)}, \omega_\psi^\sigma) \\
 & \left. \left. - 2\omega_{\chi\chi\phi} l_{(111)R_\chi R_\phi}^{(FBB),\sigma}(g_\chi, g_\phi; \omega_\chi, \omega_\phi, \omega_{\phi\chi}, \omega_\psi^\sigma) \right] \right\}. \tag{A.1}
 \end{aligned}$$

Analogously, the Yukawa coupling to the Heisenberg field  $\phi$  is given by

$$\begin{aligned}
\partial_t g_\phi^2 &= (D-4+\eta_\phi+2\eta_\psi)g_\phi^2 \\
&+ 4v_D \sum_{\sigma=\pm 1} \left\{ -g_\phi^3 l_{(11)R_\phi}^{(FB),\sigma}(g_\phi, g_\chi; \omega_\phi, \omega_\chi, \omega_{\phi\chi}, \omega_\psi^\sigma) + g_\phi^2 g_\chi l_{(11)R_\chi}^{(FB),\sigma}(g_\chi, g_\phi; \omega_\chi, \omega_\phi, \omega_{\phi\chi}, \omega_\psi^\sigma) \right. \\
&- 4g_\phi^2 g_\chi^2 \kappa_\chi \left[ g_\chi l_{(111)R_\chi}^{(FBB),\sigma}(g_\chi, g_\phi; \omega_\chi, \omega_\phi, \omega_{\phi\chi}, \omega_\psi^+, \omega_\psi^-) - g_\phi l_{(111)R_\phi}^{(FBB),\sigma}(g_\phi, g_\chi; \omega_\phi, \omega_\chi, \omega_{\phi\chi}, \omega_\psi^+, \omega_\psi^-) \right] \\
&- 2g_\phi^2 u^{(1,1)} \sqrt{2\kappa_\chi} (\sqrt{2\kappa_\chi} g_\chi + \sigma \sqrt{2\kappa_\phi} g_\phi) l_{(111)G_\phi R_\chi}^{(FBB),\sigma}(g_\chi, g_\phi; u^{(0,1)}, \omega_\chi, \omega_\phi, \omega_{\phi\chi}, \omega_\psi^\sigma) \\
&\left. - 2g_\phi^2 u^{(0,2)} \sqrt{2\kappa_\phi} (\sqrt{2\kappa_\phi} g_\phi + \sigma \sqrt{2\kappa_\chi} g_\chi) l_{(111)G_\phi R_\phi}^{(FBB),\sigma}(g_\phi, g_\chi; u^{(0,1)}, \omega_\phi, \omega_\chi, \omega_{\phi\chi}, \omega_\psi^\sigma) \right\}. \tag{A.2}
\end{aligned}$$

We have abbreviated the volume factor by  $v_D = \frac{1}{4} \text{vol}(S^{D-1}) / (2\pi)^D = (\Gamma(D/2) 2^{D+1} \pi^{d/2})^{-1}$ . The threshold functions are listed in Appendix A.2 and we have defined

$$\begin{aligned}
\omega_{\chi\chi\chi} &= \sqrt{2\kappa_\chi} (3u^{(2,0)} + 2\kappa_\chi u^{(3,0)}), \quad \omega_{\chi\chi\phi} = \sqrt{2\kappa_\phi} (u^{(1,1)} + 2\kappa_\chi u^{(2,1)}) \\
\omega_{\chi\phi\phi} &= \sqrt{2\kappa_\chi} (u^{(1,1)} + 2\kappa_\phi u^{(1,2)}). \tag{A.3}
\end{aligned}$$

$\omega_\phi$ ,  $\omega_\chi$ ,  $\omega_{\phi\chi}$ , and  $\omega_\psi^\pm$  are defined in the main text, see Sec. 4.5.1.

### A.1.2. Anomalous Dimensions

The expressions for the anomalous dimensions can also be given as a closed algebraic system of equations. Note that—although not explicitly displayed—the threshold functions also depend on the anomalous dimensions. First, we list the expressions for the anomalous dimension of the Heisenberg field  $\eta_\phi$  and the one for the Dirac fermions  $\eta_\psi$ ,

$$\begin{aligned}
\eta_\phi &= \frac{4v_D}{D} \left\{ 2\sqrt{2\kappa_\chi} u^{(1,1)} m_{(22)R_\chi G_\phi}^{(B)D,\sigma}(\sqrt{2\kappa_\chi} u^{(1,1)}, \sqrt{2\kappa_\phi} u^{(0,2)}; \omega_\chi, \omega_\phi, \omega_{\phi\chi}, u^{(0,1)}) \right. \\
&+ 2\sqrt{2\kappa_\phi} u^{(0,2)} m_{(22)R_\phi G_\phi}^{(B)D,\sigma}(\sqrt{2\kappa_\phi} u^{(0,2)}, \sqrt{2\kappa_\chi} u^{(1,1)}; \omega_\phi, \omega_\chi, \omega_{\phi\chi}, u^{(0,1)}) \\
&\left. + 2N_f d_\gamma g_\phi^2 \left[ m_{(22)}^{(F)}(\omega_\psi^+, \omega_\psi^-) - (2\kappa_\chi g_\chi^2 - 2\kappa_\phi g_\phi^2) m_{(11)}^{(F)}(\omega_\psi^+, \omega_\psi^-) \right] \right\}, \tag{A.4}
\end{aligned}$$

$$\begin{aligned}
\eta_\psi &= \frac{4v_D}{D} \sum_{\sigma} \left\{ g_\chi m_{(12)R_\chi}^{(FB)D,\sigma}(g_\chi, g_\phi; \omega_\chi, \omega_\phi, \omega_{\phi\chi}, \omega_\psi^\sigma) + 2g_\phi^2 m_{(12)G_\phi}^{(FB)}(u^{(0,1)}, \omega_\psi^\sigma) \right. \\
&\left. + g_\phi m_{(12)R_\phi}^{(FB)D,\sigma}(g_\phi, g_\chi; \omega_\phi, \omega_\chi, \omega_{\phi\chi}, \omega_\psi^\sigma) \right\}. \tag{A.5}
\end{aligned}$$

The expression for the anomalous dimension of the Ising field  $\eta_\chi$  depends on the projection prescription. Here, we distinguish between the projections onto the radial mode or onto an auxiliary Goldstone mode (see Appendix A.1.3 for technical details). Both ways are given in the following and are denoted as  $\eta_{\chi,R}$  and  $\eta_{\chi,G}$ , respectively

$$\begin{aligned}
\eta_{\chi,R} &= \frac{4v_D}{D} \left\{ m_{(40)R_\chi}^{(B)D,\sigma}(\omega_{\chi\chi\chi}, \omega_{\chi\chi\phi}; \omega_\chi, \omega_\phi, \omega_{\phi\chi}) + m_{(40)R_\phi}^{(B)D,\sigma}(\omega_{\chi\phi\phi}, \omega_{\chi\chi\phi}; \omega_\phi, \omega_\chi, \omega_{\phi\chi}) \right. \\
&+ 2m_{(22)R_\chi R_\phi}^{(B)D,\sigma}(\omega_{\chi\chi\phi}, \omega_{\chi\phi\phi}, \omega_{\chi\chi\chi}; \omega_\chi, \omega_\phi, \omega_{\phi\chi}) + 4\kappa_\chi (u^{(1,1)})^2 m_{(40)G_\phi}^{(B)D}(u^{(0,1)}) \\
&\left. + N_f d_\gamma g_\chi^2 \sum_{\sigma} \left[ m_4^{(F)}(\omega_\psi^\sigma) - (\sqrt{2\kappa_\chi} g_\chi + \sigma \sqrt{2\kappa_\phi} g_\phi)^2 m_2^{(F)}(\omega_\psi^\sigma) \right] \right\}, \tag{A.6}
\end{aligned}$$

$$\begin{aligned}
\eta_{\chi,G} = & \frac{4v_D}{D} \left\{ 2\sqrt{2\kappa_\chi} u^{(2,0)} m_{(22)R_\chi G_\chi}^{(B)D,\sigma} (\sqrt{2\kappa_\chi} u^{(2,0)}, \sqrt{\kappa_\phi} u^{(1,1)}; \omega_\chi, \omega_\phi, \omega_{\phi\chi}, u^{(1,0)}) \right. \\
& + 2\sqrt{2\kappa_\phi} m_{(2,2)R_\phi G_\chi}^{(B)D,\sigma} (\sqrt{2\kappa_\phi} u^{(1,1)} \sqrt{2\kappa_\chi} u^{2,0}; \omega_\phi, \omega_\chi, \omega_{\phi\chi}, u^{(1,0)}) \\
& \left. + N_f d_\gamma g_\chi^2 \sum_\sigma \left[ m_4^{(F)}(\omega_\psi^\sigma) - (\sqrt{2\kappa_\chi} g_\chi + \sigma \sqrt{2\kappa_\phi} g_\phi)^2 m_2^{(F)}(\omega_\psi^\sigma) \right] \right\}. \quad (A.7)
\end{aligned}$$

For our results as displayed in the main text, we use the latter definition, which in the case of the purely bosonic systems is known to yield more accurate results, cf. Appendix A.1.3.

### A.1.3. Projection Prescriptions for Anomalous Dimensions

Let us consider an  $N$ -component bosonic field  $\phi$ , which we divide into one radial and  $N-1$  Goldstone modes  $\phi = (\phi_R, \phi_G)$ . In the following discussion, we will suppress the bosonic potential, since it plays no role for the argument. Therefore, we use the truncation

$$\Gamma = \int_x \left[ \frac{1}{2} Z (\partial_\mu \phi)^2 + \frac{1}{4} Y (\partial_\mu \rho)^2 \right], \quad (A.8)$$

where we account for the first correction to the kinetic term in a derivative expansion and have defined  $\rho = \frac{1}{2} \phi^2$ . The second functional derivative of  $\Gamma$  gives

$$\frac{\delta^2 \Gamma}{\delta \phi_i \delta \phi_j} = -Z \delta_{ij} \partial_\mu^2 - \frac{1}{2} Y \left( \delta_{ij} \partial_\mu^2 \rho + \phi_j \partial_\mu^2 \phi_i \right), \quad (A.9)$$

where the derivative has to be understood as momentum squared in momentum representation. This shows that the projection  $\left. \frac{\partial}{\partial p^2} \frac{\delta^2}{\delta \phi_R^2} \partial_t \Gamma \right|_0$  yields an expression proportional to  $\partial_t Z + 2\kappa \partial_t Y$  with  $\kappa = \frac{1}{2} \phi_R^2$ . On the other hand  $\left. \frac{\partial}{\partial p^2} \frac{\delta^2}{\delta \phi_G^2} \partial_t \Gamma \right|_0$  really projects onto  $\partial_t Z$ .

To circumvent the projection onto the radial mode in the case of the one-component Ising field, we choose a truncation with  $N$  copies of it

$$\begin{aligned}
\Gamma_k = & \int d^D x \left( Z_{\Psi,k} \bar{\Psi} (\mathbb{1}_2 \otimes \gamma_\mu) \partial_\mu \Psi - \frac{1}{2} Z_{\chi,k} \chi_a \partial_\mu^2 \chi_a - \frac{1}{2} Z_{\phi,k} \phi \partial_\mu^2 \phi \right. \\
& \left. + \bar{g}_{\chi,k} \left( \sum_a \chi_a \right) \bar{\Psi} (\mathbb{1}_2 \otimes \mathbb{1}_4) \Psi + \bar{g}_{\phi,k} \phi \bar{\Psi} (\sigma \otimes \mathbb{1}_4) \Psi + U_k(\bar{\rho}_\chi, \bar{\rho}_\phi) \right). \quad (A.10)
\end{aligned}$$

The field is divided into its vacuum expectation value and the fluctuations  $\chi = (\chi_R + \Delta\chi_{R,1}, \Delta\chi_{G,1}, \dots, \Delta\chi_{G,N-1})$  and we project onto one of the Goldstone modes according to Eq. (4.56). In the end of the procedure we again set  $N = 1$ .

## A.2. Threshold Functions

The threshold functions encode the loop integrations and the regulator dependences. Here, for convenience, we define the threshold functions such that a dependence on the Yukawa couplings is included as well. In the following, we will first list the expressions for general regulator functions.

### A.2.1. General Expressions

We write the regulators in the form  $R_{i,k}^{(B)}(q) = Z_{i,k} q^2 r_{i,k}(q^2)$  with  $i \in \{\chi, \phi\}$  and  $R_k^{(F)} = i Z_{\psi,k} q_\mu (\mathbb{1}_2 \otimes \gamma_\mu) r_{\psi,k}(q)$ . Further, we define  $p_i(q) = q^2(1+r_{i,k}(q))$  and  $p_F(q) = q^2(1+r_{\psi,k}(q))^2$ . The derivative acting only on the regulator's  $t$ -dependence then reads

$$\tilde{\partial}_t = \sum_{\Phi \in \{\chi, \phi, \psi\}} \int dq \, 2q \frac{1}{Z_{\Phi,k}} \partial_t [Z_{\Phi,k} r_{\Phi,k}(q)] \frac{\delta}{\delta r_{\Phi,k}(q)}. \quad (\text{A.11})$$

For the threshold functions appearing in the flow equations for the Yukawa couplings, we then obtain

$$l_{(nm)R_\varphi}^{(FB),\sigma}(g_\varphi, g_\theta; \omega_\varphi, \omega_\theta, \omega_{\varphi\theta}, \omega_\psi^\sigma) = -\frac{1}{4v_D} k^{4-D} k^{2(n+m-2)} \tilde{\partial}_t \int_q \frac{(g_\varphi(p_\theta + k^2 \omega_\theta) - \sigma g_\theta k^2 \omega_{\varphi\theta})^m}{(p_F + k^2 \omega_\psi^\sigma)^n ((p_\varphi + k^2 \omega_\varphi)(p_\theta + k^2 \omega_\theta) - k^4 \omega_{\varphi\theta}^2)^m}, \quad (\text{A.12})$$

$$l_{(nm)G_\phi}^{(FB)}(\omega_\phi, \omega_\psi) = -\frac{1}{4v_D} k^{4-D} k^{2(n+m-2)} \tilde{\partial}_t \int_q \frac{1}{(p_F + k^2 \omega_\psi^\sigma)^n (p_\phi + k^2 \omega_\phi)^m}, \quad (\text{A.13})$$

and

$$l_{(111)R_\varphi R_\theta}^{(FBB),\sigma}(g_\varphi, g_\theta; \omega_\varphi, \omega_\theta, \omega_{\varphi\theta}, \omega_\psi^\sigma) = -\frac{1}{4v_D} k^{6-D} \tilde{\partial}_t \int_q \frac{(g_\varphi(p_\theta + k^2 \omega_\theta) - \sigma g_\theta k^2 \omega_{\varphi\theta})(g_\theta(p_\varphi + k^2 \omega_\varphi) - \sigma g_\varphi k^2 \omega_{\varphi\theta})}{(p_F + k^2 \omega_\psi^\sigma)((p_\varphi + k^2 \omega_\varphi)(p_\theta + k^2 \omega_\theta) - k^4 \omega_{\varphi\theta}^2)^2}, \quad (\text{A.14})$$

$$l_{(111)G_\phi R_\varphi}^{(FBB),\sigma}(g_\varphi, g_\theta; \omega_\phi, \omega_\varphi, \omega_\theta, \omega_{\varphi\theta}, \omega_\psi^\sigma) = -\frac{1}{4v_D} k^{6-D} \tilde{\partial}_t \int_q \frac{g_\varphi(p_\theta + k^2 \omega_\theta) - \sigma g_\theta k^2 \omega_{\varphi\theta}}{(p_F + k^2 \omega_\psi^\sigma)(p_\phi + k^2 \omega_\phi)((p_\varphi + k^2 \omega_\varphi)(p_\theta + k^2 \omega_\theta) - k^4 \omega_{\varphi\theta}^2)}, \quad (\text{A.15})$$

$$l_{(111)R_\varphi}^{(FBB),\sigma}(g_\varphi, g_\theta; \omega_\varphi, \omega_\theta, \omega_{\varphi\theta}, \omega_{\psi 1}, \omega_{\psi 2}) = -\frac{1}{4v_D} k^{6-D} \tilde{\partial}_t \int_q \frac{g_\varphi(p_\theta + k^2 \omega_\theta) - \sigma g_\theta k^2 \omega_{\varphi\theta}}{(p_F + k^2 \omega_{\psi 1})(p_F + k^2 \omega_{\psi 2})((p_\varphi + k^2 \omega_\varphi)(p_\theta + k^2 \omega_\theta) - k^4 \omega_{\varphi\theta}^2)}. \quad (\text{A.16})$$

The threshold functions appearing in the anomalous dimensions can be distinguished by their internal lines. First, we have threshold functions corresponding to purely fermionic loops

$$m_4^{(F)D}(\omega) = -\frac{1}{4v_D} k^{4-D} \tilde{\partial}_t \int_q q^4 \left( \frac{\partial}{\partial q^2} \frac{1+r_\psi}{p_F + k^2 \omega} \right)^2, \quad (\text{A.17})$$

$$m_{(22)}^{(F)D}(\omega_1, \omega_2) = -\frac{1}{4v_D} k^{4-D} \tilde{\partial}_t \int_q q^4 \left( \frac{\partial}{\partial q^2} \frac{1+r_\psi}{p_F + k^2 \omega_1} \right) \left( \frac{\partial}{\partial q^2} \frac{1+r_\psi}{p_F + k^2 \omega_2} \right), \quad (\text{A.18})$$

$$m_2^{(F)D}(\omega) = -\frac{1}{4v_D} k^{6-D} \tilde{\partial}_t \int_q q^2 \left( \frac{\partial}{\partial q^2} \frac{1}{p_F + k^2 \omega} \right)^2, \quad (\text{A.19})$$

$$m_{(11)}^{(F)D}(\omega) = -\frac{1}{4v_D} k^{6-D} \tilde{\partial}_t \int_q q^2 \left( \frac{\partial}{\partial q^2} \frac{1}{p_F + k^2 \omega_1} \right) \left( \frac{\partial}{\partial q^2} \frac{1}{p_F + k^2 \omega_2} \right). \quad (\text{A.20})$$

Then, we have purely bosonic contributions

$$m_{(22)R_\varphi R_\theta}^{(B)D}(v_1, v_2, v_3; \omega_\varphi, \omega_\theta, \omega_{\varphi\theta}) = -\frac{1}{4v_D} k^{6-D} \tilde{\partial}_t \int_q q^2 \left( \frac{\partial}{\partial q^2} \frac{(p_\varphi - k^2 \omega_\varphi)v_1 - k^2 \omega_{\varphi\theta} v_2}{(p_\varphi + k^2 \omega_\varphi)(p_\theta - k^2 \omega_\theta) - k^4 \omega_{\varphi\theta}^2} \right) \times \left( \frac{\partial}{\partial q^2} \frac{(p_\theta - k^2 \omega_\theta)v_1 - k^2 \omega_{\varphi\theta} v_3}{(p_\varphi + k^2 \omega_\varphi)(p_\theta - k^2 \omega_\theta) - k^4 \omega_{\varphi\theta}^2} \right), \quad (\text{A.21})$$

$$m_{(22)R_\varphi G_\phi}^{(B)D}(v_1, v_2; \omega_\varphi, \omega_\theta, \omega_{\varphi\theta}, \omega_\phi) = -\frac{1}{4v_D} k^{6-D} \tilde{\partial}_t \int_q q^2 \left( \frac{\partial}{\partial q^2} \frac{(p_\theta + k^2 \omega_\theta)v_1 - k^2 \omega_{\varphi\theta} v_2}{(p_\varphi + k^2 \omega_\varphi)(p_\theta - k^2 \omega_\theta) - k^4 \omega_{\varphi\theta}^2} \right) \left( \frac{\partial}{\partial q^2} \frac{1}{p_\phi + k^2 \omega_\phi} \right), \quad (\text{A.22})$$

$$m_{(40)R_\varphi}^{(B)D,\sigma}(v_1, v_2; \omega_\varphi, \omega_\theta, \omega_{\varphi\theta}) = -\frac{1}{4v_D} k^{6-D} \tilde{\partial}_t \int_q q^2 \left( \frac{\partial}{\partial q^2} \frac{(p_\theta + k^2 \omega_\theta)v_1 - k^2 \omega_{\varphi\theta} v_2}{(p_\varphi + k^2 \omega_\varphi)(p_\theta + k^2 \omega_\theta) - k^4 \omega_{\varphi\theta}^2} \right)^2, \quad (\text{A.23})$$

$$m_{(40)G_\phi}^{(B)D}(\omega_\phi) = -\frac{1}{4v_D} k^{6-D} \tilde{\partial}_t \int_q q^2 \left( \frac{\partial}{\partial q^2} \frac{1}{p_\phi + k^2 \omega_\phi} \right)^2. \quad (\text{A.24})$$

Finally, there are also threshold functions with mixed fermion-boson loops

$$m_{(12)G_\varphi}^{(FB)D}(\omega_\varphi, \omega_\psi) = -\frac{1}{4v_D} k^{4-D} \tilde{\partial}_t \int_q q^2 \frac{1+r_\psi}{p_F + k^2 \omega_\psi} \frac{\partial}{\partial q^2} \frac{1}{p_\varphi + k^2 \omega_\varphi}, \quad (\text{A.25})$$

$$m_{(12)R_\varphi}^{(FB)D,\sigma}(g_\varphi, g_\theta; \omega_\varphi, \omega_\theta, \omega_{\varphi\theta}, \omega_\psi) = -\frac{1}{4v_D} k^{4-D} \tilde{\partial}_t \int_q q^2 \frac{1+r_\psi}{p_F + k^2 \omega_\psi} \frac{\partial}{\partial q^2} \frac{g_\varphi(p_\theta + k^2 \omega_\theta) - \sigma g_\theta k^2 \omega_{\varphi\theta}}{(p_\varphi + k^2 \omega_\varphi)(p_\theta + k^2 \omega_\theta) - k^4 \omega_{\varphi\theta}^2}. \quad (\text{A.26})$$

### A.2.2. Linear Cutoff

The regulator functions for the linear cutoff are explicitly given by

$$r_{\psi,k}(q) = \left( \frac{k}{q} - 1 \right) \theta(k^2 - q^2), \quad r_{\chi/\phi,k}(q) = \left( \frac{k^2}{q^2} - 1 \right) \theta(k^2 - q^2), \quad (\text{A.27})$$

with the step function  $\theta(x) = 1$  if  $x > 0$  and  $\theta(x) = 0$  if  $x \leq 0$ . Then, the threshold functions for the linear cutoff relevant to the flow equation for the effective potential, Eq. (4.38), read

$$I_R(\omega_\chi, \omega_\phi, \omega_{\phi\chi}^2) = \frac{4v_D}{D} \frac{(1 - \frac{\eta_\phi}{D+2})(1 + \omega_\chi) + (1 - \frac{\eta_\chi}{D+2})(1 + \omega_\phi)}{(1 + \omega_\phi)(1 + \omega_\chi) - \omega_{\phi\chi}^2}, \quad (\text{A.28})$$

$$I_G(\omega) = \frac{4v_D}{D} \left( 1 - \frac{\eta_\phi}{D+2} \right) \frac{1}{1 + \omega}, \quad (\text{A.29})$$

$$I_\psi(\omega) = \frac{4v_D}{D} \left( 1 - \frac{\eta_\psi}{D+1} \right) \frac{1}{1 + \omega}. \quad (\text{A.30})$$

For the contributions to the Yukawa couplings we obtain the following threshold functions when evaluated with the linear cutoff

$$l_{(nm)R_\varphi}^{(FB),\sigma}(g_\varphi, g_\theta; \omega_\varphi, \omega_\theta, \omega_{\varphi\theta}, \omega_\psi^\sigma) = \frac{(g_\varphi(1+\omega_\theta) + \sigma g_\theta \omega_{\varphi\theta})^m}{\left((1+\omega_\varphi)(1+\omega_\theta) - \omega_{\varphi\theta}^2\right)^m (1+\omega_\psi^\sigma)^n} \\ \times \frac{2}{D} \left[ -m \left(1 - \frac{\eta_\theta}{D+2}\right) \frac{\sigma \omega_{\varphi\theta} (g_\theta(1+\omega_\varphi) - \sigma g_\varphi \omega_{\varphi\theta})}{(g_\varphi(1+\omega_\theta) - \sigma g_\theta \omega_{\varphi\theta})((1+\omega_\varphi)(1+\omega_\theta) - \omega_{\varphi\theta}^2)} \right. \\ \left. + m \left(1 - \frac{\eta_\varphi}{D+2}\right) \frac{(1+\omega_\theta)}{(1+\omega_\varphi)(1+\omega_\theta) - \omega_{\varphi\theta}^2} + n \left(1 - \frac{\eta_\psi}{D+1}\right) \frac{1}{1+\omega_\psi^\sigma} \right], \quad (A.31)$$

$$l_{(nm)G_\phi}^{(FB)}(\omega_\phi, \omega_\psi) = \frac{2}{D} \left[ m \left(1 - \frac{\eta_\phi}{D+2}\right) \frac{1}{1+\omega_\phi} + n \left(1 - \frac{\eta_\psi}{D+1}\right) \frac{1}{1+\omega_\psi} \right] \frac{1}{(1+\omega_\phi)^m (1+\omega_\psi)^n} \quad (A.32)$$

and

$$l_{(111)R_\varphi R_\theta}^{(FBB),\sigma}(g_\varphi, g_\theta; \omega_\varphi, \omega_\theta, \omega_{\varphi\theta}, \omega_\psi^\sigma) = \frac{1}{((1+\omega_\varphi)(1+\omega_\theta) - \omega_{\varphi\theta}^2)^2 (1+\omega_\psi^\sigma)} \\ \times \frac{2}{D} \left[ \left(1 - \frac{\eta_\psi}{D+1}\right) \frac{(g_\varphi(1+\omega_\theta) - \sigma g_\theta \omega_{\varphi\theta})(g_\theta(1+\omega_\varphi) - \sigma g_\varphi \omega_{\varphi\theta})}{1+\omega_\psi^\sigma} \right. \\ + \left(1 - \frac{\eta_\theta}{D+2}\right) \frac{(1+\omega_\varphi)(g_\theta(1+\omega_\varphi) - \sigma g_\varphi \omega_{\varphi\theta})(g_\varphi(1+\omega_\theta) - \sigma g_\theta \omega_{\varphi\theta})}{(1+\omega_\varphi)(1+\omega_\theta) - \omega_{\varphi\theta}^2} \\ - \left(1 - \frac{\eta_\theta}{D+2}\right) \frac{\sigma \omega_{\varphi\theta} (g_\theta(1+\omega_\varphi) - \sigma g_\varphi \omega_{\varphi\theta})^2}{(1+\omega_\varphi)(1+\omega_\theta) - \omega_{\varphi\theta}^2} \\ \left. + \left(1 - \frac{\eta_\varphi}{D+2}\right) \frac{(1+\omega_\theta)(g_\theta(1+\omega_\varphi) - \sigma g_\varphi \omega_{\varphi\theta})(g_\varphi(1+\omega_\theta) - \sigma g_\theta \omega_{\varphi\theta})}{(1+\omega_\varphi)(1+\omega_\theta) - \omega_{\varphi\theta}^2} \right] \\ - \left(1 - \frac{\eta_\varphi}{D+2}\right) \frac{\sigma \omega_{\varphi\theta} (g_\varphi(1+\omega_\theta) - \sigma g_\theta \omega_{\varphi\theta})^2}{(1+\omega_\varphi)(1+\omega_\theta) - \omega_{\varphi\theta}^2} \quad (A.33)$$

$$l_{(111)G_\phi R_\varphi}^{(FBB),\sigma}(g_\varphi, g_\theta; \omega_\phi, \omega_\varphi, \omega_\theta, \omega_{\varphi\theta}, \omega_\psi^\sigma) = \frac{1}{(1+\omega_\phi)(1+\omega_\psi^\sigma)((1+\omega_\varphi)(1+\omega_\theta) - \omega_{\varphi\theta}^2)} \\ \times \frac{2}{D} \left[ (1+\omega_\theta) \left(1 - \frac{\eta_\varphi}{D+2}\right) \frac{g_\varphi(1+\omega_\theta) - \sigma g_\theta \omega_{\varphi\theta}}{(1+\omega_\varphi)(1+\omega_\theta) - \omega_{\varphi\theta}^2} \right. \\ - \sigma \omega_{\varphi\theta} \left(1 - \frac{\eta_\theta}{D+2}\right) \frac{g_\theta(1+\omega_\varphi) - \sigma g_\varphi \omega_{\varphi\theta}}{(1+\omega_\varphi)(1+\omega_\theta) - \omega_{\varphi\theta}^2} \\ \left. + \left(1 - \frac{\eta_\phi}{D+2}\right) \frac{g_\varphi(1+\omega_\theta) - \sigma g_\theta \omega_{\varphi\theta}}{1+\omega_\phi} + \left(1 - \frac{\eta_\psi}{D+2}\right) \frac{g_\varphi(1+\omega_\theta) - \sigma g_\theta \omega_{\varphi\theta}}{1+\omega_\psi^\sigma} \right], \quad (A.34)$$

$$\begin{aligned}
l_{(111)R_\varphi}^{(F\bar{B})\sigma}(g_\varphi, g_\theta; \omega_\varphi, \omega_\theta, \omega_{\varphi\theta}, \omega_{\psi 1}, \omega_{\psi 2}) = & \frac{1}{(1 + \omega_{\psi 1})(1 + \omega_{\psi 2})((1 + \omega_\varphi)(1 + \omega_\theta) - \omega_{\varphi\theta}^2)} \\
& \times \frac{2}{D} \left[ (1 + \omega_\theta) \left( 1 - \frac{\eta_\varphi}{D+2} \right) \frac{g_\varphi(1 + \omega_\theta) - \sigma g_\theta \omega_{\varphi\theta}}{(1 + \omega_\varphi)(1 + \omega_\theta) - \sigma \omega_{\varphi\theta}^2} \right. \\
& - \sigma \omega_{\varphi\theta} \left( 1 - \frac{\eta_\theta}{D+2} \right) \frac{g_\theta(1 + \omega_\varphi) - \sigma g_\varphi \omega_{\varphi\theta}}{(1 + \omega_\varphi)(1 + \omega_\theta) - \omega_{\varphi\theta}^2} \\
& \left. + \left( 1 - \frac{\eta_\psi}{D+1} \right) (g_\varphi(1 + \omega_\theta) - \sigma g_\theta \omega_{\varphi\theta}) \left( \frac{1}{1 + \omega_{\psi 1}} + \frac{1}{1 + \omega_{\psi 2}} \right) \right]. \quad (A.35)
\end{aligned}$$

The threshold functions for linear cutoff contributing with pure fermion loops to the anomalous dimensions are

$$m_4^{(F)D}(\omega) = \frac{1}{(1 + \omega)^4} + \frac{1 - \eta_\psi}{D - 2} \frac{1}{(1 + \omega)^3} - \left( \frac{1 - \eta_\psi}{2D - 4} + \frac{1}{4} \right) \frac{1}{(1 + \omega)^2}, \quad (A.36)$$

$$\begin{aligned}
m_{(22)}^{(F)D}(\omega_1, \omega_2) = & \frac{1}{4} \left( \frac{1}{1 + \omega_1} - \frac{2}{(1 + \omega_1)^2} \right) \left( \frac{1}{1 + \omega_2} - \frac{2}{(1 + \omega_2)^2} \right) \\
& + \frac{1}{4} \frac{1 + \eta_\psi - D}{D - 2} \left[ \left( \frac{1}{1 + \omega_1} - \frac{2}{(1 + \omega_1)^2} \right) \frac{1}{1 + \omega_2} + \left( \frac{1}{1 + \omega_2} - \frac{2}{(1 + \omega_2)^2} \right) \frac{1}{1 + \omega_1} \right], \quad (A.37)
\end{aligned}$$

$$m_2^{(F)D}(\omega) = \frac{1}{(1 + \omega)^4}, \quad (A.38)$$

$$m_{(11)}^{(F)D}(\omega) = \frac{1}{(1 + \omega_1)^2(1 + \omega_2)^2}. \quad (A.39)$$

The bosonic threshold functions are given by

$$\begin{aligned}
m_{(22)R_\varphi R_\theta}^{(B)D}(v_1, v_2, v_3; \omega_\varphi, \omega_\theta, \omega_{\varphi\theta}) = & (1 + \omega_\varphi)(1 + \omega_\theta) \frac{((1 + \omega_\varphi)v_1 - \omega_{\varphi\theta}v_2)((1 + \omega_\theta)v_1 - \omega_{\varphi\theta}v_3)}{((1 + \omega_\varphi)(1 + \omega_\theta) - \omega_{\varphi\theta}^2)^4} \\
& + \omega_{\varphi\theta}^2 \frac{((1 + \omega_\theta)v_2 - \omega_{\varphi\theta}v_1)((1 + \omega_\varphi)v_3 - \omega_{\varphi\theta}v_1)}{((1 + \omega_\varphi)(1 + \omega_\theta) - \omega_{\varphi\theta}^2)^4} \\
& - \omega_{\varphi\theta}(1 + \omega_\theta) \frac{((1 + \omega_\theta)v_2 - \omega_{\varphi\theta}v_1)((1 + \omega_\theta)v_1 - \omega_{\varphi\theta}v_3)}{((1 + \omega_\varphi)(1 + \omega_\theta) - \omega_{\varphi\theta}^2)^4} \\
& - \omega_{\varphi\theta}(1 + \omega_\varphi) \frac{((1 + \omega_\varphi)v_1 - \omega_{\varphi\theta}v_2)((1 + \omega_\varphi)v_3 - \omega_{\varphi\theta}v_1)}{((1 + \omega_\varphi)(1 + \omega_\theta) - \omega_{\varphi\theta}^2)^4}, \quad (A.40)
\end{aligned}$$

$$\begin{aligned}
m_{(22)R_\varphi G_\phi}^{(B)D}(v_1, v_2; \omega_\varphi, \omega_\theta, \omega_{\varphi\theta}, \omega_\phi) = & \frac{1 + \omega_\theta}{(1 + \omega_\phi)^2} \frac{(1 + \omega_\theta)v_1 - \omega_{\varphi\theta}v_2}{((1 + \omega_\varphi)(1 + \omega_\theta) - \omega_{\varphi\theta}^2)^2} - \frac{\omega_{\varphi\theta}}{(1 + \omega_\phi)^2} \frac{(1 + \omega_\theta)v_2 - \omega_{\varphi\theta}v_1}{((1 + \omega_\varphi)(1 + \omega_\theta) - \omega_{\varphi\theta}^2)^2}, \quad (A.41)
\end{aligned}$$

$$\begin{aligned}
m_{(40)R_\varphi}^{(B)D,\sigma}(v_1, v_2; \omega_\varphi, \omega_\theta, \omega_{\varphi\theta}) = & \left[ (1 + \omega_\theta) \frac{(1 + \omega_\theta)v_1 - \omega_{\varphi\theta}v_2}{((1 + \omega_\varphi)(1 + \omega_\theta) - \omega_{\varphi\theta}^2)^2} - \omega_{\varphi\theta} \frac{(1 + \omega_\theta)v_2 - \omega_{\varphi\theta}v_1}{((1 + \omega_\varphi)(1 + \omega_\theta) - \omega_{\varphi\theta}^2)^2} \right]^2, \quad (A.42)
\end{aligned}$$

$$m_{(40)G_\phi}^{(B)D}(\omega_\phi) = \frac{1}{(1 + \omega_\phi)^4}. \quad (\text{A.43})$$

And finally, the mixed threshold functions read

$$m_{(12)G_\psi}^{(FB)D}(\omega_\varphi, \omega_\psi) = \left(1 - \frac{\eta_\varphi}{D+1}\right) \frac{1}{(1 + \omega_\psi)(1 + \omega_\varphi)^2}, \quad (\text{A.44})$$

$$\begin{aligned} m_{(12)R_\varphi}^{(FB)D,\sigma}(g_\varphi, g_\theta; \omega_\varphi, \omega_\theta, \omega_{\varphi\theta}, \omega_\psi) = \\ \frac{1}{1 + \omega_\psi} \left[ \left(1 - \frac{\eta_\varphi}{D+1}\right) (1 + \omega_\theta) \frac{g_\varphi(1 + \omega_\theta) - \sigma g_\theta \omega_{\varphi\theta}}{((1 + \omega_\varphi)(1 + \omega_\theta) - \omega_{\varphi\theta}^2)^2} \right. \\ \left. - \sigma \omega_{\varphi\theta} \left(1 - \frac{\eta_\theta}{D+1}\right) \frac{g_\theta(1 + \omega_\varphi) - \sigma g_\varphi \omega_{\varphi\theta}}{((1 + \omega_\varphi)(1 + \omega_\theta) - \omega_{\varphi\theta}^2)^2} \right]. \end{aligned} \quad (\text{A.45})$$

### A.2.3. Sharp Cutoff

We can use the threshold functions for the sharp cutoff to conveniently extract the  $\epsilon$ -expansion equations from the FRG  $\beta$ -functions. The sharp cutoff is given by [249]

$$r_{\psi,k}(q) = \lim_{a \rightarrow \infty} \left( \sqrt{a \left( \frac{k^2}{q^2} - \frac{a-1}{a} \right)} - 1 \right) \theta(k^2 - q^2), \quad r_{\chi/\phi,k}(q) = \lim_{a \rightarrow \infty} a \left( \frac{k^2}{q^2} - 1 \right) \theta(k^2 - q^2), \quad (\text{A.46})$$

where the limit has to be taken after the integration over the loop momentum  $q$ . This gives the following explicit expressions. The contribution to the flow of the effective potential from the radial modes reads

$$I_R(\omega_\chi, \omega_\phi, \omega_\phi^2) = I_R^D(0, 0, 0) - 2\nu_D \log((1 + \omega_\phi)(1 + \omega_\chi) - \omega_\phi^2). \quad (\text{A.47})$$

Accordingly, the expressions for the Goldstone and the fermionic contributions become

$$I_G(\omega) = -2\nu_D \log(1 + \omega) + I_G^D(0), \quad \text{and} \quad I_\psi(\omega) = -2\nu_D \log(1 + \omega) + I_\psi^D(0). \quad (\text{A.48})$$

Since we want to extract the  $\epsilon$ -expansion limit, we have to work in the SYM-SYM regime, which yields a large simplification in the  $\beta$  functions for the Yukawa couplings and the anomalous dimensions. For the flow equations of the Yukawa couplings, we only need the threshold function

$$\begin{aligned} \frac{1}{g_\varphi^m} l_{(nm)R_\varphi}^{(FB),\sigma}(g_\varphi, g_\theta; \omega_\varphi, \omega_\theta, \omega_{\varphi\theta}, \omega_\psi) &\xrightarrow{\text{SYM}} l_{(nm)G_\phi}^{(FB)}(\omega_\varphi, \omega_\psi) \\ l_{(nm)G_\phi}^{(FB)}(\omega_\varphi, \omega_\psi) &= l_{nm}^{(FB)}(\omega_\varphi, \omega_\psi) = \frac{1}{(1 + \omega_\psi)^n (1 + \omega_\varphi)^m}. \end{aligned} \quad (\text{A.49})$$

For the anomalous dimensions, we use

$$m_{(22)}^{(F)D}(\omega_1, \omega_2) \xrightarrow{\text{SYM}} m_4^{(F)}(\omega) = \frac{1}{(1 + \omega)^4}, \quad (\text{A.50})$$

$$\frac{1}{g_\varphi} m_{(12)R_\varphi}^{(FB)D,\sigma}(g_\varphi, g_\theta; \omega_\varphi, \omega_\theta, \omega_{\varphi\theta}, \omega_\psi) \xrightarrow{\text{SYM}} m_{(12)G_\psi}^{(FB)D}(\omega_\varphi, \omega_\psi) = \frac{1}{(1 + \omega_\psi)(1 + \omega_\varphi)^2}. \quad (\text{A.51})$$



### A.3. Check of Convergence

We have checked the convergence of our polynomial expansion of the effective potential by extending our truncation up to 12th order in both fields  $\chi$  and  $\phi$ . In most cases the critical exponents are sufficiently convergent already at LPA8' level, with the remaining truncation error from the polynomial expansion being much smaller than the uncertainty due to the neglected higher-derivative operators. The largest deviations occur for the third-largest critical exponent  $\theta_3$  of the large- $N_f$  fixed point, as displayed in Fig. A.1. Still, already from LPA8' to LPA12' only minor improvements appear and we do not expect stronger deviations at even higher orders.

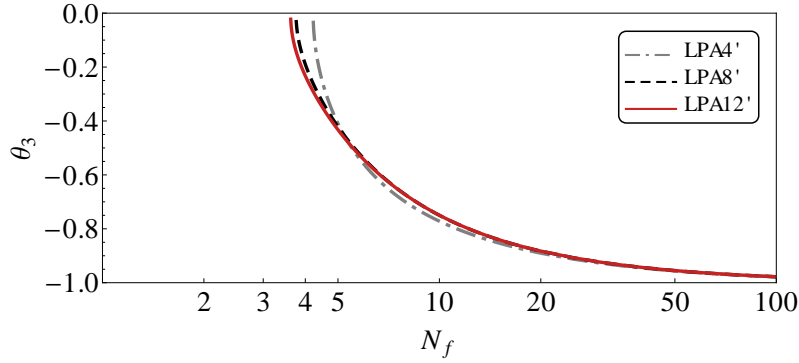


Figure A.1.: Third critical exponent in  $D = 3$  for large- $N_f$  fixed point as function of the fermion flavor number for different orders of polynomial truncation.



## APPENDIX B

---

### Interplay between Magnetism, Superconductivity and Orbital Order in Iron-Based Superconductors – Orbital Makeup and PRG Equations

---

#### B.1. Orbital Makeup

The 3-orbital, 5-band model accounts for contributions from the  $d_{xz}$ ,  $d_{yz}$  and  $d_{xy}$  iron orbitals to the low-energy excitations described by the effective Hamiltonian Eq. (5.2) in Chap. 5. The transformation from orbital to band basis then leads to so-called orbital makeup in the interaction terms, i. e. additional momentum dependences of the couplings due to the transformation. Alternatively, if we work with couplings in the orbital basis, we have to consider non-diagonal contributions of the Green's functions in the diagrams. Here we list the orbital to band transformations which we use in the pRG calculations below. For our choice of parameters, the transformation for fermions in the vicinity of the  $\Gamma$ -centered hole pockets is a rotation around the coordinate angle  $\theta_k = \arctan \frac{k_y}{k_x}$

$$\begin{pmatrix} d_{1,k,\sigma} \\ d_{2,k,\sigma} \end{pmatrix} = \begin{pmatrix} \cos \theta_k & \sin \theta_k \\ -\sin \theta_k & \cos \theta_k \end{pmatrix} \begin{pmatrix} c_{k,\sigma} \\ d_{k,\sigma} \end{pmatrix}, \quad (\text{B.1})$$

where  $d_{1/2,k,\sigma}$  label fermions in the orbital and  $c_{k,\sigma}/d_{k,\sigma}$  fermions in the band representation. The fermionic Green's functions in the orbital basis are related to  $G_{c/d}(i\omega, \mathbf{k}) = (i\omega - \epsilon_{c/d,k} - \mu)^{-1}$  in the band representation as

$$\begin{aligned} G_{d_1,d_1}(i\omega, \mathbf{k}) &= G_c(i\omega, \mathbf{k}) \cos^2 \theta_k + G_d(i\omega, \mathbf{k}) \sin^2 \theta_k \\ G_{d_2,d_2}(i\omega, \mathbf{k}) &= G_c(i\omega, \mathbf{k}) \sin^2 \theta_k + G_d(i\omega, \mathbf{k}) \cos^2 \theta_k \\ G_{d_1,d_2}(i\omega, \mathbf{k}) &= G_{d_2,d_1}(i\omega, \mathbf{k}) = [G_d(i\omega, \mathbf{k}) - G_c(i\omega, \mathbf{k})] \sin \theta_k \cos \theta_k \end{aligned} \quad (\text{B.2})$$

The Green's function of fermions around the  $M$ -hole pocket is  $G_M(i\omega, bsk) = (i\omega + k^2/(2m_M) - \epsilon_M)^{-1}$ . For the electron pockets, the transformation from orbital to band degrees of freedom is more involved and in general it does not correspond to a rotation around the coordinate angle  $\theta_k$ . Nevertheless, it can be expressed through

$$\begin{pmatrix} e_{1/2} \\ \bar{e}_{1/2} \end{pmatrix} = e^{i\phi} \begin{pmatrix} e^{i\phi_1} \cos \varphi_{1/2} & e^{i\phi_2} \sin \varphi_{1/2} \\ -e^{-i\phi_2} \sin \varphi_{1/2} & e^{-i\phi_1} \cos \varphi_{1/2} \end{pmatrix} \begin{pmatrix} f_{1/2} \\ f_{31/32} \end{pmatrix}, \quad (\text{B.3})$$

where  $e_{1/2}$  and  $\bar{e}_{1/2}$  are operators for band fermions near the electron pockets, and the functions  $\varphi_{1/2}$  and  $\phi_{1/2}$  depend on the angle  $\theta_k$  and system parameters. They determine the relative spectral weight of  $xz/yz$  and  $xy$  orbitals. We set  $e_{1/2}$  to describe the electrons in the band that crosses the Fermi level and consistently neglect contributions from  $\bar{e}_{1/2}$ . The electron propagator in orbital representation is expressed in terms of low energy fermions as

$$\begin{aligned} G_{f_{1/2}, f_{1/2}}(i\omega, \mathbf{k}) &= G_{e_{1/2}}(i\omega, \mathbf{k}) \cos^2 \varphi_{1/2} \\ G_{f_{31/32}, f_{31/32}}(i\omega, \mathbf{k}) &= G_{e_{1/2}}(i\omega, \mathbf{k}) \sin^2 \varphi_{1/2} \\ G_{f_{1/2}, f_{31/32}}(i\omega, \mathbf{k}) &= G_{f_{31/32}, f_{1/2}}(i\omega, \mathbf{k})^* = G_{e_{1/2}}(i\omega, \mathbf{k}) e^{i(\phi_1 - \phi_2)} \cos \varphi_{1/2} \sin \varphi_{1/2}, \end{aligned} \quad (\text{B.4})$$

where  $G_{e_{1/2}}(i\omega, \mathbf{k}) = (i\omega - \xi_e)^{-1}$  ( $k$  is counted from  $X$  in  $G_{e_1}$  and from  $Y$  in  $G_{e_2}$ ).

## B.2. PRG for the Toy Model

### B.2.1. PRG Equations for the 21 Couplings

Here, we list the explicit pRG equations obtained for the couplings of the toy model. As described in the main text, a subgroup of the 21 interactions decouples and flows to zero for bare values  $U' \geq J$ . Representative diagrams for the renormalizations of this group of six irrelevant couplings are shown in Fig. 5.4 in Chap. 5. The six pRG equations are:

$$\begin{aligned} 4\pi \frac{d}{dL} (\tilde{U}_4 \pm \tilde{\tilde{U}}_4) &= -c_{pp}^{(1)} (\tilde{U}_4 \pm \tilde{\tilde{U}}_4)^2 \\ 4\pi \frac{d}{dL} (\tilde{U}_5 \pm \tilde{\tilde{U}}_5) &= -c_{pp}^{(2)} (\tilde{U}_5 \pm \tilde{\tilde{U}}_5)^2 \\ 4\pi \frac{d}{dL} (U_a \pm U_b) &= -c_{pp}^{(3)} (U_a \pm U_b)^2, \end{aligned} \quad (\text{B.5})$$

where  $c_{pp}^{(1)} = \frac{1}{8}(m_c + m_d + 12 \frac{m_c m_d}{m_c + m_d} \pm \frac{(m_c - m_d)^2}{m_c + m_d})$ ,  $c_{pp}^{(2)} = m_e$  and  $c_{pp}^{(3)} = \frac{m_M m_e}{m_M + m_c} + \frac{m_M m_d}{m_M + m_d}$ . The pRG equations for the other remaining 15 couplings are

$$\begin{aligned} 4\pi \frac{d}{dL} U_1 &= A(U_1^2 + U_3^2) & 4\pi \frac{d}{dL} \bar{U}_1 &= A(\bar{U}_1^2 + \bar{U}_3^2) & 4\pi \frac{d}{dL} U_{1n} &= A_n(U_{1n}^2 + U_{3n}^2) \\ 4\pi \frac{d}{dL} U_2 &= 2AU_2(U_1 - U_2) & 4\pi \frac{d}{dL} \bar{U}_2 &= 2A\bar{U}_2(\bar{U}_1 - \bar{U}_2) & 4\pi \frac{d}{dL} U_{2n} &= 2A_n U_{2n}(U_{1n} - U_{2n}) \\ 4\pi \frac{d}{dL} U_3 &= 2AU_3(2U_1 - U_2) - A_e(U_3 U_5 + \bar{U}_3 \bar{U}_5) - A_h(U_3 U_4 + \bar{U}_3 \bar{U}_4) - A_h^-(U_3 \bar{U}_4 + \bar{U}_3 U_4) \\ &\quad - A_M U_{3n} U_c \\ 4\pi \frac{d}{dL} \bar{U}_3 &= 2A\bar{U}_3(2\bar{U}_1 - \bar{U}_2) - A_e(\bar{U}_3 U_5 + U_3 \bar{U}_5) - A_h(\bar{U}_3 U_4 + U_3 \bar{U}_4) - A_h^-(U_3 U_4 + \bar{U}_3 \bar{U}_4) \\ &\quad - A_M U_{3n} U_c \\ 4\pi \frac{d}{dL} U_{3n} &= 2A_n U_{3n}(2U_{1n} - U_{2n}) - A_e U_{3n}(U_5 + \bar{U}_5) - A_M U_{3n} U_{4n} - (A_h + A_h^-)(U_3 + \bar{U}_3) U_c \\ 4\pi \frac{d}{dL} U_4 &= -A_h(U_4^2 + \bar{U}_4^2) - 2A_h^- U_4 \bar{U}_4 - A_e(U_3^2 + \bar{U}_3^2) - A_M U_c^2 \\ 4\pi \frac{d}{dL} \bar{U}_4 &= -2A_h U_4 \bar{U}_4 - A_h^-(U_4^2 + \bar{U}_4^2) - 2A_e U_3 \bar{U}_3 - A_M U_c^2 \end{aligned}$$

$$\begin{aligned}
4\pi \frac{d}{dL} U_{4n} &= -A_M U_{4n}^2 - 2A_e U_{3n}^2 - 2(A_h + A_h^-) U_c^2 \\
4\pi \frac{d}{dL} U_5 &= -A_e (U_5^2 + \bar{U}_5^2) - A_h (U_3^2 + \bar{U}_3^2) - 2A_h^- U_3 \bar{U}_3 - A_M U_{3n}^2 \\
4\pi \frac{d}{dL} \bar{U}_5 &= -2A_e U_5 \bar{U}_5 - 2A_h U_3 \bar{U}_3 - A_h^- (U_3^2 + \bar{U}_3^2) - A_M U_{3n}^2 \\
4\pi \frac{d}{dL} U_c &= -(A_h + A_h^-) (U_4 + \bar{U}_4) U_c - A_M U_{4n} U_c - A_3 (U_3 + \bar{U}_3) U_{3n}.
\end{aligned} \tag{B.6}$$

As an example, the one-loop diagrams that renormalize  $U_{1n}$  and  $U_{3n}$  are presented in Fig. 5.5 in Chap. 5. The numerical prefactors in the r.h.s. of the pRG equations are  $A = \frac{m_e m_c}{m_e + m_c} + \frac{m_e m_d}{m_e + m_d}$ ,  $A_n = \frac{m_M m_e}{m_M + m_e}$ ,  $A_e = m_e$ ,  $A_h = \frac{3}{8}(m_c + m_d) + \frac{1}{2} \frac{m_c m_d}{m_c + m_d}$ ,  $A_h^- = \frac{1}{8} \frac{(m_c - m_d)^2}{m_c + m_d}$  and  $A_M = m_M$ . Note that the contribution  $A_h^- = (m_c - m_d)^2 / (8(m_c + m_d))$  comes from the non-diagonal part of the propagator for fermions near the  $\Gamma$ -centered hole pockets  $G_{d_1, d_2}$  (see Eq. (B.2)). To proceed, we note that, if  $U_i = \bar{U}_i$ , then  $d_L U_i = d_L \bar{U}_i$ . We have checked that the trajectory with this property is a stable one. We searched for other potential stable fixed trajectories, but did not find one. Hence we set  $U_i = \bar{U}_i$ . Introducing the dimensionless couplings  $u_{1,2} = A/(4\pi) U_{1,2}$ ,  $u_3 = A/(4\pi) a U_3$ ,  $u_4 = A_h/(4\pi) U_4$ ,  $u_5 = A_e/(4\pi) U_5$ ,  $u_{1n,2n} = A_n/(4\pi) U_{1n,2n}$ ,  $u_{3n} = A_n/(4\pi) a_n U_{3n}$ ,  $u_{4n} = A_M/(4\pi) U_{4n}$  and  $u_c = \sqrt{A_M A_h}/(4\pi) U_c$ , we obtain the pRG equations which we presented in the main text in Chap. 5. We also defined there  $a = \sqrt{A_h A_e}/A$  and  $a_n = \sqrt{A_M A_e}/A_n$  and  $b = 1 + A_h/A_h^-$ .

### B.2.2. Weakly Unstable Fixed Trajectory of the Toy Model

As described in the main text, the two stable fixed trajectories of the effective three (3pFT) and four (4pFT) pocket model are separated by a “symmetric” fixed trajectory with one unstable direction. Specifically, we obtain along this weakly unstable fixed trajectory

$$\begin{aligned}
u_i &= \gamma_i u_1 & u_1 &= \frac{1}{1 + \gamma_3^2/a^2} \frac{1}{L_0 - L} \\
\gamma_{1n} &= \gamma_1 = 1 & \frac{\gamma_{3n}}{a_n} &= \pm \frac{\gamma_3}{a} & \gamma_2 &= \gamma_{2n} = 0 \\
\gamma_3 &= \sqrt{8a^4 - a^2 + 4a^2 a_n^2 + a^2 \sqrt{15 + (8a^2 + 4a_n^2 - 1)^2}} \\
\gamma_5 &= 1 - a_n^2 - 2a^2 - \sqrt{1 + a_n^4 - a^2 + 4a^4 + a_n^2(4a^2 - \frac{1}{2})} \\
\gamma_c &= \pm a_n \frac{2a - \sqrt{2\gamma_3^2 a_n^2 + 4a^2(1 + \gamma_3^2)}}{a_n^2 + 2a^2} \\
\gamma_4 &= \pm \frac{a_n}{2a} \gamma_c + \frac{\gamma_3^2}{4a^2} - \frac{3}{4} & \gamma_{4n} &= \mp \frac{2a}{a_n} \gamma_c + \gamma_5
\end{aligned} \tag{B.7}$$

For  $a = a_n = 1$ , the  $\gamma_i$  in (B.7) reduce to

$$\begin{aligned}
\gamma_3 &= \pm \gamma_{3n} & \gamma_4 &= \gamma_{4n} = \pm \gamma_c \\
\gamma_3 &= \sqrt{11 + 2\sqrt{34}} & \gamma_4 &= -\frac{1}{3}(4 + \sqrt{34}) & \gamma_5 &= -2 - \sqrt{\frac{17}{2}}.
\end{aligned} \tag{B.8}$$

### B.3. Pomeranchuk Channel

The renormalization in the Pomeranchuk channel is not equivalent to the consideration for density waves and SC instabilities. The reason is that the polarization operator is obtained from a particle-hole bubble with zero momentum transfer, i. e. alone it does not lead to a logarithmic divergence. The Pomeranchuk vertex still flows logarithmically due to the appearance of the scale-dependent interactions in the one-loop diagrams (cf. Fig. 5.11 in Chap.5). For an explicit calculation let us label the coupling in the Pomeranchuk channel as  $U_{Pom}$  and the vertex  $\Gamma_{Pom}$ . Furthermore we consider the propagator  $G(\omega, k) = (i\omega - \epsilon_k)^{-1}$  with  $\epsilon_k = k^2/(2m)$  and set the external frequencies to zero. We obtain

$$\begin{aligned}
 d\Gamma_{Pom} &= \int_{k-dk}^k \int \frac{d^2k}{(2\pi)^2} \frac{d\omega}{2\pi} \frac{1}{(i\omega - \epsilon_k)^2} U_{Pom}(k) \Gamma_{Pom}(k) \\
 &= \lim_{\Omega \rightarrow \infty} \int \frac{d^2k}{(2\pi)^2} U_{Pom}(k) \Gamma_{Pom}(k) \frac{\partial}{\partial \epsilon_k} \int_{-\Omega}^{\Omega} \frac{d\omega}{2\pi} \frac{1}{i\omega - \epsilon_k} \\
 &= \lim_{\Omega \rightarrow \infty} \int \frac{dk}{2\pi} k U_{Pom}(k) \Gamma_{Pom}(k) \frac{2m}{k} \frac{\partial}{\partial k} \left( -\frac{i}{2\pi} \right) \ln \frac{i\Omega - \epsilon_k}{-i\Omega - \epsilon_k} \\
 &= -\frac{im}{2\pi^2} \lim_{\Omega \rightarrow \infty} \left[ \ln \frac{i\Omega - \epsilon_k}{-i\Omega - \epsilon_k} U_{Pom}(k) \Gamma_{Pom}(k) \right]_{|k-dk}^k - \int_{k-dk}^k dk \ln \frac{i\Omega - \epsilon_k}{-i\Omega - \epsilon_k} \frac{\partial}{\partial k} (U_{Pom} \Gamma_{Pom}) \\
 &\approx -\frac{im}{2\pi^2} (-i\pi) \left[ U_{Pom} \Gamma_{Pom} dk - \frac{\partial}{\partial k} (U_{Pom} \Gamma_{Pom}) dk \right] \\
 &= -\frac{m}{2\pi} \left[ -\frac{1}{2} \sqrt{2mW} e^{-L/2} U_{Pom} \Gamma_{Pom} - \frac{\partial}{\partial L} (U_{Pom} \Gamma_{Pom}) \right] dL
 \end{aligned} \tag{B.9}$$

with the logarithmic energy scale  $L = \ln(2mW/k^2)$  and the bandwidth  $W$ . To consistently sum only logarithmic terms we need to neglect the first term in the last line and set the vertex to its initial value  $\Gamma_{Pom}(k) \rightarrow \Gamma_{Pom}^0$  on the right hand side. This leads to

$$\frac{d}{dL} \Gamma_{Pom} = m \Gamma_{Pom}^0 \frac{d}{dL} U_{Pom}, \tag{B.10}$$

which we cited in the main text.

### B.4. PRG for the Full 5-Pocket Model

#### B.4.1. PRG Equations for the 40 Couplings

We now move to the full 5-band model with  $xz/yz$  orbital content on the electron pockets. Like we said, in this case we have 19 more couplings (the total number of the couplings is 40). The couplings  $\tilde{U}_4, \tilde{\tilde{U}}_4, \tilde{U}_5, \tilde{\tilde{U}}_5, U_a, U_b$  do not couple to additional terms and continue to flow to zero under the pRG. We find six additional couplings  $\tilde{V}_5, \tilde{\tilde{V}}_5, V_a, V_b, \bar{V}_a, \bar{V}_b$  that flow to zero. The corresponding pRG equations are

$$\begin{aligned}
 4\pi \frac{d}{dL} (\tilde{V}_5 \pm \tilde{\tilde{V}}_5) &= -c_{pp}^{(4)} (\tilde{V}_5 \pm \tilde{\tilde{V}}_5)^2 \\
 4\pi \frac{d}{dL} (V_a \pm V_b) &= -c_{pp}^{(5)\pm} (V_a \pm V_b)^2 \\
 4\pi \frac{d}{dL} (\bar{V}_a \pm \bar{V}_b) &= -c_{pp}^{(6)} (\bar{V}_a \pm \bar{V}_b)^2,
 \end{aligned} \tag{B.11}$$

where  $c_{pp}^{(4)} = 1/L \int d\omega \int d^2k G_{f_{31},f_{31}} G_{f_{32},f_{32}}$ ,  $c_{pp}^{(5)\pm} = 1/L \int d\omega \int d^2k (G_{f_{31},f_{31}} G_{f_1,f_1} \pm G_{f_{31},f_1} G_{f_1,f_{31}})$ , and  $c_{pp}^{(6)} = 1/L \int d\omega \int d^2k G_{f_{31},f_{31}} G_{f_2,f_2}$ . For the other couplings we make the same conjecture as for the toy model, i.e., assume that for stable and weakly unstable fixed trajectories  $U_i = \bar{U}_i, V_i = \bar{V}_i$ . The one-loop RG equations for the remaining dimensionless couplings are

$$\begin{aligned}
\dot{u}_1 &= u_1^2 + \frac{u_3^2}{d^2} \\
\dot{u}_{1n} &= u_{1n}^2 + \frac{u_{3n}^2}{d_n^2} \\
\dot{u}_2 &= 2u_2(u_1 - u_2) \\
\dot{u}_{2n} &= 2u_{2n}(u_{1n} - u_{2n}) \\
\dot{u}_3 &= 2u_3(2u_1 - u_2 - u_5) - 2bu_3u_4 - u_{3n}u_c - 2v_3v_c - 2H(u_3v_c + v_3u_5) \\
\dot{u}_{3n} &= 2u_{3n}(2u_{1n} - u_{2n} - u_5) - u_{3n}u_{4n} - 2bu_3u_c - 2v_{3n}v_c - 2H(u_{3n}v_c + v_{3n}u_5) \\
\dot{u}_4 &= -2bu_4^2 - 2u_3^2 - 2u_c^2 - 2v_3^2 - 4Hu_3v_3 \\
\dot{u}_{4n} &= -u_{4n}^2 - 2u_{3n}^2 - 2bu_c^2 - 2v_{3n}^2 - 4Hu_{3n}v_{3n} \\
\dot{u}_5 &= -2u_5^2 - 2bu_3^2 - u_{3n}^2 - 2v_c^2 - 4Hu_5v_c \\
\dot{u}_c &= -2bu_4u_c - u_{4n}u_c - 2u_3u_{3n} - 2v_3v_{3n} - 2H(v_3u_{3n} + v_{3n}u_3) \\
\dot{v}_1 &= v_1^2 + \frac{v_3^2}{c^2} \\
\dot{v}_{1n} &= v_{1n}^2 + \frac{v_{3n}^2}{c_n^2} \\
\dot{v}_2 &= 2v_2(v_1 - v_2) \\
\dot{v}_{2n} &= 2v_{2n}(v_{1n} - v_{2n}) \\
\dot{v}_3 &= 2v_3(2v_1 - v_2 - v_5) - 2bv_3u_4 - v_{3n}u_c - 2u_3v_c - 2H(v_3v_c + u_3v_5) \\
\dot{v}_{3n} &= 2v_{3n}(2v_{1n} - v_{2n} - v_5) - v_{3n}u_{4n} - 2bv_3u_c - 2u_{3n}v_c - 2H(v_{3n}v_c + u_{3n}v_5) \\
\dot{v}_5 &= -2v_5^2 - 2bv_3^2 - v_{3n}^2 - 2v_c^2 - 4Hv_5v_c \\
\dot{v}_c &= -2bv_3u_3 - 2v_5v_c - 2u_5v_c - 2v_{3n}u_{3n} - 2H(v_c^2 + v_5u_5),
\end{aligned} \tag{B.12}$$

where the additional parameters are

$$\begin{aligned}
c &= \frac{\sqrt{A_h A'_e}}{A'} \quad c_n = \frac{\sqrt{A_M A'_e}}{A'_n} \quad H = \frac{A_e^a}{\sqrt{A_e A'_e}} \\
A_e &= \frac{1}{L} \frac{1}{(2\pi)^2} \int d\omega \int d^2k G_{f_1,f_1} G_{f_1,f_1} = m_e \int \frac{d\theta}{2\pi} \cos^4 \varphi_1 \\
A'_e &= \frac{1}{L} \frac{1}{(2\pi)^2} \int d\omega \int d^2k G_{f_{31},f_{31}} G_{f_{31},f_{31}} = m_e \int \frac{d\theta}{2\pi} \sin^4 \varphi_1 \\
A' &= \frac{1}{L} \frac{1}{(2\pi)^2} \int d\omega \int d^2k G_{f_{31},f_{31}} G_{d_1,d_1} = 2 \int \frac{d\theta}{2\pi} \sin^2 \varphi_1 \left( \frac{m_c m_e}{m_c + m_e} \cos^2 \theta + \frac{m_d m_e}{m_d + m_e} \sin^2 \theta \right) \\
A'_n &= \frac{1}{L} \frac{1}{(2\pi)^2} \int d\omega \int d^2k G_{f_{31},f_{31}} G_M = 2 \frac{m_M m_e}{m_M + m_e} \int \frac{d\theta}{2\pi} \sin^2 \varphi_1 \\
A_e^a &= \frac{1}{L} \frac{1}{(2\pi)^2} \int d\omega \int d^2k G_{f_1,f_{31}} G_{f_1,f_{31}} = m_e \int \frac{d\theta}{2\pi} \sin^2 \varphi_1 \cos^2 \varphi_1.
\end{aligned} \tag{B.13}$$

### B.4.2. Fixed Trajectories

Interestingly, we find that the stable fixed trajectories of the full model lead to the same decoupling at low-energies into effective three or four pocket model, as in the toy model. In distinction to the toy model, however, now there are two 3pFT and two 4pFT (3pFT<sub>1</sub>, 3pFT<sub>2</sub>, 4pFT<sub>1</sub>, 4pFT<sub>2</sub>). These four stable fixed trajectories are specified by

$$\begin{aligned}
 & \text{(4pFT}_1\text{)} & \text{(4pFT}_2\text{)} \\
 & u_i = \gamma_i u_1 \quad v_i = g_i u_1 & u_i = \gamma_i v_1 \quad v_i = g_i v_1 \\
 & u_1 = \frac{1}{1 + \gamma_3^2/a^2} \frac{1}{L_0 - L} & v_1 = \frac{1}{1 + g_3^2/c^2} \frac{1}{L_0 - L} \\
 & \gamma_3 = \pm a \sqrt{8a^2 - 1 + 4\sqrt{1 - a^2 + 4a^4}} & g_3 = \pm c \sqrt{8c^2 - 1 + 4\sqrt{1 - c^2 + 4c^4}} \\
 & \gamma_4 = \gamma_5 = 1 - 2a^2 - \sqrt{1 - a^2 + 4a^4} & \gamma_4 = g_5 = 1 - 2c^2 - \sqrt{1 - c^2 + 4c^4} \\
 & & \text{(B.14)}
 \end{aligned}$$
  

$$\begin{aligned}
 & \text{(3pFT}_1\text{)} & \text{(3pFT}_2\text{)} \\
 & u_i = \gamma_i u_{1n} \quad v_i = g_i u_{1n} & u_i = \gamma_i v_{1n} \quad v_i = g_i v_{1n} \\
 & u_{1n} = \frac{1}{1 + \gamma_{3n}^2/a_n^2} \frac{1}{L_0 - L} & v_{1n} = \frac{1}{1 + g_{3n}^2/c_n^2} \frac{1}{L_0 - L} \\
 & \gamma_{3n} = \pm a_n \sqrt{4a_n^2 - 1 + 2\sqrt{4 - 2a_n^2 + 4a_n^4}} & g_{3n} = \pm c_n \sqrt{4c_n^2 - 1 + 2\sqrt{4 - 2c_n^2 + 4c_n^4}} \\
 & \gamma_{4n} = 2\gamma_5 = 2 - 2a_n^2 - \sqrt{4 - 2a_n^2 + 4a_n^4} & g_{4n} = 2g_5 = 2 - 2c_n^2 - \sqrt{4 - 2c_n^2 + 4c_n^4} \\
 & & \text{(B.15)}
 \end{aligned}$$

All couplings not presented in the above formulas evolve with smaller exponents. Note that the ratios of the couplings in Eqs. (B.14), (B.15) do not depend of the hybridization parameter  $H$ .

We see from Eq. (B.14) that for 4pFT<sub>1</sub> and 4pFT<sub>2</sub> all interactions involving the  $M$ -centered hole pocket become subleading, like in the toy model. For 4pFT<sub>1</sub>, the interactions involving  $xz/yz$  orbital components on the electron pockets become subleading compared to the interactions involving  $xy$  orbital component, i. e. to a first approximation the two electron pockets can be approximated as  $xy$ -pockets. For 4pFT<sub>2</sub>, the situation is opposite – the interactions involving  $xy$  orbital components on the electron pockets become subleading compared to the interactions involving  $xz/yz$  orbital components, i. e. to a first approximation the two electron pockets can be approximated as  $xz$  and  $yz$  pockets. These two fixed trajectories have been analyzed in Ref. [122]. The situation is equivalent for 3pFT<sub>1</sub> and 3pFT<sub>2</sub> in Eq. (B.15). In the first case, the interactions involving  $xz/yz$  orbital components on the electron pockets become subleading, and in the second the interactions involving  $xy$  orbital components on the electron pockets become subleading. These different effective low-energy models are sketched in Fig. 5.12 in the main text. We also note that the behavior of the different couplings along 4pFT<sub>1</sub> and 4pFT<sub>2</sub> are quite similar, see Eq. (B.14), and the same is true for the couplings along 3pFT<sub>1</sub> and 3pFT<sub>2</sub>, Eq. (B.15). Whether the system flows to 4pFT<sub>1/2</sub> or 3pFT<sub>1/2</sub> depends on the initial values of the couplings.

The stable FT's are separated by several weakly unstable ones with only a single direction along which perturbations grow. For general  $a, a_n, c, c_n$ , and  $H$  we determined these FT's and checked their stability numerically. For  $a = a_n = c = c_n = 1$  these weakly unstable FT's can be analyzed analytically. The FT's with only one unstable direction are (notations are self-evident):



(4pFT<sub>1</sub>+4pFT<sub>2</sub>)

$$\begin{aligned}
u_i &= \gamma_i u_1 \quad v_i = g_i u_1 \\
u_1 &= v_1 \quad u_3 = v_3 \quad u_5 = v_5 = v_c \\
u_1 &= \frac{1}{1 + \gamma_3^2/a^2} \frac{1}{L_0 - L} \\
\gamma_3 &= \pm \sqrt{15 + 16H + 4\sqrt{15 + 30H + 16H^2}} \\
\gamma_4 &= 2(H + 1)\gamma_5 = -3 - 4H\sqrt{15 + 30H + 16H^2}
\end{aligned} \tag{B.16}$$

(3pFT<sub>1</sub>+3pFT<sub>2</sub>)

$$\begin{aligned}
u_i &= \gamma_i u_{1n} \quad v_i = g_i u_{1n} \\
u_{1n} &= v_{1n} \quad u_{3n} = v_{3n} \quad u_5 = v_5 = v_c \\
u_{1n} &= \frac{1}{1 + \gamma_{3n}^2/a_n^2} \frac{1}{L_0 - L} \\
\gamma_{3n} &= \pm \sqrt{7 + 8H + 4\sqrt{4 + 7H + 4H^2}} \\
\gamma_{4n} &= 4(H + 1)\gamma_5 = -2 - 4H - 2\sqrt{4 + 7H + 4H^2}
\end{aligned} \tag{B.17}$$

(3pFT<sub>1</sub>+4pFT<sub>1</sub>)

$$\begin{aligned}
u_i &= \gamma_i u_1 \quad v_i = g_i u_1 \\
u_1 &= u_{1n} \quad u_3 = \pm u_{3n} \quad u_4 = u_{4n} = \pm u_c \\
u_1 &= \frac{1}{1 + \gamma_3^2/a^2} \frac{1}{L_0 - L} \\
\gamma_3 &= \sqrt{11 + 2\sqrt{34}} \quad \gamma_4 = -\frac{1}{3}(4 + \sqrt{34}) \\
\gamma_5 &= -2 - \sqrt{\frac{17}{2}}
\end{aligned} \tag{B.18}$$

(3pFT<sub>2</sub>+4pFT<sub>2</sub>)

$$\begin{aligned}
u_i &= \gamma_i v_1 \quad v_i = g_i v_1 \\
v_1 &= v_{1n} \quad v_3 = \pm v_{3n} \quad u_4 = u_{4n} = \pm u_c \\
g_3 &= \sqrt{11 + 2\sqrt{34}} \quad \gamma_4 = -\frac{1}{3}(4 + \sqrt{34}) \\
g_5 &= -2 - \sqrt{\frac{17}{2}}.
\end{aligned} \tag{B.19}$$

Again all couplings not listed in the formulas above have smaller exponents. A detailed analysis of the structure of weakly unstable FT's in the full 4-pocket model is presented in Ref. [248].

Finally there is a high-symmetry FT with two unstable directions. Along this FT all couplings

are non-zero:

$$\begin{aligned}
u_i &= \gamma_i u_1 \quad v_i = g_i u_1 \\
u_1 &= u_{1n} = v_1 = v_{1n} \quad u_3 = u_{3n} = v_3 = v_{3n} \\
u_4 &= h_{4n} = u_c \quad u_5 = v_5 = v_c \\
u_1 &= \frac{1}{1 + \gamma_3^2/a^2} \frac{1}{L_0 - L} \\
\gamma_3 &= \pm \sqrt{23 + 24H + 4\sqrt{34 + 69H + 36H^2}} \\
\gamma_4 &= \frac{4}{3}(H + 1)\gamma_5 = -\frac{10}{3} - 4H - \frac{2}{3}\sqrt{34 + 69H + 36H^2}.
\end{aligned} \tag{B.20}$$

### B.4.3. Susceptibilities

Here we present the detailed calculation of the pRG equations for the susceptibilities in the full model. The four SDW vertices flow according to

$$\begin{aligned}
\partial_L \Gamma_{SDW}^{\Gamma,1} &= \left(u_1 + \frac{u_3}{a}\right) \Gamma_{SDW}^{\Gamma,1} \\
\partial_L \Gamma_{SDW}^{\Gamma,2} &= \left(v_1 + \frac{v_3}{c}\right) \Gamma_{SDW}^{\Gamma,2} \\
\partial_L \Gamma_{SDW}^{M,1} &= \left(u_{1n} + \frac{u_{3n}}{a_n}\right) \Gamma_{SDW}^{M,1} \\
\partial_L \Gamma_{SDW}^{M,2} &= \left(v_{1n} + \frac{v_{3n}}{c_n}\right) \Gamma_{SDW}^{M,2}
\end{aligned} \tag{B.21}$$

where indices 1, 2 mean that the order parameters involve fermions on electron pockets with either  $xz(yz)$  or  $xy$  orbital content, and indices  $\Gamma$  and  $M$  mean that the SDW order parameter involves fermions from either  $\Gamma$ -centered or  $M$ -centered hole pockets. Using the values of the couplings along the FT's as inputs and solving these differential equations, we obtain  $\Gamma_{SDW}^{(i)} \sim 1/(L_0 - L)^{\beta_{SDW}^{(i)}}$ , with  $\beta_{SDW}^{(i)} = (1 + \gamma_{3i}/a_i)/(1 + \gamma_{3i}^2/a_i^2)$ , where  $i = (\Gamma, 1; \Gamma, 2; M, 1; M, 2)$  and  $\gamma_{3i} \in \{\gamma_3, g_3, \gamma_{3n}, g_{3n}\}$ ,  $a_i \in \{a, a_n, c, c_n\}$ . We verified that all  $\beta_{SDW}^i$  are smaller than 1/2, so that SDW order does not develop (if  $L_0 < L_F$ ). The largest values are for  $a = a_n = c = c_n = 1$ :  $\beta_{SDW}^{\Gamma,1} = \beta_{SDW}^{\Gamma,2} = 0.3$  and  $\beta_{SDW}^{M,1} = \beta_{SDW}^{M,2} = 0.43$ . These are the same values as in the toy model.

There are also four superconducting vertices:  $\Gamma_{SC}^{e,xz/yz}$ ,  $\Gamma_{SC}^{e,xy}$ ,  $\Gamma_{SC}^{\Gamma}$ , and  $\Gamma_{SC}^M$ . The RG equations for these vertices can be cast into the matrix equation

$$\partial_L \Gamma_{SC} = -2 \begin{pmatrix} u_5 + H v_c & v_c + H u_5 & u_3 & u_{3n} \\ v_c + H v_5 & v_5 + H v_c & v_3 & v_{3n} \\ u_3 + H v_3 & v_3 + H u_3 & u_4 & u_c \\ \frac{u_{3n} + H v_{3n}}{2} & \frac{v_{3n} + H u_{3n}}{2} & \frac{u_c}{2} & \frac{u_{4n}}{2} \end{pmatrix} \Gamma_{SC}, \tag{B.22}$$

where we introduced  $\Gamma_{SC} = (\Gamma_{SC}^{e,xz/yz}, \Gamma_{SC}^{e,xy}, \Gamma_{SC}^{\Gamma}, \Gamma_{SC}^M)^T$ . Along each FT the solution of Eq. (B.22) gives rise to a  $s^{+-}$  gap structure on the contributing pockets. The exponents are

$$\begin{aligned}
\beta_{SC}^{(4p_1)} &= \frac{-\gamma_4 - \gamma_5 + \sqrt{(\gamma_4 - \gamma_5)^2 + 4\gamma_3^2}}{1 + \gamma_3^2/a^2} \\
\beta_{SC}^{(4p_2)} &= \frac{-\gamma_4 - g_5 + \sqrt{(\gamma_4 - g_5)^2 + 4g_3^2}}{1 + g_3^2/c^2}
\end{aligned}$$

$$\begin{aligned}
\beta_{SC}^{(3p_1)} &= \frac{-\gamma_{4n} - 2\gamma_5 + \sqrt{(\gamma_{4n} - 2\gamma_5)^2 + 8\gamma_{3n}^2}}{1 + \gamma_{3n}^2/a_n^2} \\
\beta_{SC}^{(3p_2)} &= \frac{-\gamma_{4n} - 2g_5 + \sqrt{(\gamma_{4n} - 2g_5)^2 + 8g_{3n}^2}}{1 + g_{3n}^2/c_n^2}.
\end{aligned} \tag{B.23}$$

For  $a = a_n = c = c_n$  we have  $\beta_{SC}^{(4p_1)} = \beta_{SC}^{(4p_2)} = 0.86$  and  $\beta_{SC}^{(3p_1)} = \beta_{SC}^{(3p_2)} = 0.72$ , again as in the toy model. We checked that  $\beta_{SC}^{(i)} \geq 1/2$  for all  $a, a_n, c, c_n$ , i.e., the superconducting susceptibility does diverge at  $L = L_0$ .



---

## Danksagung

---

Diese Arbeit wäre nicht möglich gewesen ohne die Unterstützung meiner Betreuer, Kollegen, Familie und Freunde.

Ganz besonders möchte ich mich bei Michael Scherer bedanken für die großartige Betreuung dieser Arbeit. Er hat es verstanden passende und interessante Projekte auszuwählen und mich insbesondere auch durch die unvermeidbaren, schwierigeren Phasen der Doktorarbeit zu leiten. Durch seine Geduld und Hilfsbereitschaft zu jeder Zeit konnte ich mich weiterentwickeln und ein besseres physikalisches Verständnis erlangen. Ich habe mich und meine Arbeit immer wertgeschätzt und das Einbringen eigener Ideen gefördert gefühlt. Ebenso möchte ich seine Unterstützung und Beratung außerhalb physikalischer Themen dankend hervorheben.

Für die vielen Ratschläge und seine Unterstützung möchte ich mich auch bei Jan Pawlowski bedanken. Durch ihn wurde meine Arbeit in Heidelberg erst ermöglicht. Er hat immer eine offene Tür für mich gehabt und ich habe viel in anregenden und fordernden Diskussionen von ihm gelernt.

Ich habe auch enorm von der Zusammenarbeit mit Carsten Honerkamp, Igor Herbut und Lukas Janssen profitiert. Vor allem bei Carsten Honerkamp möchte ich mich zusätzlich zu den physikalischen Einsichten, auch für die Möglichkeit ihn zu jeder Zeit um Rat zu bitten, bedanken. Des weiteren möchte ich an dieser Stelle Igor Herbut für die Unterstützung und Beratung danken.

Für die tolle Zeit während meines zweimonatigen Aufenthalts an der School of Physics and Astronomy der University of Minnesota möchte ich mich bei Andrey Chubukov bedanken. Seine Bereitschaft physikalische Ideen zu teilen, hat mich viel gelehrt und maßgeblich zu dieser Arbeit beigetragen. Zudem danke ich der Gruppe von Andrey Chubukov und Rafael Fernandes für die freundliche Aufnahme und die angenehme Atmosphäre in Minneapolis.

Die weitaus längere Zeit habe ich natürlich am Institut für theoretische Physik verbracht und ich möchte meinen Kollegen dort für die einmaligen Bedingungen danken. Vor allem das "Dachzimmer" hat neben dem wissenschaftlichen auch für den spaßigen Teil der Doktorarbeit gesorgt.

Mein weiterer Dank gilt Manfred Salmhofer für die freundliche Übernahme der Zweitkorrektur dieser Arbeit.

Fabian Rennecke danke ich für das Korrekturlesen von Teilen dieser Arbeit.

Zudem danke ich dem Institut für theoretische Physik der Universität Heidelberg, der Studienstiftung des deutschen Volkes und der Heidelberger Graduate School of Fundamental Physics für finanzielle Unterstützung.

Schließlich möchte ich meinen Eltern und meinen Schwestern von Herzen für ihre bedingungslose Unterstützung danken. Ihr Beitrag ist nicht abschätzbar.



---

## Bibliography

---

- [1] L. Taillefer, “Scattering and pairing in cuprate superconductors,” *Annual Review of Condensed Matter Physics* **1** no. 1, (2010) 51–70.
- [2] D. J. Scalapino, “A common thread: The pairing interaction for unconventional superconductors,” *Rev. Mod. Phys.* **84** (Oct, 2012) 1383–1417.
- [3] P. Dai, “Antiferromagnetic order and spin dynamics in iron-based superconductors,” *Rev. Mod. Phys.* **87** (Aug, 2015) 855–896.
- [4] E. Fradkin, S. A. Kivelson, and J. M. Tranquada, “Colloquium : Theory of intertwined orders in high temperature superconductors,” *Rev. Mod. Phys.* **87** (May, 2015) 457–482.
- [5] K.-S. Liu and M. E. Fisher, “Quantum lattice gas and the existence of a supersolid,” *Journal of Low Temperature Physics* **10** no. 5, (1973) 655–683.
- [6] E. Kim and M. Chan, “Probable observation of a supersolid helium phase,” *Nature* **427** no. 6971, (2004) 225–227.
- [7] D. Y. Kim and M. H. W. Chan, “Absence of supersolidity in solid helium in porous vycor glass,” *Phys. Rev. Lett.* **109** (Oct, 2012) 155301.
- [8] D. R. Nelson, J. M. Kosterlitz, and M. E. Fisher, “Renormalization-group analysis of bicritical and tetracritical points,” *Phys. Rev. Lett.* **33** (Sep, 1974) 813–817.
- [9] A. Pelissetto and E. Vicari, “Critical phenomena and renormalization-group theory,” *Physics Reports* **368** no. 6, (2002) 549 – 727.
- [10] P. Calabrese, A. Pelissetto, and E. Vicari, “The critical behavior of magnetic systems described by Landau-Ginzburg-Wilson field theories,” *eprint arXiv:cond-mat/0306273* (June, 2003) , [cond-mat/0306273](#).
- [11] A. Eichhorn, D. Mesterházy, and M. M. Scherer, “Multicritical behavior in models with two competing order parameters,” *Phys. Rev. E* **88** (Oct, 2013) 042141.
- [12] I. Boettcher, “Scaling relations and multicritical phenomena from functional renormalization,” *Phys. Rev. E* **91** (Jun, 2015) 062112.

- [13] R. Shankar, “Renormalization-group approach to interacting fermions,” *Rev. Mod. Phys.* **66** (Jan, 1994) 129–192.
- [14] J. Berges, N. Tetradis, and C. Wetterich, “Non-perturbative renormalization flow in quantum field theory and statistical physics,” *Physics Reports* **363** no. 4–6, (2002) 223 – 386. Renormalization group theory in the new millennium. {IV}.
- [15] W. Metzner, M. Salmhofer, C. Honerkamp, V. Meden, and K. Schönhammer, “Functional renormalization group approach to correlated fermion systems,” *Rev. Mod. Phys.* **84** (Mar, 2012) 299–352.
- [16] I. Herbut, *A modern approach to critical phenomena*. Cambridge University Press, 2007.
- [17] P. Kopietz, L. Bartosch, and F. Schütz, *Introduction to the functional renormalization group*, vol. 798. Springer, 2010.
- [18] A. Bostwick, T. Ohta, T. Seyller, K. Horn, and E. Rotenberg, “Quasiparticle dynamics in graphene,” *Nature Physics* **3** no. 1, (2007) 36–40.
- [19] T. Wehling, A. Black-Schaffer, and A. Balatsky, “Dirac materials,” *Advances in Physics* **63** no. 1, (2014) 1–76.
- [20] S. Das Sarma, S. Adam, E. H. Hwang, and E. Rossi, “Electronic transport in two-dimensional graphene,” *Rev. Mod. Phys.* **83** (May, 2011) 407–470.
- [21] K. Novoselov, A. K. Geim, S. Morozov, D. Jiang, M. Katsnelson, I. Grigorieva, S. Dubonos, and A. Firsov, “Two-dimensional gas of massless dirac fermions in graphene,” *nature* **438** no. 7065, (2005) 197–200.
- [22] A. K. Geim and K. S. Novoselov, “The rise of graphene,” *Nature materials* **6** no. 3, (2007) 183–191.
- [23] A. H. Castro Neto, F. Guinea, N. M. R. Peres, K. S. Novoselov, and A. K. Geim, “The electronic properties of graphene,” *Rev. Mod. Phys.* **81** (Jan, 2009) 109–162.
- [24] G. G. Guzmán-Verri and L. C. Lew Yan Voon, “Electronic structure of silicon-based nanostructures,” *Phys. Rev. B* **76** (Aug, 2007) 075131.
- [25] B. Aufray, A. Kara, S. Vizzini, H. Oughaddou, C. Léandri, B. Ealet, and G. Le Lay, “Graphene-like silicon nanoribbons on ag(110): A possible formation of silicene,” *Applied Physics Letters* **96** no. 18, (2010) .
- [26] P. Vogt, P. De Padova, C. Quaresima, J. Avila, E. Frantzeskakis, M. C. Asensio, A. Resta, B. Ealet, and G. Le Lay, “Silicene: Compelling experimental evidence for graphenelike two-dimensional silicon,” *Phys. Rev. Lett.* **108** (Apr, 2012) 155501.
- [27] Y. Du, J. Zhuang, H. Liu, X. Xu, S. Eilers, K. Wu, P. Cheng, J. Zhao, X. Pi, K. W. See, G. Peleckis, X. Wang, and S. X. Dou, “Tuning the band gap in silicene by oxidation,” *ACS Nano* **8** no. 10, (2014) 10019–10025. PMID: 25248135.
- [28] S. Cahangirov, M. Topsakal, E. Aktürk, H. Şahin, and S. Ciraci, “Two- and one-dimensional honeycomb structures of silicon and germanium,” *Phys. Rev. Lett.* **102** (Jun, 2009) 236804.



- [29] E. Bianco, S. Butler, S. Jiang, O. D. Restrepo, W. Windl, and J. E. Goldberger, "Stability and exfoliation of germanane: A germanium graphane analogue," *ACS Nano* **7** no. 5, (2013) 4414–4421. PMID: 23506286.
- [30] M. Derivaz, D. Dentel, R. Stephan, M.-C. Hanf, A. Mehdaoui, P. Sonnet, and C. Pirri, "Continuous germanene layer on al(111)," *Nano Letters* **15** no. 4, (2015) 2510–2516. PMID: 25802988.
- [31] C.-H. Park, L. Yang, Y.-W. Son, M. L. Cohen, and S. G. Louie, "New generation of massless dirac fermions in graphene under external periodic potentials," *Phys. Rev. Lett.* **101** (Sep, 2008) 126804.
- [32] F. Guinea and T. Low, "Band structure and gaps of triangular graphene superlattices," *Philosophical Transactions of the Royal Society of London A: Mathematical, Physical and Engineering Sciences* **368** no. 1932, (2010) 5391–5402.
- [33] C. Ortix, L. Yang, and J. van den Brink, "Graphene on incommensurate substrates: Trigonal warping and emerging dirac cone replicas with halved group velocity," *Phys. Rev. B* **86** (Aug, 2012) 081405.
- [34] M. Yankowitz, J. Xue, D. Cormode, J. D. Sanchez-Yamagishi, K. Watanabe, T. Taniguchi, P. Jarillo-Herrero, P. Jacquod, and B. J. LeRoy, "Emergence of superlattice dirac points in graphene on hexagonal boron nitride," *Nature Physics* **8** no. 5, (2012) 382–386.
- [35] L. Ponomarenko, R. Gorbachev, G. Yu, D. Elias, R. Jalil, A. Patel, A. Mishchenko, A. Mayorov, C. Woods, J. Wallbank, *et al.*, "Cloning of dirac fermions in graphene superlattices," *Nature* **497** no. 7451, (2013) 594–597.
- [36] B. Hunt, J. D. Sanchez-Yamagishi, A. F. Young, M. Yankowitz, B. J. LeRoy, K. Watanabe, T. Taniguchi, P. Moon, M. Koshino, P. Jarillo-Herrero, and R. C. Ashoori, "Massive dirac fermions and hofstadter butterfly in a van der waals heterostructure," *Science* **340** no. 6139, (2013) 1427–1430.
- [37] P. Soltan-Panahi, J. Struck, P. Hauke, A. Bick, W. Plenkers, G. Meineke, C. Becker, P. Windpassinger, M. Lewenstein, and K. Sengstock, "Multi-component quantum gases in spin-dependent hexagonal lattices," *Nature Physics* **7** no. 5, (2011) 434–440.
- [38] G. Weick, C. Woollacott, W. L. Barnes, O. Hess, and E. Mariani, "Dirac-like plasmons in honeycomb lattices of metallic nanoparticles," *Phys. Rev. Lett.* **110** (Mar, 2013) 106801.
- [39] S. Banerjee, J. Fransson, A. M. Black-Schaffer, H. Ågren, and A. V. Balatsky, "Granular superconductor in a honeycomb lattice as a realization of bosonic dirac material," *Phys. Rev. B* **93** (Apr, 2016) 134502.
- [40] M. Gibertini, A. Singha, V. Pellegrini, M. Polini, G. Vignale, A. Pinczuk, L. N. Pfeiffer, and K. W. West, "Engineering artificial graphene in a two-dimensional electron gas," *Phys. Rev. B* **79** (Jun, 2009) 241406.
- [41] L. Tarruell, D. Greif, T. Uehlinger, G. Jotzu, and T. Esslinger, "Creating, moving and merging dirac points with a fermi gas in a tunable honeycomb lattice," *Nature* **483** no. 7389, (2012) 302–305.

- [42] M. Polini, F. Guinea, M. Lewenstein, H. C. Manoharan, and V. Pellegrini, “Artificial honeycomb lattices for electrons, atoms and photons,” *Nature nanotechnology* **8** no. 9, (2013) 625–633.
- [43] S. M. Young, S. Zaheer, J. C. Y. Teo, C. L. Kane, E. J. Mele, and A. M. Rappe, “Dirac semimetal in three dimensions,” *Phys. Rev. Lett.* **108** (Apr, 2012) 140405.
- [44] Z. K. Liu, B. Zhou, Y. Zhang, Z. J. Wang, H. M. Weng, D. Prabhakaran, S.-K. Mo, Z. X. Shen, Z. Fang, X. Dai, Z. Hussain, and Y. L. Chen, “Discovery of a three-dimensional topological dirac semimetal,  $\text{Na}_3\text{Bi}$ ,” *Science* **343** no. 6173, (2014) 864–867.
- [45] M. Neupane, S.-Y. Xu, R. Sankar, N. Alidoust, G. Bian, C. Liu, I. Belopolski, T.-R. Chang, H.-T. Jeng, H. Lin, *et al.*, “Observation of a three-dimensional topological dirac semimetal phase in high-mobility  $\text{Cd}_3\text{As}_2$ ,” *Nature communications* **5** no. 3786, (2014) .
- [46] S. Borisenko, Q. Gibson, D. Evtushinsky, V. Zabolotnyy, B. Büchner, and R. J. Cava, “Experimental realization of a three-dimensional dirac semimetal,” *Phys. Rev. Lett.* **113** (Jul, 2014) 027603.
- [47] G. W. Semenoff, “Condensed-matter simulation of a three-dimensional anomaly,” *Phys. Rev. Lett.* **53** (Dec, 1984) 2449–2452.
- [48] Y. Zhang, Y.-W. Tan, H. L. Stormer, and P. Kim, “Experimental observation of the quantum hall effect and berry’s phase in graphene,” *Nature* **438** no. 7065, (2005) 201–204.
- [49] M. Katsnelson, K. Novoselov, and A. Geim, “Chiral tunnelling and the klein paradox in graphene,” *Nature physics* **2** no. 9, (2006) 620–625.
- [50] S. Sorella and E. Tosatti, “Semi-metal-insulator transition of the hubbard model in the honeycomb lattice,” *EPL (Europhysics Letters)* **19** no. 8, (1992) 699.
- [51] D. V. Khveshchenko, “Ghost excitonic insulator transition in layered graphite,” *Phys. Rev. Lett.* **87** (Nov, 2001) 246802.
- [52] E. V. Gorbar, V. P. Gusynin, V. A. Miransky, and I. A. Shovkovy, “Magnetic field driven metal-insulator phase transition in planar systems,” *Phys. Rev. B* **66** (Jul, 2002) 045108.
- [53] O. V. Gamayun, E. V. Gorbar, and V. P. Gusynin, “Supercritical coulomb center and excitonic instability in graphene,” *Phys. Rev. B* **80** (Oct, 2009) 165429.
- [54] O. V. Gamayun, E. V. Gorbar, and V. P. Gusynin, “Gap generation and semimetal-insulator phase transition in graphene,” *Phys. Rev. B* **81** (Feb, 2010) 075429.
- [55] I. F. Herbut, “Interactions and phase transitions on graphene’s honeycomb lattice,” *Phys. Rev. Lett.* **97** (Oct, 2006) 146401.
- [56] I. F. Herbut, V. Juričić, and B. Roy, “Theory of interacting electrons on the honeycomb lattice,” *Phys. Rev. B* **79** (Feb, 2009) 085116.
- [57] C. Honerkamp, “Density waves and cooper pairing on the honeycomb lattice,” *Phys. Rev. Lett.* **100** (Apr, 2008) 146404.

- [58] I. F. Herbut, V. Juričić, and O. Vafek, “Relativistic mott criticality in graphene,” *Phys. Rev. B* **80** (Aug, 2009) 075432.
- [59] S. Raghu, X.-L. Qi, C. Honerkamp, and S.-C. Zhang, “Topological mott insulators,” *Phys. Rev. Lett.* **100** (Apr, 2008) 156401.
- [60] A. G. Grushin, E. V. Castro, A. Cortijo, F. de Juan, M. A. H. Vozmediano, and B. Valenzuela, “Charge instabilities and topological phases in the extended hubbard model on the honeycomb lattice with enlarged unit cell,” *Phys. Rev. B* **87** (Feb, 2013) 085136.
- [61] M. Daghofer and M. Hohenadler, “Phases of correlated spinless fermions on the honeycomb lattice,” *Phys. Rev. B* **89** (Jan, 2014) 035103.
- [62] T. Đurić, N. Chancellor, and I. F. Herbut, “Interaction-induced anomalous quantum hall state on the honeycomb lattice,” *Phys. Rev. B* **89** (Apr, 2014) 165123.
- [63] A. M. Black-Schaffer and S. Doniach, “Resonating valence bonds and mean-field  $d$ -wave superconductivity in graphite,” *Phys. Rev. B* **75** (Apr, 2007) 134512.
- [64] Y. Araki and G. W. Semenoff, “Spin versus charge-density-wave order in graphenelike systems,” *Phys. Rev. B* **86** (Sep, 2012) 121402.
- [65] W. Wu and A.-M. S. Tremblay, “Phase diagram and fermi liquid properties of the extended hubbard model on the honeycomb lattice,” *Phys. Rev. B* **89** (May, 2014) 205128.
- [66] L. Janssen and I. F. Herbut, “Antiferromagnetic critical point on graphene’s honeycomb lattice: A functional renormalization group approach,” *Phys. Rev. B* **89** (May, 2014) 205403.
- [67] D. D. Scherer, M. M. Scherer, and C. Honerkamp, “Correlated spinless fermions on the honeycomb lattice revisited,” *Phys. Rev. B* **92** (Oct, 2015) 155137.
- [68] Y. Volpez, D. D. Scherer, and M. M. Scherer, “Electronic instabilities of the extended Hubbard model on the honeycomb lattice from functional renormalization,” *ArXiv e-prints* (June, 2016) , [arXiv:1606.01125](#) [[cond-mat.str-el](#)].
- [69] D. Sánchez de la Peña, J. Lichtenstein, and C. Honerkamp, “Competing electronic instabilities of extended Hubbard models on the honeycomb lattice: A functional Renormalization Group calculation with high wavevector resolution,” *ArXiv e-prints* (June, 2016) , [arXiv:1606.01124](#) [[cond-mat.str-el](#)].
- [70] Z. Meng, T. Lang, S. Wessel, F. Assaad, and A. Muramatsu, “Quantum spin liquid emerging in two-dimensional correlated dirac fermions,” *Nature* **464** no. 7290, (2010) 847–851.
- [71] S. Sorella, Y. Otsuka, and S. Yunoki, “Absence of a spin liquid phase in the hubbard model on the honeycomb lattice,” *Scientific Reports* **2** no. 992, (2012) .
- [72] R. Nandkishore, L. Levitov, and A. Chubukov, “Chiral superconductivity from repulsive interactions in doped graphene,” *Nature Physics* **8** no. 2, (2012) 158–163.

- [73] M. L. Kiesel, C. Platt, W. Hanke, D. A. Abanin, and R. Thomale, “Competing many-body instabilities and unconventional superconductivity in graphene,” *Phys. Rev. B* **86** (Jul, 2012) 020507.
- [74] R. Nandkishore, G.-W. Chern, and A. V. Chubukov, “Itinerant half-metal spin-density-wave state on the hexagonal lattice,” *Phys. Rev. Lett.* **108** (May, 2012) 227204.
- [75] B. Roy, “Multicritical behavior of  $\mathbb{F}_2 \times o(2)$  gross-neveu-yukawa theory in graphene,” *Phys. Rev. B* **84** (Sep, 2011) 113404.
- [76] B. Roy and V. Juričić, “Strain-induced time-reversal odd superconductivity in graphene,” *Phys. Rev. B* **90** (Jul, 2014) 041413.
- [77] D. Elias, R. Gorbachev, A. Mayorov, S. Morozov, A. Zhukov, P. Blake, L. Ponomarenko, I. Grigorieva, K. Novoselov, F. Guinea, *et al.*, “Dirac cones reshaped by interaction effects in suspended graphene,” *Nature Physics* **7** no. 9, (2011) 701–704.
- [78] A. S. Mayorov, D. C. Elias, I. S. Mukhin, S. V. Morozov, L. A. Ponomarenko, K. S. Novoselov, A. K. Geim, and R. V. Gorbachev, “How close can one approach the dirac point in graphene experimentally?,” *Nano Letters* **12** no. 9, (2012) 4629–4634. PMID: 22935053.
- [79] T. O. Wehling, E. Şaşıoğlu, C. Friedrich, A. I. Lichtenstein, M. I. Katsnelson, and S. Blügel, “Strength of effective coulomb interactions in graphene and graphite,” *Phys. Rev. Lett.* **106** (Jun, 2011) 236805.
- [80] M. Rösner, E. Şaşıoğlu, C. Friedrich, S. Blügel, and T. O. Wehling, “Wannier function approach to realistic coulomb interactions in layered materials and heterostructures,” *Phys. Rev. B* **92** (Aug, 2015) 085102.
- [81] M. V. Ulybyshev, P. V. Buividovich, M. I. Katsnelson, and M. I. Polikarpov, “Monte carlo study of the semimetal-insulator phase transition in monolayer graphene with a realistic interelectron interaction potential,” *Phys. Rev. Lett.* **111** (Jul, 2013) 056801.
- [82] D. Smith and L. von Smekal, “Monte carlo simulation of the tight-binding model of graphene with partially screened coulomb interactions,” *Phys. Rev. B* **89** (May, 2014) 195429.
- [83] M. Golor and S. Wessel, “Nonlocal density interactions in auxiliary-field quantum monte carlo simulations: Application to the square lattice bilayer and honeycomb lattice,” *Phys. Rev. B* **92** (Nov, 2015) 195154.
- [84] H.-K. Tang, E. Laksono, J. N. B. Rodrigues, P. Sengupta, F. F. Assaad, and S. Adam, “Interaction-driven metal-insulator transition in strained graphene,” *Phys. Rev. Lett.* **115** (Oct, 2015) 186602.
- [85] V. Juričić, I. F. Herbut, and G. W. Semenoff, “Coulomb interaction at the metal-insulator critical point in graphene,” *Phys. Rev. B* **80** (Aug, 2009) 081405.
- [86] A. Katanin, “Effect of vertex corrections on the possibility of chiral symmetry breaking induced by long-range coulomb repulsion in graphene,” *Phys. Rev. B* **93** (Jan, 2016) 035132.

- [87] S. Nandi, M. G. Kim, A. Kreyssig, R. M. Fernandes, D. K. Pratt, A. Thaler, N. Ni, S. L. Bud'ko, P. C. Canfield, J. Schmalian, R. J. McQueeney, and A. I. Goldman, "Anomalous suppression of the orthorhombic lattice distortion in superconducting  $\text{Ba}(\text{Fe}_{1-x}\text{Co}_x)_2\text{As}_2$  single crystals," *Phys. Rev. Lett.* **104** (Feb, 2010) 057006.
- [88] K. Ishida, Y. Nakai, and H. Hosono, "To what extent iron-pnictide new superconductors have been clarified: A progress report," *Journal of the Physical Society of Japan* **78** no. 6, (2009) 062001.
- [89] J. Paglione and R. L. Greene, "High-temperature superconductivity in iron-based materials," *Nature Physics* **6** no. 9, (2010) 645–658.
- [90] D. C. Johnston, "The puzzle of high temperature superconductivity in layered iron pnictides and chalcogenides," *Advances in Physics* **59** no. 6, (2010) 803–1061.
- [91] H.-H. Wen and S. Li, "Materials and novel superconductivity in iron pnictide superconductors," *Annual Review of Condensed Matter Physics* **2** no. 1, (2011) 121–140, <http://dx.doi.org/10.1146/annurev-conmatphys-062910-140518>.
- [92] G. R. Stewart, "Superconductivity in iron compounds," *Rev. Mod. Phys.* **83** (Dec, 2011) 1589–1652.
- [93] R. M. Fernandes and A. V. Chubukov, "Low-energy microscopic models for iron-based superconductors: a review," *ArXiv e-prints* (July, 2016) , [arXiv:1607.00865](https://arxiv.org/abs/1607.00865) [cond-mat.str-el].
- [94] J. Lorenzana, G. Seibold, C. Ortix, and M. Grilli, "Competing orders in FeAs layers," *Phys. Rev. Lett.* **101** (Oct, 2008) 186402.
- [95] I. Eremin and A. V. Chubukov, "Magnetic degeneracy and hidden metallicity of the spin-density-wave state in ferropnictides," *Phys. Rev. B* **81** (Jan, 2010) 024511.
- [96] P. M. R. Brydon, J. Schmiedt, and C. Timm, "Microscopically derived ginzburg-landau theory for magnetic order in the iron pnictides," *Phys. Rev. B* **84** (Dec, 2011) 214510.
- [97] M. N. Gastiasoro and B. M. Andersen, "Competing magnetic double- $q$  phases and superconductivity-induced reentrance of  $C_2$  magnetic stripe order in iron pnictides," *Phys. Rev. B* **92** (Oct, 2015) 140506.
- [98] X. Wang, J. Kang, and R. M. Fernandes, "Magnetic order without tetragonal-symmetry-breaking in iron arsenides: Microscopic mechanism and spin-wave spectrum," *Phys. Rev. B* **91** (Jan, 2015) 024401.
- [99] R. M. Fernandes, S. A. Kivelson, and E. Berg, "Vestigial chiral and charge orders from bidirectional spin-density waves: Application to the iron-based superconductors," *Phys. Rev. B* **93** (Jan, 2016) 014511.
- [100] F. Krüger, S. Kumar, J. Zaanen, and J. van den Brink, "Spin-orbital frustrations and anomalous metallic state in iron-pnictide superconductors," *Phys. Rev. B* **79** (Feb, 2009) 054504.
- [101] B. Valenzuela, E. Bascones, and M. J. Calderón, "Conductivity anisotropy in the antiferromagnetic state of iron pnictides," *Phys. Rev. Lett.* **105** (Nov, 2010) 207202.

- [102] W. Lv and P. Phillips, “Orbitally and magnetically induced anisotropy in iron-based superconductors,” *Phys. Rev. B* **84** (Nov, 2011) 174512.
- [103] W.-C. Lee and P. W. Phillips, “Non-fermi liquid due to orbital fluctuations in iron pnictide superconductors,” *Phys. Rev. B* **86** (Dec, 2012) 245113.
- [104] R. Applegate, R. R. P. Singh, C.-C. Chen, and T. P. Devereaux, “Phase transitions in spin-orbital models with spin-space anisotropies for iron pnictides: Monte carlo simulations,” *Phys. Rev. B* **85** (Feb, 2012) 054411.
- [105] V. Stanev and P. B. Littlewood, “Nematicity driven by hybridization in iron-based superconductors,” *Phys. Rev. B* **87** (Apr, 2013) 161122.
- [106] P. T. Dumitrescu, M. Serbyn, R. T. Scalettar, and A. Vishwanath, “Superconductivity and Nematic Fluctuations in a model of FeSe monolayers: A Determinant Quantum Monte Carlo Study,” *ArXiv e-prints* (Dec., 2015) , [arXiv:1512.08523](https://arxiv.org/abs/1512.08523) [cond-mat.supr-con].
- [107] S. Baek, D. Efremov, J. Ok, J. Kim, J. Van Den Brink, and B. Büchner, “Orbital-driven nematicity in fese,” *Nature materials* **14** no. 2, (2015) 210–214.
- [108] Y. Gallais and I. Paul, “Charge nematicity and electronic raman scattering in iron-based superconductors,” *Comptes Rendus Physique* **17** no. 1–2, (2016) 113 – 139. Iron-based superconductors / Supraconducteurs à base de fer.
- [109] Z. Wang and A. H. Nevidomskyy, “Orbital nematic order and interplay with magnetism in the two-orbital hubbard model,” *Journal of Physics: Condensed Matter* **27** no. 22, (2015) 225602.
- [110] V. K. Thorsmølle, M. Khodas, Z. P. Yin, C. Zhang, S. V. Carr, P. Dai, and G. Blumberg, “Critical quadrupole fluctuations and collective modes in iron pnictide superconductors,” *Phys. Rev. B* **93** (Feb, 2016) 054515.
- [111] R. Fernandes, A. Chubukov, and J. Schmalian, “What drives nematic order in iron-based superconductors?,” *Nature physics* **10** no. 2, (2014) 97–104.
- [112] P. J. Hirschfeld, M. M. Korshunov, and I. I. Mazin, “Gap symmetry and structure of fe-based superconductors,” *Reports on Progress in Physics* **74** no. 12, (2011) 124508.
- [113] A. Chubukov, “Pairing mechanism in fe-based superconductors,” *Annual Review of Condensed Matter Physics* **3** no. 1, (2012) 57–92.
- [114] S. Liang, A. Moreo, and E. Dagotto, “Nematic state of pnictides stabilized by interplay between spin, orbital, and lattice degrees of freedom,” *Phys. Rev. Lett.* **111** (Jul, 2013) 047004.
- [115] K. L. Hur and T. M. Rice, “Superconductivity close to the mott state: From condensed-matter systems to superfluidity in optical lattices,” *Annals of Physics* **324** no. 7, (2009) 1452 – 1515. July 2009 Special Issue.
- [116] C. Platt, C. Honerkamp, and W. Hanke, “Pairing in the iron arsenides: a functional rg treatment,” *New Journal of Physics* **11** no. 5, (2009) 055058.



- [117] C. Platt, W. Hanke, and R. Thomale, “Functional renormalization group for multi-orbital fermi surface instabilities,” *Advances in Physics* **62** no. 4-6, (2013) 453–562.
- [118] F. Yang, F. Wang, and D.-H. Lee, “Fermiology, orbital order, orbital fluctuations, and cooper pairing in iron-based superconductors,” *Phys. Rev. B* **88** (Sep, 2013) 100504.
- [119] A. V. Chubukov, D. V. Efremov, and I. Eremin, “Magnetism, superconductivity, and pairing symmetry in iron-based superconductors,” *Phys. Rev. B* **78** (Oct, 2008) 134512.
- [120] D. Podolsky, H.-Y. Kee, and Y. B. Kim, “Collective modes and emergent symmetry of superconductivity and magnetism in the iron pnictides,” *EPL (Europhysics Letters)* **88** no. 1, (2009) 17004.
- [121] S. Maiti and A. V. Chubukov, “Renormalization group flow, competing phases, and the structure of superconducting gap in multiband models of iron-based superconductors,” *Phys. Rev. B* **82** (Dec, 2010) 214515.
- [122] A. V. Chubukov, M. Khodas, and R. M. Fernandes, “Magnetism, superconductivity, and spontaneous orbital order in iron-based superconductors: who comes first and why?,” *arXiv preprint arXiv:1602.05503* (2016) .
- [123] Y. Yamakawa, S. Onari, and H. Kontani, “Nematicity and magnetism in fese and other families of fe-based superconductors,” *Phys. Rev. X* **6** (Jun, 2016) 021032.
- [124] V. Cvetkovic and Z. Tesanovic, “Valley density-wave and multiband superconductivity in iron-based pnictide superconductors,” *Phys. Rev. B* **80** (Jul, 2009) 024512.
- [125] L. Classen, M. M. Scherer, and C. Honerkamp, “Instabilities on graphene’s honeycomb lattice with electron-phonon interactions,” *Phys. Rev. B* **90** (Jul, 2014) 035122.
- [126] M. Golor, T. Reckling, L. Classen, M. M. Scherer, and S. Wessel, “Ground-state phase diagram of the half-filled bilayer hubbard model,” *Phys. Rev. B* **90** (Nov, 2014) 195131.
- [127] L. Classen, I. F. Herbut, L. Janssen, and M. M. Scherer, “Mott multicriticality of dirac electrons in graphene,” *Phys. Rev. B* **92** (Jul, 2015) 035429.
- [128] L. Classen, I. F. Herbut, L. Janssen, and M. M. Scherer, “Competition of density waves and quantum multicritical behavior in dirac materials from functional renormalization,” *Phys. Rev. B* **93** (Mar, 2016) 125119.
- [129] M. Sigrist and K. Ueda, “Phenomenological theory of unconventional superconductivity,” *Rev. Mod. Phys.* **63** (Apr, 1991) 239–311.
- [130] D. Scalapino, “The case for dx<sup>2</sup>-y<sup>2</sup> pairing in the cuprate superconductors,” *Physics Reports* **250** no. 6, (1995) 329 – 365.
- [131] C. C. Tsuei and J. R. Kirtley, “Pairing symmetry in cuprate superconductors,” *Rev. Mod. Phys.* **72** (Oct, 2000) 969–1016.
- [132] N. P. Armitage, P. Fournier, and R. L. Greene, “Progress and perspectives on electron-doped cuprates,” *Rev. Mod. Phys.* **82** (Sep, 2010) 2421–2487.
- [133] A. J. Leggett, “A theoretical description of the new phases of liquid <sup>3</sup>He,” *Rev. Mod. Phys.* **47** (Apr, 1975) 331–414.

- [134] D. Vollhardt and P. Wölfle, “The superfluid phases of  $^3\text{He}$ ,” *Taylor & Francis, London* (1990) .
- [135] A. P. Mackenzie and Y. Maeno, “The superconductivity of  $\text{Sr}_2\text{RuO}_4$  and the physics of spin-triplet pairing,” *Rev. Mod. Phys.* **75** (May, 2003) 657–712.
- [136] B. Roy and I. F. Herbut, “Unconventional superconductivity on honeycomb lattice: Theory of Kekulé order parameter,” *Phys. Rev. B* **82** (Jul, 2010) 035429.
- [137] P. Fulde and R. A. Ferrell, “Superconductivity in a strong spin-exchange field,” *Phys. Rev.* **135** (Aug, 1964) A550–A563.
- [138] A. Larkin and I. Ovchinnikov, “Inhomogeneous state of superconductors (production of superconducting state in ferromagnet with Fermi surfaces, examining Green function),” *Soviet Physics-JETP* **20** (1965) 762–769.
- [139] R. Casalbuoni and G. Nardulli, “Inhomogeneous superconductivity in condensed matter and QCD,” *Rev. Mod. Phys.* **76** (Feb, 2004) 263–320.
- [140] M. Vojta, “Lattice symmetry breaking in cuprate superconductors: stripes, nematics, and superconductivity,” *Advances in Physics* **58** no. 6, (2009) 699–820.
- [141] S. A. Kivelson, G. Aeppli, and V. J. Emery, “Thermodynamics of the interplay between magnetism and high-temperature superconductivity,” *Proceedings of the National Academy of Sciences* **98** no. 21, (2001) 11903–11907.
- [142] P. Calabrese, A. Pelissetto, and E. Vicari, “Multicritical phenomena in  $O(n_1) \oplus O(n_2)$ -symmetric theories,” *Phys. Rev. B* **67** (Feb, 2003) 054505.
- [143] A. Eichhorn, D. Mesterházy, and M. M. Scherer, “Stability of fixed points and generalized critical behavior in multifold models,” *Phys. Rev. E* **90** (Nov, 2014) 052129.
- [144] D. Belitz, T. R. Kirkpatrick, and T. Vojta, “How generic scale invariance influences quantum and classical phase transitions,” *Rev. Mod. Phys.* **77** (Jul, 2005) 579–632.
- [145] B. Rosenstein, H.-L. Yu, and A. Kovner, “Critical exponents of new universality classes,” *Physics Letters B* **314** no. 3, (1993) 381 – 386.
- [146] K. G. Wilson, “Renormalization group and critical phenomena. i. renormalization group and the Kadanoff scaling picture,” *Phys. Rev. B* **4** (Nov, 1971) 3174–3183.
- [147] K. G. Wilson, “Renormalization group and critical phenomena. ii. phase-space cell analysis of critical behavior,” *Phys. Rev. B* **4** (Nov, 1971) 3184–3205.
- [148] S. Maiti and A. V. Chubukov, “Superconductivity from repulsive interaction,” *AIP Conference Proceedings* **1550** no. 1, (2013) 3–73.
- [149] S. Maiti and A. V. Chubukov, “Renormalization group flow, competing phases, and the structure of superconducting gap in multiband models of iron-based superconductors,” *Phys. Rev. B* **82** (Dec, 2010) 214515.



- [150] B.-J. Schaefer, R. Alkofer, C. Fischer, I. Boettcher, J. M. Pawłowski, and S. Diehl, ““physics at all scales: The renormalization group” proceedings of the 49th internationale universitätswochen für theoretische physik ultracold atoms and the functional renormalization group,” *Nuclear Physics B - Proceedings Supplements* **228** (2012) 63 – 135.
- [151] C. Wetterich, “Exact evolution equation for the effective potential,” *Physics Letters B* **301** no. 1, (1993) 90 – 94.
- [152] J. Borchardt and B. Knorr, “Global solutions of functional fixed point equations via pseudospectral methods,” *Phys. Rev. D* **91** (May, 2015) 105011.
- [153] D. F. Litim and D. Zappalà, “Ising exponents from the functional renormalization group,” *Phys. Rev. D* **83** (Apr, 2011) 085009.
- [154] D. F. Litim, “Optimisation of the exact renormalisation group,” *Physics Letters B* **486** no. 1–2, (2000) 92 – 99.
- [155] D. F. Litim, “Optimized renormalization group flows,” *Phys. Rev. D* **64** (Oct, 2001) 105007.
- [156] D. F. LITIM, “Mind the gap,” *International Journal of Modern Physics A* **16** no. 11, (2001) 2081–2087.
- [157] D. F. Litim, “Critical exponents from optimised renormalisation group flows,” *Nuclear Physics B* **631** no. 1–2, (2002) 128 – 158.
- [158] J. M. Pawłowski, M. M. Scherer, R. Schmidt, and S. J. Wetzel, “Physics and the choice of regulators in functional renormalisation group flows,” *ArXiv e-prints* (Dec., 2015) , [arXiv:1512.03598](https://arxiv.org/abs/1512.03598) [hep-th].
- [159] M. Salmhofer and C. Honerkamp, “Fermionic renormalization group flows: Technique and theory,” *Progress of Theoretical Physics* **105** no. 1, (2001) 1–35.
- [160] G. A. H. Schober, K.-U. Giering, M. M. Scherer, C. Honerkamp, and M. Salmhofer, “Functional renormalization and mean-field approach to multiband systems with spin-orbit coupling: Application to the rashba model with attractive interaction,” *Phys. Rev. B* **93** (Mar, 2016) 115111.
- [161] A. Eberlein and W. Metzner, “Superconductivity in the two-dimensional  $t$ - $t'$ -hubbard model,” *Phys. Rev. B* **89** (Jan, 2014) 035126.
- [162] S. Shimizu, H. Mukuda, Y. Kitaoka, A. Iyo, Y. Tanaka, Y. Kodama, K. Tokiwa, and T. Watanabe, “Uniform mixing of antiferromagnetism and high-temperature superconductivity in electron-doped layers of four-layered  $\text{Ba}_2\text{Ca}_3\text{Cu}_4\text{O}_8\text{F}_2$ : A new phenomenon in an electron underdoped regime,” *Phys. Rev. Lett.* **98** (Jun, 2007) 257002.
- [163] H. Zhai, F. Wang, and D.-H. Lee, “Antiferromagnetically driven electronic correlations in iron pnictides and cuprates,” *Phys. Rev. B* **80** (Aug, 2009) 064517.
- [164] S. S. Kancharla and S. Okamoto, “Band insulator to mott insulator transition in a bilayer hubbard model,” *Phys. Rev. B* **75** (May, 2007) 193103.

- [165] K. Bouadim, G. G. Batrouni, F. Hébert, and R. T. Scalettar, “Magnetic and transport properties of a coupled hubbard bilayer with electron and hole doping,” *Phys. Rev. B* **77** (Apr, 2008) 144527.
- [166] S. Sachdev, *Quantum Phase Transitions*. Cambridge University Press, 1999.
- [167] M. E. Fisher, “The renormalization group in the theory of critical behavior,” *Rev. Mod. Phys.* **46** (Oct, 1974) 597–616.
- [168] H. B. Heersche, P. Jarillo-Herrero, J. B. Oostinga, L. M. Vandersypen, and A. F. Morpurgo, “Bipolar supercurrent in graphene,” *Nature* **446** no. 7131, (2007) 56–59.
- [169] S. Ichinokura, K. Sugawara, A. Takayama, T. Takahashi, and S. Hasegawa, “Superconducting calcium-intercalated bilayer graphene,” *ACS Nano* **10** no. 2, (2016) 2761–2765.
- [170] E. R. Margine, H. Lambert, and F. Giustino, “Electron-phonon interaction and pairing mechanism in superconducting Ca-intercalated bilayer graphene,” *Scientific Reports* **6** (Feb., 2016) 21414, [arXiv:1601.06111 \[cond-mat.supr-con\]](#).
- [171] B. Uchoa and A. H. Castro Neto, “Superconducting states of pure and doped graphene,” *Phys. Rev. Lett.* **98** (Apr, 2007) 146801.
- [172] D. M. Basko and I. L. Aleiner, “Interplay of coulomb and electron-phonon interactions in graphene,” *Phys. Rev. B* **77** (Jan, 2008) 041409.
- [173] N. B. Kopnin and E. B. Sonin, “Bcs superconductivity of dirac electrons in graphene layers,” *Phys. Rev. Lett.* **100** (Jun, 2008) 246808.
- [174] M. Einenkel and K. B. Efetov, “Possibility of superconductivity due to electron-phonon interaction in graphene,” *Phys. Rev. B* **84** (Dec, 2011) 214508.
- [175] S. Piscanec, M. Lazzeri, F. Mauri, A. C. Ferrari, and J. Robertson, “Kohn anomalies and electron-phonon interactions in graphite,” *Phys. Rev. Lett.* **93** (Oct, 2004) 185503.
- [176] K. Nomura, S. Ryu, and D.-H. Lee, “Field-induced kosterlitz-thouless transition in the  $n = 0$  landau level of graphene,” *Phys. Rev. Lett.* **103** (Nov, 2009) 216801.
- [177] M. Kharitonov, “Phase diagram for the  $\nu = 0$  quantum hall state in monolayer graphene,” *Phys. Rev. B* **85** (Apr, 2012) 155439.
- [178] Y. Jia, H. Guo, Z. Chen, S.-Q. Shen, and S. Feng, “Effect of interactions on two-dimensional dirac fermions,” *Phys. Rev. B* **88** (Aug, 2013) 075101.
- [179] N. A. García-Martínez, A. G. Grushin, T. Neupert, B. Valenzuela, and E. V. Castro, “Interaction-driven phases in the half-filled spinless honeycomb lattice from exact diagonalization,” *Phys. Rev. B* **88** (Dec, 2013) 245123.
- [180] S. Capponi and A. M. Läuchli, “Phase diagram of interacting spinless fermions on the honeycomb lattice: A comprehensive exact diagonalization study,” *Phys. Rev. B* **92** (Aug, 2015) 085146.

- [181] J. Motruk, A. G. Grushin, F. de Juan, and F. Pollmann, “Interaction-driven phases in the half-filled honeycomb lattice: An infinite density matrix renormalization group study,” *Phys. Rev. B* **92** (Aug, 2015) 085147.
- [182] M. M. Scherer, S. Uebelacker, and C. Honerkamp, “Instabilities of interacting electrons on the honeycomb bilayer,” *Phys. Rev. B* **85** (Jun, 2012) 235408.
- [183] M. M. Scherer, S. Uebelacker, D. D. Scherer, and C. Honerkamp, “Interacting electrons on trilayer honeycomb lattices,” *Phys. Rev. B* **86** (Oct, 2012) 155415.
- [184] M. Lazzeri, C. Attaccalite, L. Wirtz, and F. Mauri, “Impact of the electron-electron correlation on phonon dispersion: Failure of lda and gga dft functionals in graphene and graphite,” *Phys. Rev. B* **78** (Aug, 2008) 081406.
- [185] E. Cappelluti and G. Profeta, “Hopping-resolved electron-phonon coupling in bilayer graphene,” *Phys. Rev. B* **85** (May, 2012) 205436.
- [186] J. Jiang, R. Saito, G. G. Samsonidze, S. G. Chou, A. Jorio, G. Dresselhaus, and M. S. Dresselhaus, “Electron-phonon matrix elements in single-wall carbon nanotubes,” *Phys. Rev. B* **72** (Dec, 2005) 235408.
- [187] C.-H. Park, F. Giustino, M. L. Cohen, and S. G. Louie, “Electron-phonon interactions in graphene, bilayer graphene, and graphite,” *Nano Letters* **8** no. 12, (2008) 4229–4233.
- [188] H. C. Fu, C. Honerkamp, and D.-H. Lee, “Renormalization group study of the electron-phonon interaction in high- $T_c$  cuprates,” *EPL (Europhysics Letters)* **75** no. 1, (2006) 146.
- [189] C. Honerkamp, H. C. Fu, and D.-H. Lee, “Phonons and  $d$ -wave pairing in the two-dimensional hubbard model,” *Phys. Rev. B* **75** (Jan, 2007) 014503.
- [190] S. Uebelacker and C. Honerkamp, “Self-energy feedback and frequency-dependent interactions in the functional renormalization group flow for the two-dimensional hubbard model,” *Phys. Rev. B* **86** (Dec, 2012) 235140.
- [191] K.-U. Giering and M. Salmhofer, “Self-energy flows in the two-dimensional repulsive hubbard model,” *Phys. Rev. B* **86** (Dec, 2012) 245122.
- [192] C. Chamon, “Solitons in carbon nanotubes,” *Phys. Rev. B* **62** (Jul, 2000) 2806–2812.
- [193] C.-Y. Hou, C. Chamon, and C. Mudry, “Electron fractionalization in two-dimensional graphenelike structures,” *Phys. Rev. Lett.* **98** (May, 2007) 186809.
- [194] A. L. Tchougreeff and R. Hoffmann, “Charge and spin density waves in the electronic structure of graphite: application to analysis of stm images,” *The Journal of Physical Chemistry* **96** no. 22, (1992) 8993–8998.
- [195] W. Bao, J. Velasco, F. Zhang, L. Jing, B. Standley, D. Smirnov, M. Bockrath, A. H. MacDonald, and C. N. Lau, “Evidence for a spontaneous gapped state in ultraclean bilayer graphene,” *Proceedings of the National Academy of Sciences* **109** no. 27, (2012) 10802–10805.

- [196] J. Velasco Jr, L. Jing, W. Bao, Y. Lee, P. Kratz, V. Aji, M. Bockrath, C. Lau, C. Varma, R. Stillwell, *et al.*, “Transport spectroscopy of symmetry-broken insulating states in bilayer graphene,” *Nature Nanotechnology* **7** no. 3, (2012) 156–160.
- [197] A. S. Mayorov, D. C. Elias, M. Mucha-Kruczynski, R. V. Gorbachev, T. Tudorovskiy, A. Zhukov, S. V. Morozov, M. I. Katsnelson, A. K. Geim, and K. S. Novoselov, “Interaction-driven spectrum reconstruction in bilayer graphene,” *Science* **333** no. 6044, (2011) 860–863.
- [198] O. Vafek and K. Yang, “Many-body instability of coulomb interacting bilayer graphene: Renormalization group approach,” *Phys. Rev. B* **81** (Jan, 2010) 041401.
- [199] O. Vafek, “Interacting fermions on the honeycomb bilayer: From weak to strong coupling,” *Phys. Rev. B* **82** (Nov, 2010) 205106.
- [200] R. E. Throckmorton and O. Vafek, “Fermions on bilayer graphene: Symmetry breaking for  $b = 0$  and  $\nu = 0$ ,” *Phys. Rev. B* **86** (Sep, 2012) 115447.
- [201] V. Cvetkovic, R. E. Throckmorton, and O. Vafek, “Electronic multicriticality in bilayer graphene,” *Phys. Rev. B* **86** (Aug, 2012) 075467.
- [202] Y. Lemonik, I. L. Aleiner, C. Toke, and V. I. Fal’ko, “Spontaneous symmetry breaking and lifshitz transition in bilayer graphene,” *Phys. Rev. B* **82** (Nov, 2010) 201408.
- [203] Y. Lemonik, I. Aleiner, and V. I. Fal’ko, “Competing nematic, antiferromagnetic, and spin-flux orders in the ground state of bilayer graphene,” *Phys. Rev. B* **85** (Jun, 2012) 245451.
- [204] J. Yuan, D.-H. Xu, H. Wang, Y. Zhou, J.-H. Gao, and F.-C. Zhang, “Possible half-metallic phase in bilayer graphene: Calculations based on mean-field theory applied to a two-layer hubbard model,” *Phys. Rev. B* **88** (Nov, 2013) 201109.
- [205] O. Pavlovsky, A. Sinelnikova, and M. Ulybyshev, “Monte-Carlo simulation of graphene in terms of occupation numbers for the excitonic order parameter at hexagonal lattice,” [arXiv:1311.2420](https://arxiv.org/abs/1311.2420) [*cond-mat.str-el*].
- [206] A. Eberlein, “Fermionic two-loop functional renormalization group for correlated fermions: Method and application to the attractive hubbard model,” *Phys. Rev. B* **90** (Sep, 2014) 115125.
- [207] L. Rosa, P. Vitale, and C. Wetterich, “Critical exponents of the gross-neveu model from the effective average action,” *Phys. Rev. Lett.* **86** (Feb, 2001) 958–961.
- [208] F. Höfling, C. Nowak, and C. Wetterich, “Phase transition and critical behavior of the  $d = 3$  gross-neveu model,” *Phys. Rev. B* **66** (Nov, 2002) 205111.
- [209] F. F. Assaad and I. F. Herbut, “Pinning the order: The nature of quantum criticality in the hubbard model on honeycomb lattice,” *Phys. Rev. X* **3** (Aug, 2013) 031010.
- [210] L. Wang, P. Corboz, and M. Troyer, “Fermionic quantum critical point of spinless fermions on a honeycomb lattice,” *New Journal of Physics* **16** no. 10, (2014) 103008.

- [211] G. P. Vacca and L. Zambelli, “Multimeson yukawa interactions at criticality,” *Phys. Rev. D* **91** (Jun, 2015) 125003.
- [212] L. Kärkkäinen, R. Lacaze, P. Lacock, and B. Petersson, “Critical behaviour of the three-dimensional gross-neveu and higgs-yukawa models,” *Nuclear Physics B* **415** no. 3, (1994) 781 – 796.
- [213] Y. Otsuka, S. Yunoki, and S. Sorella, “Universal quantum criticality in the metal-insulator transition of two-dimensional interacting dirac electrons,” *Phys. Rev. X* **6** (Mar, 2016) 011029.
- [214] I. F. Herbut and Z. Tešanović, “Herbut and tešanović reply:,” *Phys. Rev. Lett.* **78** (Feb, 1997) 980–980.
- [215] L. Fei, S. Giombi, I. R. Klebanov, and G. Tarnopolsky, “Three loop analysis of the critical  $o(n)$  models in  $6 - \epsilon$  dimensions,” *Phys. Rev. D* **91** (Feb, 2015) 045011.
- [216] F. Gehring, H. Gies, and L. Janssen, “Fixed-point structure of low-dimensional relativistic fermion field theories: Universality classes and emergent symmetry,” *Phys. Rev. D* **92** (Oct, 2015) 085046.
- [217] F. D. M. Haldane, “Model for a quantum hall effect without landau levels: Condensed-matter realization of the “parity anomaly”,” *Phys. Rev. Lett.* **61** (Oct, 1988) 2015–2018.
- [218] J. M. Pawłowski, M. M. Scherer, R. Schmidt, and S. J. Wetzel, “Physics and the choice of regulators in functional renormalisation group flows,” *arXiv preprint arXiv:1512.03598* (2015) .
- [219] V. I. Yukalov and S. Gluzman, “Self-similar exponential approximants,” *Phys. Rev. E* **58** (Aug, 1998) 1359–1382.
- [220] M. Campostrini, M. Hasenbusch, A. Pelissetto, P. Rossi, and E. Vicari, “Critical exponents and equation of state of the three-dimensional heisenberg universality class,” *Phys. Rev. B* **65** (Apr, 2002) 144520.
- [221] M. Hasenbusch, “Finite size scaling study of lattice models in the three-dimensional ising universality class,” *Phys. Rev. B* **82** (Nov, 2010) 174433.
- [222] F. Parisen Toldin, M. Hohenadler, F. F. Assaad, and I. F. Herbut, “Fermionic quantum criticality in honeycomb and  $\pi$ -flux hubbard models: Finite-size scaling of renormalization-group-invariant observables from quantum monte carlo,” *Phys. Rev. B* **91** (Apr, 2015) 165108.
- [223] I. S. Gradshteyn and I. M. Ryzhik, *Table of integrals, series, and products*. Academic press, 2014.
- [224] N. Khan, J. M. Pawłowski, F. Rennecke, and M. M. Scherer, “The Phase Diagram of QC2D from Functional Methods,” *ArXiv e-prints* (Dec., 2015) , [arXiv:1512.03673 \[hep-ph\]](#).
- [225] B.-J. Schaefer and J. Wambach, “The phase diagram of the quark–meson model,” *Nuclear Physics A* **757** no. 3, (2005) 479 – 492.

- [226] J. M. Pawłowski and F. Rennecke, “Higher order quark-mesonic scattering processes and the phase structure of qcd,” *Phys. Rev. D* **90** (Oct, 2014) 076002.
- [227] G. van Miert and C. M. Smith, “Dirac cones beyond the honeycomb lattice: A symmetry-based approach,” *Phys. Rev. B* **93** (Jan, 2016) 035401.
- [228] Z. Yin, K. Haule, and G. Kotliar, “Spin dynamics and orbital-antiphase pairing symmetry in iron-based superconductors,” *Nature Physics* **10** no. 11, (2014) 845–850.
- [229] A. F. Kemper, T. A. Maier, S. Graser, H.-P. Cheng, P. J. Hirschfeld, and D. J. Scalapino, “Sensitivity of the superconducting state and magnetic susceptibility to key aspects of electronic structure in ferropnictides,” *New Journal of Physics* **12** no. 7, (2010) 073030.
- [230] S. Graser, T. A. Maier, P. J. Hirschfeld, and D. J. Scalapino, “Near-degeneracy of several pairing channels in multiorbital models for the fe pnictides,” *New Journal of Physics* **11** no. 2, (2009) 025016.
- [231] V. Cvetkovic and O. Vafek, “Space group symmetry, spin-orbit coupling, and the low-energy effective hamiltonian for iron-based superconductors,” *Phys. Rev. B* **88** (Oct, 2013) 134510.
- [232] M. D. Watson, T. K. Kim, A. A. Haghighirad, N. R. Davies, A. McCollam, A. Narayanan, S. F. Blake, Y. L. Chen, S. Ghannadzadeh, A. J. Schofield, M. Hoesch, C. Meingast, T. Wolf, and A. I. Coldea, “Emergence of the nematic electronic state in fese,” *Phys. Rev. B* **91** (Apr, 2015) 155106.
- [233] Y. Suzuki, T. Shimojima, T. Sonobe, A. Nakamura, M. Sakano, H. Tsuji, J. Omachi, K. Yoshioka, M. Kuwata-Gonokami, T. Watashige, R. Kobayashi, S. Kasahara, T. Shibauchi, Y. Matsuda, Y. Yamakawa, H. Kontani, and K. Ishizaka, “Momentum-dependent sign inversion of orbital order in superconducting fese,” *Phys. Rev. B* **92** (Nov, 2015) 205117.
- [234] Y. Zhang, M. Yi, Z.-K. Liu, W. Li, J. Lee, R. Moore, M. Hashimoto, N. Masamichi, H. Eisaki, S.-K. Mo, *et al.*, “Distinctive momentum dependence of the band reconstruction in the nematic state of fese thin film,” *arXiv preprint arXiv:1503.01556* (2015) .
- [235] P. Zhang, T. Qian, P. Richard, X. P. Wang, H. Miao, B. Q. Lv, B. B. Fu, T. Wolf, C. Meingast, X. X. Wu, Z. Q. Wang, J. P. Hu, and H. Ding, “Observation of two distinct  $d_{xz}/d_{yz}$  band splittings in fese,” *Phys. Rev. B* **91** (Jun, 2015) 214503.
- [236] K. Kothapalli, A. Böhmer, W. Jayasekara, B. Ueland, P. Das, A. Sapkota, V. Taufour, Y. Xiao, E. Alp, S. Bud’ko, *et al.*, “Strong cooperative coupling of pressure-induced magnetic order and nematicity in fese,” *arXiv preprint arXiv:1603.04135* (2016) .
- [237] A. Fedorov, A. Yaresko, T. K. Kim, E. Kushnirenko, E. Haubold, T. Wolf, M. Hoesch, A. Grueneis, B. Buechner, and S. V. Borisenko, “Effect of nematic ordering on electronic structure of FeSe,” *ArXiv e-prints* (June, 2016) , [arXiv:1606.03022 \[cond-mat.supr-con\]](#).
- [238] R. M. Fernandes, M. Khodas, and A. V. Chubukov, “,” *in preparation* (2016) .

- [239] R. M. Fernandes, A. V. Chubukov, J. Knolle, I. Eremin, and J. Schmalian, “Preemptive nematic order, pseudogap, and orbital order in the iron pnictides,” *Phys. Rev. B* **85** (Jan, 2012) 024534.
- [240] P. C. Canfield and S. L. Bud’Ko, “Feas-based superconductivity: a case study of the effects of transition metal doping on  $\text{BaFe}_2\text{As}_2$ ,” *arXiv preprint arXiv:1002.0858* (2010) .
- [241] O. Vafek and A. V. Chubukov, “,” *in preparation* (2016) .
- [242] R. M. Fernandes and O. Vafek, “Distinguishing spin-orbit coupling and nematic order in the electronic spectrum of iron-based superconductors,” *Phys. Rev. B* **90** (Dec, 2014) 214514.
- [243] M. N. Gastiasoro, I. Eremin, R. M. Fernandes, and B. M. Andersen, “Scanning tunneling spectroscopy as a probe of multi-q magnetic states of itinerant magnets,” *arXiv preprint arXiv:1607.04711* (2016) .
- [244] P. Chandra, P. Coleman, and A. I. Larkin, “Ising transition in frustrated heisenberg models,” *Phys. Rev. Lett.* **64** (Jan, 1990) 88–91.
- [245] C. Fang, H. Yao, W.-F. Tsai, J. Hu, and S. A. Kivelson, “Theory of electron nematic order in  $\text{LaFeAsO}$ ,” *Phys. Rev. B* **77** (Jun, 2008) 224509.
- [246] C. Xu, M. Müller, and S. Sachdev, “Ising and spin orders in the iron-based superconductors,” *Phys. Rev. B* **78** (Jul, 2008) 020501.
- [247] F. K. Kunst, C. Delerue, C. M. Smith, and V. Juričić, “Kekule versus hidden superconducting order in graphene-like systems: Competition and coexistence,” *Phys. Rev. B* **92** (Oct, 2015) 165423.
- [248] R.-Q. Xing, L. Classen, M. Khoads, and A. V. Chubukov, “,” *in preparation* (2016) .
- [249] L. Janssen and H. Gies, “Critical behavior of the  $(2 + 1)$ -dimensional thirring model,” *Phys. Rev. D* **86** (Nov, 2012) 105007.